X-ray binary systems and the internal structure of compact stars

Gabriela Urbancová

DISSERTATION

Silesian University in Opava, Faculty of Philosophy and Science
Centre of Interdisciplinary studies

X-ray binary systems and the internal structure of compact stars

Gabriela Urbancová

Supervisor: doc. RNDr. Gabriel Török, Ph.D.

DISSERTATION OPAVA 2021

SLEZSKÁ UNIVERZITA V OPAVĚ
Filozoficko-přírodovědecká fakulta v Opavě

ZADÁNÍ DISERTAČNÍ PRÁCE

Akademický rok: 2021/2022

Zadávající ústav: Ústav fyziky

Studentka: Mgr. Gabriela Urbancová

UČO: 26821

Program: Fyzika (čtyřletá)

Obor: Teoretická fyzika a astrofyzika

Téma práce: Rentgenové binární systémy a vnitřní struktura kompaktních hvězd

Téma práce anglicky: X-ray binary systems and the internal structure of compact stars

Zadání: Student se zaměří na výzkum vnitřní struktury neutronových hvězd, implikovanou geometrií vnějšího prostoročasu a související podpisy této struktury ve variabilitě a spektrech pozorovaného záření rentgenových binárních systémů.

Literatura:

Lewin, W.; van der Klis, M.: Compact Stellar X-ray Sources. Compact Stellar X-ray Sources, by Edited by Walter Lewin, Michiel van der Klis, Cambridge, UK: Cambridge University Press, 2010.

F. Weber: Pulsars as astrophysical laboratories for nuclear and particle physics, Bristol, U. K., Institute of Physics, 1999. QB

Török, G.; Bakala, P.; Šrámková, E.; Stuchlík, Z.; Urbanec, M.: On Mass Constraints Implied by the Relativistic Precession Model of Twin-peak Quasi-periodic Oscillations in Circinus X-1, The Astrophysical Journal, Volume 714, Issue 1, pp. 748-757, 2010.

Hartle, J.B.; Thorne, K. S.: Slowly Rotating Relativistic Stars. II. Models for Neutron Stars and Supermassive Stars, The Astrophysical Journal, Volume 153, 1968.

Vedoucí práce: doc. RNDr. Gabriel Török, Ph.D.

Datum zadání práce: 27. 10. 2021

Souhlasím se zadáním (podpis, datum):

.....
RNDr. Tomáš Gráf, Ph.D.
vedoucí ústavu

Acknowledgment

I would like to thank my supervisor Dr. Gabriel Török for his leadership, help, and encouragement, and Prof. Zdeněk Stuchlík for numerous helpful suggestions and comments. I thank Dr. Stanislav Hledík, whose Latex class I used to compile this work.

Special thanks go to my colleagues and close friends Katka, Debi, Monika, Eva, Andrea and Lenka for lots of discussions and endless help.

Many thanks also belong to Prof. Vladimír Karas and Dr. Michal Dovčiak, and others from the Astronomical Institute of the Czech Academy of Sciences in Prague for a warm welcome and very kind hospitality during my stay at their Institute.

I would like to thank Prof. John Miller for all fruitful discussions and advice connected to the slowly rotating neutron stars and for a very kind hospitality during our stays at the University of Oxford.

I am very grateful to my parents Jana and Zdeněk, and my sisters Radka and Alena, for their endless support and patience during the whole study. Finally, great thanks go to my beloved husband, Martin, thanks to whom I found enough strength to write this thesis.

Contents

II. Collection of the papers

„Pulsars are in an ideal part of the universe to test Einstein's theory of relativity - so far, it's holding up well. They may even one day act as navigational beacons for spacecraft. I'll never tire of them; they really are the most extraordinary objects."

Jocelyn Bell Burnell

Preface

This dissertation thesis written in the form of annotated collection of papers presents results I have achieved in the field of astrophysics of neutron stars during my doctoral study. I collaborated on four papers that have been published in prestigious international journals and four proceedings papers. In two papers I was the main author. I am also a co-author of two more papers in preparation that have a direct relation to the subject of this dissertation.

The list of published papers

- TÖRÖK, G.; URBANEC, M.; ADÁMEK, K. & URBANCOVÁ, G.: Appearance of innermost stable circular orbits of accretion discs around rotating NSs. *Astronomy & Astrophysics: Letters*, **564**, L5, 2014, 1403.3728.

- HAMIL, O.; STONE, J. R.; URBANEC, M. & URBANCOVÁ, G.: Braking index of isolated pulsars. *Physical Review D*, **91**, 063007, 2015, 1608.01383.

- TÖRÖK, G.; GOLUCHOVÁ, K.; URBANEC, M.; ŠRÁMKOVÁ, E.; ADÁMEK, K.; URBANCOVÁ, G.; PECHÁČEK, T.; BAKALA, P.; STUCHLÍK, Z.; HORÁK, J. & JURYŠEK, J.: Constraining Models of Twin-Peak Quasi-periodic Oscillations with Realistic Neutron Star Equations of State. *The Astrophysical Journal*, **833**, 273, 2016, 1611.06087.

- URBANCOVÁ, G.; URBANEC, M.; TÖRÖK, G.; STUCHLÍK, Z.; BLASCHKE, M. & MILLER, JOHN C.: Epicyclic Oscillations in the Hartle-Thorne External Geometry. *The Astrophysical Journal*, **877**, 66, 2019, 1905.00730.

The list of proceedings and submitted papers

- TÖRÖK G.; GOLUCHOVÁ K.; URBANEC M.; ŠRÁMKOVÁ E.; ADÁMEK K.; URBANCOVÁ G.; PECHÁČEK T.; BAKALA P.; STUCHLÍK Z.; HORÁK J. &

JURYŠEK J.: Confronting models of twin peak quasi-periodic oscillations: Mass and spin estimates fixed by neutron star equation of state. *Proceedings of RAGtime 14-16: Workshops on black holes and neutron stars*, pp. 269-282, December 2014.

- URBANCOVÁ G.; TÖRÖK G. & URBANEC M.: Neutron Star Parameters Implied by Models of Quasi-periodic Oscillations. *Proceedings of the 23rd Annual Conference of Doctoral Students – WDS 2014*, pp. 26–31, 2014, ISBN 978-80-7378-276-4.

- HAMIL O.; STONE J. R.; URBANEC M. & URBANCOVÁ, G.: Braking index of isolated uniformly rotating magnetized pulsars. *Conference proceeding: Compact Stars in the QCD Phase Diagram IV (CSQCDIV)* September 26-30, 2014, Prerow, Germany, `1503.09122`.

- GOLUCHOVÁ K.; TÖRÖK G.; URBANEC M.; URBANCOVÁ G. & ŠRÁMKOVÁ E.: Innermost stable circular orbits around compact stars: Terms that are quadratic in spin.*Proceedings of RAGtime 17-19: Workshops on Black Holes and Neutron Stars*, pp. 23-32, December 2017.

- TÖRÖK G.; KOTRLOVÁ A.; MATUSZKOVÁ M.; KLIMOVIČOVÁ K.; LANČOVÁ D.; URBANCOVÁ G. & ŠRÁMKOVÁ E.: Simple analytic formula relating the mass and spin of accreting compact objects to their rapid X-ray variability. *Submitted to The Astrophysical Journal*.

- MATUSZKOVÁ M.; KLIMOVIČOVÁ K.; URBANCOVÁ G.;LANČOVÁ D.; HORÁK J.; ŠRÁMKOVÁ E.; URBANEC M. & TÖRÖK G.: Oscillation and precession frequencies of fluid in accretion disks around neutron stars: practical formulae. *To be submitted to Astronomy & Astrophysics*.

I. Annotation

Chapter 1

Introduction: Exploring relativistic binary systems via X-ray observations

The annotation consists of five chapters whose aim is to briefly review our results and put them into a broader context of the X-ray astrophysics. In this chapter, we introduce X-ray satellites as a powerful tool for exploring the strong gravity physics and ultra-dense matter behaviour. In the second chapter, we focus on the neutron star (NS) interior, its influence on the external spacetime, and our particular results in the field of NS modelling. The third chapter summarises our published work on the exploration of geodesic orbital motion in the innermost parts of NS accretion disks and the research on quasi-periodic oscillations observed in the NS sources. The following chapter then introduces our present collaboration on the complex continuation of this research work. Finally, the last chapter provides a brief summary, including some remarks on the overall context of our work and our further future plans.

1.1. Pioneers of X-ray astronomy

The X-ray sky allows us to study a rich variety of fascinating astrophysical systems including those producing X-ray radiation through accretion onto relativistic compact objects [1, 2]. Because the Earth's atmosphere is opaque for X-rays, the discovery of Wilhelm Conrad Röntgen wasn't valuable for astronomers for the first 50 years. However, the importance of X-ray astronomy became evident when they began to use sounding rockets that flew to higher altitudes instead of balloons.

The real beginning of X-ray astronomy was the year 1948 when American scientists used a German-made V-2 sounding rocket and discovered that the hot corona of the Sun radiates in the X-ray part of the spectrum. Then, on April 19, 1960, an Aerobee-Hi rocket carried a pinhole camera, which detected the X-rays on photographic film, and the first solar X-ray photo has finally appeared,

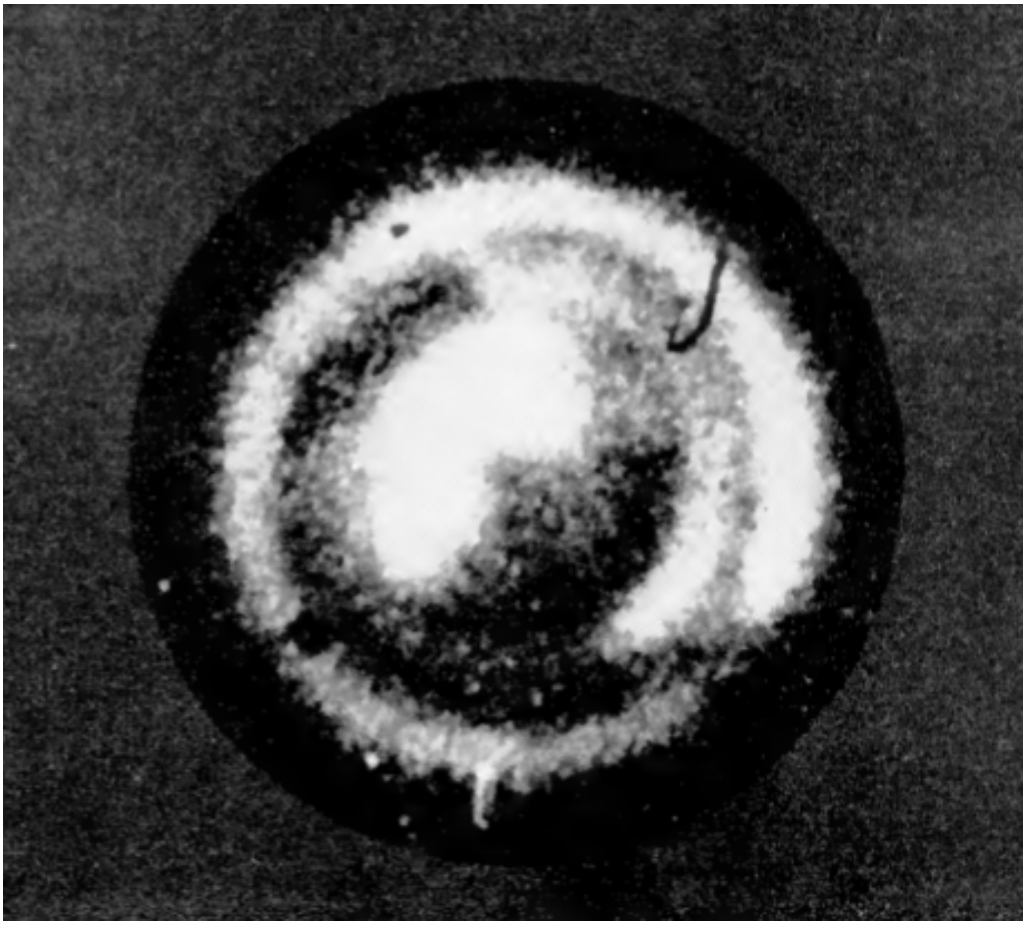

Figure 1.1. The X-ray image of the Sun obtained on April 19, 1960. The image was blurred in azimuth due to camera rotation during exposure. The X-ray areas correspond to the bright spots of the picture. The upward direction corresponds to the north, the western to the right.

see Figure 1.1 adopted from [3]. In the early 1970s, the first X-ray telescope, the Apollo Telescope Mount [4] aboard the Skylab, was launched into space, uploading more than 35 000 full-disk images of the Sun, orbiting the Earth for nine months.

In 1962, a team under Riccardo Giacconi (received the Nobel Prize in Physics in 2002) launched an Aerobee 150 sounding rocket [5]. Due to a highly sensitive soft X-ray detector on-board developed by Frank Paolini, the rocket detected a mysteriously strong signal in soft X-rays. Although the rocket's trajectory was slightly off course, it still saw X-rays, which certainly did not come from the Moon. They incidentally discovered the first X-ray source outside the Solar System and named it Scorpius X-1. After this discovery, primarily teams of

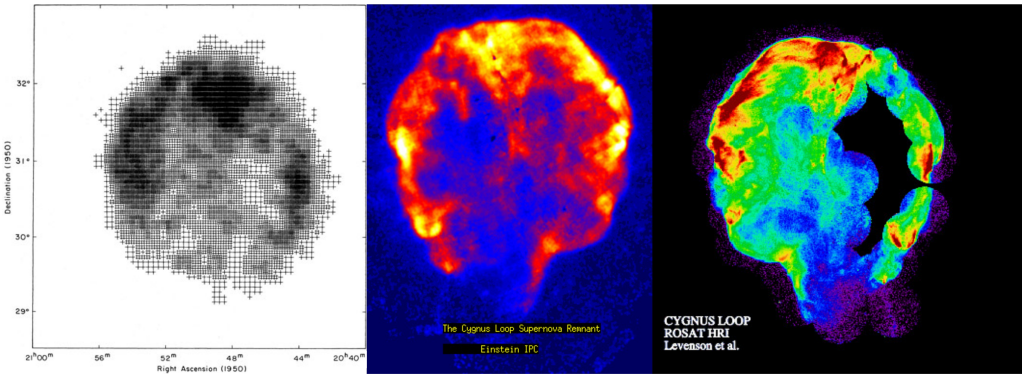

Figure 1.2. Comparison of X-ray images of the Cygnus Loop supernova remnants from the Virgo cluster of galaxies from three different observation devices.
From the left: image by early X-ray telescopes mounted on sounding rockets [6], image by Einstein (HEAO-2) (Credit: https://heasarc.gsfc.nasa.gov/) and image by the ROSAT's Position Sensitive Proportional Counter (PSPC) instrument [7].

American and British scientists saw a huge opportunity to find more X-ray sources. So they launched several others X-ray detectors board-on sounding rockets.

For astronomers to use X-ray mirrors and thus have much more accurate X-ray images, they first had to develop electronic detectors. These had to be very sensitive to light, i.e., to count every single X-ray photon captured on the detector accurately. The first such detectors include the microchannel plate detector and the imaging proportional counter. Later, they developed even more sensitive detectors, namely CCD spectrometers and imaging gas scintillation proportional counters.

The first extra-solar X-ray object was photographed in 1975 by scientists around Paul Gorenstein. Saul Rappaport [6] from MIT used Wolter's optics in 1977 to process the image. They used 7000 X-ray events to get the first authentic picture of the Cygnus Loop supernova remnants; see the left panel of Figure 1.2.

1.2. Advanced X-ray missions

Astronomers from NASA made another vital improvement in the history of X-ray astronomy in 1970 when NASA launched the very first Small Astronomy Satellite (SAS–A) into Earth's orbit from the Italian platform San Marco off the coast of Kenya. Kenya was celebrating the seventh anniversary of its independence that year, and in recognition of the hospitality of the Kenyan people, the satellite was named Uhuru [8] - freedom in Swahili. Uhuru's task was to search for sources

Figure 1.3. The Uhuru sattelite. Credit: https://heasarc.gsfc.nasa.gov/

radiating in the X-ray, gamma-ray, UV, and other spectral regions. Its primary mission was to systematically scan the entire sky at energies (2-20) keV to create the first-ever catalog of cosmic X-ray sources. The mission ended in March 1973.

Uhuru has led to tremendous scientific progress. For example, scientists had the opportunity to discover and study in detail the pulsing accretion-powered binary X-ray sources, such as Centaurus X–3, Vela X–1, and Hercules X–1. Uhuru also identified the first strong candidate for an astrophysical black hole (BH), Cygnus X–1, and other significant extragalactic sources. Over time, they published 4 Uhuru catalogs in a row; the last 4U catalog [9] is the final one and contains a total of 339 objects in the energy range of 3-6 keV and is available from HEASARC Browse. In Figure 1.3, see the fully rebuilt satellite as displayed at the National Air and Space Museum in Washington, D.C.

Another significant achievement by NASA was launching extensive scientific facilities called HEAO (High Energy Astronomy Observatories). The first of this mission in 1977, HEAO–1 [10], explored the entire X-ray sky in the energy band 0.2 keV – 10 MeV and managed to continuously monitor X-ray sources near the ecliptic. HEAO–1 carried four sets of instruments; one of them, the A1 instrument (the NRL Large Area Sky Survey Experiment (LASS)), achieved full sky coverage and created the first-ever All-Sky X-ray Catalog [11], see Figure 1.4. HEAO–1 completed great goals, for example, the study of aperiodic variability in Cyg X–1 on timescales on a few milliseconds [12] and almost 100 articles have been published. There are 13 catalogues and databases to obtain information about observations and detected sources, available at the HEASARC archive.

The second of HEAO NASA's mission, HEAO–2 [13], renamed to honour Albert Einstein after launch in 1978, was the first fully imaging X-ray telescope

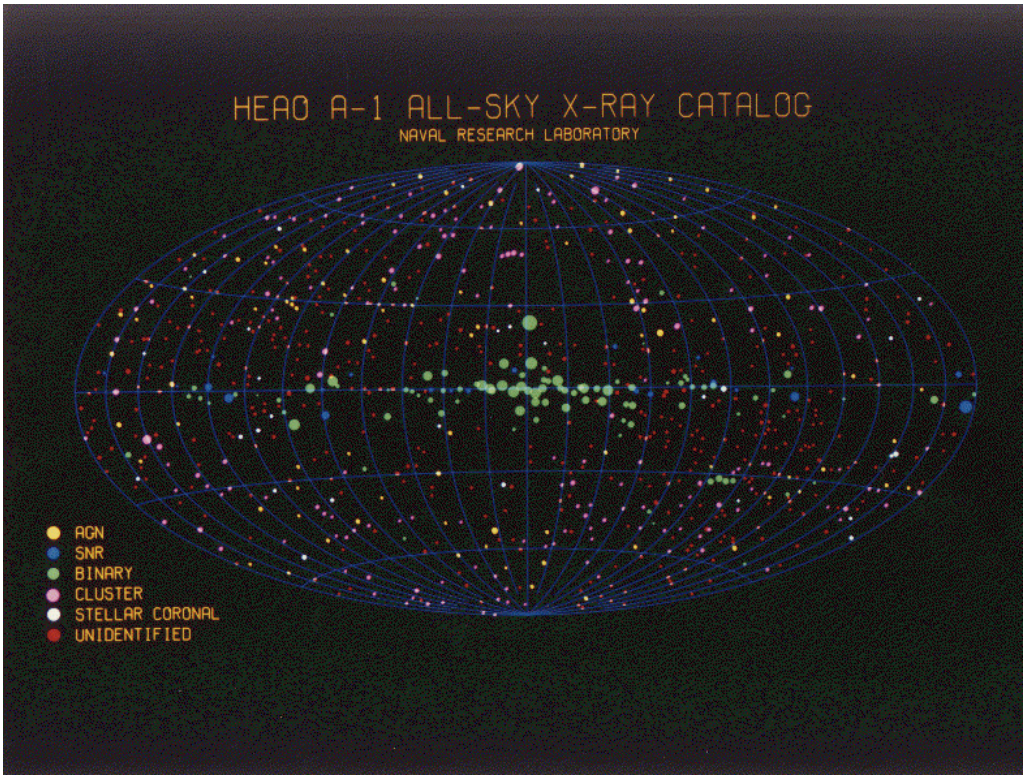

Figure 1.4. The A1 sky map shows about 1000 sources covering almost all essential astrophysical types of objects. Credit: United States Naval Research Laboratory, https://www.nrl.navy.mil/

put into space. This telescope could detect weak sources for the first time because it provided unprecedented sensitivity levels in the energy range (0.15-4.5) keV. During the mission, around five thousand sources of X-ray emission were discovered and resolved an image of the observed sources, for example, the Cygnus Loop, the middle picture on Figure 1.2. In addition, measurements showed that a large part of a uniform diffuse X-ray background across the sky originated from distant point sources, and searches with more advanced X-ray experiments have confirmed and improved this conclusion [14]. Observations with Einstein also showed that all stars emit X-rays and indicated that the corona of main-sequence stars radiates more strongly in X-rays than expected at that time, although they generate only a tiny portion compared to their total radiation. Whereas in the case of NSs, most of their total radiation comes in X-rays [14]. It meant another huge breakthrough and an irreversible change in X-ray astronomy. There are 23 catalogues and databases fulfilled with data from the Einstein mission, available at the HEASARC archive.

Europe was not left behind either. European Space Agency (ESA) launched

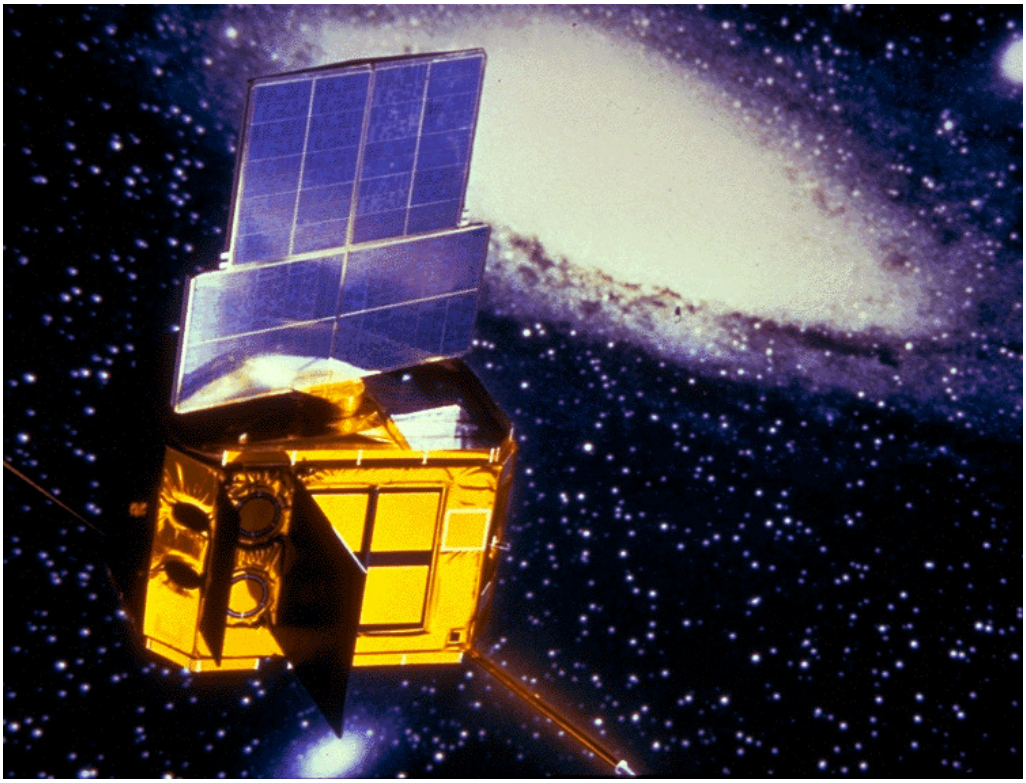

Figure 1.5. An artist's conception of the EXOSAT satellite.
Credit: ESA, https://www.esa.int/

in 1983 its first uncrewed mission, EXOSAT [15] (see Fig. 1.5), to study the X-ray universe and carry an onboard computer. It operated over a wide energy band of (0.05-50) keV and could see X-ray sources beyond the solar system due to its highly eccentric orbit. This mission made numerous breakthrough discoveries. It made almost 1800 observations of a wide variety of objects, for example, low mass X-ray binaries (LMXBs), cataclysmic variables, white dwarfs, supernova remnants, and discovered QPOs in LMXBs [16, 17], X-ray Pulsars and much more. In addition, the observation of several active galaxies and their rapidly changing emissions gave rise to the first suspicion that supermassive BHs might exist at their centre. Thanks to the three-year EXOSAT mission, almost 1000 scientific articles have been published, and one can browse 14 catalogues and databases at the HEASARC archive.

Another essential device was the Roentgen Satellite ROSAT [18], launched in 1990 and operated for almost nine years. The Max Planck Institute for Extraterrestrial Research in Germany created ROSAT with NASA and the British Science and Engineering Research Council. This mission was exceptional for that time, bringing the largest imaging X-ray telescope with a sensitivity of about

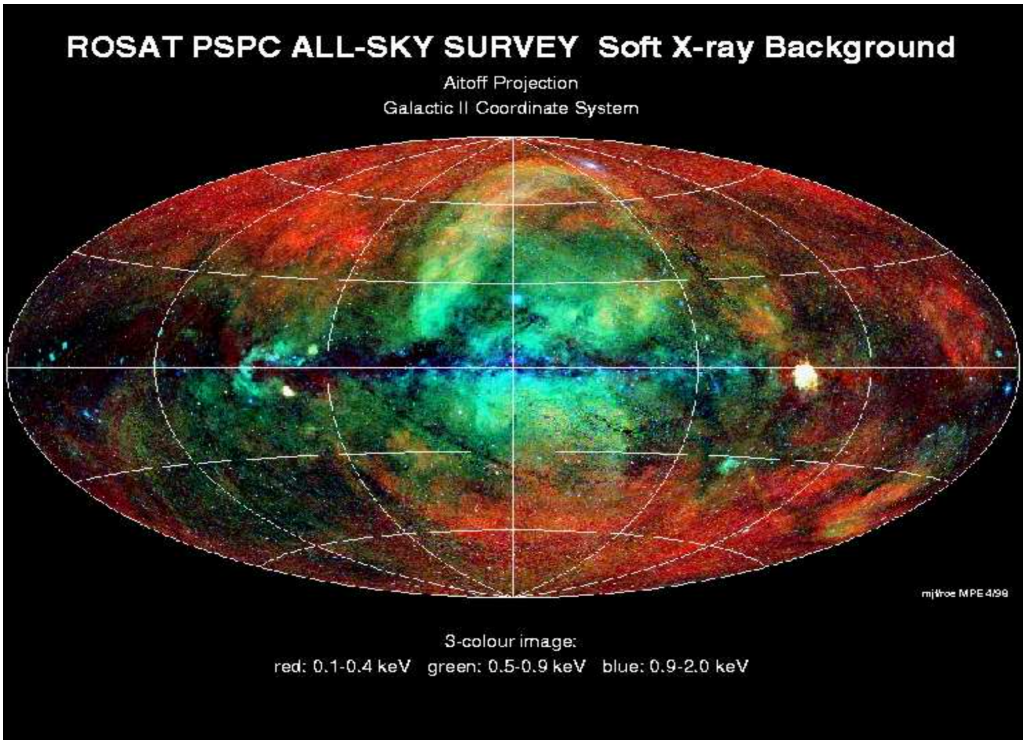

Figure 1.6. The ROSAT all-sky map in the soft X-ray band. Credit: Max Planck Institute for Extraterrestrial Physics, https://www.mpe.mpg.de/ROSAT

a factor of 1000 better than that of UHURU. The main tasks of the mission were to survey the entire sky in X-rays (0.1-2.4 keV)/extreme ultraviolet (42-210 eV) and produce the first maps of the soft X-ray diffuse background [19], see Figure 1.6. In addition, the mission program also contained a pointed observation of selected astrophysical sources. By the end, ROSAT detected more than 150 000 X-ray objects, 479 extreme ultraviolet objects, observed hot gas clouds in galaxy clusters, identified isolated NSs, found an X-ray emission from comets and much more.

Another milestone in X-ray astronomy was using CCD detectors. Japan succeeded and used them in their fourth space satellite X-ray mission ASCA [20] (Advanced Satellite for Cosmology and Astrophysics). It is also the second mission in which JAXA (Japan Aerospace Exploration Agency) cooperates with the United States. The satellite was launched in February 1993, and the first eight months performed verification of ASCA's four instruments. Then, astronomers working in Japan, the U.S. and member states of the ESA had an opportunity to request observation time. ASCA combined imaging capability within an energy range of (0.5-10) keV, good spectral resolution, and a large effective area. These properties promised the possibility of the X-ray spectroscopy of astrophysical

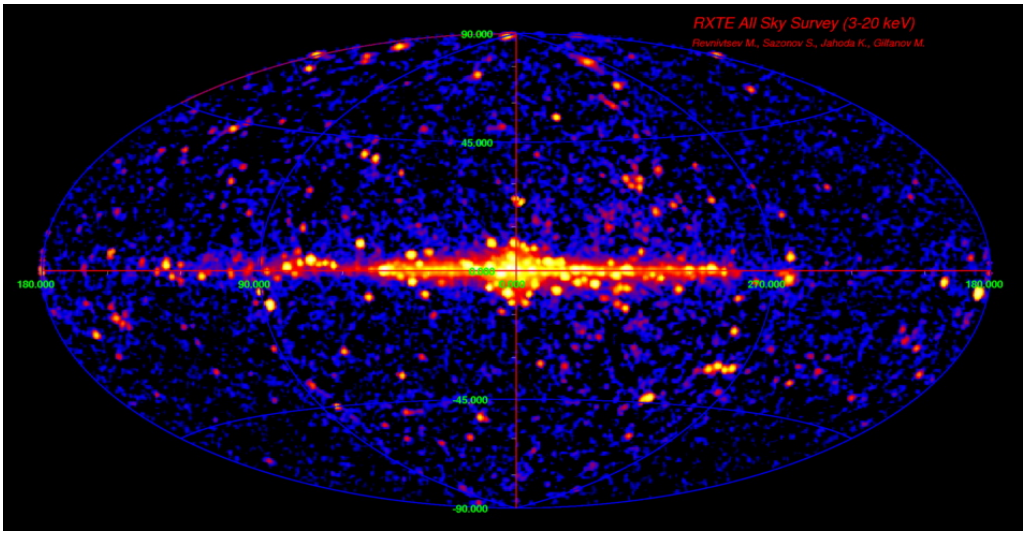

Figure 1.7. The X-ray map of the Universe obtained with RXTE/PCA.

plasma, emission lines and absorption edges. The ASCA results showed broad Fe lines coming from an active galactic nucleus (AGN) in our Galaxy and due to strong gravity effects observed near the centre supported the idea that there is a massive BH. The ASCA made over 3000 observations and the archive is still full of raw data despite the production of over 1000 articles in refereed journals so far. Nevertheless, the mission operated successfully for more than seven years.

The next interesting NASA mission was the Rossi X-ray Timing Explorer (RXTE) [21], named after physicist Bruno Rossi. It had a unique ability to study the rapid time variation in the emission of cosmic X-ray sources with a moderate spectral resolution in the energy range (2-250) keV, specially designed to review X-rays coming from NSs, BHs, pulsars and bursts. RXTE was launched in 1995 and was supposed to work for two years, but it worked for more than 16 years. RXTE again had an undeniable impact on the development of X-ray astrophysics. For example, it was found that the diffuse background X-ray glow in our Galaxy comes from other stars' coronae and identified previously undetected white dwarfs. In addition, scientists used data from RXTE as evidence of the frame-dragging effect [22] predicted by Albert Einstein and identified the smallest known BH. Using data from two RXTE instruments, the All Sky Monitor and the Proportional Counter Array (PCA), astronomers used about 20 million seconds of data and constructed an X-ray map of the entire sky (see Fig. 1.7 adopted from [23]). Results of the RXTE mission have been used for over 90 PhD theses, and more than 1900 refereed publications.

For our purposes, the most exciting observation of RXTE was the initial one

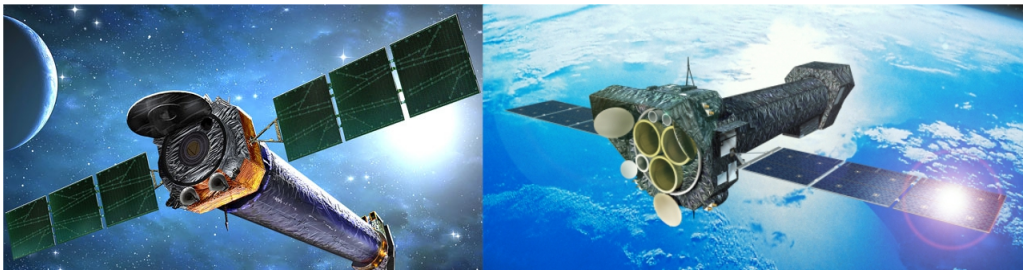

Figure 1.8. Artist's impression of the Chandra X-ray Observatory (left) and the XMM-Newton spacecraft (right). Credit: NASA, ESA/D. Ducros

in 1996, where two new simultaneous QPOs at frequencies in the kilohertz range were discovered. The power spectrum of 4U 1728–34 displayed a QPO peak near 800 Hz, the first-ever "kHz" phenomenon. In the case of the Sco X–1, the power spectrum showed a peak near 1100 Hz, the first-ever "sub-millisecond" phenomenon [24, 25].

In 1996, another European X-ray mission, SAX (in Italian "Satellite per Astronomia X"), was sent into orbit and, after a successful launch, renamed after Italian physicist Giuseppe (Beppo) Occhialini, BeppoSAX [26]. It was a cooperation of the Italian Space Agency, the Netherlands Agency for Aerospace Programmes, several Italian scientific institutes, the Netherlands Institute for Space Research (SRON), and ESA. This mission was unique because it simultaneously observed targets over an extensive spectral coverage (0.1-300) keV, with balanced performances from low and high energy instrumentation and moderate imaging capability. In addition, BeppoSAX showed beneficial connections of X-ray imaging sources with Gamma-ray bursts, discovering their positions with unprecedented accuracy and monitoring the X-ray afterglow, some of the most energetic explosions in the cosmos. Unfortunately, the BeppoSAX mission ended in April 2002.

1.3. Present X-ray missions

The actual golden age began with the launch of two compelling X-ray missions in 1999 and continues till now. NASA launched the Chandra X-ray Observatory in July, ESA the XMM-Newton in December of that year, see Figure 1.8. Both are equipped with X-ray cameras, spectrometers and complementary instruments in operation at the same time. However, Chandra has optics and devices with a very high angular resolution, while XMM-Newton's tools have a more extensive field of view and a higher effective area, allowing very sensitive observations

over large sky areas. It is awesome that nearly 22 years later, both Chandra and XMM-Newton are still operating when the missions were initially planned for 5 and 10 years, respectively.

The Chandra telescope [27], named after the Nobel Prize-winning astrophysicist Subrahmanyan Chandrasekhar, flies on a very eccentric elliptical high-Earth orbit, taking about 1/3 of the distance to the lunar orbit before returning closer to Earth. This odd orbit allows long-duration uninterrupted exposures of celestial objects without the intervention of Earth eclipsing the target. In addition, Chandra carries four sets of nested mirrors, allowing it to detect sources more than twice as far away and create images with five times more detail. Interestingly, these mirrors have been polished to the smoothness of several atoms. In the case of a similar smoothing of the Earth's surface, this would mean that the highest mountain would be less than 2 meters high. Data obtained by Chandra have significantly influenced X-ray astronomy, and till today, over 8 500 articles have been published in refereed journals, and results have been used for over 300 PhD theses. We selected only a few outputs, which we will mention here, but an inquisitive reader can find many more.

Chandra has detected the first X-ray emission from the region around the supermassive BH in the centre of the Milky Way galaxy, Sagittarius A* [28] and found a new type of a BH in galaxy Messier 82 - mid-mass object, supposedly the missing link between stellar-sized BHs and super massive BHs [29]. Moreover, in 2006, they also discovered that the collision of galaxies in the cluster separated ordinary matter from dark matter, and this strong evidence contributed to the further study of dark matter and dark energy [30].

Chandra observed the Crab Nebula within weeks of being located in orbit and, for the first time, saw a bright ring of high-energy particles around the nebula's heart and jets that earlier telescopes had partially seen [31]. One can see the first image of the Crab Nebula on the left panel of Figure 1.9, released on September 28, 1999, and it took only 1 hour of observational time. Since then, Chandra has frequently observed The Crab Nebula because we have a piece of firm historical evidence for when the star exploded, and we can study the explosion and its aftermath in detail. The Crab Nebula is a remnant of a supernova explosion observed by Chinese astronomers in 1054 AD. It is located in a distance of 6 500 light-years from the Earth and there is a rapidly spinning NS at the centre that rotates once every 33 milliseconds.

In 2006, we could see the first clear view of the faint boundary of the Crab's pulsar wind nebula, the right image in Figure 1.9. There is a cocoon of high-energy particles surrounding the pulsar. One can see the inner X-ray ring, and it is considered that it can be a shock wave, which indicates the bound-

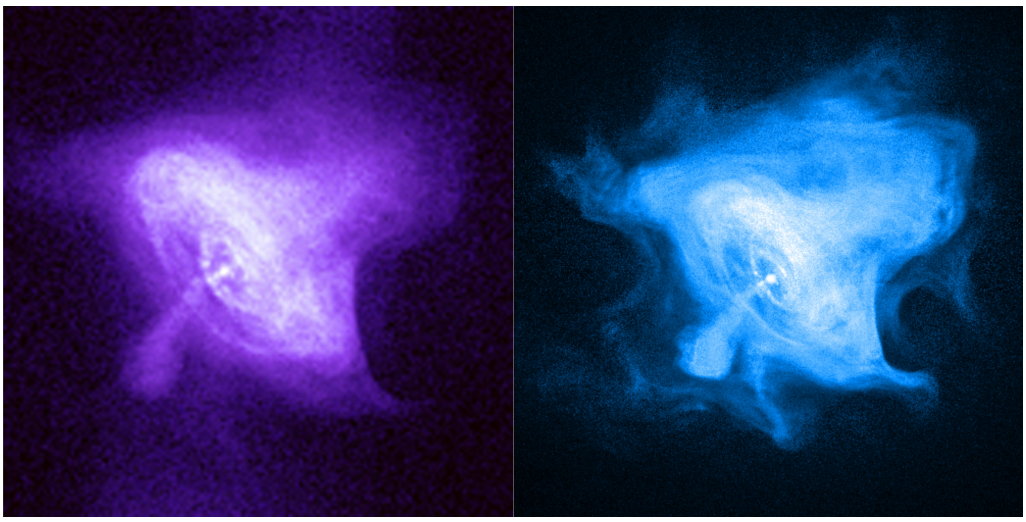

Figure 1.9. Two images of a rapidly spinning NS at the centre of the Crab Nebula, the left picture was taken in 1999, the right one in 2006. Credit: NASA/CXC/SAO

ary between the flow of matter from the pulsar and the surrounding nebula. Particles move outward from this ring to brighten the outer ring and create an extended X-ray glow. Scientists found structures in all directions of the Crab Nebula, which they named as ”fingers”, ”loops”, and ”bays”. Data indicate that filamentary material or the magnetic field governs the motion of the electrons and positrons. The particles can move fast along the magnetic field and travel several light years before radiating away their energy. In contrast, they move much more slowly perpendicular to the magnetic field and travel only a short distance before losing their energy [32].

The Crab Nebula is a very popular object to observe, and the resulting images look stunning. Therefore, thanks to multiwavelength pictures from the past, scientists could have created Figure 1.10. They combined data from five different telescopes: The VLA (radio) in red; Spitzer Space Telescope (infrared) in yellow; Hubble Space Telescope (visible) in green; XMM-Newton (ultraviolet) in blue; and Chandra X-ray Observatory (X-ray) in purple; covering almost the entire range of electromagnetic radiation.

The XMM-Newton observatory (X-ray Multi-Mirror Mission) [33], see the right image in Figure 1.8, named in honour of Sir Isaac Newton, is the biggest scientific satellite ever built in Europe and its telescope mirrors are among the most powerful ever developed in the world. It is the most sensitive imaging X-ray observatory, working in the energy range (0.1-12) keV. XMM-Newton combines the CCD cameras, grating spectrometer, nickel mirrors with gold coating and provides exceptional spectral and imaging abilities for studying

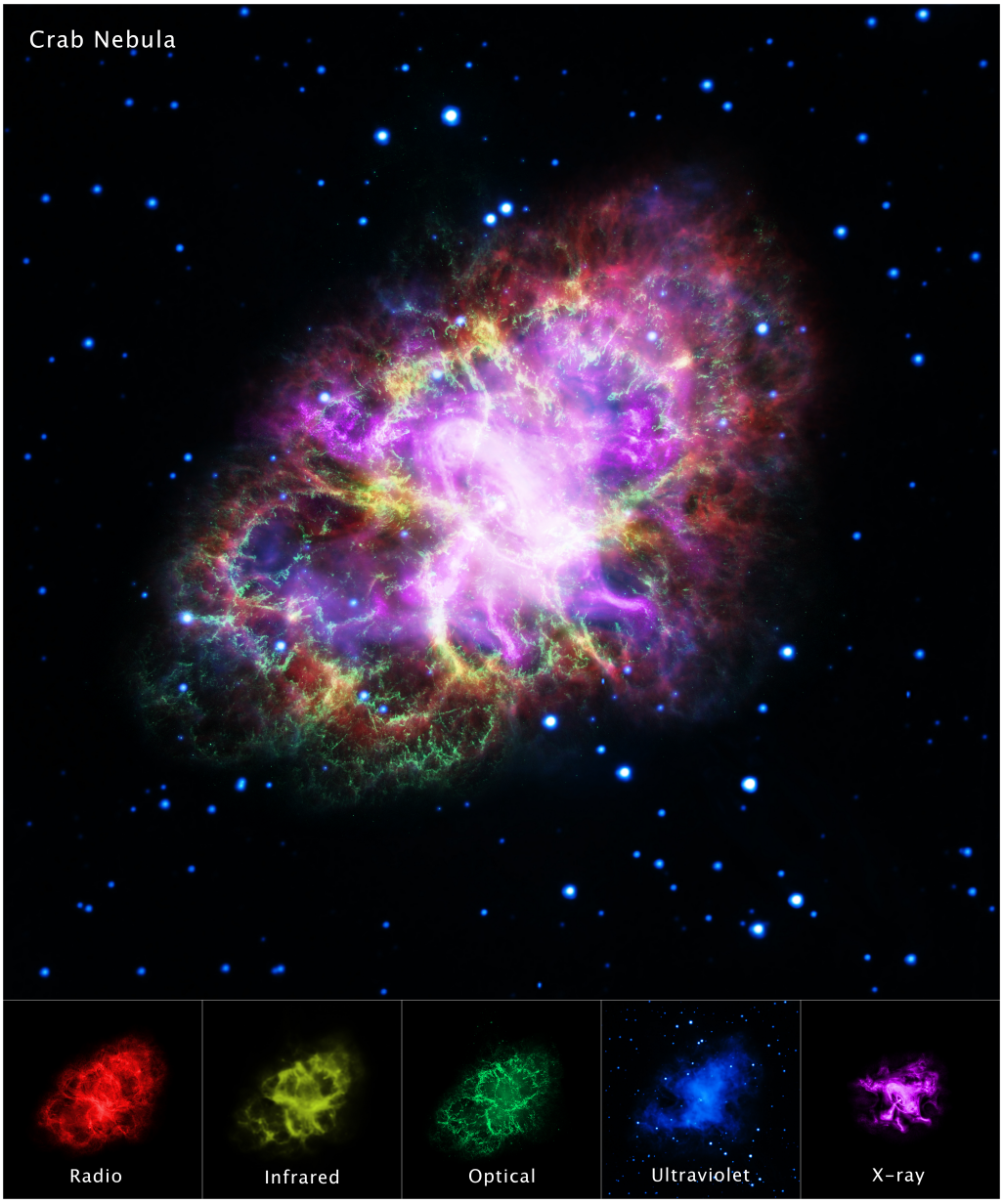

Figure 1.10. A highly detailed view of the Crab Nebula created in 2017. Credit: X-ray: NASA/CXC/SAO; Optical: NASA/STScI; Infrared: NASA/JPL/Caltech; Radio: NSF/NRAO/VLA; Ultraviolet: ESA/XMM-Newton

astrophysical sources. Most importantly, all six instruments work concurrently over an unprecedented effective area and provide highly sensitive surveys with long uninterrupted exposures. XMM-Newton also carries a sensitive optical telescope to observe the same sky parts by UV and visible light. In Figure 1.10, the ultraviolet part is taken by XMM-Newton, and it is a combination of 75

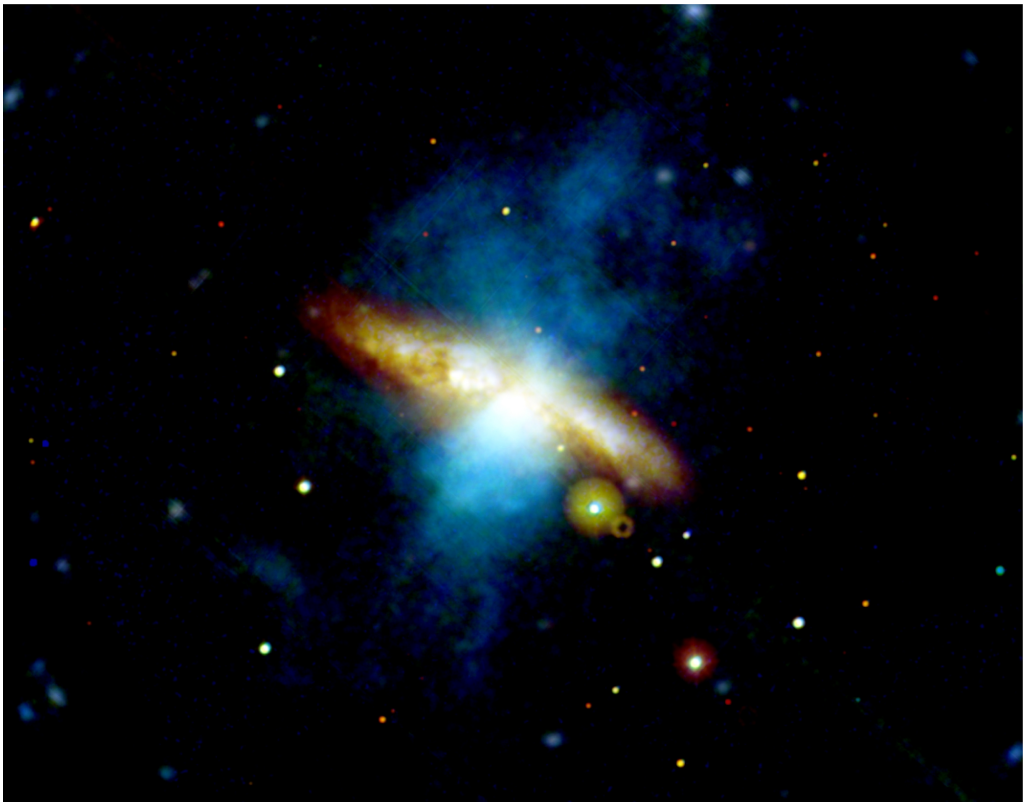

Figure 1.11. A highly detailed view of the starburst galaxy M82 obtained with the XMM-Newton observatory. Credit: ESA/XMM-Newton

images acquired between 2001 and 2015. Before this one, there existed just a few pictures in UV.

Data from XMM-Newton provide unprecedented observations of star coronas, accretion-driven binary systems containing compact objects, supernova remnants, AGN, clusters of galaxies with a hot inter-cluster medium and many more. There are over 7 700 refereed articles and 405 PhD theses based both on scientific results (making use of XMM-Newton observations and numerical predictions) and on ”technical” work (hardware and software development, calibration, or operations). Again, we selected only some outputs, which we will mention here, but one can find many more.

We highlighted some of the results about the starburst galaxy Messier 82 (M82 or the Cigar Galaxy or NGC 3034), located in the constellation Ursa Major (the Great Bear) and about 12 million light-years far. Figure 1.11 shows M82; this image was released to celebrate the International Year of Astronomy 2009 and as part of the 100 Hours of Astronomy project. It is assembled from X-ray, UV and visible spectra surveys using different XMM-Newton observations, including the

special observation for the International Year of Astronomy 2009 and 52.5 hours of observing time in total. M82 is one of the most studied galaxies in the sky because it shows a high rate of active star formation in its interior, affecting the gas and dust in its interstellar medium. In Figure 1.11, one can see bright knots in the plane of the Galaxy, which means intensive star formation and very intense bursts out of the galactic disk (in blue) blowing in X-rays.

Scientists used long XMM-Newton observations and reported evidence that in M82, there is simultaneously present a low-frequency break and a QPO in the power spectrum [34]. Furthermore, another group discovered X-ray QPOs coming from an ultraluminous X-ray source in M82 and confirmed that the source is a compact object [35]. Thus, the brightest X-ray source in the galaxy M82 was renamed M82 X–1 and considered an intermediate-mass BH. In 2014, Pasham et al. (2014) [36] estimated the BH mass based on twin-peak QPOs coming from M82 X–1 and were able to extrapolate the BH mass to be 428 ± 105 $M_{\odot}$. When they used the relativistic precession model, they got a value of 415 ± 63 $M_{\odot}$.

Another NASA's mission, the NuSTAR (Nuclear Spectroscopic Telescope Array) [37], was launched on June 13, 2012, and placed in a low-Earth, near-equatorial orbit. NuSTAR is led by Caltech and managed by JPL (Jet Propulsion Laboratory) for NASA's Science Mission Directorate in Washington. This mission was developed in partnership with the Technical University of Denmark and the Italian Space Agency (ASI). The telescope has accurate high-sensitive focusing optics for high-energy X-rays for the first time and operates in the range of (3-79) keV. Using its combination of sensitivity, spatial and spectral resolution, NuSTAR tracks five primary scientific objectives [37]:

1. explore the masked AGN activity (at $z \lesssim 2$) by observing selected areas of the sky;
2. research the population of compact objects emitting high-energy X-ray radiation in the Galaxy by surveying the central areas of the Milky Way;
3. study the hard X-ray continuum and the radiation from the radioactive element ^{44}Ti in young supernova remnants;
4. observe blazars with ground-based radio, optical, TeV telescopes, Fermi and Swift, all at the same time to constrain the composition of AGN jets;
5. detect line and continuum emission from core-collapse supernovae in the Local Group and from nearby Type Ia events to constrain explosion models.

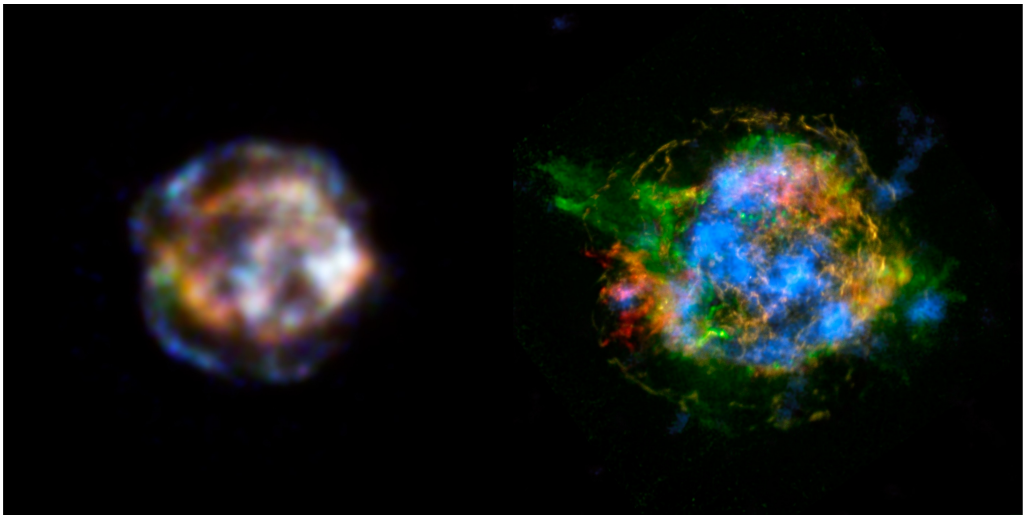

Figure 1.12. The new view of the historical remnants of Cassiopeia A by NuSTAR. The left image was taken in January 2013, the right image in February 2014. NuSTAR has made the first-ever picture of this source in the hard X-rays, shown blue. Red and green indicate an overlapping of the lower energy range of NuSTAR with NASA's Chandra X-ray Observatory. Credit: NASA/JPL-Caltech, NASA/JPL-Caltech/CXC/SAO

Figure 1.12 shows an example of data obtained from the NuSTAR. They observed the remains of Cassiopeia A, the remnants of an exploded star placed 11 000 light-years far away. Even if the star is dead for a very long time, the shock wave from the supernova explosion still hits the surrounding material (the outer blue ring) and accelerates the particles very significantly [38]. Observations with NuSTAR should answer how these particles are accelerated. On the right side of Figure 1.12, the blue colour illustrates high-energy X-rays coming from the radioactive titanium ^{44}Ti [39]. Detection of radioactive elements is very crucial. It offers a more direct method for exploring supernova blasts because radioactive materials emit X-rays no matter what, while non-radioactive materials light up not until the explosion and don't offer a direct look at the blast itself. Results obtained by NuSTAR show clumps of titanium mainly located at the heart of the star, suggesting a model of supernova explosions, where the inner core slosh. It is considered that this sloshing helps trigger stars to blow up and throw out their outer layers.

Since the launch, NuSTAR has shown its utility in a wide range of astrophysical research. As a result, there are over a thousand refereed articles. NuSTAR was deployed for a two-year mission, but fortunately, it still continues to collect data.

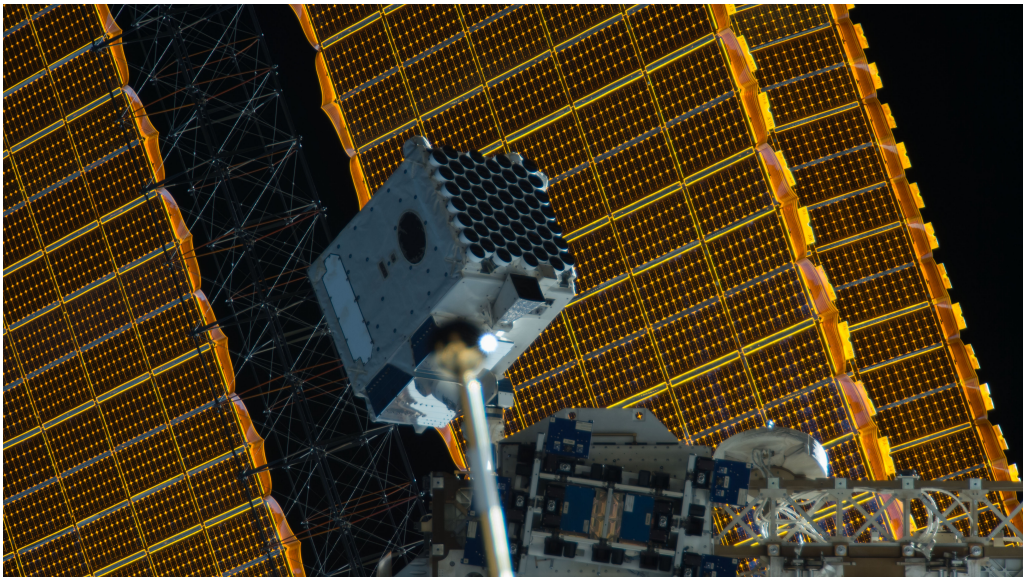

Figure 1.13. NASA's Neutron star Interior Composition Explorer (NICER) situated aboard the International Space Station. Credit: NASA/NICER

NASA's Neutron star Interior Composition ExploreR (NICER) [40] shown on Figure 1.13 is situated aboard the International Space Station. It was launched on a SpaceX Falcon 9 rocket on June 3, 2017, and started operating on June 14. It is devoted to studying the unique gravitational, electromagnetic, and nuclear-physics conditions embodied by NSs, investigating the exotic states of matter where density and pressure are higher than in atomic nuclei through rotation-resolved X-ray spectroscopy, and measuring NSs radius and mass with increased accuracy.

NICER observes the X-ray band sky (0.2-12) keV with a sizeable collective area and a fine time resolution. In addition, NICER has unique capabilities: coincidental fast timing and spectroscopy, with low background and high throughput, and spacecraft pulsar navigation will be demonstrated for the first time through the Station Explorer for X-ray Timing and Navigation Technology (SEXTANT) improvement to the mission.

In May 2018, scientists analysed the first data from NICER and discovered an X-ray pulsar in the fastest stellar orbit yet detected [41]. The pulsar and its companion star revolve around each other every 38 minutes, which is the shortest-known orbital period for a specific binary pulsar system called an accreting millisecond X-ray pulsar (AMXP). The star called IGR J17062–6143 is a rapidly spinning superdense pulsar and the second star seems to be a hydrogen-poor white dwarf. They are only about 300 000 kilometres apart, less than the distance between Earth and the Moon. In 2008, the RXTE mission observed the same source for 20 minutes and was only able to set a lower

limit for its orbital period [42]. NICER was focused on IGR J17062–6143 for more than seven hours over 5.3 days in August 2017, then again in October and November. After that, they combined data from that observations to confirm the record-setting orbital period.

We will not mention other incredible discoveries of NICER because there are over 150 refereed articles till now. However, if one is interested in more results, they summarise important activities and outcomes under NICER Science Nuggets on the HEASARC web page each week. The NICER mission should operate for 18 months, but it was prolonged in March 2019 and is still working.

Another interesting X-ray space mission is the Russian–German Spektr-RG (Spectrum + Röntgen + Gamma; SRG; Spectrum-X-Gamma or SXG) [43], launched on July 13, 2019, from the Baikonur Cosmodrome in Kazakhstan. Although the mission name contains "Gamma", there is no device capable of detecting gamma radiation. The name is retained for historical reasons because the earlier mission proposal also included a gamma-ray detector [44]. The instruments began to work after reaching an orbit around the Sun, about 1.5 million kilometres distant from Earth, rotating the Earth-Sun L2 Lagrange point in December 2019. Its main goal was to build all-sky maps by scanning the observable Universe in a wide range from the soft to the hard X-ray over six months for the first four years. After that, it should switch to observations of selected galaxy clusters and AGNs. Spektr-RG works in the energy range (0.2-30) keV, and X-ray mirror optics get together moderate resolution imaging with a great broad field of view. The Spektr-RG observatory carries two unique X-ray telescopes: ART-XC (IKI RAS, Russia) and eROSITA (MPI, Germany), functioning based on the principle of an oblique impact.

eROSITA (the extended ROentgen Survey with an Imaging Telescope Array) [45] is the primary device on the Spektr-RG mission. It was developed at the Max Planck Institute for Extraterrestrial Physics in collaboration with institutes in Bamberg, Hamburg, Potsdam and Tübingen. Its sensitivity range is (0.3-10) keV. The first eROSITA all-sky survey was managed for six months by allowing the telescope to spin continuously, thus providing an even exposure of about 150-200 seconds over most of the sky, enabling a more deep view on the ecliptic poles. As eROSITA inspects the sky, the energy of the collected photons is measured with an accuracy of (2-6) %. The eROSITA device was designed to detect large samples of galaxy clusters up to redshifts $z > 1$, test cosmological models including dark matter and dark energy, discover a few million AGNs, including covered objects, bright X-ray binaries, supernova remnants, active stars with magnetically active hot coronae, star-forming regions and more.

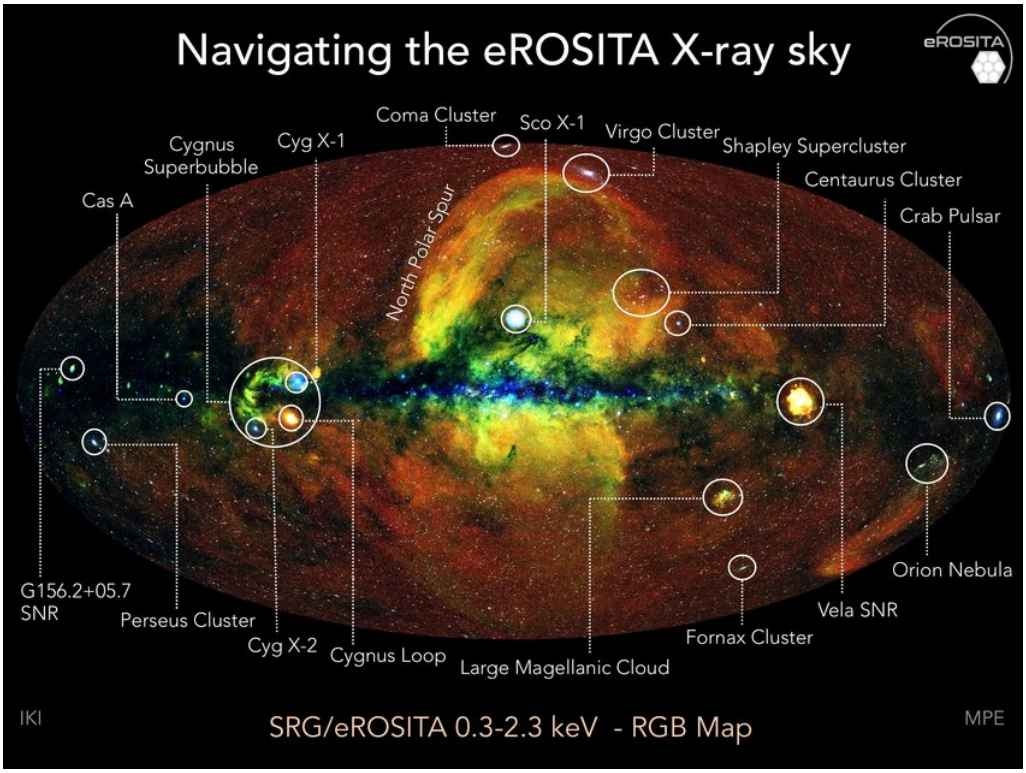

Figure 1.14. Annotated version of the energetic Universe as seen with the eROSITA X-ray telescope. Credit: Jeremy Sanders, Hermann Brunner, Andrea Merloni and the eSASS team (MPE); Eugene Churazov, Marat Gilfanov (on behalf of IKI)

In Figure 1.14 [46], one can see the incredible result of the eROSITA all-sky survey. The whole sky is projected onto an ellipse (the Aitoff projection) with the centre of the Milky Way in the middle and the body of the Galaxy going horizontally, and photons have been colour-coded by their energy (red for energies (0.3-0.6) keV, green for (0.6-1) keV and blue for (1-2.3) keV). The diffuse red glare off from the galactic plane is the hot gas emission in the solar system's vicinity (the Local Bubble). Along the plane itself, the blue colour in the image indicates only high-energy sources because the lowest-energy X-rays are absorbed by dust and gas. The Milky Way itself has a very turbulent history, which is shown in green and yellow colours, such as explosions of supernova and perhaps a past burst from the supermassive BH in the centre of our Galaxy. Mostly white coloured sources uniformly distributed over the sky are hundreds of thousands of X-ray emitters. One can find between them outlying AGNs visible as point sources and clusters of galaxies as expanded X-ray nebulosities. It is unbelievable, but the eROSITA X-ray sky image displays about one million detected X-ray sources, which is really stunning and will hold the scientists busy for the upcoming

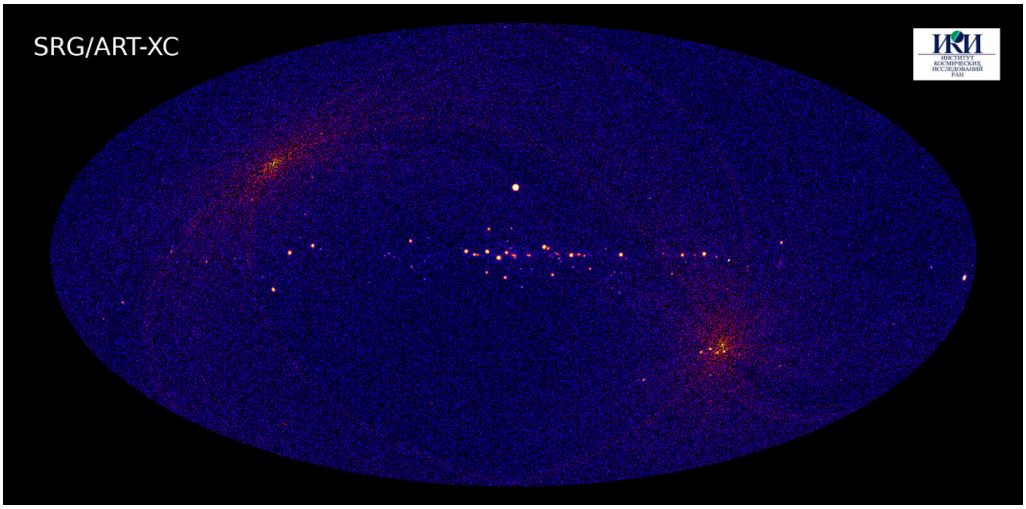

Figure 1.15. The all-sky map obtained by ART-XC telescope in the (4-12) keV energy band. Credit: M. Pavlinsky; IKI

years. One can compare the now discussed eROSITA image with the ROSAT all-sky map, shown in Figure 1.6, and see the vast difference between detectors' sensitivity (eROSITA is 25 times more sensitive than ROSAT [47]).

ART-XC (The Astronomical Roentgen Telescope – X-ray Concentrator) [48] is the second X-ray telescope on the Spektr-RG mission. The instrument was built by the Space Research Institute (IKI) and the All-Russian Scientific Research Institute for Experimental Physics (VNIIEF). In addition, the NASA Marshall Space Flight Center (MSFC) has developed and calibrated mirror systems. Its seven identical grazing incidence mirrors in a nested shell design can capture X-ray photons in a high-energy X-ray band (5-30) keV. The high-energy X-rays can come through huge amounts of dust so that ART-XC can observe obscured objects hidden to telescopes operating in lower energies. It completed the 3rd six-month observation of a planned eight all-sky surveys on June 12, 2021. ART-XC has already detected nearly 600 objects. About two-thirds of them are in the Milky Way and the rest beyond our Galaxy.

In Figure 1.15 [49], one can see the first all-sky map made by ART-XC. The plane of the Milky Way goes horizontally through the centre of the map. The ecliptic poles are the bright areas in the upper left and the lower right of the image. These are more highly exposed due to the path along which the telescope moves. The all-sky survey will be repeated over the following years, building up exposure to detect ever-fainter sources and monitor changes in the X-ray sky. ART-XC is expected to discover thousands of hard X-ray sources from nearby cataclysmic variables to distant active supermassive BHs.

To summarise, scientists assume that Spektr-RG can find almost all massive clusters of galaxies in the observable Universe. It should take four years of survey mode. Furthermore, it should detect around three million supermassive BHs in AGNs, hundreds of thousands of stars with active coronae, accreting white dwarfs, tens of thousands of active star formation galaxies. Almost 200 refereed articles based on the analysis of data from Spektr-RG have been published till now. The original mission is planned for seven years of operations.

1.4. Future X-ray missions

So far, thanks to better and better telescopes and more sophisticated software, scientists from all around the world have managed to push the boundaries of knowledge incredibly, not only in our Galaxy. However, we will now mention some of the upcoming high-energy X-ray astrophysics missions because there are still many to discover.

In late 2022, NASA expects to launch the Imaging X-ray Polarimetry Explorer (IXPE) [50] with a considerable Italian contribution through the Italian Space Agency (ASI), the National Institute for Nuclear Physics (INFN) and the National Institute of Astrophysics (INAF). IXPE will operate at (2-8) keV energies and determine the mechanism for X-ray production in objects such as NSs, pulsars, wind nebulae, stellar and supermassive BHs.

In the Japanese Fiscal Year 2022 (April 2022 – March 2023), the X-ray Imaging and Spectroscopy Mission (XRISM) [51] will be launched. It is a JAXA/NASA collaborative mission, with ESA participation. XRISM (formerly the X-ray Astronomy Recovery Mission, XARM) will recover the high-resolution spectroscopic capabilities of Hitomi[1]. XRISM will investigate celestial X-ray objects with high-resolution spectroscopy and high-throughput imaging in a soft X-ray energy band (0.3-12) keV. The research will be focused on the evolution of the most extensive structures in the Universe, the behaviour of matter in extreme gravitational fields, the spin of BHs, the inner composition of NSs, and the mechanism of acceleration of particles in jets.

In 2027, the enhanced X-ray Timing and Polarimetry mission (eXTP) [53] is planned to launch. The eXTP international consortium is led by the Institute of High Energy Physics, the Chinese Academy of Sciences, involving about 50

[1] We did not mention the Hitomi mission because scientists lost contact with the telescope after one month of operating due to multiple incidents leading to an uncontrolled spin rate and breakup. [52]

institutions from China and Europe, including the Czech Republic, with participating scientific institutes from Japan, the United States and India. The eXTP mission will study the state of matter under extreme conditions of density, gravity and magnetism, primarily isolated and binary NSs, magnetars, and stellar-mass and supermassive BHs. The eXTP telescope will equip four science instruments covering the energy band (0.5-50) keV.

The last mission we will mention is Athena (the Advanced Telescope for High-Energy Astrophysics) [54], which should launch in the early 2030s. ESA selected Athena in 2014 within the Cosmic Vision Program as the next large X-ray observatory offering spatially-resolved X-ray spectroscopy and deep wide-field X-ray spectral imaging with performance exceeding current X-ray observatories like XMM-Newton, Chandra and SRG/eROSITA or by future missions like XRISM. In addition, it should address the scientific theme of the hot and energetic Universe. Athena will operate in the energy range of (0.2-12) keV. It will consist of a single X-ray telescope and two additional instruments - WFI (the Wide Field Imager) and X-IFU (the X-ray Integral Field Unit). The WFI is developed by an international consortium composed of ESA member states and led by the Max Planck Institute for Extraterrestrial Physics with partners in the United States. The X-IFU Consortium was officially endorsed in December 2018. It gathered 11 European countries (Belgium, the Czech Republic, Finland, France, Germany, Ireland, Italy, Netherlands, Poland, Spain, Switzerland), plus Japan and the United States. Athena should be another milestone for high-energy astrophysics, as it should answer two critical questions about the vast structures, namely the ordinary matter from which they are created and how BHs grow and shape the Universe.

1.5. Compact object diagnostics

The development of X-ray astronomy and its missions helped us discover and understand the most energetic phenomena happening in the Universe. Many of these observations are connected to the behaviour of matter in the close vicinity, or directly at the surface, of compact objects (white dwarfs, NSs and BHs). For example, observations and analysis of X-rays help us investigate strong gravity regimes, and general relativistic effects have to be included in the proper physical model of processes behind these observations. It includes gravitational redshift, light bending, effects of general relativity on the trajectories of particles, and many others. In this section, we only focus on discoveries that are connected to NSs for the sake of brevity.

Diagnosis of NSs from X-ray observations is usually made by measuring the NS mass and radius. These are then compared with theoretical values obtained from the modelling of NSs. The theoretical values from modelling are given by the assumed equation of state (EoS) of dense nuclear matter, and therefore, NSs serve as a diagnostic tool of nuclear physics in a regime that is very different from the one we know on Earth, or from other astronomical situations like nuclear burning in stellar interiors.

Some of the missions were deployed with focusing devices to take pictures of the X-ray sources. For example, we have already seen pictures of the Crab Nebula taken by Chandra X-ray Observatory in Figure 1.9.

Walker et al. [55] have discovered close NS RX J1856.35–3754 in X-rays. The analysis of thermal radiation from its surface enabled us to constrain the NS's apparent radius. The apparent radius is the star's radius on the observer's screen, which is for NSs affected by the light bending. Since the gravity is strong close to the NS's surface, the light-bending causes the star to seem larger than its own circumferential radius. The analysis is sensitive to the distance of the source. For example, Pons et al. [56] assumed the distance to be 51, 61, or 71 pc, and put limits on mass and radius for different atmosphere models. Later, in [57], the authors reported the distance by measuring parallax with Hubble Space Telescope to be 123^{+11}_{-15} pc. A different analysis of RX J1856.35–3754 was performed in [58]. The analysis of nearby isolated NS sources of X-rays can therefore be a very useful diagnostic tool of NSs and can give us information about the interior of NSs.

Another X-ray tool to diagnose the NS structure via measuring the mass and radius is the analysis of pulse profiles. The light curve of the X-ray pulsars shows periodical increases in the power generated by hot-spot(s) on the star's surface. The waveform is affected by the position of the hot-spot on the star's surface with respect to the axis of rotation and the line of sight to the observer, and effects such as Doppler shift or light bending. Thus, for a given rotational frequency, the different mass and radius of the star will produce a different waveform, and analysis of the waveform can be used to measure the star's mass or radius. The recent development in the pulse profile modelling was enabled by installing NICER on the International Space Station. The team has reported the measurements of the mass and radius of PSR J00307+451 in [59, 60] and recently the analysis of PSR J0740+6620 in [61, 62]. The NICER team works in two different independent groups, one in Europe and one in the USA.

NSs in binaries exhibit various phenomena observed in X-rays. Some LMXBs exhibit a sudden rise in X-ray luminosity followed by a slower but still a relatively fast decay. The timescale for the rise in luminosity is usually $\sim$ 1 s, while the timescale for the decrease is $\sim$ 15-50 s [63]. These rises are known as Type-I X-ray bursts and are related to the thermonuclear explosion of accreted matter on the surface of a NS. Before and after the burst, hectohertz oscillations can be detected and used to measure the star's rotational frequency; for an overview, see, e.g. [64]. The Type I X-ray bursts can be used to measure the NS mass and radius by analysing the flux and temperature during the different stages of the burst. The Eddington luminosity is measured during the "touchdown" when the photosphere reaches the star's surface. Apart from measuring the mass and radius of a particular source, one can combine different sources to constrain the EoS more robustly. The analysis of three X-ray bursters and another three X-ray NSs where the apparent size was measured was used to constrain the mass-radius relation and EoS parameters in a novel approach in [65].

A promising tool that can be used for the analysis of NSs is associated to the kHz QPOs. These two peaks in the power spectra are detected in binaries with a NS or a BH. The detected frequencies are close to frequencies of orbital motion, and therefore analysis of orbital motion around rotating NSs is needed. The spacetime around rotating NSs is not known analytically, but approximative analytical spacetimes may be used for astrophysical sources rotating with observed spin frequencies. We focus on the Hartle-Thorne spacetime, which results from perturbation of Schwarzschild spacetime up to terms quadratic in star's angular velocity Ω. The Hartle-Thorne spacetime is given by three parameters: gravitational mass of the central body M, its angular momentum J, and quadrupole moment Q [2]. The parameters are found for rotating NSs with given central energy density and angular velocity by solving the structure equations assuming the EoS of NS matter. Different EoS give different combinations of M, J, and Q. Analysis of motion of particles in the Hartle-Thorne spacetime and its comparison with observed QPO frequencies give us limits on M, J, and Q, and therefore we can test which EoS enables such combinations. The presented thesis is focused mainly on this astrophysical phenomena.

[2] We follow the convention of taking Q to be *positive for an oblate object*, as used by Hartle & Thorne.

Chapter 2

NSs in X-ray binaries and Hartle-Thorne spacetime

An X-ray binary is a system that consists of a star of the main sequence (in most cases), an evolved star (a red giant), or a white dwarf (rarely, in BH binaries), which transfers mass onto a compact object - a BH, a NS, or a white dwarf and the whole system emits X-rays.[1] The matter is accreted from the companion star onto the compact object through the Roche lobe overflow or the stellar wind. Then, as the inflowing matter has an angular momentum associated with the influence of a gravitational potential of the compact object, the matter spirals onto the compact star and forms an accretion disk. Many particles collide in the inflowing matter which heats the gas up to about (10^7-10^8) K and results to X-ray radiation. We are interested mainly in low mass X-ray binaries (LMXBs), where the donor is less massive than the compact object, the NS in our case. Such a system emits almost all of its radiation in X-rays.

To describe the external spacetime around a rotating NS, we use the Hartle-Thorne metric, which gives a convenient description for the rotation frequencies of more than 95% of known pulsars, so it is sufficiently accurate for most purposes.

The Hartle-Thorne metric [66] is an exact solution of the Einstein's vacuum field equations that describes the external gravitational field of a slowly and rigidly rotating, stationary and axially symmetric body. We confine our attention to NSs that are axially symmetric, slowly rotating and made up of a perfect fluid. The metric is calculated with the accuracy of up to first order in the quadrupole moment and second order in the angular momentum. The spacetime interval can be written as [66]

[1] When the compact star is a white dwarf, then the binary system is called a cataclysmic variable.

$$
\begin{aligned}
\mathrm{d}s^2 = &+ \left(1-2\frac{M}{r}+2\frac{J^2}{r^4}\right)\left\{1+2\left[\frac{J^2}{Mr^3}\left(1+\frac{M}{r}\right)\right.\right.\\
&+ \left.\left.\frac{5}{8}\frac{Q-J^2/M}{M^3}Q_2^2\left(\frac{r}{M}-1\right)\right]P_2(\cos\theta)\right\}\mathrm{d}t^2\\
&- \left(1-2\frac{M}{r}+2\frac{J^2}{r^4}\right)^{-1}\left\{1-2\left[\frac{J^2}{Mr^3}\left(1-\frac{5M}{r}\right)\right.\right.\\
&+ \left.\left.\frac{5}{8}\frac{Q-J^2/M}{M^3}Q_2^2\left(\frac{r}{M}-1\right)\right]P_2(\cos\theta)\right\}\mathrm{d}r^2\\
&- r^2\left[1+2\left\langle-\frac{J^2}{Mr^3}\left(1+\frac{2M}{r}\right)+\frac{5}{8}\frac{Q-J^2/M}{M^3}\left\{\frac{2M}{[r(r-2M)]^{1/2}}\right.\right.\right.\\
&\times \left.\left.\left.Q_2^1\left(\frac{r}{M}-1\right)-Q_2^2\left(\frac{r}{M}-1\right)\right\}\right\rangle P_2(\cos\theta)\right]\\
&\times \left\{\mathrm{d}\theta^2+\sin^2\theta\left[\mathrm{d}\phi-\left(\frac{2J}{r^3}\right)\mathrm{d}t\right]^2\right\}, \qquad (2.1)
\end{aligned}
$$

where M is the total mass of the rotating star, J is the star's total angular momentum and Q the star's mass quadrupole moment, $P_2(\cos\theta)=\frac{1}{2}(3\cos^2\theta-1)$ is the Legendre polynomial of the second order, Q_j^k is the associated Legendre function of the second kind (taken from [67]):

$$
\begin{aligned}
Q_2^1(\zeta) &= \left(\zeta^2-1\right)^{1/2}\left[\frac{3\zeta^2-2}{\zeta^2-1}-\frac{3}{2}\zeta\ln\left(\frac{\zeta+1}{\zeta-1}\right)\right], \qquad (2.2)\\
Q_2^2(\zeta) &= \frac{3}{2}\left(\zeta^2-1\right)\ln\left(\frac{\zeta+1}{\zeta-1}\right)-\frac{3\zeta^3-5\zeta}{\zeta^2-1}. \qquad (2.3)
\end{aligned}
$$

In our special case, we have $\zeta=\left(\frac{r}{M}-1\right)$ and therefore

$$
Q_2^1\left(\frac{r}{M}-1\right)=\left[\frac{r(r-2M)}{M^2}\right]^{1/2}\left[\frac{M^2-6Mr+3r^2}{(r-2M)r}+\frac{3(M-r)}{2M}\ln\left(\frac{r}{r-M}\right)\right], \qquad (2.4)
$$

$$
Q_2^2\left(\frac{r}{M}-1\right)=\frac{2M(2M^3+4M^2r-9Mr^2+3r^3)}{2M^2(2M-r)r}+\frac{3r^2(-2M+r)^2}{2M^2(2M-r)r}\ln\left(\frac{r}{r-M}\right). \qquad (2.5)
$$

The original form of the metric 2.1 contains also higher-order parts. We use a rewritten version of this external metric in terms of the dimensionless angular

momentum $j = J/M^2$, and a dimensionless quadrupole moment $q = Q/M^3$ [68], see Section 2.2.

2.1. Models of rotating NSs

The density of matter in a NS exceeds that in the atomic nucleus. What are the collective properties of elementary particles occurring there is not yet well understood. There are many EoS that we can use and based on which the model of a NS can be calculated. Nevertheless, the mass-radius (M-R) relation of a NS is still unknown from the observations, however, a constraint can be put (see e.g. [65]). The orbital motion around a NS is affected by NS properties, which determine the spacetime metric, and it is also limited by the position of the NS surface. Therefore, one can study motion of particles aiming to investigate fundamental properties of the NS matter.

Here we present part of the results published in our paper [69], where we showed relations connecting the main properties of a rotating NSs described by a range of EoS, using the Hartle-Thorne approach. We have selected a set of EoS describing nuclear matter forming a NS, see Table 2.1. For each selected EoS, we calculated a sequence of models rotating at 400 Hz (with masses up to the maximal) and a similar sequence with zero rotation. These models of the rotating NSs are the results of the solution of a set of ordinary differential equations for the perturbation function; the approach we used will not be repeated here, but one can find it, e.g. [66, 70–74].

Table 2.1. EoS we used in [69]. The individual columns indicate the maximum mass, the corresponding radius, the central baryon number density and the relevant reference for each EoS.

EoS	$M_{\max}[M_\odot]$	R[km]	n_c [fm^{-3}]	Reference
Sly4	2.04	9.96	1.21	Stone et al. 2003 [75]
UBS	2.20	12.1	0.68	Urbanec et al. 2010 [76]
APR	2.21	10.2	1.12	Akmal et al. 1998 [77]
FPS	1.80	9.25	0.726	Lorenz et al. 1993 [78]
Gandolfi	2.20	9.82	1.16	Gandolfi et al. 2010 [79]
NRAPR	1.93	9.85	1.29	Steiner et al. 2005 [80]
KDE0v1	1.96	9.72	1.29	Agrawal et al. 2005 [81]

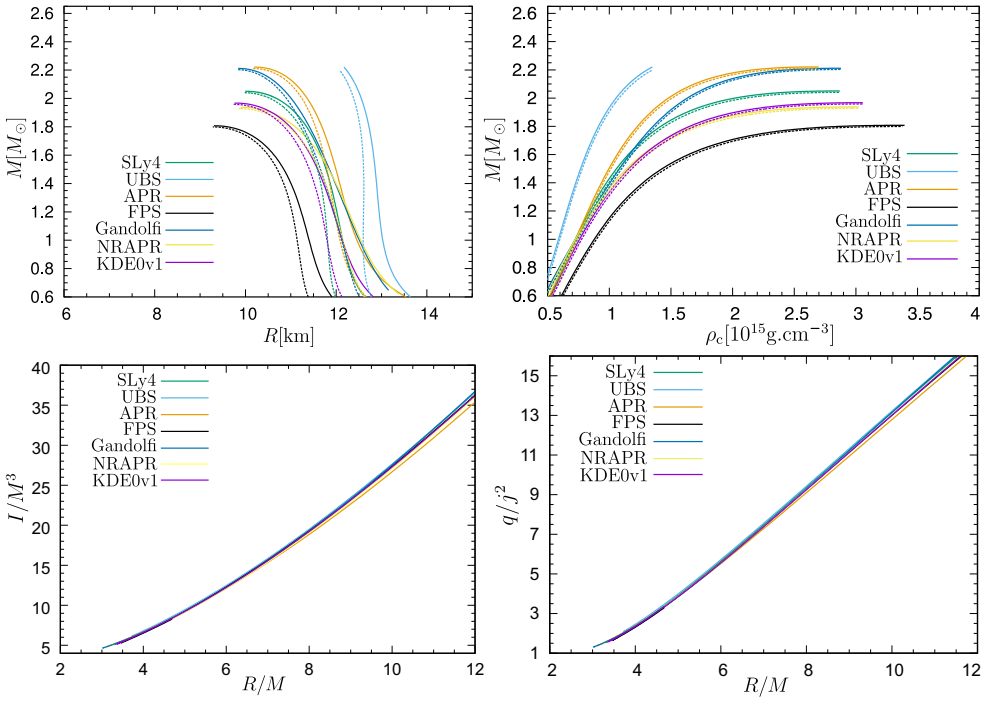

Figure 2.1. *Top:* Mass vs radius (left) and mass vs central energy density (right) are plotted for a selected EoS, with the sequences of rotating (solid lines) and non-rotating (dashed lines) stars. All the rotating ones were calculated with the rotational frequency of 400 Hz and $R = R_{\mathrm{eq}}$ (the equatorial radius). *Bottom:* The dimensionless quantities I/M^3 (left) and $q/j^2 = QM/J^2$ (right) are plotted against the inverse compactness R/M. All of the quantities in the bottom panels are in geometrical units, with $c = G = 1$.

Our selected EoS led to different NS models due to various approaches to nuclear matter. One can see the results in Fig. 2.1 showing mass-radius relations (top left) and mass as a function of the central energy density (top right) for both rotating models (solid lines) and non-rotating models (dashed lines). Different colours represent different EoS. For the rotating models, the equatorial radius is the quantity plotted as R. When one compares the left and right panels, one can see that more compact stars (for a given mass having a smaller radius) poses also higher central energy densities. The right panel shows that when EoS approaches the maximum mass, it then becomes less sensitive to the central energy density. One of the ways how to test correctness of a given EoS is to compare the maximum mass with the astronomical observations. Unfortunately, due to relatively recent observations of two solar mass NSs [82, 83], many EoS have been eliminated, including FPS we used in our selection.

The bottom panels of Fig. 2.1 show that for a given M and R, one can directly get the value of the dimensionless moment of inertia I/M^3 and calculate

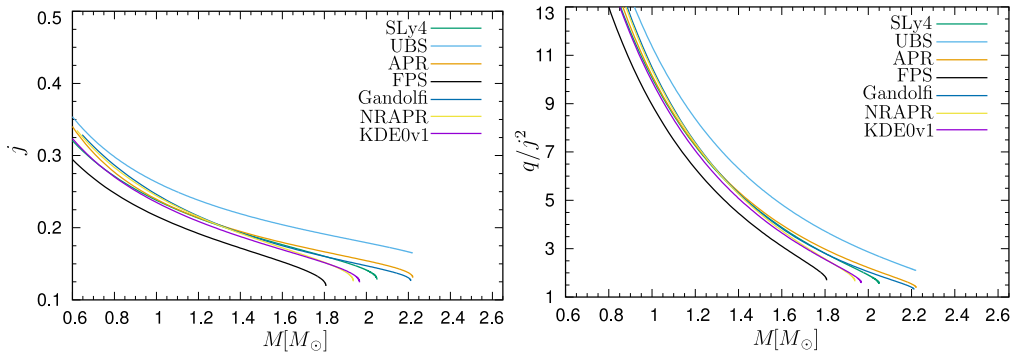

Figure 2.2. Values of $j = J/M^2$ (left) and $\tilde{q} = q/j^2 = QM/J^2$ (right) as functions of the gravitational mass for stars rotating at 400 Hz.

the dimensionless angular momentum $j = J/M^2 = 2\pi f_{\rm rot} I/M^2$ for particular values of star's rotational frequency $f_{\rm rot}$. The dimensionless quadrupole moment $q = Q/M^3$ can be obtained by using the relation in the bottom right panel together with the value of j. This kind of behaviour, in which particular combinations of the NS parameters are universally associated with the inverse compactness R/M, can be really convenient for orbital motion investigation.

The left panel of Fig. 2.2 presents values of j as a function of the gravitational mass for stars rotating with $f_{\rm rot} = 400$ Hz. Due to the Hartle-Thorne approach, one can use simple linear scaling to get $j = J/M^2$ for other values of $f_{\rm rot}$. The maximal value for a rotating NS reaches $j \in (0.65 - 0,7)$ [84]. The right panel of Fig. 2.2 shows the values of $\tilde{q} = QM/J^2$ as a function of the gravitational mass. One can see that the values of $\tilde{q}$ are less than 10 for NSs with $M \geq 1.2 M_\odot$.

We have obtained some limits on j and q, which will be used later for a further investigation. We have shown that by using only mass and radius of the star, we could calculate all parameters of the external spacetime for the required rotational frequency, and therefore skip all complicated calculations for NS models based on all possible EoS.

2.2. The external Hartle–Thorne geometry

The internal solution of the Hartle-Thorne metric is found by solving the Einstein field equations in the case when the stress-energy tensor is that of a rigidly rotating perfect fluid with angular velocity Ω. The exterior part of the Hartle-Thorne metric is found by solving the Einstein field equations in the case when the stress-energy tensor is zero. The constants that appear in the calculations are

determined by comparing the external and internal solutions on the star's surface.[2]

To investigate the free-particle motion outside the surface of rotating NSs, we used the external Hartle–Thorne geometry expressed in terms of three parameters: the gravitational mass M, the dimensionless angular momentum $j = J/M^2$ and the dimensionless quadrupole moment $q = Q/M^3$, in the form [68][3]:

$$\begin{aligned} g_{tt} &= -(1-2M/r)[1+j^2F_1(r)+qF_2(r)], \\ g_{rr} &= (1-2M/r)^{-1}[1+j^2G_1(r)-qF_2(r)], \\ g_{\theta\theta} &= r^2[1+j^2H_1(r)+qH_2(r)], \\ g_{\phi\phi} &= r^2\sin^2\theta[1+j^2H_1(r)+qH_2(r)], \\ g_{t\phi} &= g_{\phi t} = -2(M^2/r)j\sin^2\theta, \end{aligned} \tag{2.6}$$

where

$$\begin{aligned} F_1(r) &= -[8Mr^4(r-2M)]^{-1} \\ &\quad [u^2(48M^6-8M^5r-24M^4r^2-30M^3r^3-60M^2r^4+135Mr^5-45r^6) \\ &\quad +(r-M)(16M^5+8M^4r-10M^2r^3-30Mr^4+15r^5)]+A_1(r), \\ F_2(r) &= [8Mr(r-2M)]^{-1}(5(3u^2-1)(r-M)(2M^2+6Mr-3r^2))-A_1(r), \\ G_1(r) &= [8Mr^4(r-2M)]^{-1}((L(r)-72M^5r)-3u^2(L(r)-56M^5r))-A_1(r), \\ L(r) &= (80M^6+8M^4r^2+10M^3r^3+20M^2r^4-45Mr^5+15r^6), \\ A_1(r) &= \frac{15(r^2-2M)(1-3u^2)}{16M^2}\ln\left(\frac{r}{r-2M}\right), \\ H_1(r) &= (8Mr^4)^{-1}(1-3u^2)(16M^5+8M^4r-10M^2r^3+15Mr^4+15r^5)+A_2(r), \\ H_2(r) &= (8Mr)^{-1}(5(1-3u^2)(2M^2-3Mr-3r^2))-A_2(r), \\ A_2(r) &= \frac{15(r^2-2M^2)(3u^2-1)}{16M^2}\ln\left(\frac{r}{r-2M}\right), \\ u &= \cos\theta. \end{aligned}$$

For $j = 0$ and $q = 0$, the external Hartle–Thorne geometry reduces to the standard Schwarzschild one. Using the standard Boyer-Lindquist coordinates, the Kerr geometry taken up to second order in the angular momentum $a = Mj$

[2] For all models we discuss here, there are no density discontinuities at the star's surface. If there, however, were some, there would be a way of avoiding getting wrong values for the rotational corrections to the mass, see [85, 86].

[3] Note misprints in the original paper.

can be obtained from the external Hartle–Thorne geometry by setting $q = j^2$ and performing coordinate transformations based on [87][4] in the form:

$$r_{\rm BL} = r - \frac{a^2}{2r^3}[(r+2M)(r-M) - \cos^2\theta(r-2M)(r+3M)], \quad (2.7)$$

$$\theta_{\rm BL} = \theta - \frac{a^2}{2r^3}(r+2M)\cos\theta\sin\theta. \quad (2.8)$$

[4] Note that both the original transformation equations by Hartle & Thorne and their reproduction in [68] contain a sign error.

Chapter 3

Orbital motion around NSs and QPOs

Observations of some relativistic X-ray binaries exhibit the phenomenon of twin high-frequency quasi-periodic oscillations (QPOs) [88].

The first prediction that millisecond variability will naturally occur in the accretion of matter onto a stellar-mass compact object was there since 1971 [89]. After this was noted, there could exist a millisecond quasi-periodic variability caused by clumps orbiting in an accretion disk closely around a BH [90]. Using the EXOSAT telescope, scientists have discovered QPOs in LMXBs [16]. Specifically, they found a peak at frequencies of 20-35 Hz in the power spectrum of the EXOSAT data of GX 5–1, later called 4U 1758–25. The RXTE mission meant significant progress by observing Sco X–1 and 4U 1728–34. The first-ever detected kHz QPOs were discovered in their power density spectra [24, 25].

Section 3.1 in this chapter presents some of the results based on our paper [69], where we focused on the dependence of the radial profiles of the orbital and epicyclic frequencies on the parameters j and q to investigate free-particle motion only in the region outside the surface of the rotating NS.

In section 3.2, we describe the behaviour of selected orbital models of QPOs, which are associated to particular combinations of frequencies calculated from the Hartle-Thorne metric. We also analyse the locations of the frequency ratios of oscillatory modes, specifically for the $3:2$ and $5:4$ ratios. The presented results are again based on [69].

The results reported in section 3.3 are based on our paper [91], where we studied a critical value of the marginally stable circular orbit and a mass distribution of NS with an external marginally stable circular orbit in LMXBs using four EoS.

Section 3.4 shows the results of detailed calculations aimed to confront NS parameters from QPO fits with parameters of NS models based on realistic EoS. We examined the impact of NS quadrupole moment using the Kerr spacetime and also the Hartle-Thorne spacetime and showed that the selected NS models

and a particular QPO model yield specific mass-angular-momentum relations. These results are based on our paper [92].

3.1. The orbital frequency and the epicyclic frequencies

Relations for frequencies of circular and epicyclic motion in the external Hartle–Thorne spacetime have been calculated in [68] and used by many authors, see, e.g. [91, 93–95]. We present formulas for the orbital (Keplerian) frequency and the radial and vertical epicyclic frequencies that are required by twin HF QPO models related to geodesic quasi-circular motion. These were presented in [93].

The Keplerian frequency is given by

$$\nu_K(r;M,j,q) = \frac{c^3}{2\pi GM}\frac{M^{3/2}}{r^{3/2}}\left[1 - j\frac{M^{3/2}}{r^{3/2}} + j^2 E_1(r) + qE_2(r)\right], \qquad (3.1)$$

where

$$\begin{aligned} E_1(r) &= [48M^7 - 80M^6 r + 4M^5 r^2 - 18M^4 r^3 + 40M^3 r^4 + 10M^2 r^5 \\ &\quad + 15Mr^6 - 15r^7][16M^2(r-2M)r^4]^{-1} + G(r), \\ E_2(r) &= \frac{5(6M^4 - 8M^3 r - 2M^2 r^2 - 3Mr^3 + 3r^4)}{16M^2(r-2M)r} - G(r), \\ G(r) &= \frac{15(r^3 - 2M^3)}{32M^3}\ln\left(\frac{r}{r-2M}\right). \end{aligned}$$

The radial epicyclic frequency ν_r and the vertical epicyclic frequency ν_θ are given by

$$\nu_r^2(r;M,j,q) = \left(\frac{c^3}{2\pi GM}\right)^2 \frac{M^3(r-6M)}{r^4}[1 + jC_1(r) - j^2 C_2(r) - qC_3(r)], \qquad (3.2)$$

$$\nu_\theta^2(r;M,j,q) = \left(\frac{c^3}{2\pi GM}\right)^2 \frac{M^3}{r^3}[1 - jD_1(r) + j^2 D_2(r) + qD_3(r)], \qquad (3.3)$$

where

$$C_1(r) = \frac{6M^{3/2}(r+2M)}{r^{3/2}(r-6M)},$$

$$C_2(r) = [8M^2r^4(r-2M)(r-6M)]^{-1}[384M^8 - 720M^7r - 112M^6r^2 - 76M^5r^3 - 138M^4r^4 - 130M^3r^5 + 635M^2r^6 - 375Mr^7 + 60r^8] + B_1(r),$$

$$C_3(r) = \frac{5(48M^5 + 30M^4r + 26M^3r^2 - 127M^2r^3 + 75Mr^4 - 12r^5)}{8M^2r(r-2M)(r-6M)} - B_1(r)$$

$$B_1(r) = \frac{15r(r-2M)(2M^2 + 13Mr - 4r^2)}{16M^3(r-6M)} \ln\left(\frac{r}{r-2M}\right),$$

$$D_1(r) = \frac{6M^{3/2}}{r^{3/2}},$$

$$D_2(r) = [8M^2r^4(r-2M)]^{-1}[48M^7 - 224M^6r + 28M^5r^2 + 6M^4r^3 - 170M^3r^4 + 295M^2r^5 - 165Mr^6 + 30r^7] - B_2(r),$$

$$D_3(r) = \frac{5(6M^4 + 34M^3r - 59M^2r^2 + 33Mr^3 - 6r^4)}{8M^2r(r-2M)} + B_2(r),$$

$$B_2(r) = \frac{15(2r-M)(r-2M)^2}{16M^3} \ln\left(\frac{r}{r-2M}\right).$$

To show the dependence of radial profiles of the orbital and epicyclic frequencies on the j and q parameters, we chose the range of values relevant for application to astrophysically attractive models of NSs, specifically $j = 0.1, 0.2, 0.3, 0.5$. There is a limit of validity for the slow-rotation approximation $(j/j_{\max})^2 \ll 1$, and it should therefore be true that $j_{\max} \sim 0.65 - 0.7$ for NSs [84]. For a less compact object, the value of $j_{\max}$ could be significantly larger.

For the quadrupole parameter q, we took $\tilde{q} = q/j^2 = 1, 2, 3, 4, 5, 10$ for each of the values of j. This selection of values for j and q is based on modeling of the NSs as described in section 2.1 and, for example, in [96].

The radial position of the marginally stable circular orbit is in the external Hartle-Thorne metric given by

$$r_{\rm ms} = 6M\left[1 \mp j\frac{2}{3}\sqrt{\frac{2}{3}} + j^2\left(\frac{251647}{2592} - 240\,\ln\frac{3}{2}\right) + q\left(-\frac{9325}{96} + 240\,\ln\frac{3}{2}\right)\right], \tag{3.4}$$

where the $-$ and $+$ sign indicates co-rotating and counter-rotating motion, respectively. The left panel of Fig. 3.1 shows the properties of a marginally stable circular orbit r_{ms}. Close to $j = 0$, $r_{\rm ms}$ always decreases with increasing j, but it can reach a minimum and then start to increase for higher values of j for a large enough q/j^2. This kind of behavior can have a relevant impact on the observed distribution of rotational frequencies of the QPO sources [91]. The zoomed area in the left panel of Fig. 3.1 shows the curve for $q/j^2 = 5$ with a dot indicating the position of the stellar surface. Due to the direct relation of q/j^2 to the inverse compactness of the star R/M, one can calculate the position of the surface of the NS from the universal relations (see the bottom right panel of Fig. 2.1 or [97]). The radius of the marginally stable orbit $r_{\rm ms}$ is located above (for $q/j^2 < 5$) or below (for $q/j^2 > 5$) the surface of the NS for the rest of the selected values of q/j^2.

The right panel of Fig. 3.1 shows the dependence of the orbital frequency at $r_{\rm ms}$ plotted against j and calculated up to second order in the star's angular velocity as

$$f_{\rm ms} = \frac{c^3}{2\pi GM6\sqrt{6}}\left[1 + \frac{11j}{6\sqrt{6}} + \frac{1}{864}j^2\left(-160583 + 397710\,\ln\frac{3}{2}\right) + \frac{5}{32}q\left(1193 - 2946\,\ln\frac{3}{2}\right)\right]. \tag{3.5}$$

Local extrema of the radial epicyclic frequency

We investigated the radial epicyclic frequency, which is non-monotonic in r/M as the only one from the three frequencies discussed earlier. We focused on the radius at which $\nu_{\rm r}$ has its maximum and the values which this frequency takes there. The position of the maximum is given by the condition

$$\frac{d\nu_r}{dr} = 0. \tag{3.6}$$

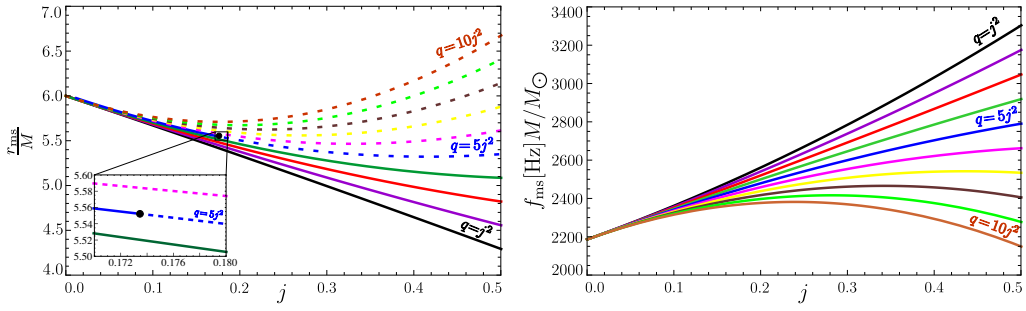

Figure 3.1. Left: the radial position of the marginally stable circular orbit $r_{\rm ms}$; dashed lines correspond to the derived location of the marginally stable orbit occurring below the surface of the NS. Right: the orbital frequency $f_{\rm ms}$ at $r_{\rm ms}$.

We found the solution in the form

$$r_{\rm max} = 8M\left[1-\frac{47}{64\sqrt{2}}j+\frac{-12596207+43683840\ln\frac{4}{3}}{147456}j^2 - \frac{5}{576}\left(-9835+34128\ln\frac{4}{3}\right)q\right], \tag{3.7}$$

then the radial epicyclic frequency at $r_{\rm max}$ is given by

$$\nu_{\rm r}(r_{\rm max}) = \frac{c^3}{64\sqrt{2}\pi GM}\left[1+\frac{15}{16\sqrt{2}}j+\frac{-3972109+13824000\ln\frac{4}{3}}{8192}j^2 + \frac{5}{16}q\left(1553-5400\ln\frac{4}{3}\right)\right]^{1/2}, \tag{3.8}$$

or, in a simplified form,

$$\nu_{\rm r}(r_{\rm max}) = \frac{714.011}{M}\sqrt{(1+0.663j+0.587j^2-0.15q)}. \tag{3.9}$$

The left panel of Figure 3.2 displays locations of the maximum $r_{\rm max}$ as a function of j, and the right panel presents the values of $\nu_{\rm r}$ at $r_{\rm max}$. One can see a similar influence of q/j^2 as that of the marginally stable circular orbit. The minimum appears only for larger values of q/j^2 and moves to smaller values of j as q/j^2 increases. The right panel shows that the largest values of q/j^2 may even cause $\nu_{\rm r}(r_{\rm max})$ to become a decreasing function of j at high rotation frequencies.

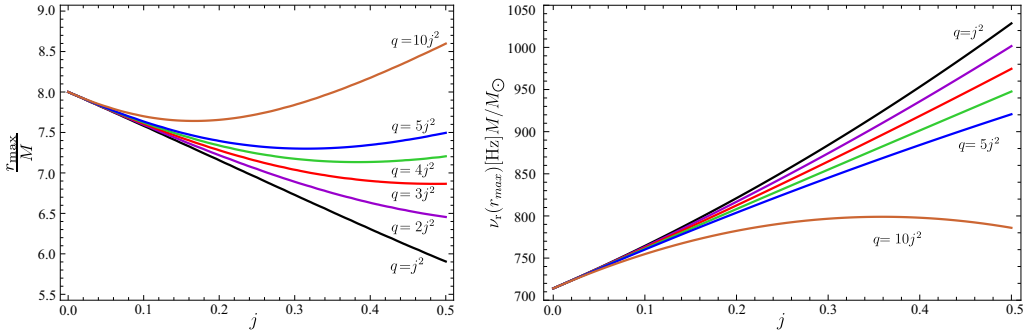

Figure 3.2. Left: the radius at which the profile of the radial epicyclic frequency ν_{r} has its maximum. Right: the value of ν_{r} at $r_{\max}$.

Precession frequencies

The periastron or the nodal precession frequency can play an important role in investigating the observed quantities. The combinations of the epicyclic frequencies may better describe the situation when matter orbits around a NS rather than the frequencies themselves.

The periastron precession frequency is given by

$$\nu_{\mathrm{P}}^{\mathrm{r}} = \nu_K - \nu_r, \tag{3.10}$$

and the nodal precession frequency is given by

$$\nu_{\mathrm{P}}^{\theta} = \nu_K - \nu_\theta, \tag{3.11}$$

where ν_K, ν_r and ν_θ are given by equations (3.1), (3.2) and (3.3).

For the computation of the precession frequencies, we took $j = 0.1, 0.2, 0.3, 0.5$ and varied the quadrupole parameter q in the range $q/j^2 = 1, 2, 3, 4, 5, 10$ for each value of j. Figures 3.3 and 3.4 show our results. As one can see, the impact of q/j^2 becomes progressively more significant as j increases in both cases. Note the situation when the radial epicyclic frequency is higher than the orbital one, the nodal precession frequency can be negative. In the case of low values of j, it occurs only very near to $r = 3M$ for a large q/j^2. For larger values of j, it occurs also for smaller q/j^2.

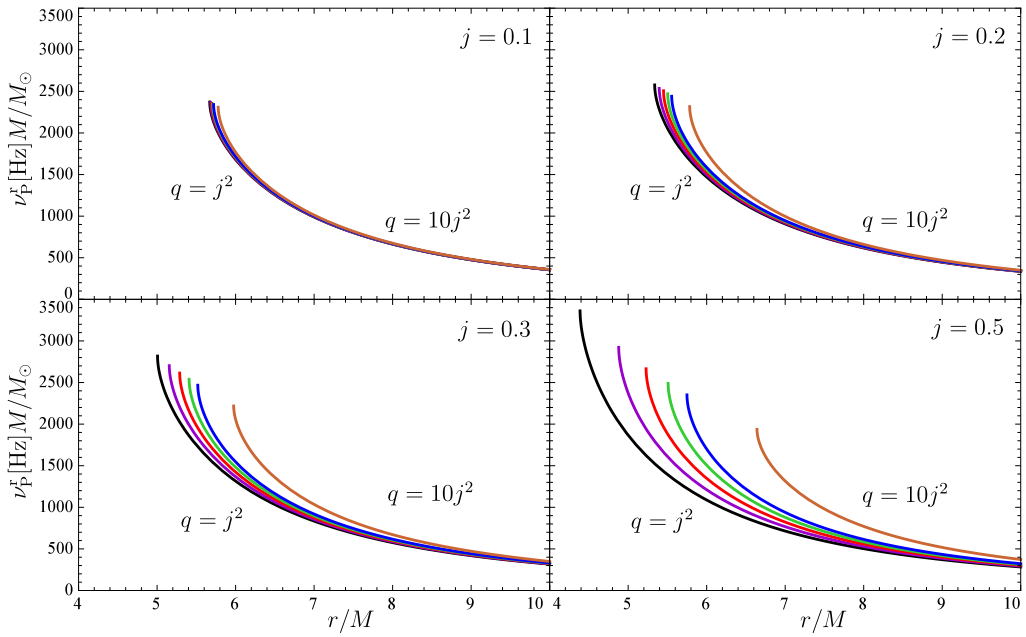

Figure 3.3. The radial profile of the periastron precession frequency $\nu_{\rm P}^{\rm r}$.

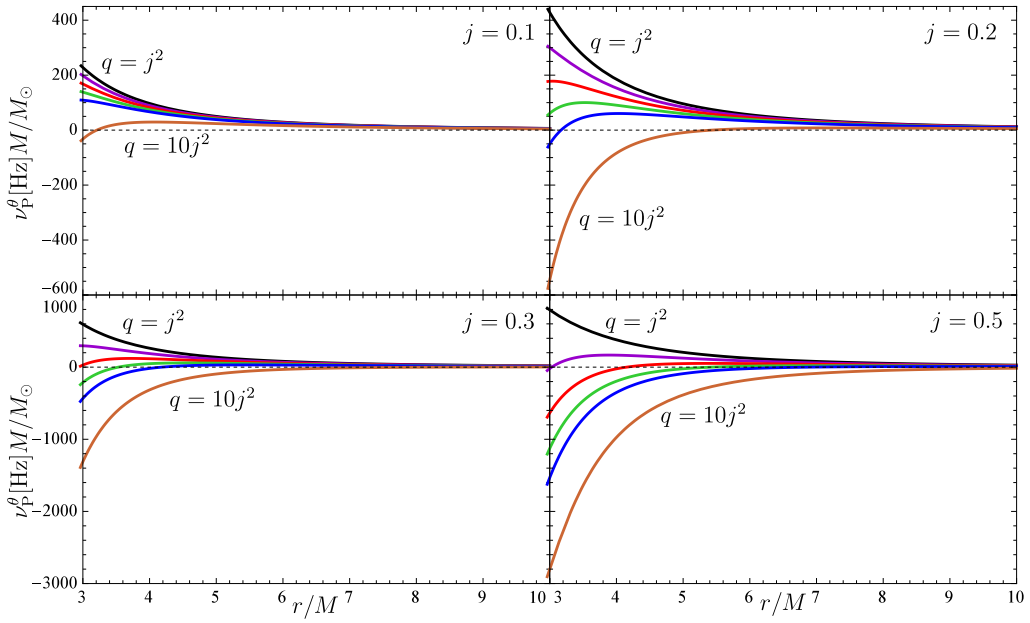

Figure 3.4. The radial profile of the nodal precession frequency $\nu_{\rm P}^{\theta}$.

Comparison of the Keplerian frequency and the vertical epicyclic frequency

The Newtonian theory points that when a central object is oblate enough, the vertical epicyclic frequency can be larger than the frequency of orbital motion [98]. In general relativity, this can happen for NSs even if they are *not* very non-spherical. We computed the ratio of vertical epicyclic frequency to the Keplerian frequency of the orbital motion and explored the unusual situation in which it was larger than one. The square of the ratio of these two frequencies can be written as

$$\left[\frac{\nu_\theta(r;M,j,q)}{\nu_K(r;M,j,q)}\right]^2 = 1 - jK(r) + j^2L(r) - qM(r), \tag{3.12}$$

where

$$\begin{aligned}
K(r) &= 4M^{3/2}r^{-3/2},\\
L(r) &= \frac{3}{8}M^{-2}r^{-2}(8M^4+35M^2r^2-30Mr^3+15r^4)+N(r),\\
M(r) &= \frac{15}{8}M^{-2}(7M^2-6Mr+3r^3)+N(r),\\
N(r) &= \frac{45}{16}M^{-3}(M-r)(2M^2-2Mr+r^2)\ln\left(\frac{r}{r-2M}\right).
\end{aligned}$$

The results are plotted in Figure 3.5 with pointing the cases where the Keplerian frequency is equal to the vertical epicyclic frequency. These points match situations where the relativistic nodal frequency disappears and changes its sign.

The impact of the switching of the nodal frequency sign is relevant only in regions where the circular geodesic motion is stable against perturbations, i.e., outward of the marginally stable circular orbit at $r_{\rm ms}$. One has to compare the position where the nodal frequency disappears with that of the marginally stable circular geodesic for the j and q/j^2 values. We used equation (3.4) and calculated the locations of $r_{\rm ms}$, these are shown as vertical lines in Figure 3.5 with the line-style corresponding to that for the $\nu_\theta/\nu_{\rm K}$ profile with the same value of q/j^2. For low values of j, there are some cases where $\nu_\theta/\nu_{\rm K}=1$ occurs at a radius under $r_{\rm ms}$. For higher values of j and q/j^2, $\nu_\theta > \nu_{\rm K}$ can also occur for orbits that are stable for radial perturbations.

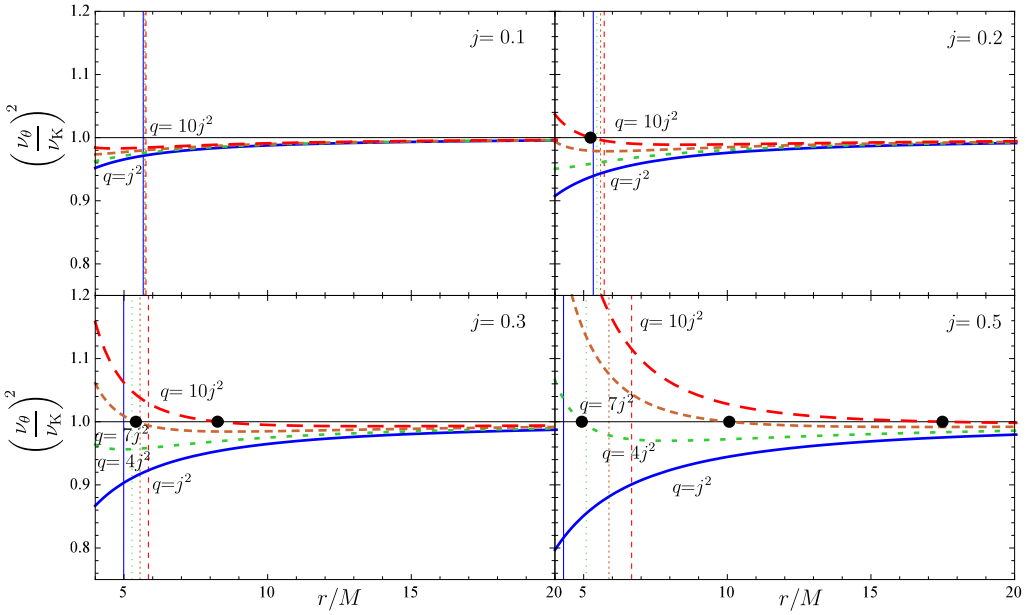

Figure 3.5. The ratio of the vertical epicyclic frequency to the Keplerian frequency with the indication of the points at which these quantities are equal.

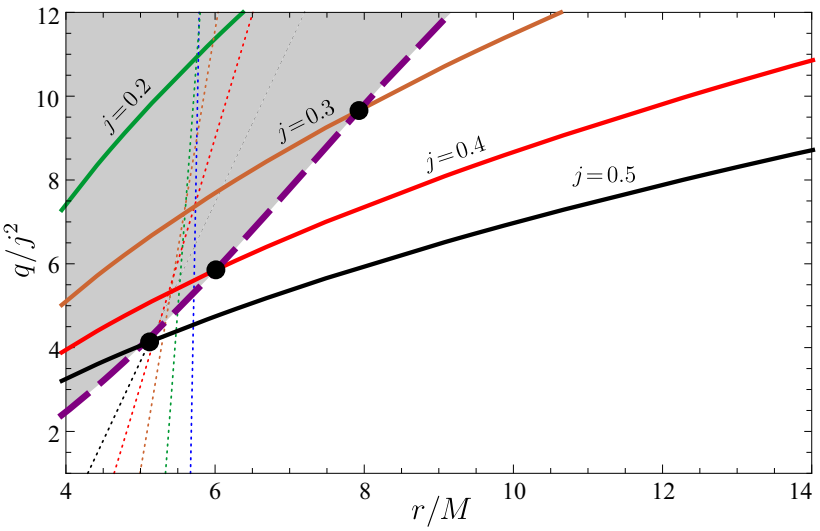

Figure 3.6. The value of q/j^2 giving $\nu_\theta = \nu_K$ plotted as a function of r/M for various values of j. The dotted lines show the value of r_{ms} for each j and the purple dashed line marks the stellar surface.

We furthermore investigated locations where

$$\left[\frac{\nu_\theta(r;M,j,q)}{\nu_K(r;M,j,q)}\right]^2 = 1. \tag{3.13}$$

In the non-rotating Schwarzschild case, ν_θ always equals ν_K, and it is impossible to find the location for the nodal switching point as an expansion around the Schwarzschild value. The values of q/j^2 satisfying (3.13) are given by

$$\frac{q}{j^2} = 1 + \frac{64M^{9/2}\sqrt{r} - 48jM^5}{15jr^2\left[-2M\left(7M^2-6Mr+3r^2\right) - 3(M-r)\left(2M^2-2Mr+r^2\right)\ln\left(\frac{r}{r-2M}\right)\right]}, \tag{3.14}$$

The result of q/j^2 giving $\nu_\theta = \nu_\mathrm{K}$ is plotted in Figure 3.6 against r/M for $j = 0.2, 0.3, 0.4, 0.5$. The dotted lines show values of r_ms for each j and the purple dashed line marks the stellar surface; we indicated the point on each of the j curves beyond which r is greater than both of those limits.

3.2. Models of twin HF QPOs and the QPO frequency ratios

The previous section described the behaviour of the orbital, epicyclic and precession frequencies. We have shown that with increasing j, the role of the quadrupole term has become increasingly important. This section focuses on specific combinations of frequencies that play crucial roles for models of QPOs - the twin peaks seen in the power spectra of LMXBs. The cause of these peaks is still not known but it is intensively studied. There are many candidate models that utilize frequencies connected to orbital motion around the central object.

For our investigation, we considered the specific models presented in Table 3.1, where we also show the combinations of frequencies that are associated with the upper and lower observed peaks in each case. These currently used models allow us to study the behaviour of the frequencies of oscillatory modes that can explain the origin of the twin HF QPOs observed in the atoll and Z-sources, where a NS accretes matter from a low-mass companion (for differences between the atoll and Z-sources, see [99]).

We selected these orbital models of QPO based on [100]. None of the models is currently uniquely preferred because each of them has (different) theoretical problems.

Table 3.1. An overview of the orbital models of QPOs, with specification of the upper $\nu_{\rm U}$ and lower $\nu_{\rm L}$ frequencies.

Frequency	RP	TD	WD	RP1	RP2	ER
$\nu_{\rm U}$	$\nu_{\rm K}$	$\nu_{\rm K}+\nu_{\rm rad}$	$2\nu_{\rm K}-\nu_{\rm rad}$	ν_θ	$2\nu_{\rm K}-\nu_\theta$	ν_θ
$\nu_{\rm L}$	$\nu_{\rm K}-\nu_{\rm rad}$	$\nu_{\rm K}$	$2(\nu_{\rm K}-\nu_{\rm rad})$	$\nu_{\rm K}-\nu_{\rm rad}$	$\nu_{\rm K}-\nu_{\rm rad}$	$\nu_{\rm rad}$

Our selection of orbital models can be described as follows:

RP - The Relativistic Precession model based on [101] considers that the kHz QPOs are a direct consequence of the relativistic epicyclic motion of blobs at various radii in the inner parts of the accretion disk;

TD - The Tidal Disruption model based on [102] proposes that the QPOs are generated by tidal disruption of large accreting inhomogeneities;

WD - The Warped Disk model based on [103] considers a somewhat exotic disk geometry that causes a doubling of the observed lower QPO frequency;

ER - The Epicyclic Resonance model based on [104] involves different combinations of axisymmetric disk-oscillation modes;

RP1/RP2 - The RP1 model is based on [105] and The RP2 based on [106] use different combinations of non-axisymmetric disk-oscillation modes.

Here, we studied geodesic oscillation models in which the oscillatory modes are combinations of the orbital and epicyclic frequencies of near-circular geodesic motion in the equatorial plane.

In our computations, we repeatedly used the same values $j = 0.1, 0.2, 0.3, 0.5$ including the maximal range of the spin parameter j for the Hartle–Thorne approximation [96]. The value of the quadrupole moment q was calculated from j for different values of $q/j^2 = 1, 3, 5, 10$.

Figure 3.7 presents radial profiles of the frequency ratio $\nu_{\rm U}/\nu_{\rm L}$ for all of the six studied QPO models. For the RP model, the $\nu_{\rm U}/\nu_{\rm L} = 3/2$ ratio occurs slightly outside the location of the marginally stable orbit, meaning that the QPOs will be generally associated with the region very close to the inner edge of the accretion disk, but in the case of the TD and WD models, the radius is larger, and it is even more so for the ER model. However, all the analysed models give the radius where $\nu_{\rm U}/\nu_{\rm L} = 3/2$ is between $r_{\rm ms}$ and $r = 11M$. The RP, RP1 and RP2 models give remarkably similar profiles, with only very minor differences. The profiles of the WD and TD models are different, but they always cross each other at the frequency ratio of 3 : 2. The ratio for the ER model diverges at the marginally stable orbit since the radial epicyclic frequency has to vanish there.

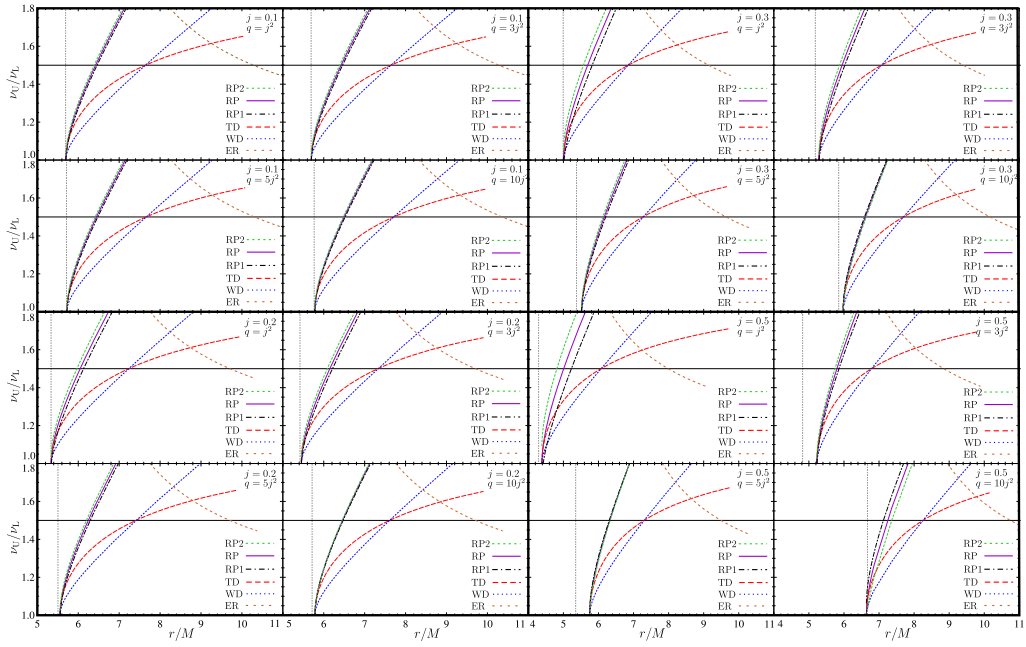

Figure 3.7. The dependence of ν_U/ν_L on r/M for all selected orbital models of QPOs (with $j = 0.1,\ 0.2,\ 0,3,\ 0.5$). The vertical dotted line indicates the location of the marginally stable orbit r_{ms}, as given by equation (3.4), and the horizontal line indicates the ratio $\nu_U : \nu_L = 3 : 2$.

The ER model is the only one where the ratio decreases with increasing radius. In all of the models, the radial profiles depend only slightly on the quadrupole parameter for small values of $j < 0.2$, but the dependence grows with increasing j, and for $0.3 < j < 0.5$ it can be very strong, especially close to the marginally stable orbit.

Figure 3.8 presents results for each of the QPO models separately, using $j = 0.1, 0.2, 0.3, 0.5$ and $q/j^2 = 1, 2, 3, 4, 5, 10$. Note the influence of j and q/j^2 on the position of the marginally stable orbit. One can see that the ER model results are qualitatively different compared to the results related to other models.

The observed QPO data exhibit clustering of the frequency ratio round 3 : 2 [107]. We therefore calculated how the position where this ratio is generated changes as a function of j. The left panels of Figure 3.9 present the results for each of our QPO model for $q/j^2 = 1, 2, 3, 4, 5, 10$. The behaviour of $r_{3:2}/M$ confirms a qualitatively similar behaviour to that for the position of the marginally stable orbit: for small values of q/j^2, the resonance radius decreases with increasing spin, as for Kerr BHs, but, for a large enough q/j^2, it reaches a minimum and then increases again.

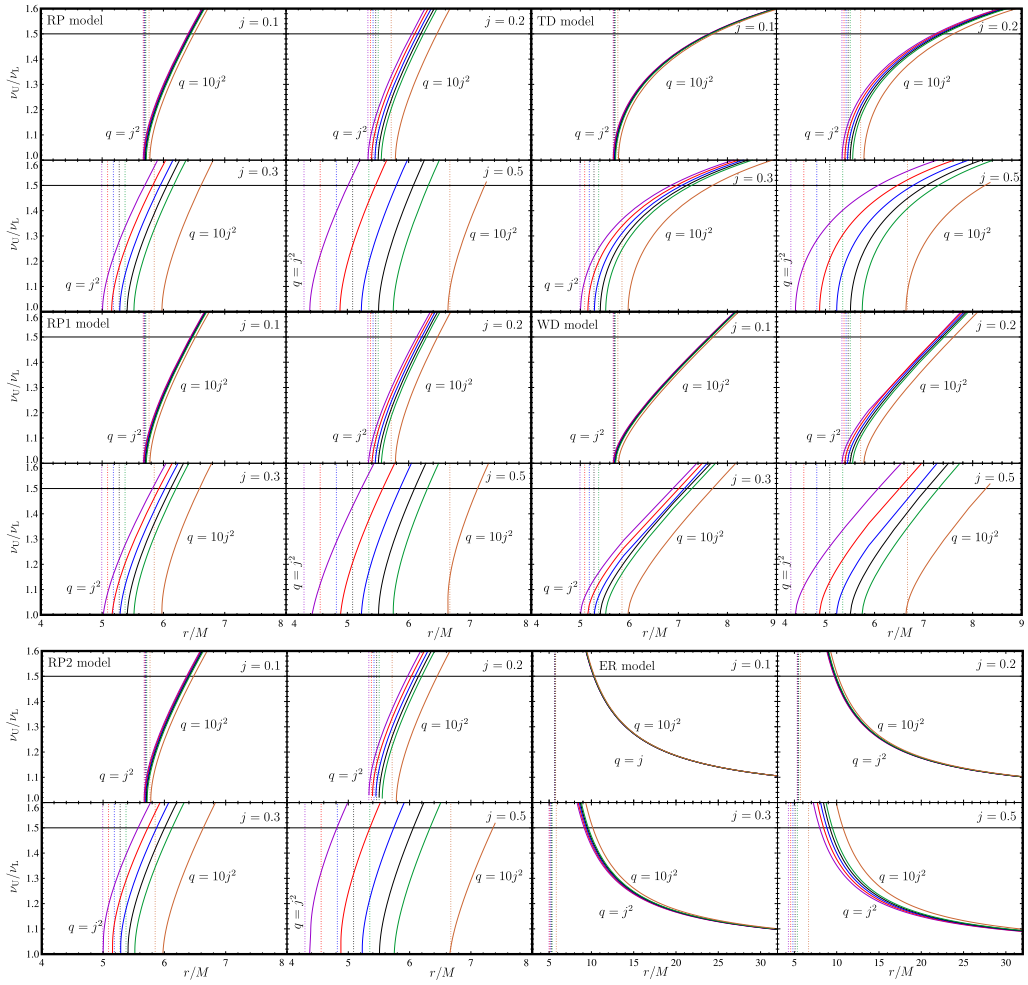

Figure 3.8. The ratio ν_U/ν_L plotted against r/M for each model separately: RP, RP1, RP2, TD, WD, ER (top left to bottom right). The vertical dotted lines indicate the location of the marginally stable orbit r_{ms} for each value of q.

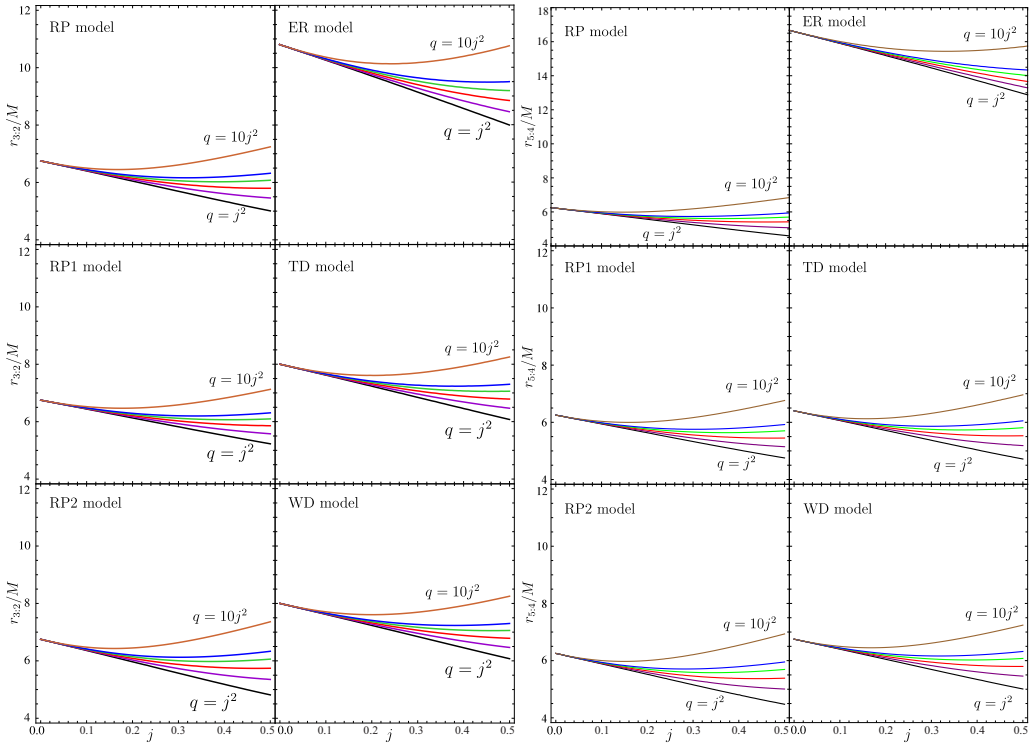

Figure 3.9. The positions where the resonant QPO ratios 3:2 and 5:4 are generated: For each of the models, $r_{3:2}/M$ (left panels) and $r_{5:4}/M$ (right panels) are plotted against j for $q/j^2 = 1,2,3,4,5,10$.

The right panels of Figure 3.9 present analogous results for the 5:4 ratio. They are quite similar to the above consideration.

3.3. Innermost stable circular orbit of accretion disks around rotating NSs

When we investigate orbital motion of a test particle circulating a spherical central mass M, we realise that, in Newtonian theory, such a particle trajectory is stable to small radial perturbations at any radii r, and that the trajectories are only limited by the position of the surface of the central mass. In the case of general relativity, such trajectories report an instability below the critical radius of the marginally stable circular orbit $r_{\rm ms}$. We define the innermost stable circular orbit (ISCO) of an accretion disk orbiting a NS as $r_{\rm ISCO} = r_{\rm ms}$ if the $r_{\rm ms}$ is located outside the NS surface and we identify it with the $R_{\rm NS}$ in the other case. We have already shown that the position of $r_{\rm ms}$ decreases with growing angular momentum j of the NS, see Figure 3.1. At the same time, the position of $r_{\rm ms}$ increases with the increasing influence of the NS quadrupole moment q.

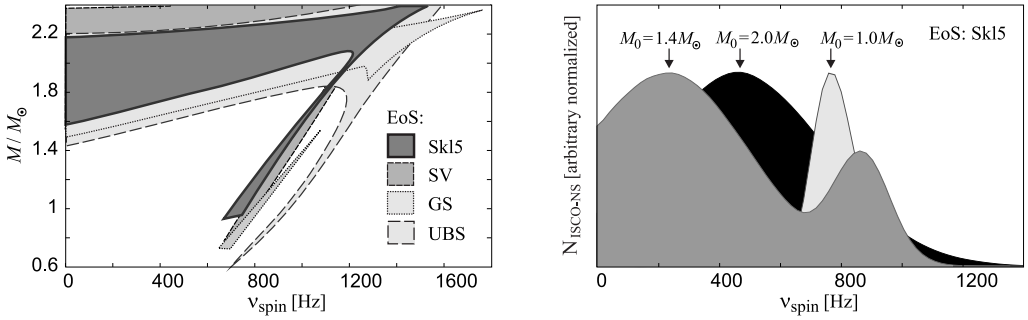

Figure 3.10. Left: Mass-spin regions that allow the appearance of marginally stable orbit calculated for selected EoS. The displayed drawing is the result of $\sim 10^5$ computations of NS configurations. Right: NSs with an external $r_{\rm ms}$ spin distribution expected for the SKl5 EoS and three different referential values of M_0.

The results that we describe here are based on [91]. There we studied the behaviour of the $r_{\rm ms}(j,\ q)$ function calculated from equation (3.4) based on the Hartle-Thorne approximation, see section 3.1. We found that $r_{\rm ms}$ had a minimum for $\tilde{q} \gtrsim 2.8$. The related angular momentum and the quadrupole moment of the central object were given as follows:

$$\tilde{q}_{\rm min} = 1 + \frac{32\left(9\sqrt{6}+4j_{\rm min}\right)}{135\, j_{\rm min}\left[4608\log(3/2)-1865\right]}\,. \tag{3.15}$$

Then the smallest permitted marginally stable radius was given by

$$r_{\rm min} = 6 - 2j_{\rm min}\sqrt{2/3}\,. \tag{3.16}$$

We also studied a mass distribution of NSs with an external $r_{\rm ms}$ in LMXBs. We used NS models based on the UBS EoS [108] and three more EoS: the SKl5, the SV and the GS, all representing different parametrisation of the Skyrme potential (see [109] and references therein). Based on a simple analytical analysis and the consideration of NS models underlying different EoS, our results imply a strong restriction on distribution of the NS parameters with external $r_{\rm ms}$. We are aware that this particular distribution could differ from the (so far unknown) distribution of all NSs in LMXBs. We illustrate these restrictions using an example calculated for the Skl5 EoS and the simplified assumption that all NSs follow a two dimensional Gaussian distribution in the mass–spin space. We set mean values for the distribution of all NSs as $M_0 \in \{1M_\odot,\ 1.4M_\odot,\ 2M_\odot\}$, and $\nu^0_{\rm spin} = 500$ Hz together with scales $\sigma_M = 0.2M_\odot$ and $\sigma_{\nu{\rm spin}} = 300$ Hz. The subsets of NSs with external $r_{\rm ms}$ were then determined by the map depicted in

the left panel of Figure 3.10. The right panel shows the spin distribution of these subsets. One can see that if the NSs are distributed around a high mass, $M_0 = 2M_\odot$, the spin distribution of NSs with external $r_{\rm ms}$ is almost the same as the spin distribution of all NSs that peak around $\nu^0_{\rm spin}$. On the other hand, when this mass is low, $M_0 = 1M_\odot$, the distribution of NSs with external $r_{\rm ms}$ has a peak only around a high value of $\nu_{\rm spin}$. A different situation occurs for an intermediate value of $M_0 = 1.4M_\odot$, which implies a distribution of NSs with external $r_{\rm ms}$ divided into two groups of slow and fast rotators.

The predictions on the NSs parameters would be robust if the external $r_{\rm ms}$ presence or absence in the individual systems were observationally confirmed. Moreover, one can speculate on some consequences for the evolution of the spinning-up sources.

3.4. Confronting the QPO fits with realistic NS models

This section aims to comment on the part of the results based on our paper [92] that touches on the topic of this dissertation. There we confronted selected QPO models with a collection of 18 NS models calculated from realistic EoS. Our selection of NS models was motivated by low values of a scaled quadrupole moment q/j^2, which is related to rotationally induced oblateness of NS. For a detailed comparison, we used selected QPO models within Kerr spacetimes and the Hartle-Thorne spacetime (see section 3.2 and Table 3.1 for a detailed description of QPO models in the Hartle-Thorne spacetime). In addition, we paid special attention to the atoll source 4U 1636–53 and evaluated mass–angular-momentum relations for all considered QPO models. An overview of the EoS we used in our calculations can be found in Table 2 in [92].

A part of the results is captured in Figure 3.11. The top right panel shows a comparison between predictions of the RP model and selected NS models. The horizontal dashed red line together with the horizontal shaded bar indicate additional limitations on the RP model arising from the consideration of the Lense-Thirring precession, as discussed in [111]. The red spot roughly indicates the combination of mass and spin inferred from the common consideration of the RP model, NS spin frequency of 580 Hz and 4 NS EoSs as discussed by [111]. The green cross-marker denotes the mass and angular momentum combinations reported for 4U 1636–53 and the RP model. One can obtain other exciting information by comparing overlaps between the RP model relation and curves denoting the requirements of individual NS models. For example, the overlaps showed in the top right panel of Figure 3.11 differ from the overlaps obtained by

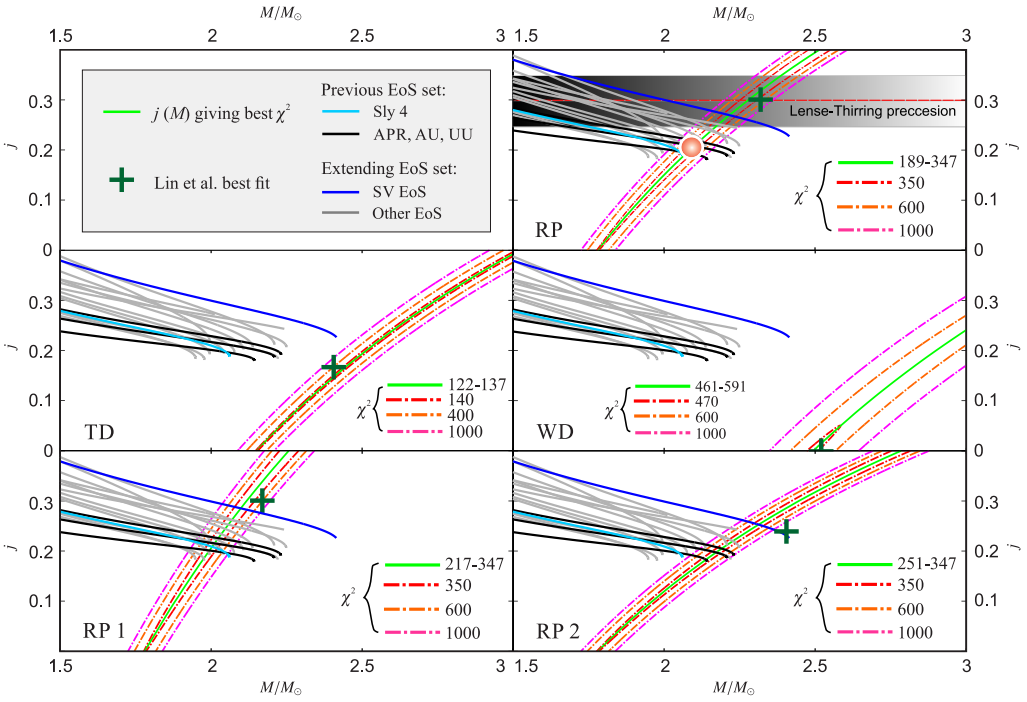

Figure 3.11. χ^2 maps (20 d.o.f.) calculated from data of the atoll source 4U 1636-53 and individual QPO models within Kerr spacetimes vs mass–angular-momentum relations predicted by models of NSs based on selected EoS. The green line symbolises the best χ^2 for a fixed M. The green cross-markers indicate the mass and angular momentum combinations reported for 4U 1636-53 and individual QPO models by [110].

[111] (here marked as the red spot in Fig. 3.11) thanks to the new selection of EoS. Due to this set of EoS, the quadrupole moment of NS leads to an increase of the angular momentum. For instance, there is $j \approx 0.19$ for Sly4 vs. $j \approx 0.28$ for SV EoS. Such an effect can be significant for taking into account the Lense-Thirring precession and low-frequency QPOs within the framework of the RP model.

The other panels of Fig. 3.11 are made in the same way but for the other four QPO models [110]. The QPO model predictions are drawn for simplified calculations assuming the Kerr background geometry. All NS models based on a realistic set of EoS are assumed for the rotational frequency of 580 Hz deduced from the X-ray burst observations. By analysing Fig. 3.11, one can see a direct confrontation of NS models and that the TD (and also WD) model entirely fails to meet the requirements given by the inclusion of the NS models.

Here, we briefly described some of the results of paper [92]. We explored more restrictions on the QPO models and performed consistent calculations in the Hartle-Thorne spacetimes. For more information, see our paper.

Chapter 4

Up-to-date constraints on NS mass and spin based on the rapid X-ray variability

So far, we mostly concentrated on geodesic orbital motion in Hartle-Thorne spacetimes. In this chapter, we shift our focus from the geodesic approximations to our ongoing research that relies on a further comparison of up-to-date QPO models and the large amount of the available data (see Figure 4.1 for an illustration).

4.1. Oscillations and instabilities of the flow close to ISCO

In [113], a new model of QPOs, which deals with oscillations of fluid in marginally overflowing tori, was proposed - see the works of [104, 114–117] for a broader context. The model relies on the consideration of perturbed closed equipressure structures that terminate the innermost accretion disk by cusps. Hereafter, we refer to this model shortly as the CT model. Within the CT model, the lower QPO frequency corresponds to the radial oscillations of the inner accretion flow. The upper QPO frequency is then given as the co-rotation (Keplerian) frequency associated to instabilities of the flow that grows for some time but does not survive due to the stabilization effects [118–121].

According to preliminary estimates, the CT model provides overall better fits of the NS QPO data compared to the RP model [113]. It also implies a significantly higher upper limit on the Galactic microquasars BH spin [117]. While the model's predictions on the QPO frequencies have to be calculated numerically, a short analytic formula has been noticed to well reproduce these predictions in Schwarzschild spacetimes [122].

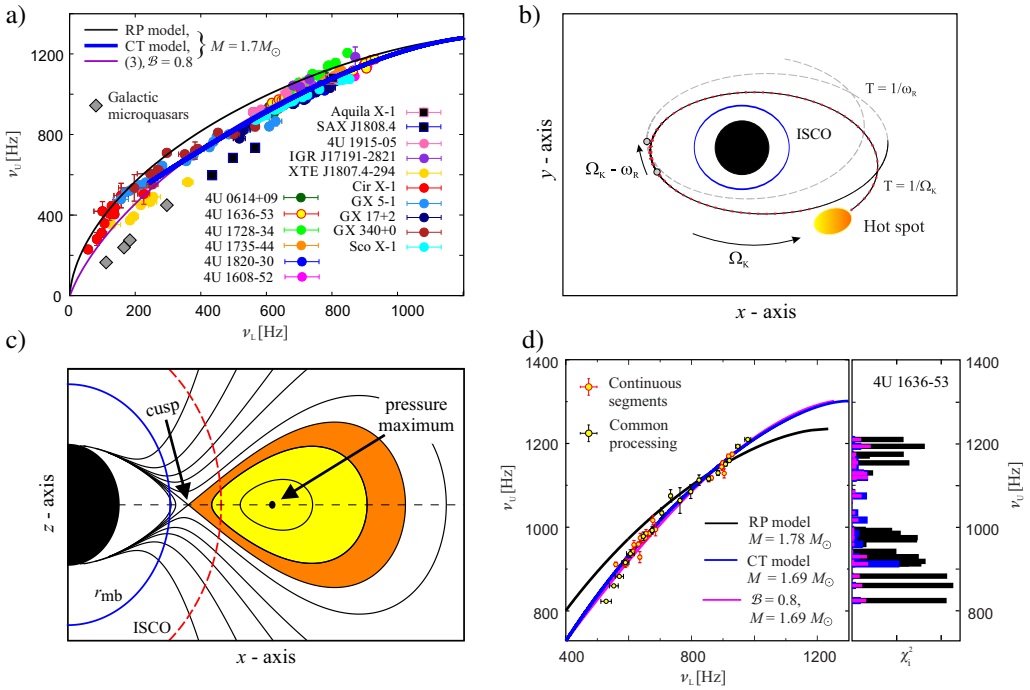

Figure 4.1. Frequencies of HF QPOs in LMXBs sources and their models - an illustration from our recently submitted paper [112]. a) The data of several sources and examples of the expected frequency relations that are drawn for $M = 1.7M_\odot$. The expected frequency relations are drawn for a non-rotating NS. b) Sketch of the trajectory of a test particle on a slightly eccentric orbit which plays a crucial role in the hot-spot interpretation of QPOs. c) The CT model relies on a specific selfcrossing topology of equipotential surfaces that determine the spatial distribution of fluid in thick accretion disks. d) The data of the atoll source 4U 1636-53 and their best fits for non-rotating NS. The violet curve denotes the prediction given by our approximative relation 4.1. For the sake of clarity, the data-set which corresponds to the individual continuous observations is compared to the data-set associated with the common processing of all observations - see [113].

4.2. A formula determining the QPO frequencies

In our present work, we extend the investigation of the CT model to Hartle-Thorne spacetimes [123].

Although our work is based on fairly long input equations and related numerical calculations, we arrive at a surprisingly simple approximative formula that can be written as follows

$$\nu_L = \nu_U \left[1 - \mathcal{B}\sqrt{1 + 8j\mathcal{V}_0 - 6\mathcal{V}_0^{2/3} - \mathcal{Q}\mathcal{V}_0^{4/3}} \right], \tag{4.1}$$

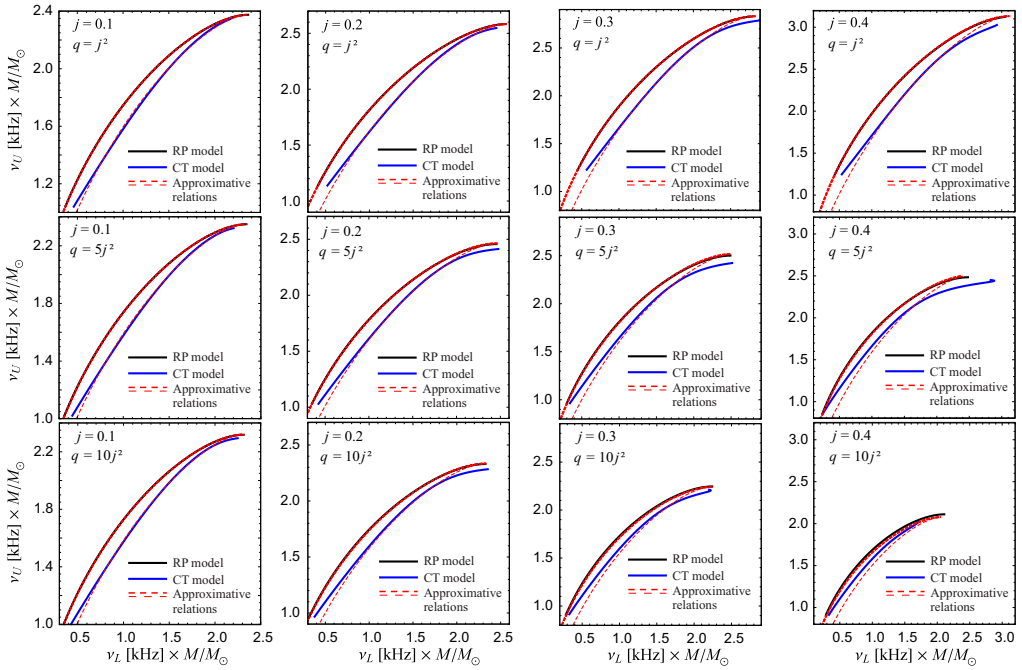

Figure 4.2. Comparison between the expected QPO frequencies. The continuous curves denote frequencies calculated numerically for the CT and RP models. The dashed curves denote frequencies calculated using the approximative relation for the CT ($\mathscr{B} = 0.8 - 0.2j$) and RP ($\mathscr{B} = 1$) models.

where

$$\mathscr{B} = 0.8 - 0.2j, \qquad \mathscr{V}_0 \equiv \frac{\nu_{\rm U}/\nu_0}{6^{3/2} - j\nu_{\rm U}/\nu_0},$$
$$\mathscr{Q} = \frac{1}{3}(8j^2 - 17q), \qquad \nu_0 = 2198\frac{\rm M_\odot}{M}.$$

For the above choice of $\mathscr{B}$, this relation with a high accuracy provides frequencies predicted by the CT model. Choosing a constant $\mathscr{B}$, $\mathscr{B} = 1$, it (almost exactly) provides frequencies predicted by the RP model. It is therefore applicable for both models in the case of rotating oblate NSs. This is illustrated in Figure 4.2. We note that for high QPO frequencies, corresponding to radii very close to ISCO, when $\nu_{\rm L}$ approaches $\nu_{\rm U}$, there are discrepancies between the illustrated relations related to the considered accuracy up to the second-order terms in q. The inaccuracies however grow only when the difference between the two QPO frequencies is smaller than 10%.

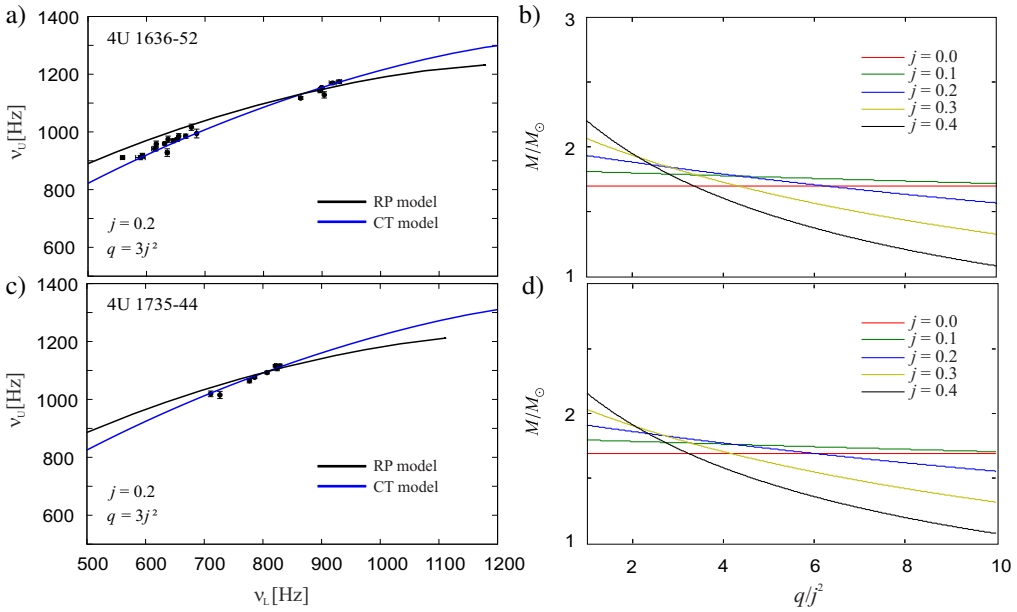

Figure 4.3. a) Best fits of the data of the 4U 1636–53 atoll source found for the RP and CT models and a particular choice of the NS spin and oblateness. For the other choices within the considered range of parameters, $j \in [0, 0.4]$ and $q/j^2 \in [1, 10]$, the resulting fits are similar. b) The best fitting mass corresponding to the CT model as it depends on q/j^2. c) The same as in panel a) but for the 4U 1735–44 atoll source. c) The same as in panel b) but for the 4U 1735–44 atoll source. At this place we note that while for the 4U 1735–44 source the rotational frequency of the source is so far not well known, for the 4U 1735–44 it was inferred from the X-ray burst measurements [124]. This is further utilized in the last Chapter of our annotation.

4.3. Application to atoll source 4U 1636-53

Following [113], we can apply our relation 4.1 to the data of the atoll source 4U 1636–53. The main outputs of our investigation are illustrated in Figure 4.3. Figure 4.3a includes examples of the best fits given by the CT model. Fits given by the RP model are shown as well for the sake of comparison. Figure 4.3b depicts how the best fitting M depends on j and q/j^2. It shows that for very compact NSs with $q/j^2 \sim 1$ the best fitting M increases with increasing j, reaching values of $M \in [2, 2.2]M_\odot$ for $j \in [0.2, 0.4]M_\odot$. This is in agreement with the investigation of [113] limited to the case of very compact stars. On the other hand, for stars of high oblateness, $q/j^2 > 4$, the best fitting M decreases with increasing j. For stars of moderate oblateness, $q/j^2 \sim 3$, there is only a very weak dependency on j and the estimated mass is around $M = 1.75M_\odot$.

4.4. Other sources

The same investigation but performed for the atoll source 4U 1735–44 is illustrated in Figures 4.3b and c showing a picture very similar to the 4U 1636–53 case. In analogy to that case, we obtain fits better than those of the RP model and a similar quadrupole moment dependence. For very compact stars, $q/j^2 \sim 1$, the best fitting M increases with increasing j, reaching values of $M \in [1.9, 2.2]M_\odot$ for $j \in [0.2, 0.4]M_\odot$, while for stars of high oblateness, $q/j^2 > 4$, the best fitting M decreases with increasing j. For stars of moderate oblateness, $q/j^2 \sim 3$, there is only a very weak dependency on j and the estimated mass is around $M = 1.9M_\odot$. In the same way, we investigated another four atoll sources with high amount of available data [111, 125, 126]. Overall, based on the CT model, we can expect that for stars of moderate oblateness, $q/j^2 \sim 3$, the mass should be within the interval of $M \in [1.6, 1.9]M_\odot$.

Chapter 5

Summary and future perspectives

Within our research devoted to NS models, external spacetime properties and their observable implications, we studied different aspects of orbital motion taking place in a close vicinity of the NS. We in particular explored motion of particles while performing a systematic analysis of properties of frequencies of the Keplerian and epicyclic motion. Our investigation of conditions determining the presence of external marginally stable orbit reveals that, in principle, the X-ray variability features may differ depending on the speed of the NS rotation. Namely, it may significantly differ for moderately rotating NSs compared to slowly and rapidly rotating NSs. Also, we investigated in detail a variety of QPO models. Utilizing the available observational data and the limits on their precision, we found that application of concrete EoS along with a given QPO model yielded a specific mass-angular-momentum relation instead of a particular pair of mass and angular momentum. The degeneracy in mass and angular momentum could be eliminated by considering restrictions following from the NS spin frequency measurements based on X-ray burst observations.

We conclude that our investigation leads to a number of individual outcomes regarding the rotating NSs. Furthermore, it has inspired us to initiate several follow-up research projects that are presently being carried out. One of them is described in Chapter 4 where we present our findings that, in the Hartle-Thorne spacetime, the CT model provides much better fits of the data than the RP model. Motivated by this promising result, we would like to work in our future study with a larger set of sources and, more importantly, with a full set of available up-to-date NS EoS.

5.1. Implications for the research devoted to NSs and their rapid X-ray variability

The possible future strategy of a full confrontation between EoS and QPO data is illustrated in Figure 5.1. There we plot relations between the NS parameters

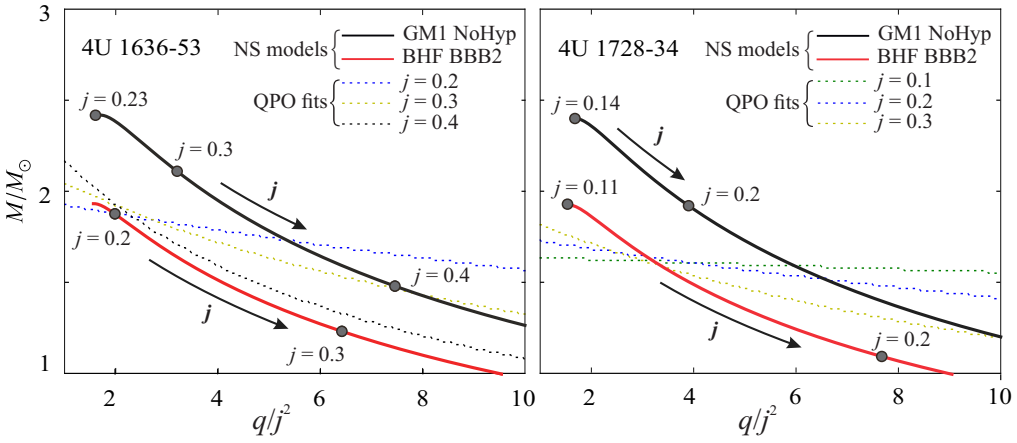

Figure 5.1. The best fitting mass corresponding to the CT model as it depends on q/j^2 (dotted curves) vs. relations calculated for the particular BHF BBB2 and GM1 NoHyp EoS (solid curves). Left: Consideration of the atoll source 4U 1636–53. For the NS models we fix the rotational frequency to the value of 581 Hz given by the X-ray burst measurements. Right: Consideration of the atoll source 4U 1735–44. For the NS models we fix the rotational frequency to the value of 363 Hz given by the X-ray burst measurements.

providing best fits of the data of the atoll source 4U 1636–53 that were discussed in Chapter 4 along with the predictions calculated for a choice of two particular EoS. In our calculations, we have benefited from the CompOSE (CompStar Online Supernovæ Equations of State) library [127] and use the BHF BBB2 [128] and GM1 NoHyp [129] EoS.

In the left panel of Figure 5.1, we utilize our knowledge of the spin frequency of the 4U 1636–53 source, of which the value 581 Hz has been inferred from X-ray burst observations [124]. Figure 5.1 demonstrates that predictions of the NS parameters following from fitting of the QPO data are in full agreement with the prediction of the BHF BBB2 EoS for $j = 0.2$ and $M \doteq 1.8 M_\odot$. For the GM1 NoHyp EoS, on the other hand, which implies a lower NS compactness, the same predictions are clearly incompatible. A similar consideration, but for another source, is shown in the right panel of Figure 5.1. In this case, the rotational frequency of the source is 363 Hz. Here, the BHF BBB2 EoS is well compatible with the outputs of fitting of the QPO data for $j \doteq 0.15$ and $M \doteq 1.6 M_\odot$ while the GM1 NoHyp EoS once again yields rather incompatible results. At this point, we can state that our approach has a high predictive power in relation to falsifiability of the QPO models and EoS. Here we note that the CT model so far appears to be compatible with the modern EoS.

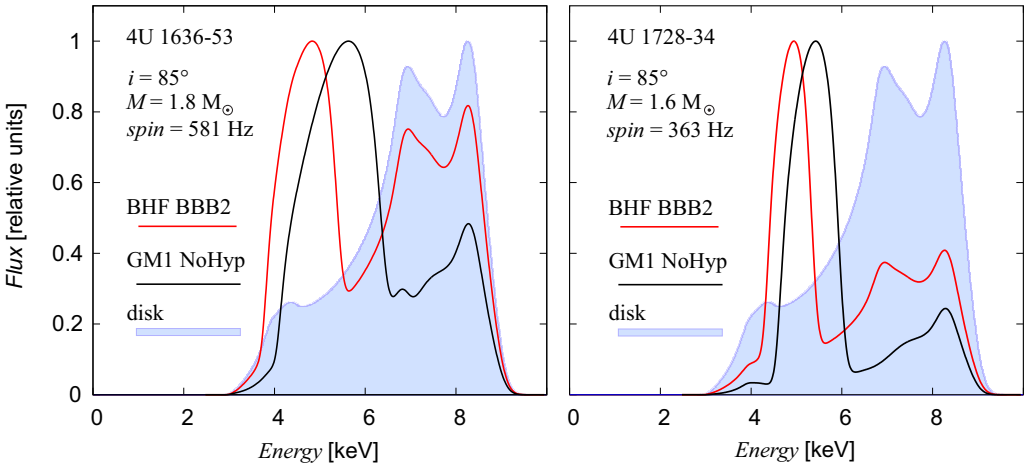

Figure 5.2. Iron line profiles calculated for the system of a radiating star and its accretion disk. The blue region indicates the line from the disk alone. The black and red curves correspond to the total flux from the disk and star together (obscuration effects are included). The two different EoS are considered. Parameters of the stars are given by fitting of the QPO data along with spin frequencies inferred from X-ray burst measurements (see Figure 5.1).

5.2. A further prospect: X-ray spectra

Apart from our main focus devoted to X-ray timing and its relation to NS models, we started a collaboration on research devoted to X-ray spectra. In Figure 5.2, we show an illustration based on the very recently initiated research in this field. The figure depicts an impact of NS EoS on the relativistic iron line profile in the spectra of radiation emitted from the innermost accretion region. Within the figure, we compare the shape of the iron line calculated from the disk with the shape calculated for the composed radiation of the whole system of the star and the disk. In the calculations of the NS models, we use the parameters inferred from the variability of the above mentioned two sources (see Figure 5.1).

Clearly, the consideration of different EoS may result in a very different shape of the iron line in the expected spectra of the source. More specifically, the presence of a less compact NS underlying a stiff EoS suppresses more strongly the high-energy part of the peak from the disk. Note that we assume almost an edge-on (equatorial) view of the source.[1] Presumably, in this situation, the

[1] We also note that for our illustration we consider a very simplified example of the Novikov-Thorne disk [130] and a spherical star with a constant surface X-ray emissivity. This approximation should be further improved by including a more realistic description of the star along with some boundary layer model. What is also needed is to adjust the proper parameters of such a model of the full radiating system as well as to investigate the related parameter space.

iron line profile calculations are not much influenced by the external metric approximation [131]. Consequently, the most important thing for determining the shape of the broadened peak is then solely the choice of a particular EoS that determines the value of the NS radius. Hence, to calculate a photon propagation, the non-spherical effects given by the NS rotation are here neglected and we utilize the results of full relativistic ray-tracing within the Schwarzschild geometry. On the other hand, for much different inclination angles close to vertical axes (top view), it will be necessary to perform the ray-tracing in the Hartle-Thorne spacetime. A self-consistent incorporation of such ray-tracing (which would reflect the NS oblateness) into the X-ray spectral and timing research, represents one of our possible future research directions.

References

[1] S. L. SHAPIRO & S. A. TEUKOLSKY: *Black holes, white dwarfs and neutron stars*. John Wilery and Sons, New York, 1983.

[2] LEWIN, W. H. G. & VAN DER KLIS, M., editors: *Compact Stellar X-Ray sources*. Cambridge University Press, 2006.

[3] BLAKE, R. L.; CHUBB, T. A.; FRIEDMAN, H. & UNZICKER, A. E.: Interpretation of X-Ray Photograph of the Sun. *The Astrophysical Journal*, **137**, p. 3, January 1963.

[4] TOUSEY, R.: Apollo Telescope Mount of Skylab: an overview. *Appl. Opt.*, **16**(4), pp. 825–836, April 1977, URL `https://doi.org/10.1364/AO.16.000825`.

[5] GIACCONI, R.: Nobel Lecture: The dawn of x-ray astronomy. *Rev. Mod. Phys.*, **75**, pp. 995–1010, Aug 2003, URL `https://link.aps.org/doi/10.1103/RevModPhys.75.995`.

[6] RAPPAPORT, S.; PETRE, R.; KAYAT, M. A.; EVANS, K. D.; SMITH, G. C. & LEVINE, A.: X-ray image of the Cygnus loop. *The Astrophysical Journal*, **227**, pp. 285–290, January 1979.

[7] LEVENSON, N. A.; GRAHAM, J. R.; ASCHENBACH, B. & BRINKMANN, W.: The ROSAT-HRI survey of the Cygnus Loop. H. U. ZIMMERMANN; J. TRÜMPER & H. YORKE, editors, *Roentgenstrahlung from the Universe*, pp. 263–264, February 1996.

[8] The Uhuru Satellite. *NASA*, URL `https://heasarc.gsfc.nasa.gov/docs/uhuru/uhuru.html`.

[9] FORMAN, W.; JONES, C.; COMINSKY, L.; JULIEN, P.; MURRAY, S.; PETERS, G.; TANANBAUM, H. & GIACCONI, R.: The fourth Uhuru catalog of X-ray sources. *The Astrophysical Journal Supplement Series*, **38**, pp. 357–412, December 1978.

[10] The High Energy Astrophysics Observatory-1. *NASA*, URL `https://heasarc.gsfc.nasa.gov/docs/heao1/heao1.html`.

[11] WOOD, K. S.; MEEKINS, J. F.; YENTIS, D. J.; SMATHERS, H. W.; MCNUTT, D. P.; BLEACH, R. D.; BYRAM, E. T.; CHUPP, T. A.; FRIEDMAN, H. & MEIDAV, M.: The HEAO A-1 X-ray source catalog. *The Astrophysical Journal Supplement Series*, **56**, pp. 507–649, December 1984.

[12] MEEKINS, J. F.; WOOD, K. S.; HEDLER, R. L.; BYRAM, E. T.; YENTIS, D. J.; CHUBB, T. A. & FRIEDMAN, H.: Millisecond variability of Cygnus X-1. *The Astrophysical Journal*, **278**, pp. 288–297, March 1984.

[13] GIACCONI, R.; BRANDUARDI, G.; BRIEL, U.; EPSTEIN, A.; FABRICANT, D.; FEIGELSON, E.; FORMAN, W.; GORENSTEIN, P.; GRINDLAY, J.; GURSKY, H. ET AL.: The Einstein (HEAO 2) X-ray Observatory. *The Astrophysical Journal*, **230**, pp. 540–550, June 1979.

[14] TUCKER, WALLACE H. & TUCKER, KAREN: *The cosmic inquirers: modern telescopes and their makers*. Cambridge, Mass.: Harvard University Press, 1986, ISBN 0674174356, 1986.

[15] WHITE, N. E. & PEACOCK, A.: The EXOSAT Observatory. *Memorie della Societa Astronomica Italiana*, **59**, pp. 7–29, January 1988.

[16] VAN DER KLIS, M.; JANSEN, F.; VAN PARADIJS, J.; LEWIN, W. H. G.; VAN DEN HEUVEL, E. P. J.; TRUMPER, J. E. & SZATJNO, M.: Intensity-dependent quasi-periodic oscillations in the X-ray flux of GX5 - 1. *Nature*, **316**, pp. 225–230, July 1985.

[17] STELLA, L.: Quasi-periodic oscillations in low mass X-ray binaries. *Memorie della Societa Astronomica Italiana*, **59**, pp. 185–211, January 1988.

[18] ROSAT. *Wikipedia*, URL `https://en.wikipedia.org/wiki/ROSAT`.

[19] SNOWDEN, S. L.; FREYBERG, M. J.; PLUCINSKY, P. P.; SCHMITT, J. H. M. M.; TRUEMPER, J.; VOGES, W.; EDGAR, R. J.; MCCAMMON, D. & SANDERS, W. T.: First Maps of the Soft X-Ray Diffuse Background from the ROSAT XRT/PSPC All-Sky Survey. *The Astrophysical Journal*, **454**, p. 643, December 1995.

[20] TANAKA, Y.; INOUE, H. & HOLT, S. S.: The X-Ray Astronomy Satellite ASCA. *Publications of the Astronomical Society of Japan*, **46**, pp. L37–L41, June 1994.

[21] HEASARC: RXTE Guest Observer Facility. *NASA*, URL `https://heasarc.gsfc.nasa.gov/docs/xte/xte_1st.html`.

[22] CUI, W.; ZHANG, S. N. & CHEN, W.: Evidence for Frame Dragging around Spinning Black Holes in X-Ray Binaries. *The Astrophysical Journal*, **492**(1), pp. L53–L57, January 1998, `astro-ph/9710352`.

[23] REVNIVTSEV, M.; SAZONOV, S.; JAHODA, K. & GILFANOV, M.: RXTE all-sky slew survey. Catalog of X-ray sources at $|b| > 10^o$. *Astronomy and Astrophysics*, **418**, pp. 927–936, May 2004, `astro-ph/0402414`.

[24] VAN DER KLIS, M.: Kilohertz Quasi-Periodic Oscillations in Low-Mass X-Ray Binaries. *Astronomical Time Series*, volume 218 of *Astrophysics and Space Science Library*, p. 121, January 1997, `astro-ph/9710016`.

[25] VAN DER KLIS, M.: Millisecond Oscillations in X-ray Binaries. *Annual Review of Astronomy and Astrophysics*, **38**, pp. 717–760, 2000, `astro-ph/0001167`.

[26] BOELLA, G.; BUTLER, R. C.; PEROLA, G. C.; PIRO, L.; SCARSI, L. & BLEEKER,

J. A. M.: BeppoSAX, the wide band mission for X-ray astronomy. *Astronomy and Astrophysics Supplement Series*, **122**, pp. 299–307, April 1997.

[27] DUNBAR, B.: Chandra X-ray Observatory Quick Facts. *NASA*, Aug 1999, URL `https://www.nasa.gov/centers/marshall/news/background/facts/cxoquick.html`.

[28] BAGANOFF, F. K.; MAEDA, Y.; MORRIS, M.; BAUTZ, M. W.; BRANDT, W. N.; CUI, W.; DOTY, J. P. ET AL.: Chandra X-Ray Spectroscopic Imaging of Sagittarius A* and the Central Parsec of the Galaxy. *The Astrophysical Journal*, **591**(2), pp. 891–915, July 2003, `astro-ph/0102151`.

[29] GRIFFITHS, R. E.; PTAK, A.; FEIGELSON, E. D.; GARMIRE, G.; TOWNSLEY, L.; BRANDT, W. N.; SAMBRUNA, R. & BREGMAN, J. N.: Hot Plasma and Black Hole Binaries in Starburst Galaxy M82. *Science*, **290**(5495), pp. 1325–1328, November 2000.

[30] CLOWE, D.; BRADAČ, M.; GONZALEZ, A. H.; MARKEVITCH, M.; RANDALL, S. W.; JONES, C. & ZARITSKY, D.: A direct empirical proof of the existence of dark matter. *The Astrophysical Journal*, **648**(2), pp. L109–L113, aug 2006, URL `https://doi.org/10.1086/508162`.

[31] WEISSKOPF, M. C.; HESTER, J. J.; TENNANT, A. F.; ELSNER, R. F.; SCHULZ, N. S.; MARSHALL, H. L.; KAROVSKA, M.; NICHOLS, J. S. ET AL.: Discovery of Spatial and Spectral Structure in the X-Ray Emission from the Crab Nebula. *The Astrophysical Journal*, **536**(2), pp. L81–L84, June 2000, `astro-ph/0003216`.

[32] SEWARD, F. D.; TUCKER, W. H. & FESEN, R. A.: Faint x-ray structure in the crab pulsar wind nebula. *The Astrophysical Journal*, **652**(2), pp. 1277–1287, dec 2006, URL `https://doi.org/10.1086/508532`.

[33] JANSEN, F.; LUMB, D.; ALTIERI, B.; CLAVEL, J.; EHLE, M.; ERD, C.; GABRIEL, C.; GUAINAZZI, M.; GONDOIN, P.; MUCH, R.; MUNOZ, R.; SANTOS, M.; SCHARTEL, N.; TEXIER, D. & VACANTI, G.: XMM-Newton observatory. I. The spacecraft and operations. *Astronomy and Astrophysics*, **365**, pp. L1–L6, January 2001.

[34] DEWANGAN, G. C.; TITARCHUK, L. & GRIFFITHS, R. E.: Black Hole Mass of the Ultraluminous X-Ray Source M82 X-1. *The Astrophysical Journal*, **637**(1), pp. L21–L24, January 2006, `astro-ph/0509646`.

[35] RANALLI, P.; COMASTRI, A.; ORIGLIA, L. & MAIOLINO, R.: A deep X-ray observation of M82 with XMM-Newton. *Monthly Notices of the Royal Astronomical Society*, **386**(3), pp. 1464–1480, May 2008, `0802.2943`.

[36] PASHAM, D. R.; STROHMAYER, T. E. & MUSHOTZKY, R. F.: A 400-solar-mass black hole in the galaxy M82. *Nature*, **513**(7516), pp. 74–76, September 2014, `1501.03180`.

[37] HARRISON, F. A.; CRAIG, W. W.; CHRISTENSEN, F. E.; HAILEY, C. J.; ZHANG, W. W.; BOGGS, S. E.; STERN, D.; COOK, W. R.; FORSTER, K.; GIOMMI, P.; GREFENSTETTE, B. W. ET AL.: The Nuclear Spectroscopic Telescope Array (NuS-

TAR) High-energy X-Ray Mission. *The Astrophysical Journal*, **770**(2), 103, June 2013, 1301.7307.

[38] GREFENSTETTE, B. W.; REYNOLDS, S. P.; HARRISON, F. A.; HUMENSKY, T. B.; BOGGS, S. E.; FRYER, C. L.; DELANEY, T.; MADSEN, K. K.; MIYASAKA, H.; WIK, D. R.; ZOGLAUER, A. ET AL.: Locating the Most Energetic Electrons in Cassiopeia A. *The Astrophysical Journal*, **802**(1), 15, March 2015, 1502.03024.

[39] GREFENSTETTE, B. W.; FRYER, C. L.; HARRISON, F. A.; BOGGS, S. E.; DELANEY, T.; LAMING, J. M.; REYNOLDS, S. P.; ALEXANDER, D. M.; BARRET, D.; CHRISTENSEN, F. E.; CRAIG, W. W. ET AL.: The Distribution of Radioactive ^{44}Ti in Cassiopeia A. *The Astrophysical Journal*, **834**(1), 19, January 2017, 1612.02774.

[40] GENDREAU, K. C.; ARZOUMANIAN, Z. & OKAJIMA, T.: The Neutron star Interior Composition ExploreR (NICER): an Explorer mission of opportunity for soft x-ray timing spectroscopy. *Space Telescopes and Instrumentation 2012: Ultraviolet to Gamma Ray*, volume 8443, p. 844313, September 2012.

[41] STROHMAYER, T. E.; ARZOUMANIAN, Z.; BOGDANOV, S.; BULT, P. M. ET AL.: NICER Discovers the Ultracompact Orbit of the Accreting Millisecond Pulsar IGR J17062–6143. *The Astrophysical Journal*, **858**(2), p. L13, may 2018, URL https://doi.org/10.3847/2041-8213/aabf44.

[42] STROHMAYER, T. & KEEK, L.: IGR J17062–6143 Is an Accreting Millisecond X-Ray Pulsar. *The Astrophysical Journal*, **836**(2), p. L23, feb 2017, URL https://doi.org/10.3847/2041-8213/aa5e51.

[43] PAVLINSKY, M.; SUNYAEV, R.; CHURAZOV, E.; VIKHLININ, A.; SAZONOV, S. ET AL.: "Spectrum-RG astrophysical project". *Optics for EUV, X-Ray, and Gamma-Ray Astronomy IV*, volume 7437, pp. 68 – 78, International Society for Optics and Photonics, SPIE, 2009, URL https://doi.org/10.1117/12.837361.

[44] CRUISE, A. M.; HOLDAWAY, R. & CURTIS, W. J.: Spectrum-Roentgen-Gamma and the Jet-X telescope. *Journal of the British Interplanetary Society*, **43**, pp. 139–142, April 1990.

[45] PREDEHL, P.; ANDRITSCHKE, R.; BECKER, W.; BORNEMANN, W.; BRÄUNINGER, H. ET AL.: eROSITA on SRG. *Space Telescopes and Instrumentation 2014: Ultraviolet to Gamma Ray*, volume 9144 of *Society of Photo-Optical Instrumentation Engineers (SPIE) Conference Series*, p. 91441T, July 2014.

[46] MAX PLANCK INSTITUTE FOR EXTRATERRESTRIAL PHYSICS: Our deepest view of the X-ray sky, 06 2020, URL https://www.mpe.mpg.de/7461761/news20200619.

[47] PREDEHL, P.; ANDRITSCHKE, R.; AREFIEV, V.; BABYSHKIN, V.; BATANOV, O.; BECKER, W.; BÖHRINGER, H.; BOGOMOLOV, A.; BOLLER, T.; BORM, K.; BORNEMANN, W.; BRÄUNINGER, H. ET AL.: The eROSITA X-ray telescope on SRG. *Astronomy & Astrophysics*, **647**, A1, March 2021, 2010.03477.

[48] PAVLINSKY, M.; LEVIN, V.; AKIMOV, V.; KRIVCHENKO, A.; ROTIN, A. ET AL.: ART-XC / SRG overview. *Space Telescopes and Instrumentation 2018: Ultraviolet to Gamma Ray*, volume 10699, pp. 468 – 477, International Society for Optics and Photonics, SPIE, 2018, URL https://doi.org/10.1117/12.2312053.

[49] PAVLINSKY, M.; SAZONOV, S.; BURENIN, R.; FILIPPOVA, E.; KRIVONOS, R.; AREFIEV, V.; BUNTOV, M.; CHEN, C. T.; EHLERT, S.; LAPSHOV, I.; LEVIN, V.; LUTOVINOV, A.; LYAPIN, A.; MEREMINSKIY, I. ET AL.: SRG/ART-XC all-sky X-ray survey: Catalog of sources detected during the first year, 2021, 2107.05879.

[50] INFN, INAF: "IXPE mission: Italy and NASA for new X-ray astronomy", 01 2017, URL https://www.researchitaly.it/en/projects/ixpe-mission-italy-and-nasa-for-new-x-ray-astronomy/.

[51] EVANS, D.: "Participation in the X-Ray Astronomy Recovery Mission (XARM) — American Astronomical Society", 08 2017, URL https://aas.org/posts/2017/08/participation-x-ray-astronomy-recovery-mission-xarm.

[52] CLARK, S.: Attitude control failures led to break-up of Japanese astronomy satellite – Spaceflight Now, 04 2016, URL https://spaceflightnow.com/2016/04/18/spinning-japanese-astronomy-satellite-may-be-beyond-saving/.

[53] ZHANG, S. N.; FEROCI, M.; SANTANGELO, A.; DONG, Y. W.; FENG, H.; LU, F. J.; NANDRA, K.; WANG, Z. S. & ET AL.: eXTP: Enhanced X-ray Timing and Polarization mission. *Space Telescopes and Instrumentation 2016: Ultraviolet to Gamma Ray*, Jul 2016, URL http://dx.doi.org/10.1117/12.2232034.

[54] NANDRA, K.; BARRET, D.; BARCONS, X.; FABIAN, A.; DEN HERDER, J.-W.; PIRO, L.; WATSON, M.; ADAMI, C.; AIRD, J.; AFONSO, J. M.; ALEXANDER, D. ET AL.: The Hot and Energetic Universe: A White Paper presenting the science theme motivating the Athena+ mission, 2013, 1306.2307.

[55] WALTER, F. M.; WOLK, S. J. & NEUHÄUSER, R.: Discovery of a nearby isolated neutron star. *Nature*, **379**(6562), pp. 233–235, January 1996.

[56] PONS, J. A.; WALTER, F. M.; LATTIMER, J. M.; PRAKASH, M.; NEUHÄUSER, R. & AN, P.: Toward a Mass and Radius Determination of the Nearby Isolated Neutron Star RX J185635-3754. *The Astrophysical Journal*, **564**(2), pp. 981–1006, January 2002, astro-ph/0107404.

[57] WALTER, F. M.; EISENBEISS, T.; LATTIMER, J. M.; KIM, B.; HAMBARYAN, V. & NEUHÄUSER, R.: Revisiting the Parallax of the Isolated Neutron Star RX J185635-3754 Using HST/ACS Imaging. *The Astrophysical Journal*, **724**(1), pp. 669–677, November 2010, 1008.1709.

[58] TRÜMPER, J. E.; BURWITZ, V.; HABERL, F. & ZAVLIN, V. E.: The puzzles of RX J1856.5-3754: neutron star or quark star? *Nuclear Physics B Proceedings Supplements*, **132**, pp. 560–565, June 2004, astro-ph/0312600.

[59] RILEY, T. E.; WATTS, A. L.; BOGDANOV, S.; RAY, P. S.; LUDLAM, R. M.;

GUILLOT, S.; ARZOUMANIAN, Z.; BAKER, C. L.; BILOUS, A. V.; CHAKRABARTY, D.; GENDREAU, K. C.; HARDING, A. K.; HO, W. C. G.; LATTIMER, J. M. ET AL.: A NICER View of PSR J0030+0451: Millisecond Pulsar Parameter Estimation. *The Astrophysical Journal Letters*, **887**(1), L21, December 2019, 1912.05702.

[60] MILLER, M. C.; LAMB, F. K.; DITTMANN, A. J.; BOGDANOV, S.; ARZOUMANIAN, Z.; GENDREAU, K. C.; GUILLOT, S.; HARDING, A. K.; HO, W. C. G. ET AL.: PSR J0030+0451 Mass and Radius from NICER Data and Implications for the Properties of Neutron Star Matter. *The Astrophysical Journal Letters*, **887**(1), L24, December 2019, 1912.05705.

[61] RILEY, T. E.; WATTS, A. L.; RAY, P. S.; BOGDANOV, S.; GUILLOT, S.; MORSINK, S. M.; BILOUS, A. V.; ARZOUMANIAN, Z.; CHOUDHURY, D.; DENEVA, J. S.; GENDREAU, K. C. ET AL.: A NICER View of the Massive Pulsar PSR J0740+6620 Informed by Radio Timing and XMM-Newton Spectroscopy. *The Astrophysical Journal Letters*, **918**(2), L27, September 2021, 2105.06980.

[62] MILLER, M. C.; LAMB, F. K.; DITTMANN, A. J.; BOGDANOV, S.; ARZOUMANIAN, Z.; GENDREAU, K. C.; GUILLOT, S.; HO, W. C. G.; LATTIMER, J. M.; LOEWENSTEIN, M. ET AL.: The Radius of PSR J0740+6620 from NICER and XMM-Newton Data. *The Astrophysical Journal Letters*, **918**(2), L28, September 2021, 2105.06979.

[63] ÖZEL, F. & FREIRE, P.: Masses, Radii, and the Equation of State of Neutron Stars. *Annual Review of Astronomy and Astrophysics*, **54**, pp. 401–440, September 2016, 1603.02698.

[64] WATTS, A. L.: Thermonuclear Burst Oscillations. *Annual Review of Astronomy and Astrophysics*, **50**, pp. 609–640, September 2012, 1203.2065.

[65] STEINER, A. W.; LATTIMER, J. M. & BROWN, E. F.: The Equation of State from Observed Masses and Radii of Neutron Stars. *The Astrophysical Journal*, **722**(1), pp. 33–54, October 2010, 1005.0811.

[66] HARTLE, J. B. & THORNE, K. S.: Slowly Rotating Relativistic Stars. II. Models for Neutron Stars and Supermassive Stars. *The Astrophysical Journal*, **153**, p. 807, September 1968.

[67] HARTLE, J. B.: Slowly rotating relativistic stars I. Equations of structure. *The Astrophysical Journal*, **150**, pp. 1005–1029, 1967.

[68] ABRAMOWICZ, M. A.; ALMERGREN, G. J. E.; KLUZNIAK, W. & THAMPAN, A. V.: The Hartle-Thorne circular geodesics. *ArXiv General Relativity and Quantum Cosmology e-prints gr-qc/0312070*, December 2003, gr-qc/0312070.

[69] URBANCOVÁ, G.; URBANEC, M.; TÖRÖK, G.; STUCHLÍK, Z.; BLASCHKE, M. & MILLER, J. C.: Epicyclic Oscillations in the Hartle-Thorne External Geometry. *The Astrophysical Journal*, **877**(2), 66, June 2019, 1905.00730.

[70] CHANDRASEKHAR, S. & MILLER, J. C.: On slowly rotating homogeneous masses in general relativity. *Monthly Notices of the Royal Astronomical Society*, **167**, pp.

63–80, April 1974.

[71] MILLER, J. C.: Quasi-stationary gravitational collapse of slowly rotating bodies in general relativity. *Monthly Notices of the Royal Astronomical Society*, **179**, pp. 483–498, May 1977.

[72] WEBER, F. & GLENDENNING, N. K.: Application of the improved Hartle method for the construction of general relativistic rotating neutron star models. *The Astrophysical Journal*, **390**, pp. 541–549, May 1992.

[73] BENHAR, O.; FERRARI, V.; GUALTIERI, L. & MARASSI, S.: Perturbative approach to the structure of rapidly rotating neutron stars. *Physical Review D*, **72**(4), 044028, August 2005, gr-qc/0504068.

[74] PASCHALIDIS, V. & STERGIOULAS, N.: Rotating stars in relativity. *Living Reviews in Relativity*, **20**, 7, November 2017, 1612.03050.

[75] STONE, J. R.; MILLER, J. C.; KONCEWICZ, R.; STEVENSON, P. D. & STRAYER, M. R.: Nuclear matter and neutron-star properties calculated with the Skyrme interaction. *Physical Review C*, **68**(3), 034324, September 2003.

[76] URBANEC, M.; BETÁK, E. & STUCHLÍK, Z.: Observational Tests of Neutron Star Relativistic Mean Field Equations of State. *Acta Astronomica*, **60**, pp. 149–163, June 2010, 1007.3446.

[77] AKMAL, A.; PANDHARIPANDE, V. R. & RAVENHALL, D. G.: Equation of state of nucleon matter and neutron star structure. *Physical Review C*, **58**, pp. 1804–1828, September 1998, arXiv:hep-ph/9804388.

[78] LORENZ, C. P.; RAVENHALL, D. G. & PETHICK, C. J.: Neutron star crusts. *Physical Review Letters*, **70**, pp. 379–382, January 1993.

[79] GANDOLFI, S.; ILLARIONOV, A. Y.; FANTONI, S.; MILLER, J. C.; PEDERIVA, F. & SCHMIDT, K. E.: Microscopic calculation of the equation of state of nuclear matter and neutron star structure. *Monthly Notices of the Royal Astronomical Society*, **404**, pp. L35–L39, May 2010, 0909.3487.

[80] STEINER, A. W.; PRAKASH, M.; LATTIMER, J. M. & ELLIS, P. J.: Isospin asymmetry in nuclei and neutron stars [review article]. *Physics Reports*, **411**, pp. 325–375, June 2005, nucl-th/0410066.

[81] AGRAWAL, B. K.; SHLOMO, S. & AU, V. K.: Determination of the parameters of a Skyrme type effective interaction using the simulated annealing approach. *Physical Review C*, **72**(1), 014310, July 2005, nucl-th/0505071.

[82] DEMOREST, P. B.; PENNUCCI, T.; RANSOM, S. M.; ROBERTS, M. S. E. & HESSELS, J. W. T.: A two-solar-mass neutron star measured using Shapiro delay. *Nature*, **467**, pp. 1081–1083, October 2010, 1010.5788.

[83] ANTONIADIS, J.; FREIRE, P. C. C.; WEX, N.; TAURIS, T. M.; LYNCH, R. S.; VAN KERKWIJK, M. H.; KRAMER, M.; BASSA, C. ET AL.: A Massive Pulsar in a Compact Relativistic Binary. *Science*, **340**, p. 448, April 2013, 1304.6875.

[84] LO, K.-W. & LIN, L.-M.: The Spin Parameter of Uniformly Rotating Compact Stars. *The Astrophysical Journal*, **728**, 12, February 2011, 1011.3563.

[85] REINA, B. & VERA, R.: Revisiting Hartle's model using perturbed matching theory to second order: amending the change in mass. *Classical and Quantum Gravity*, **32**(15), 155008, August 2015, 1412.7083.

[86] REINA, B.: Slowly rotating homogeneous masses revisited. *Monthly Notices of the Royal Astronomical Society*, **455**, pp. 4512–4517, February 2016, 1503.07835.

[87] GLAMPEDAKIS, K. & BABAK, S.: Mapping spacetimes with LISA: inspiral of a test body in a 'quasi-Kerr' field. *Classical and Quantum Gravity*, **23**(12), pp. 4167–4188, June 2006, gr-qc/0510057.

[88] VAN DER KLIS, M.: *Stellar X-Ray Sources*. ed. W. H. G. Lewin, Cambridge University Press, Cambridge, 2006.

[89] SHVARTSMAN, V. F.: Halos around "Black Holes". *Soviet Astronomy*, **15**, p. 377, December 1971.

[90] SYUNYAEV, R. A.: Variability of X Rays from Black Holes with Accretion Disks. *Soviet Astronomy*, **16**, pp. 941–944, 1973.

[91] TÖRÖK, G.; URBANEC, M.; ADÁMEK, K. & URBANCOVÁ, G.: Appearance of innermost stable circular orbits of accretion discs around rotating neutron stars. *Astronomy & Astrophysics: Letters*, **564**, L5, April 2014, 1403.3728.

[92] TÖRÖK, G.; GOLUCHOVÁ, K.; URBANEC, M.; ŠRÁMKOVÁ, E.; ADÁMEK, K.; URBANCOVÁ, G.; PECHÁČEK, T.; BAKALA, P.; STUCHLÍK, Z.; HORÁK, J. & JURYŠEK, J.: Constraining Models of Twin-Peak Quasi-periodic Oscillations with Realistic Neutron Star Equations of State. *The Astrophysical Journal*, **833**, 273, December 2016, 1611.06087.

[93] TÖRÖK, G.; BAKALA, P.; STUCHLÍK, Z. & CECH, P.: Modeling the Twin Peak QPO Distribution in the Atoll Source 4U 1636-53. *Acta Astronomica*, **58**, pp. 1–14, March 2008a.

[94] BOSHKAYEV, K.; BINI, D.; RUEDA, J.; GERALICO, A.; MUCCINO, M. & SIUTSOU, I.: What can we extract from quasiperiodic oscillations? *Gravitation and Cosmology*, **20**, pp. 233–239, October 2014, 1412.8214.

[95] BOSHKAYEV, K.; RUEDA, J. & MUCCINO, M.: Extracting multipole moments of neutron stars from quasi-periodic oscillations in low mass X-ray binaries. *Astronomy Reports*, **59**, pp. 441–446, June 2015.

[96] URBANEC, M.; MILLER, J. C. & STUCHLÍK, Z.: Quadrupole moments of rotating neutron stars and strange stars. *Monthly Notices of the Royal Astronomical Society*, **433**, pp. 1903–1909, August 2013, 1301.5925.

[97] YAGI, K. & YUNES, N.: Approximate Universal Relations for Neutron Stars and Quark Stars. *ArXiv e-prints*, December 2006, gr-qc/1608.02582v1.

[98] GONDEK-ROSIŃSKA, D.; KLUŹNIAK, W.; STERGIOULAS, N. & WIŚNIEWICZ, M.:

Epicyclic frequencies for rotating strange quark stars: Importance of stellar oblateness. *Physical Review D*, **89**(10), 104001, May 2014, 1403.1129.

[99] HASINGER, G. & VAN DER KLIS, M.: Two patterns of correlated X-ray timing and spectral behaviour in low-mass X-ray binaries. *Astronomy & Astrophysics*, **225**, pp. 79–96, November 1989.

[100] TÖRÖK, G.; KOTRLOVÁ, A.; ŠRÁMKOVÁ, E. & STUCHLÍK, Z.: Confronting the models of 3:2 quasiperiodic oscillations with the rapid spin of the microquasar GRS 1915+105. *Astronomy & Astrophysics*, **531**, pp. A59+, July 2011, 1103.2438.

[101] STELLA, L. & VIETRI, M.: kHz Quasiperiodic Oscillations in Low-Mass X-Ray Binaries as Probes of General Relativity in the Strong-Field Regime. *Physical Review Letters*, **82**, pp. 17–20, January 1999, astro-ph/9812124.

[102] ČADEŽ, A.; CALVANI, M. & KOSTIĆ, U.: On the tidal evolution of the orbits of low-mass satellites around black holes. *Astronomy & Astrophysics*, **487**, pp. 527–532, August 2008, 0809.1783.

[103] KATO, S.: Basic Properties of Thin-Disk Oscillations. *PASJ*, **53**, pp. 1–24, February 2001.

[104] ABRAMOWICZ, M. A. & KLUŹNIAK, W.: A precise determination of black hole spin in GRO J1655-40. *Astronomy & Astrophysics*, **374**, pp. L19–L20, August 2001, astro-ph/0105077.

[105] BURSA, M.: High-frequency QPOs in GRO J1655-40: Constraints on resonance models by spectral fits. S. HLEDÍK & Z. STUCHLÍK, editor, *RAGtime 6/7: Workshops on black holes and neutron stars*, pp. 39–45, December 2005.

[106] TÖRÖK, G.; STUCHLÍK, Z. & BAKALA, P.: A remark about possible unity of the neutron star and black hole high frequency QPOs. *Central European Journal of Physics*, **5**, pp. 457–462, December 2007.

[107] BOUTELIER, M.; BARRET, D.; LIN, Y. & TÖRÖK, G.: On the distribution of frequency ratios of kHz quasi-periodic oscillations. *Monthly Notices of the Royal Astronomical Society*, **401**, pp. 1290–1298, January 2010, 0909.2990.

[108] URBANEC, M.; BETAK, E. & STUCHLIK, Z.: Observational tests of neutron star relativistic mean field equations of state. *Acta Astronomica*, **60**, 07 2010.

[109] RIKOVSKA STONE, J.; MILLER, J. C.; KONCEWICZ, R.; STEVENSON, P. D. & STRAYER, M. R.: Nuclear matter and neutron-star properties calculated with the skyrme interaction. *Phys. Rev. C*, **68**, p. 034324, Sep 2003, URL https://link.aps.org/doi/10.1103/PhysRevC.68.034324.

[110] LIN, Y.-F.; BOUTELIER, M.; BARRET, D. & ZHANG, S.-N.: Studying Frequency Relationships of Kilohertz Quasi-periodic Oscillations for 4U 1636-53 and Sco X-1: Observations Confront Theories. *The Astrophysical Journal*, **726**, 74, January 2011, 1010.6198.

[111] TÖRÖK, G.; BAKALA, P.; ŠRÁMKOVÁ, E.; STUCHLÍK, Z.; URBANEC, M. & GOLUCHOVÁ, K.: Mass-Angular-momentum Relations Implied by Models of Twin Peak Quasi-periodic Oscillations. *The Astrophysical Journal*, **760**, 138, December 2012, 1408.4220.

[112] TÖRÖK, G.; KOTRLOVÁ, A.; MATUSZKOVÁ, M.; KLIMOVIČOVÁ, K.; LANČOVÁ, D.; URBANCOVÁ, G. & ŠRÁMKOVÁ, E.: Simple analytic formula relating the mass and spin of accreting compact objects to their rapid X-ray variability. *Submitted to The Astrophysical Journal*.

[113] TÖRÖK, G.; GOLUCHOVÁ, K.; HORÁK, J.; ŠRÁMKOVÁ, E.; URBANEC, M.; PECHÁČEK, T. & BAKALA, P.: Twin peak quasi-periodic oscillations as signature of oscillating cusp torus. *Monthly Notices of the Royal Astronomical Society: Letters*, **457**, pp. L19–L23, March 2016, 1512.03841.

[114] KLUŹNIAK, W. & ABRAMOWICZ, M. A.: Strong-Field Gravity and Orbital Resonance in Black Holes and Neutron Stars — kHz Quasi-Periodic Oscillations (QPO). *Acta Phys. Polonica B*, **32**, p. 3605, November 2001.

[115] REZZOLLA, L.; YOSHIDA, S. & ZANOTTI, O.: Oscillations of vertically integrated relativistic tori - I. Axisymmetric modes in a Schwarzschild space-time. *Monthly Notices of the Royal Astronomical Society*, **344**, pp. 978–992, September 2003, astro-ph/0307488.

[116] DE AVELLAR, M. G. B.; PORTH, O.; YOUNSI, Z. & REZZOLLA, L.: Kilohertz QPOs in low-mass X-ray binaries as oscillation modes of tori around neutron stars - I. *MNRAS*, **474**, pp. 3967–3975, March 2018.

[117] KOTRLOVÁ, A.; ŠRÁMKOVÁ, E.; TÖRÖK, G.; GOLUCHOVÁ, K.; JIŘÍ, H.; STRAUB, O.; LANČOVÁ, D.; STUCHLÍK, Z. & ABRAMOWICZ, M.: Models of high-frequency quasi-periodic oscillations and black hole spin estimates in Galactic microquasars. *Astronomy & Astrophysics*, **643**(A31), arXiv:2008.12963, August 2020, 2008.12963.

[118] HAWLEY, J. F. & BALBUS, S. A.: The Dynamical Structure of Nonradiative Black Hole Accretion Flows. *The Astrophysical Journal*, **573**(2), pp. 738–748, July 2002, astro-ph/0203309.

[119] DE VILLIERS, J.-P. & HAWLEY, J. F.: A Numerical Method for General Relativistic Magnetohydrodynamics. *The Astrophysical Journal*, **589**(1), pp. 458–480, May 2003, astro-ph/0210518.

[120] TAGGER, M. & VARNIÈRE, P.: Accretion-Ejection Instability, MHD Rossby Wave Instability, Diskoseismology, and the High-Frequency QPOs of Microquasars. *The Astrophysical Journal*, **652**(2), pp. 1457–1465, December 2006, astro-ph/0608123.

[121] BLAES, O. M.; ŠRÁMKOVÁ, E.; ABRAMOWICZ, M. A.; KLUŹNIAK, W. & TORKELSSON, U.: Epicyclic Oscillations of Fluid Bodies: Newtonian Nonslender Torus. *The Astrophysical Journal*, **665**(1), pp. 642–653, August 2007, 0706.4483.

[122] TÖRÖK, G.; GOLUCHOVÁ, K.; ŠRÁMKOVÁ, E.; HORÁK, J.; BAKALA, P. & URBANEC, M.: On one-parametric formula relating the frequencies of twin-peak quasi-periodic oscillations. *Monthly Notices of the Royal Astronomical Society*, **473**, pp. L136–L140, January 2018, 1710.10901.

[123] TÖRÖK, G.; KOTRLOVÁ, A.; MATUSZKOVÁ, M.; KLIMOVIČOVÁ, K.; LANČOVÁ, D.; URBANCOVÁ, G. & ŠRÁMKOVÁ, E.: Simple analytic formula relating the mass and spin of accreting compact objects to their rapid X-ray variability, submitted to APJ.

[124] STROHMAYER, T. E. & MARKWARDT, C. B.: Evidence for a Millisecond Pulsar in 4U 1636-53 during a Superburst. *The Astrophysical Journal*, **577**(1), pp. 337–345, September 2002, astro-ph/0205435.

[125] BARRET, D.; OLIVE, J.-F. & MILLER, M. C.: An abrupt drop in the coherence of the lower kHz quasi-periodic oscillations in 4U 1636-536. *Monthly Notices of the Royal Astronomical Society*, **361**, pp. 855–860, August 2005, astro-ph/0505402.

[126] BARRET, D.; OLIVE, J.-F. & MILLER, M. C.: Drop of coherence of the lower kilo-Hz QPO in neutron stars: Is there a link with the innermost stable circular orbit? *Astronomische Nachrichten*, **326**, pp. 808–811, November 2005, astro-ph/0510094.

[127] compOSE: CompStar Online Supernovæ Equations of State, Jan 2018, URL https://compose.obspm.fr/home.

[128] BALDO, M.; BOMBACI, I. & BURGIO, G. F.: Microscopic nuclear equation of state with three-body forces and neutron star structure. *Astronomy and Astrophysics*, **328**, pp. 274–282, December 1997, astro-ph/9707277.

[129] GLENDENNING, N. K. & MOSZKOWSKI, S. A.: Reconciliation of neutron-star masses and binding of the Λ in hypernuclei. *Phys. Rev. Lett.*, **67**, pp. 2414–2417, Oct 1991, URL https://link.aps.org/doi/10.1103/PhysRevLett.67.2414.

[130] NOVIKOV, I. D. & THORNE, K. S.: Astrophysics of black holes. *Black Holes (Les Astres Occlus)*, pp. 343–450, January 1973.

[131] BAUBÖCK, M.; PSALTIS, D. & ÖZEL, F.: Narrow Atomic Features from Rapidly Spinning Neutron Stars. *The Astrophysical Journal*, **766**(2), 87, April 2013, 1209.0768.

II. Collection of the papers

- TÖRÖK, G.; URBANEC, M.; ADÁMEK, K. & URBANCOVÁ, G.: Appearance of innermost stable circular orbits of accretion discs around rotating neutron stars. *Astronomy & Astrophysics: Letters*, **564**, L5, 2014, 1403.3728.

- HAMIL, O.; STONE, J. R.; URBANEC, M. & URBANCOVÁ, G.: Braking index of isolated pulsars. *Physical Review D*, **91**, 063007, 2015, 1608.01383.

- TÖRÖK, G.; GOLUCHOVÁ, K.; URBANEC, M.; ŠRÁMKOVÁ, E.; ADÁMEK, K.; URBANCOVÁ, G.; PECHÁČEK, T.; BAKALA, P.; STUCHLÍK, Z.; HORÁK, J. & JURYŠEK, J.: Constraining Models of Twin-Peak Quasi-periodic Oscillations with Realistic Neutron Star Equations of State. *The Astrophysical Journal*, **833**, 273, 2016, 1611.06087.

- URBANCOVÁ, G.; URBANEC, M.; TÖRÖK, G.; STUCHLÍK, Z.; BLASCHKE, M. & MILLER, JOHN C.: Epicyclic Oscillations in the Hartle-Thorne External Geometry. *The Astrophysical Journal*, **877**, 66, 2019, 1905.00730.

Paper I

II.1. Appearance of innermost stable circular orbits of accretion discs around rotating neutron stars

Török Gabriel, Urbanec Martin, Adámek Karel & Urbancová Gabriela

Astronomy & Astrophysics: Letters, 2014,
Volume 564, article id. L5, 4 pp.

A&A 564, L5 (2014)
DOI: 10.1051/0004-6361/201423541

Astronomy & Astrophysics

L E

Appearance of innermost stable circular orbits of accretion discs around rotating neutron stars

Gabriel Török, Martin Urbanec, Karel Adámek, and Gabriela Urbancová

Institute of Physics, Faculty of Philosophy and Science, Silesian University in Opava, Bezručovo nám. 13, 74601 Opava, Czech Republic
e-mail: gabriel.torok@physics.cz

Received 30 January 2014 / Accepted 5 March 2014

ABSTRACT

The innermost stable cicular orbit (ISCO) of an accretion disc that orbits a neutron star (NS) is often assumed to be a unique prediction of general relativity. However, it has been argued that ISCO also appears around highly elliptic bodies described by Newtonian theory. In this sense, the behaviour of an ISCO around a rotating oblate neutron star is formed by the interplay between relativistic and Newtonian effects. Here we briefly explore the consequences of this interplay using a straightforward analytic approach as well as numerical models that involve modern NS equations of state. We examine the ratio K between the ISCO radius and the radius of the neutron star. We find that, with growing NS spin, the ratio K first decreases, but then starts to increase. This non-monotonic behaviour of K can give rise to a neutron star spin interval in which ISCO appears for two very different ranges of NS mass. This may strongly affect the distribution of neutron stars that have an ISCO (ISCO-NS). When (all) neutron stars are distributed around a high mass M_0, the ISCO-NS spin distribution is roughly the same as the spin distribution corresponding to all neutron stars. In contrast, if M_0 is low, the ISCO-NS distribution can only have a peak around a high value of spin. Finally, an intermediate value of M_0 can imply an ISCO-NS distribution divided into two distinct groups of slow and fast rotators. Our findings have immediate astrophysical applications. They can be used for example to distinguish between different models of high-frequency quasiperiodic oscillations observed in low-mass NS X-ray binaries.

Key words. accretion, accretion disks – stars: neutron – X-rays: binaries

1. Introduction

In Newtonian theory, circular trajectories of test particles orbiting around a spherical central body of mass M are stable to small radial perturbations at any external radii r. The same trajectories calculated using a general relativistic description exhibit an instability below the critical radius of the marginally stable cicular orbit $r_{\rm ms}$ (e.g., Bardeen et al. 1972). This radius is frequently considered as the innermost stable circular orbit (ISCO) of an accretion disc that orbits a black hole or a neutron star (NS), $r_{\rm ISCO} = r_{\rm ms}$. The ISCO is often assumed as a unique prediction of Einstein's general relativity. Several decades after the ISCO concept has been introduced, it was argued that ISCO also appears around highly elliptic bodies described by the Newtonian theory (see works of Zdunik & Gourgoulhon 2001; Amsterdamski et al. 2002; Kluźniak & Rosinska 2013). In this sense, several phenomena related to rotating oblate neutron stars can be well understood in terms of the interplay between the effects of general relativity and Newtonian theory. Namely, as in the Lense-Thirring or Kerr spacetime, the position of ISCO decreases with growing angular momentum j of the neutron star (given by the NS spin). At the same time, it increases with the increasing influence of the NS quadrupole moment q (which determines the oblateness parameter $\tilde{q} \equiv q/j^2$, see, e.g., Urbanec et al. 2013).

In this Letter we explore the consequences of this interplay on the behaviour of NS compactness. Finally, we focus on low-mass X-ray binary systems (LMXBs) and find astrophysical implications for the distribution of neutron stars with an ISCO (ISCO-NS).

2. Behaviour of ISCO radius and NS compactness

Numerous works have investigated the behaviour of test particle motion, Keplerian frequencies, and the properties of ISCO in the vinicity of a rotating neutron star (e.g. Kluźniak et al. 1990; Shibata & Sasaki 1998; Pachón et al. 2006, 2012; Bakala et al. 2012; Gutierrez et al. 2013). It has been shown that for geodesic motion, these are well described by formulae derived considering NS spacetime approximated by the Hartle-Thorne metric (Hartle & Thorne 1968; Abramowicz et al. 2003; Berti et al. 2005). Here we explore in more detail the behaviour of function $r_{\rm ISCO}(j\,,\,q)$ calculated by using this approximation[1]. We find that for $\tilde{q} \gtrsim 2.8$, $r_{\rm ISCO}$ has a minimum when the angular momentum and the quadrupole moment of the central object are related as follows:

$$\tilde{q}_{\rm min} = 1 + \frac{32\left(9\sqrt{6} + 4j_{\rm min}\right)}{135\, j_{\rm min}\left(4608\log(3/2) - 1865\right)}. \quad (1)$$

The smallest allowed ISCO radius is then given by

$$r_{\rm min} = 6 - 2j_{\rm min}\sqrt{2/3}. \quad (2)$$

In the left panel of Fig. 1 we illustrate the behaviour of ISCO and the turning points $[r_{\rm min}, j_{\rm min}]$ for several values of $\tilde{q}$. Apparently, for $\tilde{q} \gtrsim 7$, the turning points arise for low angular momentum values, $j \lesssim 0.27$.

[1] The appropriate explicit formulae determining the function $r_{\rm ISCO}$ are too long to be included in this Letter. They are given, e.g., in Abramowicz et al. (2003) or Török et al. (2008).

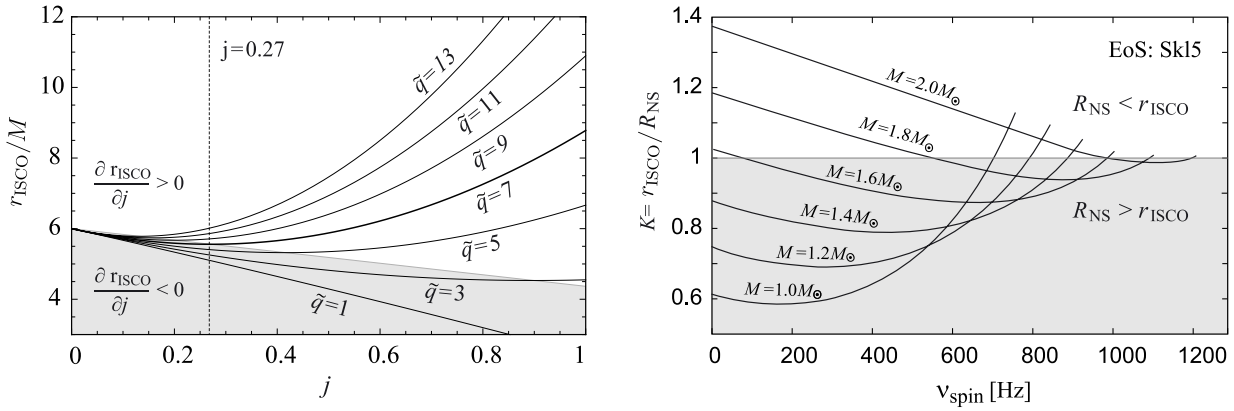

Fig. 1. *Left*: dependence of the geodesic ISCO radius $r_{ISCO} = r_{ms}$ on the NS angular momentum j and the oblateness factor $\tilde{q}$. The shaded area indicates the Kerr-like region where r_{ISCO} decreases with increasing j. We note that for the concrete NS models we assume here, a fixed value of $\tilde{q}$ corresponds to a fixed NS central density ρ. Moreover, in the limit of $\tilde{q} = 1$ the NS spacetime approaches the Kerr spacetime and values of $\tilde{q} \in (1, 3)$ correspond to the highest possible values of ρ (the oblateness parameter $\tilde{q}$ is also called the Kerr parameter). *Right*: dependence of compactness K on the NS spin frequency ν_{spin} and mass M. The shaded area indicates the region of $K < 1$ where the ISCO does not appear above the NS surface.

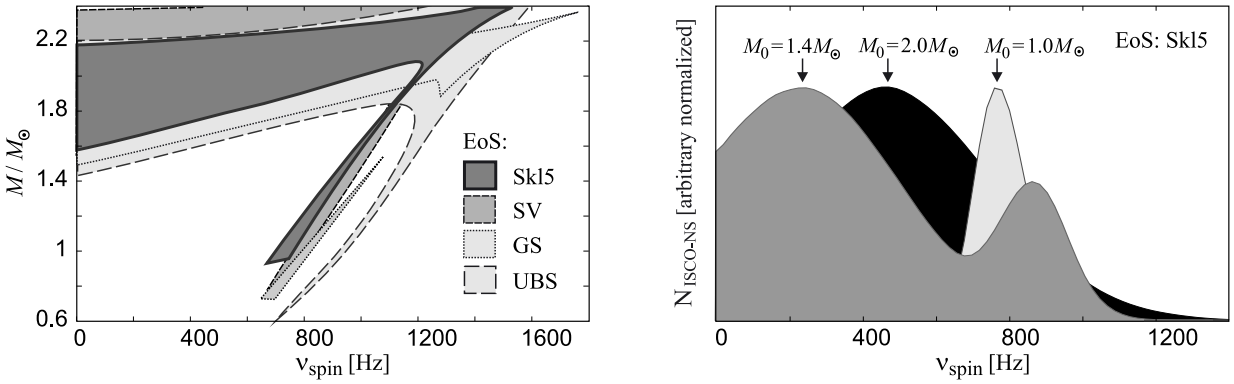

Fig. 2. *Left*: mass-spin regions that allow the appearance of ISCO calculated for SKl5 and three other EoS. The displayed drawing is the result of $\sim 10^5$ computations of NS configurations. *Right*: ISCO-NS spin distribution expected for the SKl5 EoS and three different referential values of M_0.

2.1. ISCO calculated for particular NS models

So far we have only considered the behaviour of ISCO without focusing on its relation to NS models. Models of neutron stars based on modern equations of state (EoS) have been extensively developed through the use of various numerical methods and codes (see Lattimer & Prakash 2001, 2007, for a review). Results of the published studies indicate that in contrast to the behaviour of r_{ISCO}, the NS radius R_{NS} very slowly evolves with the NS spin. Taking this into account, one can expect that the non-monotonicity of the ISCO behaviour discussed above may imply a non-monotonicity of the quantity $K \equiv r_{ISCO}/R_{NS}$ (hereafter denoted as compactness factor). Considering concrete NS models we confirm this expectation using the numerical code of Urbanec et al. (2013).

In the right panel of Fig. 1 we plot the NS compactness factor K calculated for the SKl5 Skyrme EoS (e.g., Stone et al. 2003). We assume in the figure several values of the neutron star mass M and spin frequency ν_{spin}, which range from the non-rotating limit to highest frequencies corresponding to the mass-shedding limit. To obtain smooth curves we have computed 600 NS configurations. One can clearly see that K is not a monotonic function of ν_{spin}. Its extrema arise for very different values of ν_{spin}. For a high neutron star mass, ($M \sim 2\ M_\odot$), they arise close to the mass-shedding limit, above 1000 Hz. For a low neutron star mass, ($M \sim 1\ M_\odot$), they arise for low values of ν_{spin}, below $\nu_{spin} = 200$ Hz.

3. Appearance and disappearance of ISCO and the consequences

Using the right panel of Fig. 1 we can directly compare the NS radii and the ISCO radii. Apparently, when M is high, the ISCO is located above the NS surface for almost any ν_{spin}. On the other hand, when M is low, the ISCO arises for only high values of ν_{spin}. For an intermediate mass, $M \sim 1.6\ M_\odot$, the ISCO only occurs for two short intervals of ν_{spin} – one close to the non-rotating limit and the other one at high frequencies.

In the left panel of Fig. 2 we show the map of mass-spin regions where the ISCO arises above the NS surface for Skl5 EoS. This map, which relates to curves drawn in the right panel of Fig. 1, is emphasized by the thick line and dark colour. Remarkably, for $\nu_{spin} \sim 800$ Hz, there are two intervals of M that allow an ISCO appearance. On the other hand, for $\nu_{spin} \lesssim 700$ Hz (or $\nu_{spin} \gtrsim 1200$ Hz), there is only one such interval of M. For the sake of comparison we also consider three other EoS

within the same figure: the SV and GS EoS, which represent two more parametrizations of the Skyrme potential (see Stone et al. 2003, and references therein), and the UBS EoS (Urbanec et al. 2010a). Apparently, these EoS display a similar behaviour as the Skl5 EoS.

3.1. Possible double-peaked spin distribution of ISCO-NS

While it is often speculated that most neutron stars in LMXBs may have ISCO, little clear observational evidence for this claim has been achieved yet, and the mass and spin distribution of these possible ISCO-NS remains puzzling (see, however Barret et al. 2005, 2006; Török et al. 2010, 2012; Wang et al. 2013). The mass distribution of neutron stars in LMXBs has hardly been explored so far. The mean mass is currently estimated as $M_0 \in (1.4\ M_\odot - 1.8\ M_\odot)$. More accurate estimates on NS mass distribution are available in double NS binary systems where masses are concentrated in a very narrow peak around $1.4\ M_\odot$ (see Lattimer 2012)[2]. Accurate measurements for NS spin frequencies are available in radio pulsars where the distribution of rotational frequencies is narrowed around two peaks - one is of order of Hz, while the other is ∼100 Hz (Manchester et al. 2005). Spin measurements are much less frequent in LMXBs. The spin frequencies inferred from the observed X-ray oscillations seem to be significantly higher than those of radio pulsars, reaching typical values of few hundreds of Hz. Nevertheless, several slowly rotating sources have been discovered as well (e.g., IGR J17480-2446 in globular cluster Terzan X-5 with $\nu_{\rm spin} = 11$ Hz, Bordas et al. 2010; Markwardt & Strohmayer 2010). An overview of the currently measured spins of more than 20 LMXB NSs along with detailed references can be found in Lamb & Boutloukos (2008) and Patruno & Watts (2014).

Motivated by a simple analytical analysis and justified by the consideration of NS models assuming modern EoS, our results imply strong restrictions on distribution of the ISCO-NS parameters. This distribution could be very different from the (so far unknown) distribution of all NS in LMXBs. We illustrate these restrictions using an example calculated for the Skl5 EoS and the simplified assumption that all NS follow a two dimensional Gaussian distribution in the mass–spin space. For the distribution of all NS we set mean values $M_0 \in \{1\ M_\odot,\ 1.4\ M_\odot,\ 2\ M_\odot\}$, and $\nu^0_{\rm spin} = 500$ Hz together with scales $\sigma_M = 0.2\ M_\odot$ and $\sigma_{\nu{\rm spin}} = 300$ Hz. The subsets of ISCO-NS were then determined by the map depicted in the left panel of Fig. 2. We show the spin distribution of these subsets in the right panel of Fig. 2. We can see that when the neutron stars were distributed around high mass $M_0 = 2\ M_\odot$, the ISCO-NS spin distribution is approximately the same as the spin distribution of all NS that peak around $\nu^0_{\rm spin}$. On the other hand, when this mass was low, $M_0 = 1\ M_\odot$, the ISCO-NS distribution had a peak only around a high value of $\nu_{\rm spin}$. A different situation occurs for an intermediate value of $M_0 = 1.4\ M_\odot$, which implies an ISCO-NS distribution divided into two groups of slow and fast rotators.

4. Discussion and conclusions

Our analysis clearly revealed the non-monotonicity of the dependence of the compactness factor K on NS spin. The occurence of an NS spin interval in which the ISCO appears for two very different ranges of NS mass (and the inferred double-peaked ISCO-NS spin distribution) depends on the detailed behaviour of K.

For the four EoS discussed here, this behaviour is rather similar. However, normalization of K and its exact dependence on $\nu_{\rm spin}$ and M depend on the particular EoS. More detailed investigation that takes into account a large set of EoS needs to be performed to make better astrophysical assessments. Moreover, we assumed here the simplified identity $r_{\rm ISCO} = r_{\rm ms}$, but various effects might lead to a decrease or increase of K (e.g. viscosity, pressure forces, or magnetic field influence), and the chosen spacetime description can play some role as well (e.g. Alpar & Psaltis 2008; Straub & Šrámková 2009; Bakala et al. 2010, 2012; Kotrlová et al. 2008). Despite these uncertainties, which need to be adressed in the subsequent analysis, our findings can be useful in several astrophysical applications. Clearly, the predictions on the NS parameters would be strong if the ISCO presence or absence in the individual systems were observationally confirm ed. Moreover, one can speculate on some consequences for evolution of the spinning-up sources.

Although more development is required, some implications can be consired immediately. One possibility is to use our results in a study aimed to distinguish between different models of high-frequency quasiperiodic oscillations (HF QPOs). There is no consensus as yet on the HF QPO origin, and various models have been proposed (e.g., Alpar & Shaham 1985; Lamb et al. 1985; Miller at al. 1998; Psaltis et al. 1999; Stella & Vietri 1999; Abramowicz & Kluźniak 2001; Titarchuk & Wood 2002; Rezzolla et al. 2003; Pétri 2005; Zhang 2005; Šrámková et al. 2007; Stuchlík et al. 2008, and several others). Among numerous ideas, it was suggested that the strong luminosity variations observed on the kHz time-scales in the neutron star X-ray binaries result from the modulation of accretion flow that heats the boundary layer between the flow and the NS surface (Paczynski 1987; Horák 2005; Abramowicz et al. 2007). Motivated by this suggestion, Urbanec et al. (2010b) assumed the Paczynski modulation mechanism for the specific epicyclic resonance QPO model and investigated the implied restrictions on the NS mass and angular momentum. Taking into account our present findings and the general idea that (any) disc oscillations are responsible for exciting the Paczynski modulation mechanism, one might expect that the spin distribution of the HF QPO sources is double-peaked when NS masses are distributed around the intermediate value $M_0 \sim 1.4\ M_\odot$.

Acknowledgements. We would like to acknowledge the support of the Czech grant GAČR 209/12/P740 and the project CZ.1.07/2.3.00/20.0071 "Synergy", aimed to foster international collaboration of the Institute of Physics of SU Opava. Furthermore, we acknowledge financial support from the internal grants of SU Opava SGS/11/2013 and SGS/23/2013. We thank the anonymous referee for his or her comments and suggestions that helped to improve the paper.

[2] This rather brief description of situation does not include recent observations of the pulsar J0348+0432 with mass $2.01 \pm 0.04\ M_\odot$, which currently represents the most massive confirmed neutron star (Antoniadis 2013).

References

Abramowicz M. A., & Kluźniak W. 2001, A&A, 374, L19
Abramowicz, M. A., Almergren, G. J. E., Kluźniak, W., & Thampan, A. V. 2003, unpublished [arXiv:gr-qc/0312070]
Abramowicz, M. A., Horák, J., & Kluźniak, W. 2007, Acta Astron., 57, 1
Alpar, M. A., & Psaltis, D. 2008, MNRAS, 391, 1472
Alpar, M. A., & Shaham, J. 1985, Nature, 316, 239
Amsterdamski, P., Bulik, T., Gondek-Rosinska, D., Kluzniak, W. 2002, A&A, 381, L21
Antoniadis, J., Freire, P. C. C., Wex, N., et al. 2013, Science, 340, 448
Bakala, P., Šrámková, E., Stuchlík, Z., & Török, G. 2010, Class. Quantum. Grav., 27, 045001
Bakala, P., Urbanec, M., Šrámková, E., Stuchlík, Z., & Török, G. 2012, Class. Quantum Grav., 29, 065012

Bardeen, J. M., Press, W. H., & Teukolsky, S. A. 1972, ApJ, 178, 347
Barret, D., Olive, J. F., & Miller, M. C. 2005, MNRAS, 361, 855
Barret, D., Olive, J. F., & Miller, M. C. 2006, MNRAS, 370, 1140
Berti, E., White, F., Maniopoulou, A., & Bruni, M. 2005, MNRAS, 358, 923
Bordas, P., Kuulkers, E., Alfonso-Garzzon, J., et al. 2010, ATel, 2919, 1
Gutierrez-Ruiz, A. F., Valenzuela-Toledo, C. A., & Pachon, L. A. 2013, Universitas Scientiarum, 19, 63
Hartle, J. B., & Thorne, K. S. 1968, ApJ, 153, 807
Horák, J. 2005, Astron. Nachr., 326, 84
Kluzniak, W., & Rosinska, D. 2013, MNRAS, 434, 2825
Kluźniak, W., Michelson, P., Wagoner, R. V. 1990, ApJ, 358, 538
Kotrlová, A., Stuchlík, Z., & Török, G. 2008, Class. Quantum. Grav., 25, 225016
Lamb, F. K., & Boutloukos, S. 2008, In Short-Period Binary Stars: Observations, Analyses, and Results, eds. E. F. Milone, D. A. Leahy, & D. W. Hobill (Berlin: Springer)
Lamb, F. K., Shibazaki, N., Alpar, M. A., & Shaham, J. 1985, Nature, 317, 681
Lattimer, J. M. 2012, Ann. Rev. Nucl. Part. Sci., 62, 485
Lattimer, J. M., & Prakash, M. 2001, ApJ, 550, 426,
Lattimer, J. M., & Prakash, M. 2007, Phys. Rep., 442, 109
Manchester, R. N., Hobbs, G. B., Teoh, A., & Hobbs, M. 2005, AJ, 129, 1993
Markwardt, C. B., & Strohmayer, T. E. 2010, ApJ, 717, L149
Miller, M. C., Lamb, F. K., & Psaltis, D. 1998, ApJ, 508, 791
Pachón, L. A., Rueda, J. A., Sanabria-Gómez, J. D. 2006, Phys. Rev. D, 73, 104038
Pachón, L. A., Rueda, J. A., & Valenzuela-Toledo, C. A. 2012, ApJ, 756, 82
Paczynski, B. 1987, Nature, 327, 303
Patruno, A., & Watts, A. L. 2014, in Timing neutron stars: pulsations, oscillations and explosions, eds. T. Belloni, M. Mendez, & C. M. Zhang, ASSL, Springer, in press [arXiv:1206.2727]
Pétri, J. 2005, A&A, 439, L27
Psaltis, D., Wijnands, R., Homan, J., et al. 1999, ApJ, 520, 763
Rezzolla, L., Yoshida S., & Zanotti O. 2003, MNRAS, 344, 978
Shibata, M., & Sasaki, M. 1998, Phys. Rev. D, 58, 104011
Šrámková, E., Torkelsson, U., & Abramowicz, M. A. 2007, A&A, 467, 641
Stella, L., & Vietri, M. 1999, Phys. Rev. Lett., 82, 17
Stone, J., Miller, J. C., Koncewicz, R., Stevenson, P. D., & Strayer, M. R. 2003, Phys. Rev. C, 68, 3
Straub, O., & Šrámková, E. 2009, Class. Quantum. Grav., 26, 055011
Stuchlík, Z., Konar, S., Miller, J. C., & Hledík, S. 2008, A&A, 489, 963
Titarchuk, L., & Wood, K. 2002, ApJ, 577, L23
Török, G., Bakala, P., Šrámková, E., et al. 2012, ApJ, 760, 2
Török, G., Bakala, P., Stuchlík, Z., & Čech, P. 2008, Acta Astron., 58, 1
Török, G., Bakala, P., Šrámková, E., Stuchlík, Z., & Urbanec, M. 2010, ApJ, 714, 748
Urbanec, M., Běták, E., & Stuchlík, Z. 2010a, Acta Astron., 60, 149
Urbanec, M., Török, G., Šrámková, E., et al. 2010b, A&A, 522, A72
Urbanec, M., Miller, J. C., & Stuchlík, Z. 2013, MNRAS, 433, 1903
Wang, D. H., Chen, L., Zhang, C. M., Lei, Y. J., & Qu, J. L. 2013, MNRAS, 435, 3494
Zdunik, J., & Gourgoulhon, E. 2001, Phys. Rev. D, 63, 8
Zhang, C. M. 2005, Chin. J. Astron. Astrophys., 5, 21

Paper II

II.2. Braking index of isolated pulsars

Hamil Oliver, Stone Jirina, Urbanec Martin & Urbancová Gabriela

Physical Review D, 2015,
Volume 91, Issue 6, article id. 063007

PHYSICAL REVIEW D **91,** 063007 (2015)

Braking index of isolated pulsars

O. Hamil[*]
Department of Physics and Astronomy, University of Tennessee, Knoxville, Tennessee 37996, USA

J. R. Stone[†]
Department of Physics and Astronomy, University of Tennessee, Knoxville, Tennessee 37996, USA and Department of Physics, Oxford University, Oxford, United Kingdom

M. Urbanec[‡] and G. Urbancová[§]
Institute of Physics, Faculty of Philosophy and Sciences, Silesian University in Opava, CZ 74601 Opava, Czech Republic

(Received 2 February 2015; published 19 March 2015)

Isolated pulsars are rotating neutron stars with accurately measured angular velocities Ω, and their time derivatives that show unambiguously that the pulsars are slowing down. Although the exact mechanism of the spin-down is a question of detailed debate, the commonly accepted view is that it arises through emission of magnetic dipole radiation (MDR) from a rotating magnetized body. Other processes, including the emission of gravitational radiation, and of relativistic particles (pulsar wind), are also being considered. The calculated energy loss by a rotating pulsar with a constant moment of inertia is assumed proportional to a model dependent power of Ω. This relation leads to the power law $\dot{\Omega} = -K\Omega^n$ where n is called the braking index. The MDR model predicts n exactly equal to 3. Selected observations of isolated pulsars provide rather precise values of n, individually accurate to a few percent or better, in the range $1 < n < 2.8$, which is consistently less than the predictions of the MDR model. In spite of an extensive investigation of various modifications of the MDR model, no satisfactory explanation of observation has been found yet. The aim of this work is to determine the deviation of the value of n from the canonical $n = 3$ for a star with a frequency dependent moment of inertia in the region of frequencies from zero (static spherical star) to the Kepler velocity (onset of mass shedding by a rotating deformed star), in the macroscopic MDR model. For the first time, we use microscopic realistic equations of state (EoS) of the star to determine its behavior and structure. In addition, we examine the effects of the baryonic mass M_B of the star, and possible core superfluidity, on the value of the braking index within the MDR model. Four microscopic equations of state are employed as input to two different computational codes that solve Einstein's equations numerically, either exactly or using the perturbative Hartle-Thorne method, to calculate the moment of inertia and other macroscopic properties of rotating neutron stars. The calculations are performed for fixed values of M_B (as masses of isolated pulsars are not known) ranging from 1.0–2.2$M_\odot$, and fixed magnetic dipole moment and inclination angle between the rotational and magnetic field axes. The results are used to solve for the value of the braking index as a function of frequency, and find the effect of the choice of the EoS, M_B. The density profile of a star with a given M_B is calculated to determine the transition between the crust and the core and used in estimation of the effect of core superfluidity on the braking index. Our results show conclusively that, within the model used in this work, any significant deviation of the braking index away from the value $n = 3$ occurs at frequencies higher than about ten times the frequency of the slow rotating isolated pulsars most accurately measured to date. The rate of change of n with frequency is related to the softness of the EoS and the M_B of the star as this controls the degree of departure from sphericity. Change in the moment of inertia in the MDR model alone, even with the more realistic features considered here, cannot explain the observational data on the braking index and other mechanisms have to be sought.

DOI: 10.1103/PhysRevD.91.063007 PACS numbers: 97.60.Jd, 26.60.Dd, 26.60.Gj, 97.60.Gb

I. INTRODUCTION

The slowing down of rotating neutron stars has been observed and modeled for decades. The simplest models relate the loss the kinetic rotational energy of the star to the emission of magnetic radiation from a rotating dipolar magnetic field (MDR), attached to the star [1–5]. The

[*]ohamil@vols.utk.edu
[†]j.stone@physics.ox.ac.uk
[‡]martin.urbanec@fpf.slu.cz
[§]gabriela.urbancova@fpf.slu.cz

calculated energy loss by a rotating pulsar is assumed proportional to a model dependent power of Ω. This relation leads to the power law $\dot{\Omega} = -K\Omega^n$ where n is called the braking index. The value of n can, in principle, be determined from observation of higher-order frequency derivatives related to n by [6]

$$n = \frac{\Omega\ddot{\Omega}}{\dot{\Omega}^2} \tag{1}$$

$$n(2n-1) = \frac{\Omega^2\dddot{\Omega}}{\dot{\Omega}^3}. \tag{2}$$

When the star is taken as a magnetized sphere, rotating in vacuum, with a constant moment of inerta (MoI) and a constant magnetic dipole moment, misaligned at a fixed angle to its axis of rotation, n is equal to 3 (for derivation see Sec. I A).

Extraction of the rotational frequency and its time derivatives from observation involves a detailed analysis of the time evolution of the pulses, and of the spectra and luminosity of radiation from the related nebulae in a wide range of wavelengths. Although data on many pulsars are available in the literature, there are only eight pulsars generally accepted to yield reliable data on the pulsar's spin-down (see Table. I, recent compilation [7] and Refs. therein). The third derivative is known only for the Crab pulsar [8], and PSR B1509-58 [9].

Examination of Table I shows that $n = 3$ does not agree with observation. There have been many attempts to extend/modify the basics of the MDR model. These include consideration of magnetic field activity (e.g., [13,18–23]), superfluidity and superconductivity of the matter within pulsars (e.g., [24–26]), and modifications of the power law and related quantities (e.g., [7,27]). Time dependence of the constants in the MDR model has also been considered [18,28–30]. In particular, time evolution of the inclination angle between spin and magnetic dipole axes has been recently addressed [6,31]. However, there is no model currently available that would yield, consistently, the typical spread of values of n as illustrated in Table I.

TABLE I. Selected pulsars adopted from [6,7,10]. $n_{\rm freq}$ is the value of n obtained for the given pulsar, at the given frequency, with changing MoI calculated in this work.

PSR	Frequency (Hz)	n	$n_{\rm freq}$	Ref.
B1509 − 58	6.633598804	2.839 ± 0.001	2.999	[11]
J1119 − 6127	2.4512027814	2.684 ± 0.002	2.999	[12]
J1846 − 0258	3.062118502	2.65 ± 0.1	2.999	[11]
		2.16 ± 0.13		[13]
B0531 + 21 (Crab)	30.22543701	2.51 ± 0.01	2.995	[14]
B0540 − 69	19.8344965	2.140 ± 0.009	2.997	[11,15]
J1833 − 1034	16.15935711	1.8569 ± 0.001	2.999	[16]
B0833 − 45 (Vela)	11.2	1.4 ± 0.2	2.999	[17]
J1734 − 3333	0.855182765	0.9 ± 0.2	3.000	[10]

Models outside the MDR have also been introduced. For example, energy loss through emission of accelerated charged particles, forming a massive wind from the surface of rotating stars [21,32], or emission of higher multipole electromagnetic radiation, including the gravitational quadrupole component [33,34], has been studied. Competition of different mechanisms, MDR, emission of gravitational waves, and particle winds was also investigated by [35,36].

In this work we focus on determination of the maximum deviation of the braking index from the value $n = 3$ by introducing two modifications of the simple MDR model: frequency dependence of MoI, related to the change of shape of a deformable star due to rotation, and superfluidity of the pulsar core. The correction to the expression of the braking index arising from these modifications following Glendenning [37] is derived, and included in the calculation, using four realistic equations of state (EoS) over a range of baryonic mass (M_B). We study the relation between the softness of the EoS and the rate of change of the braking index as a function of frequency and the M_B. The four EoS were also used to obtain mass density profiles of the pulsars needed to determine the transition region between the crust and core. These results were utilized in the simulation of an effect of superfluid conditions that eliminates the angular momentum exchange at the threshold between the crust and core. The calculation is performed over a full range of frequencies of the pulsar from zero to the Kepler frequency and a range of M_B from 1.0 to 2.2 $M_\odot$, representing the gravitational mass range from about 0.8 to 2.0 $M_\odot$.

The paper is organized as follows: The braking index, as calculated in the canonical MDR model, and its extensions introduced in this work, are presented Secs. I A–I B. Section II contains the computational method employed in this work, followed by Sec. III where the main results are reported. The main findings of this work, discussion, and outline of future development are summarized in Sec. IV.

A. Simple MDR model

The total energy loss by a rotating magnetized sphere can be expressed in terms of the time derivative of the radiated energy as [2,6,37]

$$\frac{dE}{dt} = -\frac{2}{3}\mu^2\Omega^4\sin^2\alpha, \tag{3}$$

where μ is the magnetic dipole moment of the pulsar, $\mu = BR^3$. R is the radial coordinate of a surface point with the surface magnetic field strength B, Ω is the rotational frequency, and α is the angle of inclination between the dipole moment and the axis of rotation [37].

Substituting the kinetic energy of a rotating body, dependent on the MoI I,

$$E = \frac{1}{2} I\Omega^2, \tag{4}$$

into (3) yields

$$\frac{d}{dt}\left(\frac{1}{2} I\Omega^2\right) = -\frac{2}{3}\mu^2\Omega^4 \sin^2\alpha. \tag{5}$$

Assuming constant MoI, $dI/dt = 0$, we get

$$\dot{\Omega} = -\frac{2}{3}\frac{\mu^2}{I}\Omega^3 \sin^2\alpha. \tag{6}$$

Setting $K = \frac{2}{3}\frac{\mu^2}{I}\sin^2\alpha$ in (6) and taking μ and α constant leads to the commonly used braking power law describing the pulsar spin-down due to dipole radiation:

$$\dot{\Omega} = -K\Omega^3. \tag{7}$$

Differentiating (7) with respect to time

$$\ddot{\Omega} = -3K\Omega^2\dot{\Omega}, \tag{8}$$

and combining (7) and (8) to eliminate K we get the value of the braking index n,

$$n = \frac{\Omega\ddot{\Omega}}{\dot{\Omega}^2} = 3. \tag{9}$$

B. MDR model with frequency dependent MoI

The simple MDR value $n = 3$ (9) is derived taking the I, μ, and α as independent of frequency and constant in time. However, in reality the MoI of rotating pulsars changes with frequency and, consequently, with time [37,38]. The equlibrium state of a rotating pulsar includes the effect of centrifugal forces, acting against gravity. The shape of the pulsar is ellipsoidal with decrease (increase) in radius along the equatorial (polar) direction with respect to the rotation axis as the pulsar spins down. Thus, the MoI, and, consequently, the braking index, are both frequency dependent.

It is convenient to rewrite (5) as

$$\frac{d}{dt}\left(\frac{1}{2} I\Omega^2\right) = -C\Omega^4, \tag{10}$$

where $C = \frac{2}{3}\mu^2\sin^2\alpha$. Assuming this time that dI/dt is nonzero, differentiation of (10) with respect to time gives

$$2I\dot{\Omega} + \Omega\dot{I} = -2C\Omega^3. \tag{11}$$

Differentiating once more gives

$$2I\ddot{\Omega} + 2\dot{\Omega}\dot{I} + \dot{\Omega}\dot{I} + \Omega\ddot{I} = -6C\Omega^2\dot{\Omega}. \tag{12}$$

Using the chain rule we can write $\dot{I}$ in terms of $\dot{\Omega}$,

$$\frac{dI}{dt} = \frac{d\Omega}{dt}\frac{dI}{d\Omega}, \tag{13}$$

and obtain

$$\dot{I} = I'\dot{\Omega} \tag{14}$$

$$\ddot{I} = \dot{\Omega}^2 I'' + I'\ddot{\Omega}, \tag{15}$$

where the primed notation represents the derivative with respect to Ω.

Substituting the identities shown above into (11)–(12), we get the following relations for $\dot{\Omega}$ and $\ddot{\Omega}$:

$$\dot{\Omega} = \frac{-2C\Omega^2}{(2I + \Omega I')} \tag{16}$$

$$\ddot{\Omega} = \frac{-6C\dot{\Omega}\Omega^2 - \dot{\Omega}^2(3I' + \Omega I'')}{(2I + \Omega I')}. \tag{17}$$

After some algebra it is easy to show that the expression of the braking index as a function of angular velocity reads

$$n(\Omega) = \frac{\Omega\ddot{\Omega}}{\dot{\Omega}^2} = 3 - \frac{(3\Omega I' + \Omega^2 I'')}{(2I + \Omega I')}. \tag{18}$$

We note that the magnetic dipole moment of the nonspherical pulsar may, in principle, also change with frequency. Estimation of this effect would require knowledge of the origin and distribution of the dipole moment, which is lacking. We therefore ignore such a change here and restrict ourselves to analysis of the two effects described.

II. CALCULATION METHOD

Previous modeling of the braking index using the simple MDR model with constant MoI assumed a pulsar with $1.4M_\odot$ gravitational mass and a radius ~10 km. In this work, which includes frequency dependent MoI and varying M_B, we solve the equations of motion of rotating stars with realistic EoS using two different numerical methods.

A. The codes

The PRNS9 code, developed by Weber [39,40], is based on a perturbative approach to the equations of motion of slowly rotating near-spherical objects [41,42]. To ensure the reliability of the PRNS9 code results, we also used the RPN code. This code by Rodrigo Negreiros [43] is based on a publicly available algorithm, RNS, developed by Stergioulas and Friedman [44]. The equations of motion are derived directly from Einstein's equations, following the Cook, Shapiro, and Teukolsky approach [45], described in

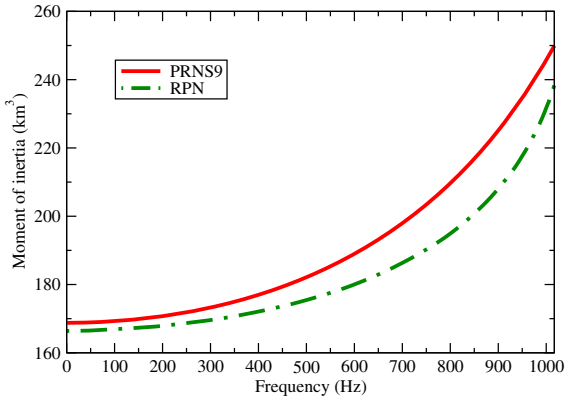

FIG. 1 (color online). MoI as a function of frequency for a pulsar with $M_B = 2.0\,M_\odot$ as calculated with both RPN and PRNS9 numerical codes.

detail in [46]. Both codes are applicable to rotating stars with all frequencies up to the Kepler limit.

A comparison of the results of the two codes is demonstrated in Fig. 1, which shows MoI as a function of frequency for a pulsar with the QMC700 EoS and $M_B = 2.0$ M$_\odot$ (see Sec. II B). They differ most, but by less than 10%, as the Kepler frequency is approached. This difference has no consequence in practical applications as no pulsars rotating with frequencies in the Kepler region (see Table II for EoS and M_B used in this paper) have been observed. The small difference at near zero frequency (about 1.25%), due to the difference in behavior of the two low density EoS (see Sec. II B), is negligible in the context of calculating neutron star macroscopic properties.

Unless stated otherwise, present the PRNS9 code results as this code provides calculation of some observables, not readily available in the RPN code, which are needed in our study (see Sec. III).

B. The equation of state

An essential input to the calculation of macroscopic properties of rotating neutron stars is the EoS. The EoS is constructed for two physically different regimes, the high density core and the relatively low density crust.

The microscopic composition of high density matter in the cores of neutron stars is not well understood. We have chosen two EoS, which assume that the core is made only of nucleons, KDE0v1 [47] and NRAPR [48]. These EoS were selected by Dutra *et al.* [49] as being among the very few that satisfied an extensive set of experimental and observational constraints on properties of high density matter. In addition, we use two more realistic EoS that include in the core the heavy strange baryons (hyperons) as well as nucleons. The QMC700 EoS has been derived in the framework of the Quark-Meson-Coupling (QMC) model [50,51] and the Hartree V (HV) EoS [52] is based on a relativistic mean-field theory of nuclear forces. The maximum mass of a static star, calculated using the Tolman-Oppenheimer-Volkof equation, is 1.96, 1.93, 1.98, and 1.98 M$_\odot$ for KDE0v1, NRAPR, QMC700, and HV, respectively, which is close to the gravitational mass of the heaviest known neutron stars [53,54]. The EoS are illustrated in Fig. 2, which shows pressure as a function of energy density ϵ in units of nuclear saturation energy density $\epsilon_0 = 140$ MeV/fm^3. We observe that the pressure increases as a function of energy density almost monotonically for KDE0v1, NRAPR, and HV, whereas QMC700 EoS predicts a change in the rate of increase at about 4 ϵ_0. This change, and the subsequent softening of the EoS, happens at the transition energy density marking the threshold for appearance of hyperons in the matter. Such a change is not observed in the HV EoS. The main reason for the difference between the two hyperonic models is that the QMC700 distinguishes between the nucleon-nucleon and nucleon-hyperon interactions (neglecting the poorly known hyperon-hyperon interaction), whereas the HV model uses a universal set of parameters for all hadrons. Inclusion of both the QMC700 and HV EoS in this work reflects the uncertainty in the theory of dense matter in the cores of neutron stars.

In order to ease the numerical calculation within the different architecture of the RPN and PRNS9 codes, two

TABLE II. Kepler frequencies in Hz for EoS and $M_B/M_\odot$ used in this work.

EoS/M_B	1.0	1.5	2.0	2.2
KDE0v1	820	1024	1230	1327
NRAPR	778	985	1198	1312
QMC700	745	888	1017	1070
HV	612	761	908	985

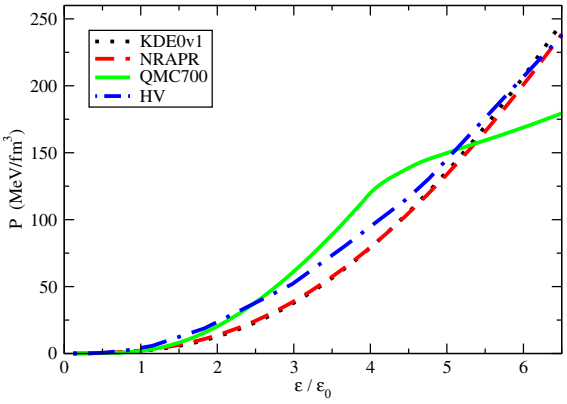

FIG. 2 (color online). Pressure vs energy density ϵ (in units of the energy density of symmetric nuclear matter at saturation ϵ_0) as predicted by the four EoS used in this work.

different EoS in the low density region (neutron star crust) have been used. The Baym-Bethe-Pethick (see [55] and Table V in [56]) at about 0.1 fm^{-3}, which is augmented by Baym-Pethick-Sutherland [56] at about 0.0001 fm^{-3}, going down to $\sim 6.0 \times 10^{-12}$ fm^{-3}, was adopted in the RPN code. For the PRNS9 code, the high density EoS was matched to the Harrison-Wheeler [57], taken for the outer crust of the star, and Negele-Vautherin [58] EoS for the inner crust.

III. RESULTS AND DISCUSSION

As detailed in the previous section, the calculation of the frequency dependence of the braking index has been done for a multiple combination of codes, EoS and M_B of the rotating star. We show only typical examples of the results, usually for the QMC700 EoS, unless stated otherwise.

A. Braking index with frequency dependent MoI

As a general feature, we find that any appreciable deviation of the braking index from the generic value $n = 3$ is observed only at rotational frequencies higher than about 250 Hz. The sensitivity of this deviation to the EoS and M_B is demonstrated in Figs. 3–4. As can be seen in Fig. 3, the biggest change in the braking index of a 2.0 $M_\odot$ star pulsar is predicted by the HV EoS, followed by the QMC700, reaching $\sim$ values 1.75 and 2.15 at 750 Hz, respectively. The two nucleon-only EoS, KDE0v1 and NRAPR, behave in a very similar way and predict a larger value of $n = 2.5$ at this frequency. These trends can be directly related to the properties of the EoS. Figure 4 shows the sensitivity to M_B for the QMC700 EoS. The effect clearly increases with decreasing M_B.

We recall that the stiffness/softness of the EoS relates to the rate of change of pressure with changing energy density ϵ. For each EoS the frequency dependent ϵ is given in Table III. Using Fig. 2 we obtain the corresponding pressures. Figure 5 plots the pressure vs ϵ relation for each EoS, the slope indicating the stiffness/softness in each case. The maximum change in the braking index in Fig. 3, observed for the HV EoS, is seen to be associated with the smallest change in pressure with increasing ϵ, i.e., the largest softness. The stiffest EoS, KDE0v1 and NRAPR, predict the smallest response to the pulsar's rotational deformation. This conclusion is further supported by results shown in Fig. 4. Pulsars with the lowest M_B, governed by the softest EoS, exhibit the largest change in the braking index at high frequency.

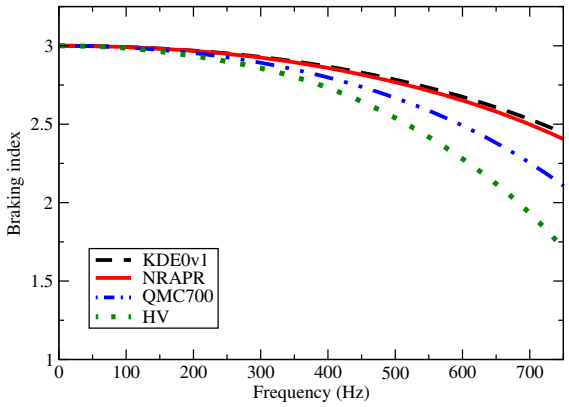

FIG. 3 (color online). Braking index as a function of frequency calculated for a pulsar with $M_B = 2.0\,M_\odot$ with all EoS adopted in this work.

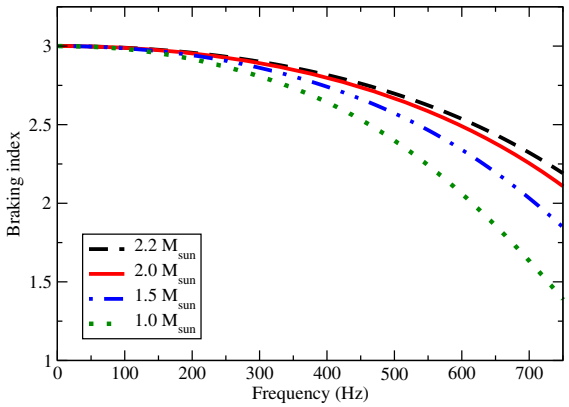

FIG. 4 (color online). Braking index as a function of frequency calculated of pulsars with $M_B = 1.0$–2.2 $M_\odot$.

B. Superfluidity of the core

The effects demonstrated in Figs. 3–4 were calculated assuming that the whole body of a pulsar contributes to the total (core+crust) MoI. However, some theories suggest the

TABLE III. Central energy density (in units of the ϵ_0) of a pulsar with HV, QMC700, NRAPR, KDE0v1 EoS, and $M_B = 2.0$ $M_\odot$ as a function of decreasing rotational frequency. For more explanation see the text.

Frequency [Hz]	HV	QMC700	NRAPR	KDE0v1
1200	–	–	5.04	5.09
1100	–	–	5.23	5.26
1000	–	3.05	5.40	5.41
900	3.32	3.14	5.57	5.55
800	3.54	3.22	5.72	5.68
700	3.75	3.30	5.84	5.80
600	3.94	3.36	5.96	5.90
500	4.11	3.43	6.06	5.98
400	4.30	3.48	6.15	6.06
300	4.40	3.52	6.21	6.11
200	4.47	3.54	6.25	6.15
100	4.52	3.56	6.28	6.17
0	4.54	3.57	6.29	6.18

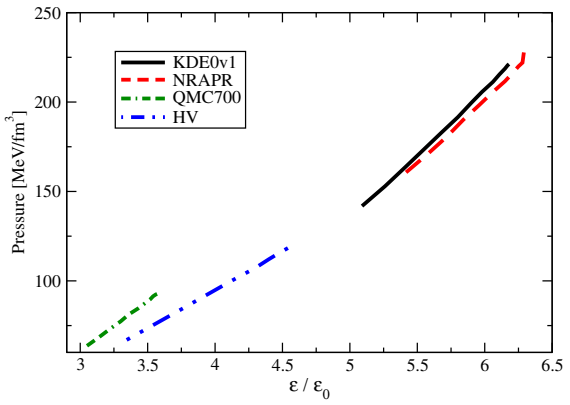

FIG. 5 (color online). Pressure as a function central density of a pulsar with $M_B = 2.0$ M$_\odot$, rotating with frequencies decreasing from the Kepler limit to zero as predicted by the four EoS used in this work. Relation between the central density and frequency is given in Table III. For more explanation see the text.

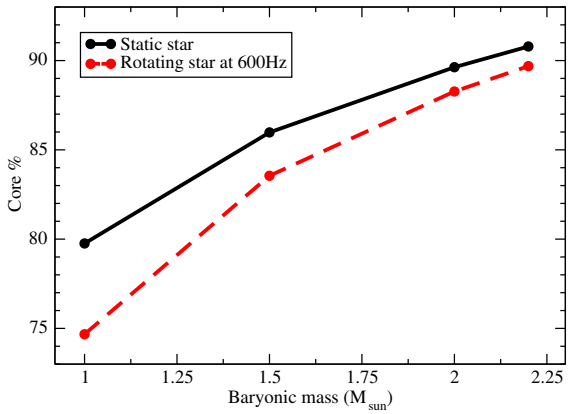

FIG. 6 (color online). Percentage of the core in a static star and a star rotating at 600 Hz as a function of M_B. For more explanation see the text.

conditions inside a pulsar are consistent with the presence of superfluid/superconducting matter, both in the crust and in the core [24–26,59]. Superfluid material would contribute to the rotation, thus reducing the MoI.

In this work we considered an extreme case in which the whole contribution of the core to the total MoI is removed. This scenario could be realized, for example, if either the whole core is superfluid or there is a layer of superfluid material between the core and the inner crust of the star, preventing an angular momentum transfer between the core and the crust. Either scenario simply results in removal of the contribution of the core to the MoI. To model this effect, it was necessary to locate the transition between the two phases of neutron star matter, which is assumed to occur roughly at 120 MeV/fm^3. The corresponding pressure is dependent on the EoS and is used to locate the physical position of the transition along the equatorial radius. The results are schematically illustrated in Fig. 6, which shows the proportion of the core radius in a static star and a star rotating at an arbitrarily chosen frequency of 600 Hz as a function of M_B, as predicted by the KDE0v1 EoS. We observe that the proportion is different for a static and rotating star, mainly because of the varying shape of the star. The expansion (compression) along the equatorial (polar) direction with respect to the rotational axis leads to larger deformation of the less dense crust than that of the denser core.

Elimination of the core contribution can lead to a dramatic lowering of the total MoI by more than a factor of three, as shown, for example, in Fig. 7 for the 1.0 M$_\odot$ baryon mass and the QMC700 EoS. The difference between the total and crust-only MoI shows a weak frequency dependence with a slight increase above about 600 Hz. In turn, the reduction of the MoI by removal of the core contribution leads to additional changes in the braking index, on top of the changes due to the frequency dependent MoI (see Fig. 4) as shown in Fig. 8. This change is, as expected, larger for higher mass stars that contain a more significant proportion of dense core material than for lower mass stars that are more crustlike throughout.

For the purpose of this work, we assumed that there is substantial superfluid material located in the core of the star but made no assumption on the superfluidity (or not) of the crust. The effects reported here should be taken as illustrative rather than definitive of the possible effects of superfluidity.

C. Summary

The variation of braking index of isolated rotating neutron stars with $M_B = 1.0$, 1.5, 2.0, and 2.2 M$_\odot$ with rotational frequency from zero to the Kepler limit within

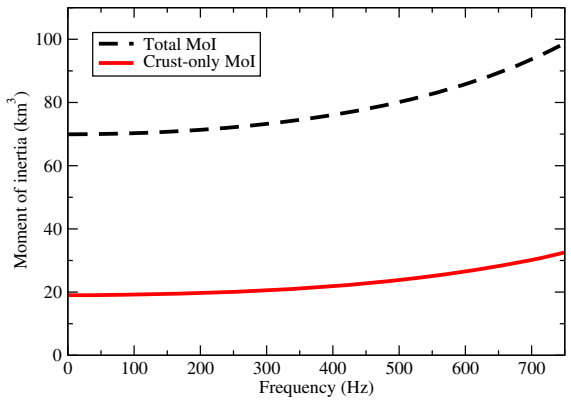

FIG. 7 (color online). Total (crust and core) and the crust-only MoI as a function of frequency, calculated for a pulsar with $M_B = 1.0$ M$_\odot$.

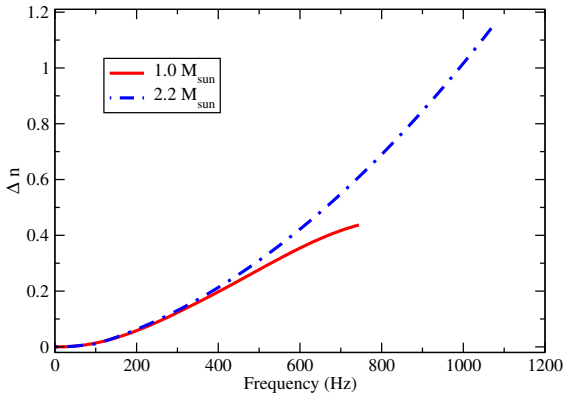

FIG. 8 (color online). Δ n represent the difference in braking index as a function of frequency between stars with (see Fig. 4) and without core contribution to the MoI. Each curve is displayed up to the Kepler frequency of the star.

the MDR model with frequency dependent MoI has been investigated. The microphysics of the star was included through utilizing realistic EoS of the pulsar matter. An illustration of the possible effect of superfluidity in the star core has been included in the study.

Compiling results of all models used in this work, including the superfluidity effect, we deduce a definitive upper and lower limit on the braking index as a function of frequency, shown in Fig. 9. The maximum change in the braking index is obtained with the QMC700 EoS and 1.0 $M_\odot$; the least effect is found for KDE0v1 and the

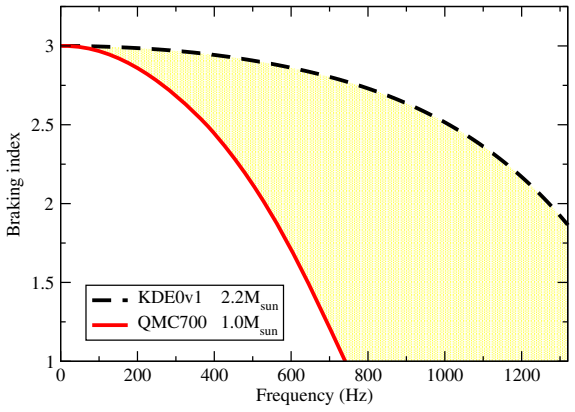

FIG. 9 (color online). Lower and upper limits on values of the braking index as a function of frequency, including results from both numerical codes, all EoS, M_B, and the superfluid condition. The (yellow) shaded area between the two lines defines the location of all results within the limits. The pulsar with baryonic $M_B = 2.2$ $M_\odot$ and the KDE0v1 EoS has the highest Kepler frequency (see Table II) and defines the frequency limit in this work.

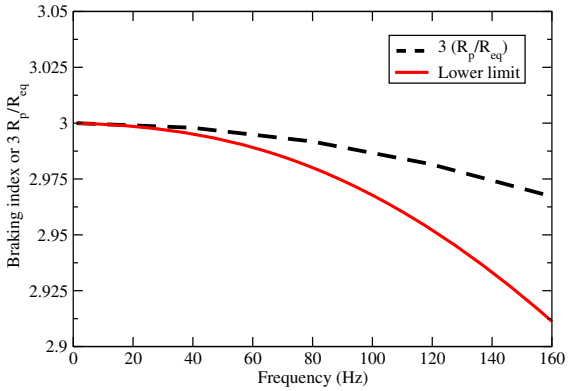

FIG. 10 (color online). The lower limit of the braking index (see Fig. 9) as a function of frequency (solid line) compared with the ratio between polar (R_p) and equatorial radii ($R_{\rm eq}$), normalized to three, which determines deformation of the star. The difference between the two lines represents a correlation between deviations of the braking index from $n = 3$ and deformation for a 1.0 $M_\odot$ pulsar rotating at frequencies below 160 Hz (notice the expanded y scale). It is seen that the shape deformation, even for this most deformable star, is small at these frequencies and quite unable to reproduce the observed range of braking indices.

2.2 $M_\odot$ star. Reduction of the braking index from the simple MDR model value $n = 3$ happens only at frequencies that are some significant fraction of the Kepler frequency. The calculation predicts that isolated pulsars with the braking index most deviating from $n = 3$ have low M_B. For the frequencies of known isolated pulsars with accurately measured braking indices (see Table I), the reduction away from $n = 3$ found in this model is negligible.

IV. CONCLUSIONS AND OUTLOOK

In the model of isolated pulsars used in this work, the rate of change in rotational frequency of a spherical magnetized pulsar *in vacuo* depends on three factors: the MoI (constant or frequency dependent), the magnitude of the magnetic dipole moment, and the inclination angle between the magnetic and rotational axes. The braking index is related to changes of these observables. In this work we considered effects due to changes to the MoI and its variation and showed that any significant deviation from the $n = 3$ value appears only at frequencies much higher than the frequency range of observed isolated pulsars with reliable braking index. As MoI is related to the shape of the star, this result is consistent with the assumption of the simple MDR model that the pulsar is spherical at low frequencies. We show in Fig. 10 the correlation between the braking index and the deformation of the star in terms of the polar to equatorial radii ratio $R_p/R_{\rm eq}$ (normalized to 3 for display). It follows that changes in MoI alone cannot

explain the observed deviation of the braking index at low frequencies from the simple MDR model predictions. If the MDR model is to be sustained, attention has to be paid to changes in the magnitude magnetic dipole moment and/or in the inclination angle. As stated above, the lack of knowledge of the origin and properties of the pulsar's magnetic field makes the former task difficult but the latter may be worth pursuing, particularly in the view of recent work by Lyne *et al.* [6,31].

Finally, we have shown that the simple exclusion of the core due to the superfluidity, or some superfluid barrier between the crust and core, does not have a strong effect on braking in the frequency range of observed isolated pulsars. Further development of the idea of a macroscopic description of superfluidity would be interesting. Change of the magnetic field due to superfluidity and possible magnetic field expulsion, and a consequential increase in surface magnetic field strength B could also be usefully explored.

ACKNOWLEDGMENTS

J. R. S. wishes to thank Jocelyn Bell Burnell for suggesting the topic of this work and helpful discussions, Fridolin Weber for help with understanding the PRNS9 code, and Nick Stone for discussions and advice concerning all of the physics relevant to this work. Discussions with John Miller are also gratefully acknowledged. O. H. is grateful for discussions with Rodrigo Negreiros, and use of the RPN code. J. R. S. and O. H. thank the Institute of Physics in Opava for hospitality at the final stages of this work. G. U. and M. U. thank the Oak Ridge National Laboratory for kind hospitality. M. U. acknowledges support of the Czech Grant No. GAČR 209/12/P740 and Grant No. CZ.1.07/2.3.00/20.0071 "Synergy," aimed to foster international collaboration of the Institute of Physics of the Silesian University, Opava. The research was also supported in part by the Department of Physics and Astronomy, University of Tennessee.

[1] F. Pacini, Nature (London) **216**, 567 (1967).
[2] F. Pacini, Nature (London) **219**, 145 (1968).
[3] T. Gold, Nature (London) **218**, 731 (1968).
[4] T. Gold, Nature (London) **221**, 25 (1969).
[5] H. C. Goldwire, Jr. and F. C. Michel, Astrophys. J. **156**, L111 (1969).
[6] A. G. Lyne, C. A. Jordan, F. Graham-Smith, C. M. Espinoza, B. W. Stappers, and P. Weltevrede, Mon. Not. R. Astron. Soc. **446**, 857 (2015).
[7] N. S. Magalhaes, T. A. Miranda, and C. Frajuca, Astrophys. J. **755**, 54 (2012).
[8] A. G. Lyne, R. S. Pritchard, and F. G. Smith, Mon. Not. R. Astron. Soc. **233**, 667 (1988).
[9] V. M. Kaspi, R. N. Manchester, B. Siegman, S. Johnston, and A. G. Lyne, Astrophys. J. **422**, L83 (1994).
[10] C. M. Espinoza, A. G. Lyne, M. Kramer, R. N. Manchester, and V. M. Kaspi, Astrophys. J. **741**, L13 (2011).
[11] M. A. Livingstone, V. M. Kaspi, F. P. Gavriil *et al.*, Astron. Astrophys. **308**, 317 (2007).
[12] P. Waltevrede, S. Johnston, and C. M. Espinoza, Mon. Not. R. Astron. Soc. **411**, 1917 (2011).
[13] M. A. Livingstone, C. Y. Ng, V. M. Kaspi, F. P. Gavriil, and E. V. Gotthelf, Astrophys. J. **730**, 66 (2011).
[14] A. G. Lyne, R. S. Pritchard, and F. G. Smith, Mon. Not. R. Astron. Soc. **265**, 1003 (1993).
[15] P. T. Boyd, G. W. van Citters, J. F. Dolan, K. G. Wolinski, J. W. Percival, R. C. Bless, J. L. Elliot, M. J. Nelson, and M. J. Taylor, Astrophys. J. **448**, 365 (1995).
[16] J. Roy, Y. Gupta, and W. Lewandowski, Mon. Not. R. Astron. Soc. **424**, 2213 (2012).
[17] A. G. Lyne, R. S. Pritchard, F. G. Smith, and F. Camilo, Nature (London) **381**, 497 (1996).
[18] R. D. Blandford and R. W. Romani, Mon. Not. R. Astron. Soc. **234**, 57P (1988).
[19] A. Melatos, Mon. Not. R. Astron. Soc. **288**, 1049 (1997).
[20] A. G. Lyne, in *IAU Symposium 218, Young Neutron Stars and their Environments, 2004,* edited by F. Camilo and B. M. Gaensler (ASP, San Francisco, 2004), p. 257.
[21] A. K. Harding, I. Contopoulos, and D. Kazanas, Astrophys. J. **525**, L125 (1999).
[22] M. Kramer, A. G. Lyne, J. T. O'Brien, C. A. Jordan, and D. R. Lorimer, Science **312**, 549 (2006).
[23] A. Lyne, G. Hobbs, M. Kramer, I. Stairs, and B. Stappers, Science **329**, 408 (2010).
[24] A. Sedrakian and J. M. Cordes, Astrophys. J. **502**, 378 (1998).
[25] W. C. G. Ho and N. Andersson, Nature (London) **8**, 787 (2012).
[26] D. Page, J. M. Lattimer, M. Prakash, and A. W. Steiner, arXiv:1302.6626 [Oxford University Press (to be published)].
[27] S. Johnston and D. Galloway, Mon. Not. R. Astron. Soc. **306**, L50 (1999).
[28] I. Contopoulos and A. Spitkovsky, Astrophys. J. **643**, 1139 (2006).
[29] S. N. Zhang and Y. Xiee, Astrophys. J. **761**, 102 (2012).
[30] K. N. Gourgouliatos and A. Cumming, Mon. Not. R. Astron. Soc. **446**, 1121 (2015).
[31] A. Lyne, F. Graham-Smith, P. Weltevrede, C. Jordan, B. Stappers, C. Bassa, and M. Kramer, Science **342**, 598 (2013).
[32] F. C. Michel, Astrophys. J. **157**, 1183 (1969).
[33] J. P. Ostriker and J. E. Gunn, Astrophys. J. **157**, 1395 (1969).
[34] M. Alford and K. Schwenzer, Astrophys. J. **781**, 26 (2014).

[35] A. Carraminana and C. Alvarez, in *Pulsars: Problems and Progress*, edited by S. Johnston, M. A. Walker, and M. Bailes (ASP Conference Series, 1996), Vol. 105, p. 107.
[36] C. Alvarez and A. Carraminana, Astron. Astrophys. **414**, 651 (2004).
[37] N. K. Glendenning, *Compact Stars*, 2nd ed. (Springer, New York, 2000).
[38] N. K. Glendenning, S. Pei, and F. Weber, Phys. Rev. Lett. **79**, 1603 (1997).
[39] F. Weber (private communication).
[40] F. Weber, *Pulsars as Astrophysical Laboratories for Nuclear and Particle Physics* (Taylor & Francis, London, 1999).
[41] J. B. Hartle and K. S. Thorne, Astrophys. J. **S153**, 807 (1968).
[42] J. B. Hartle, Astrophys. Space Sci. **24**, 385 (1973).
[43] R. Negreiros, Ph.D. thesis, Clairemont Graduate University, San Diego State University, 2009.
[44] N. Stergioulas and J. L. Friedman, Astrophys. J. **444**, 306 (1995).
[45] G. B. Cook, S. L. Shapiro, and S. A. Teukolsky, Astrophys. J. **398**, 203 (1992).
[46] H. Komatsu, Y. Eriguchi, and I. Hachisu, Mon. Not. R. Astron. Soc. **237**, 355 (1989).
[47] B. K. Agrawal, S. Shlomo, and V. K. Au, Phys. Rev. C **72**, 014310 (2005).
[48] A. W. Steiner, M. Prakash, J. M. Lattimer, and P. J. Ellis, Phys. Rep. **411**, 325 (2005).
[49] M. Dutra, O. Lourenco, J. S. Sa Martins, A. Delfino, J. R. Stone, and P. D. Stevenson, Phys. Rev. C **85**, 035201 (2012).
[50] P. A. M. Guichon, H. H. Matevosyan, N. Sandulescu, and A. W. Thomas, Nucl. Phys. **772**, 1 (2006).
[51] J. R. Stone, P. A. M. Guichon, H. H. Matevosyan, and A. W. Thomas, Nucl. Phys. **A792**, 341 (2007).
[52] F. Weber and M. K. Weigel, Nucl. Phys. **A505**, 779 (1989).
[53] P. B. Demorest, T. Pennucci, S. M. Ransom, M. S. E. Roberts, and J. W. T. Hessels, Nature (London) **467**, 1081 (2010).
[54] J. Antoniadis *et al.*, Science **340**, 6131 (2013).
[55] G. Baym, H. Bethe, and C. Pethick, Nucl. Phys. **A175**, 225 (1971).
[56] G. Baym, C. Pethick, and P. Sutherland, Astrophys. J. **170**, 299 (1971).
[57] B. K. Harrison *et al.*, *Gravitation Theory and Gravitational Collapse* (University of Chicago Press, Chicago, 1965).
[58] J. W. Negele and D. Vautherin, Nucl. Phys. **A207**, 298 (1973).
[59] J. Hooker, W. G. Newton, and B. A. Li, arXiv:1308.0031.

Paper III

II.3. Constraining Models of Twin-Peak Quasi-periodic Oscillations with Realistic Neutron Star Equations of State

Török Gabriel, Goluchová Kateřina, Urbanec Martin, Šrámková Eva, Adámek Karel, Urbancová Gabriela, Pecháček Tomáš, Bakala Pavel, Stuchlík Zdeněk, Horák Jiří & Juryšek Jakub

The Astrophysical Journal, 2016,
Volume 833, Issue 2, article id. 273, 11 pp.

The Astrophysical Journal, 833:273 (11pp), 2016 December 20 doi:10.3847/1538-4357/833/2/273

CONSTRAINING MODELS OF TWIN-PEAK QUASI-PERIODIC OSCILLATIONS WITH REALISTIC NEUTRON STAR EQUATIONS OF STATE

Gabriel Török[1], Kateřina Goluchová[1,2], Martin Urbanec[1], Eva Šrámková[1], Karel Adámek[1,2,3], Gabriela Urbancová[1], Tomáš Pecháček[1], Pavel Bakala[1], Zdeněk Stuchlík[2], Jiří Horák[4], and Jakub Juryšek[1,5]
[1] Research Centre for Computational Physics and Data Processing, Institute of Physics, Faculty of Philosophy & Science, Silesian University in Opava, Bezručovo nám. 13, CZ-746, 01 Opava, Czech Republic; gabriel.torok@gmail.com, katka.g@seznam.cz, martin.urbanec@physics.cz, eva.sramkova@fpf.slu.cz, karel.adamek@fpf.slu.cz, gabi.urbancova@gmail.com, pechacek_t@seznam.cz, pavel.bakala@fpf.slu.cz, jakubjurysek@astronomie.cz
[2] Research Centre for Theoretical Physics and Astrophysics, Institute of Physics, Faculty of Philosophy & Science, Silesian University in Opava, Bezručovo nám. 13, CZ-746, 01 Opava, Czech Republic; zdenek.stuchlik@fpf.slu.cz
[3] University of Oxford, Oxford e-Research Centre, 7 Keble Road, Oxford, OX1 3QG
[4] Astronomical Institute, Bocni II 1401/2a, CZ-14131 Praha 4 - Sporilov, Czech Republic; hjirkoun@gmail.com
[5] Astronomical Institute, Charles University Prague, Faculty of Mathematics and Physics, V Holešovičkách 2, Praha 8, CZ-180 00, Czech Republic.
Received 2016 January 11; revised 2016 October 26; accepted 2016 October 26; published 2016 December 21

ABSTRACT

Twin-peak quasi-periodic oscillations (QPOs) are observed in the X-ray power-density spectra of several accreting low-mass neutron star (NS) binaries. In our previous work we have considered several QPO models. We have identified and explored mass–angular-momentum relations implied by individual QPO models for the atoll source 4U 1636-53. In this paper we extend our study and confront QPO models with various NS equations of state (EoS). We start with simplified calculations assuming Kerr background geometry and then present results of detailed calculations considering the influence of NS quadrupole moment (related to rotationally induced NS oblateness) assuming Hartle–Thorne spacetimes. We show that the application of concrete EoS together with a particular QPO model yields a specific mass–angular-momentum relation. However, we demonstrate that the degeneracy in mass and angular momentum can be removed when the NS spin frequency inferred from the X-ray burst observations is considered. We inspect a large set of EoS and discuss their compatibility with the considered QPO models. We conclude that when the NS spin frequency in 4U 1636-53 is close to 580 Hz, we can exclude 51 of the 90 considered combinations of EoS and QPO models. We also discuss additional restrictions that may exclude even more combinations. Namely, 13 EOS are compatible with the observed twin-peak QPOs and the relativistic precession model. However, when considering the low-frequency QPOs and Lense–Thirring precession, only 5 EOS are compatible with the model.

Key words: accretion, accretion disks – equation of state – stars: neutron – X-rays: binaries

1. INTRODUCTION

Accreting neutron stars (NS) are believed to be the compact component in more than 20 low-mass X-ray binaries (LMXBs). In these systems, the mass is transferred from the companion by overflowing the Roche lobe and forming an accretion disk that surrounds the NS. The disk contributes significantly to the high X-ray luminosity of these objects, while most of the radiation comes from its inner parts and the disk–NS boundary layer. According to their X-ray spectral and timing properties, the NS LMXBs have been further classified into Z and atoll sources, whose names have been inspired by the shapes of the tracks they trace in the color–color diagram (e.g., van der Klis 2005). While the Z sources are generally more stable and brighter, the atoll sources are weaker and show significant changes in the X-ray luminosity. Both classes exhibit a variability over a wide range of frequencies. Except for irregular changes, their power spectra also contain relatively coherent features known as quasi-periodic oscillations (QPOs).

The so-called low-frequency QPOs have frequencies in the range of 1–100 Hz. In the case of Z sources they have been further classified into horizontal, flaring, and normal branch oscillations (HBO, FBO, and NBO, respectively) depending on the position of the source in the color–color diagram. Oscillations of properties similar to HBOs have also been observed in several atoll sources (see van der Klis 2006, p. 39, for a review). Much attention among theoreticians is attracted to the kilohertz QPOs (100–1000 Hz), however, because their high frequencies are comparable to the orbital timescale in the vicinity of a NS. It is believed that this coincidence represents a strong indication that the corresponding signal originates in the innermost parts of the accretion disks or close to the surface of the NS itself. This belief has also been supported by means of the Fourier-resolved spectroscopy (e.g., Gilfanov et al. 2000).

The kHz QPOs have similar properties in both Z and atoll sources. They are frequently observed in pairs and are often called twin-peak QPOs. Their "upper" and "lower" QPO frequencies (ν_U and ν_L, respectively) exhibit a strong and remarkably stable positive correlation and clustering around the rational ratios. These ratios are emphasized either by the intrinsic source clustering, or by a weakness of the two QPOs outside the limited frequency range (suggesting a possible resonant energy exchange between two physical oscillators, Abramowicz et al. 2003a; Belloni et al. 2005, 2007; Barret & Boutelier 2008; Török et al. 2008a, 2008b, 2008c; Horák et al. 2009; Boutelier et al. 2010). Other properties of each oscillation (e.g., the rms-amplitude and the quality factor) seem to mostly depend on its frequency, and the way in which they vary is different for the upper and lower oscillation. These differences often help to identify the type of kHz QPO in cases when only one peak is present in the power spectra (Barret et al. 2005, 2006; Méndez 2006; Török 2009).

Many models have been proposed to explain the rich phenomenology of twin-peak QPOs (Alpar & Shaham 1985; Lamb et al. 1985; Miller et al. 1998; Psaltis et al. 1999;

Table 1
Models Examined in this Work

Model	Relations	ν_L–ν_U Relation
RP	$\nu_L = \nu_K - \nu_r$,	$\nu_L = \nu_U\left\{1 - \left[1 + \frac{8j\nu_U}{\mathcal{F}-j\nu_U} - 6\left(\frac{\nu_U}{\mathcal{F}-j\nu_U}\right)^{2/3} - 3j^2\left(\frac{\nu_U}{\mathcal{F}-j\nu_U}\right)^{4/3}\right]^{1/2}\right\}$
	$\nu_U = \nu_K$	
TD	$\nu_L = \nu_K$,	$\nu_U = \nu_L\left\{1 + \left[1 + \frac{8j\nu_L}{\mathcal{F}-j\nu_L} - 6\left(\frac{\nu_L}{\mathcal{F}-j\nu_L}\right)^{2/3} - 3j^2\left(\frac{\nu_L}{\mathcal{F}-j\nu_L}\right)^{4/3}\right]^{1/2}\right\}$
	$\nu_U = \nu_K + \nu_r$	
WD	$\nu_L = 2(\nu_K - \nu_r)$,	$\nu_U = 2\nu_K - \nu_r$
RP1	$\nu_L = \nu_K - \nu_r$,	$\nu_U = \nu_\theta$
RP2	$\nu_L = \nu_K - \nu_r$,	$\nu_U = 2\nu_K - \nu_\theta$

Wagoner 1999; Abramowicz & Kluźniak 2001; Kato 2001, 2007, 2008; Kluźniak & Abramowicz 2001; Wagoner et al. 2001; Titarchuk & Wood 2002; Abramowicz et al. 2003b, 2003c; Rezzolla et al. 2003; Kluźniak et al. 2004; Bursa 2005; Pétri 2005; Zhang 2005; Török et al. 2007, 2016; Čadež et al. 2008; Stuchlík et al. 2008; Germanà et al. 2009; Kostić et al. 2009; Mukhopadhyay 2009; Stuchlík et al. 2013, 2014, 2015; Wang et al. 2015, and several others). While any acceptable model should address both the excitation mechanism and subsequent modulation of the resulting X-ray signal as well as their overall observational properties, most of the theoretical effort has so far been devoted to the observed frequencies. Clearly, their correlations serve as a first test of the model viability.

1.1. Aims and Scope of this Paper

Comparison between the observed and the expected frequencies can reveal the mass and angular momentum of the NS. These can be confronted with models of rotating NS based on a modern equation of state (EoS, e.g., Urbanec et al. 2010b). In Török et al. (2012) we have identified and explored mass–angular-momentum relations implied in Kerr spacetimes by individual QPO models. We have also discussed that the degeneracy in mass and angular momentum can be removed when the NS spin frequency is known.

Here we extend our study and confront QPO models with a large set of NS EoS while focusing on the influence of NS quadrupole moment that is related to its rotationally induced oblateness. The paper is arranged as follows. In Section 2 we very briefly recall individual QPO models that we consider together with previously obtained results. We present here the completed simplified calculations that assume Kerr background geometry and the atoll source 4U 1636-53. These follow previous comparison between predictions of the relativistic precession (RP) model and 5 EoS. The consideration is extended to other models and a large set of 18 EoS. Sections 3.1 and 4 bring detailed consequent calculations of RP model predictions considering the influence of the NS quadrupole moment within Hartle–Thorne spacetimes. We show here that the application of concrete Sly 4 EoS within the model in Hartle–Thorne spacetime brings a specific mass-spin relation. This relation is confronted with the NS spin frequency inferred from the X-ray burst observations. In Section 5 we present analogical results for the whole set of 5 QPO models and 18 EoS and outline their implications. We also discuss here the implications of the consideration of low-frequency QPOs.

2. TWIN-PEAK QPO MODELS APPROXIMATED IN KERR SPACETIMES

Within the framework of many QPO models, the observable frequencies can be expressed directly in terms of epicyclic frequencies. Formulae for the geodesic Keplerian and radial and vertical epicyclic frequencies in Kerr spacetimes were first derived by Aliev & Galtsov (1981). In a commonly used form (e.g., Török & Stuchlík 2005) they read

$$\Omega_K = \frac{\mathcal{F}}{j + x^{3/2}}, \quad \nu_r = \Gamma\Omega_K, \quad \nu_\theta = \Delta\Omega_K, \tag{1}$$

where

$$\Gamma = \sqrt{\frac{-3j^2 + 8j\sqrt{x} + (-6 + x)x}{x^2}},$$
$$\Delta = \sqrt{1 + \frac{j(3j - 4\sqrt{x})}{x^2}}, \tag{2}$$

$x \equiv r/M$, and the "relativistic factor" $\mathcal{F}$ reads $\mathcal{F} \equiv c^3/(2\pi GM)$. We note that Kerr geometry represents an applicable approximation of NS spacetimes when the mass of the compact object is high (Török et al. 2010; Urbanec et al. 2013).

The above formulae are valid for Kerr spacetimes and describe (epicyclic) slightly perturbed circular geodesic motion well. This description of epicyclic motion of test particles that is relevant to standard thin accretion disks may also well approximate epicyclic motion in fluid accretion flow provided that the pressure effects in the fluid are negligible and linear quasi-incompressible modes are considered. Formulae for geodesic epicyclic oscillations are often assumed within several QPO models based on accretion disk hot-spot as well as global fluid motion (e.g., Stella & Vietri 1999, 2001; Abramowicz & Kluźniak 2001; Kluźniak & Abramowicz 2002). Here we investigate a subset of models that have previously been considered in the study of Török et al. (2012).

2.1. Individual Models of QPOs and their Predictions

The RP model explains the kHz QPOs as a direct manifestation of modes of relativistic epicyclic motion of blobs at various radii r in the inner parts of the accretion disk (Stella & Vietri 1999). For the RP model, one can easily solve relations defining the upper and lower QPO frequencies in terms of the orbital frequencies and arrive at an explicit formula that relates the upper and lower QPO frequencies in units of

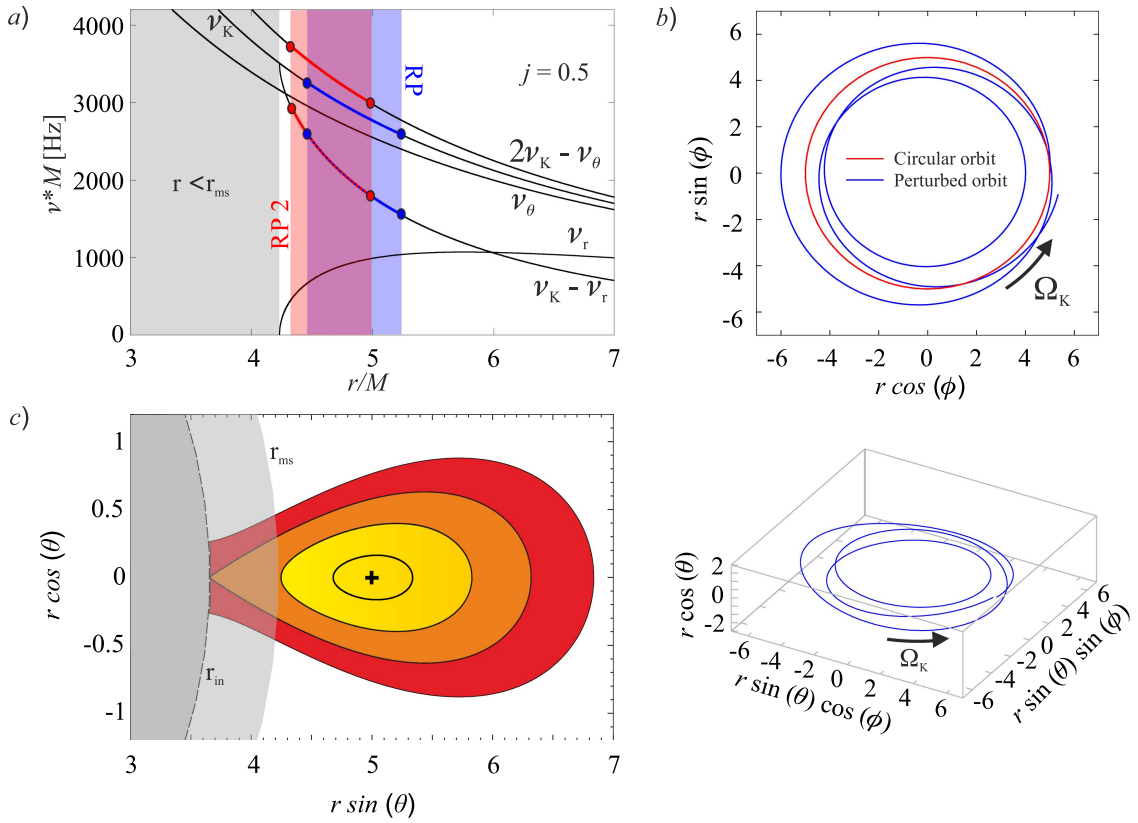

Figure 1. Frequencies of orbital motion and illustration of models of QPOs in the atoll source 4U 1636-53. (a) Behavior of characteristic orbital frequencies in Kerr spacetimes. The blue area denotes a radial region associated with the RP model, i.e., the region where orbital and periastron precession frequencies can be identified with the frequencies observed in the atoll source 4U 1636-53. The red area denotes the same, but for the RP2 model frequencies. The gray area corresponds to the region below the marginally stable circular orbit, $r < r_{ms}$. (b) Example of a free test particle trajectory and its projection onto the equatorial plane. The figure corresponds to the situation drawn in panel (a) and the RP model ($r = 5\,M$). The red circle indicates an unperturbed circular trajectory. (c) Equipotencial surfaces determining the shape of the torus located at $r = 5\,M$ drawn for different values of torus thickness β. The slender torus limit ($\beta = 0$) is denoted by the black cross. In this limit, and when the RP2 model is assumed, the torus oscillates with frequencies $\nu_K(r) - \nu_r(r)$ and $2\nu_K(r) - \nu_\theta(r)$. In the limit of $j = 0$, these frequencies coincide with the RP model frequencies $\nu_K(r) - \nu_r(r)$ and $\nu_K(r)$. Although the two models predict the same frequencies in the limit of non-rotating NS, the associated physical mechanisms are not the same.

Hertz (Török et al. 2010). We show this relation in Table 1. The concept of the tidal disruption (TD) model is similar to the RP model, but the QPOs are atributed to a disruption of large accreting inhomogenities (Germanà et al. 2009). The explicit relation between the two observed QPO frequencies can be evaluated in a way similar to the case of the RP model (Török et al. 2012), and we also include this relation in Table 1.

While the former two models assume motion of a hot-spot propagating within the accretion disk, the warp disk (WD) model assumes non-axisymmetric oscillation modes in a thick disk (Kato 2001). The two other considered models, RP1 and RP2, also deal with non-axisymmetric disk-oscillation modes. The frequencies of these modes coincide with the frequencies predicted by the RP model in the limit of $j = 0$ (Bursa 2005; Török et al. 2010). Although the relevant frequencies coincide in the case of non-rotating NS, they correspond to a different physical situation (see Figure 1 for an illustration). We include the expressions for lower and upper QPO frequency for all the three disk-oscillation models in Table 1.

Török et al. (2010, 2012) assumed a high-mass (Kerr) approximation of NS spacetimes and relations from Table 1. We have demonstrated that for each twin-peak QPO model and a given source, the model consideration results in a specific relation between the NS mass M and angular momentum j rather than in their single preferred combination. We payed special attention to the atoll source 4U 1636-53 and evaluated mass–angular-momentum relations for all discussed QPO models.[6]

2.2. Twin-Peak QPO Models versus NS EoS

Török et al. (2012) compared a χ^2 map describing the quality of the RP model fit of the 4U 1636-53 data to the $M - j$ relations implied by five specific NS EoS. These $M - j$ relations were calculated assuming that the NS spin frequency ν_S is 580 Hz (Strohmayer & Markwardt 2002; Galloway et al. 2008; Watts 2012). In these calculations we used the approach

[6] Lin et al. (2011) have performed a similar analysis assuming a different set of twin-peak QPO frequency data points for the atoll source 4U 1636-53. The data points in their study have been obtained via common processing of a large amount of data, while the data points used by Török et al. (2012) correspond to individual continuous observations of the source. It was shown in Török et al. (2012) that the results of the two studies are consistent (see also the NS parameteres resulting within the two studies denoted in Figure 2 and in Török et al. 2016).

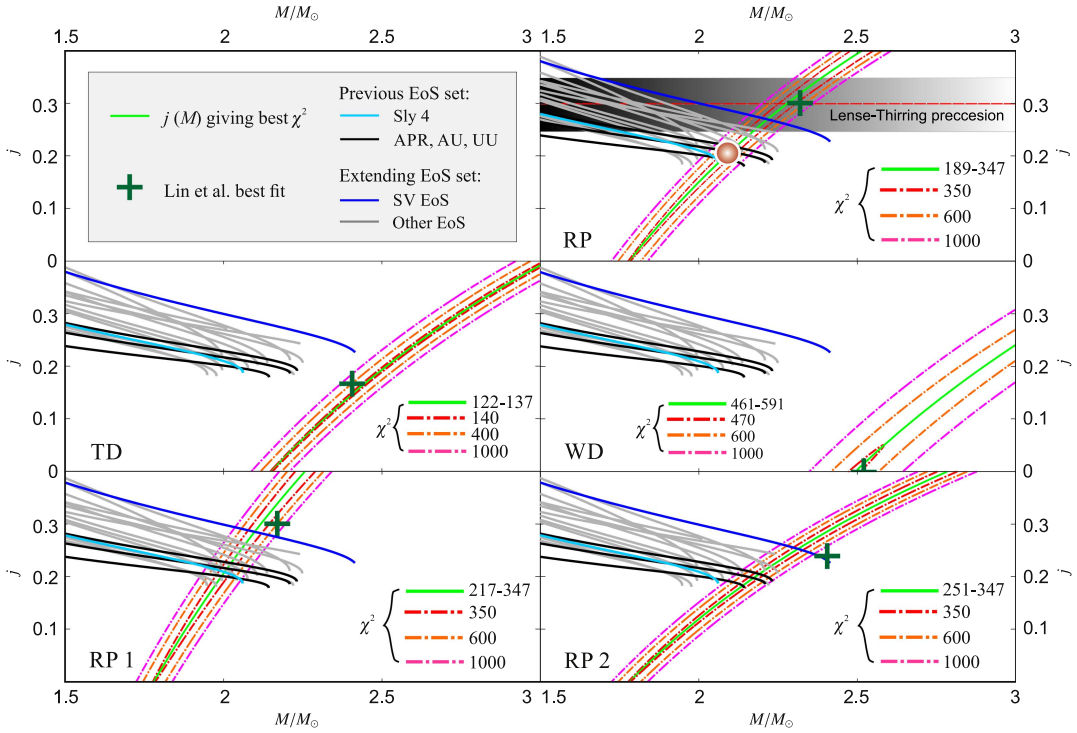

Figure 2. χ^2 maps (20d.o.f.) calculated from data of the atoll source 4U 1636-53 and individual QPO models within Kerr spacetimes vs. mass–angular-momentum relations predicted by NS EoS. For the calculations we consider 14 more EOS in addition to 4 EoS (SLy 4, APR, AU-WFF1, and UU-WFF2) assumed in Török et al. (2012). The full set of 18 EoS is listed in Table 2. In each panel the green line indicates the best χ^2 for a fixed M, while the dashed green line denotes its quadratic approximation. The white lines indicate the corresponding 1σ and 2σ confidence levels. The NS EoS are assumed for the rotational frequency of 580 Hz inferred from the X-ray burst observations. The green crosses denote the mass and angular momentum combinations reported for 4U 1636-53 and individual QPO models by Lin et al. (2011). The red spot roughly indicates the combination of mass and spin inferred from the common consideration of the RP model, NS spin frequency of 580 Hz, and 4 EoS as discussed by Török et al. (2012). The horizontal dashed red line together with the horizontal shaded bar indicate additional restrictions on the RP model that follow from consideration of Lense–Thirring precession, as discussed in Török et al. (2012).

of Hartle (1967), Hartle & Thorne (1968), Chandrasekhar & Miller (1974), Miller (1977), and Urbanec et al. (2010a).

In the top panel of Figure 2 we show a comparison between predictions of the RP model and 4 EoS carried out in Török et al. (2012). We note that the choice of concrete EoS used within that paper was motivated by low values of a scaled quadrupole moment $\tilde{q} \equiv q/j^2$ of the assumed NS configurations.[7] Although QPO model predictions are drawn for simplified calculations assuming Kerr background geometry, in following we do not restrict ourselves to high-mass (compactness) NS. We thus add 14 more EoS, which are indicated within the figure. The full set of 18 EoS considered hereafter is listed in Table 2. In the other panels of Figure 2 we make the same comparison, but for the other four considered QPO models.

Török et al. (2012) directly compared (a few) EoS and the RP model. Inspecting our overall extended Figure 2, we can expect that QPO models place strong restrictions on NS parameters and EoS, or vice versa. For instance, a direct confrontation of EoS and TD model predictions strongly suggests that the model (favored within the study of Lin et al. 2011) entirely fails to meet the requirements given by the consideration of NS EoS. Moreover, by comparing overlaps between the RP model relation and curves denoting the requirements of individual EoS, other interesting information can be obtained: there is a difference between overlaps considered in Török et al. (2012), which are denoted here by the red spot in Figure 2, and overlaps given by the newly considered EoS. Clearly, the high quadrupole moment of NS configurations related to the latter set of EoS increases the required NS angular momentum. For instance, there is $j \doteq 0.19$ for Sly 4 versus $j \doteq 0.28$ for SV EoS. It is also apparent that this effect can be important for the consideration of Lense–Thirring precession and low-frequency QPOs within the framework of the RP model.

Motivated by these findings, below we explore restrictions on QPO models in detail and perform consistent calculations in Hartle–Thorne spacetimes.

3. CALCULATIONS IN HARTLE–THORNE SPACETIMES

So far, we have considered only a Kerr approximation of the rotating NS spacetime assuming that the star is very compact. In this case the NS quadrupole moment q related to its rotationally induced oblateness reaches low values, and we have $\tilde{q} \approx 1$. In a more general case of $\tilde{q} > 1$, one should

[7] Török et al. (2012) also assumed one more EOS (WS, Wiringa et al. 1988; Stergioulas & Friedman 1995). We do not consider this EOS here since it does not fulfill the requirements of the current observational tests.

Table 2
EoS Examined in this Work

EoS	$M_{\max}$	R (km)	n_c ($[fm]^{-3}$)	References
Sly 4	2.04	9.96	1.21	1
SkI5	2.18	11.3	0.97	1
SV	2.38*	11.9	0.80	1
SkO	1.97	10.3	1.19	1
Gs	2.08	10.8	1.07	1
SkI2	2.11	11.0	1.03	1
SGI	2.22	10.9	1.01	1
APR	2.21	10.2	1.12	2
AU	2.13	9.39	1.25	3
UU	2.19	9.81	1.16	3
UBS	2.20*	12.1	0.68	4
GLENDNH3	1.96	11.4	1.05	5
Gandolfi	2.20	9.82	1.16	6
QMC700	1.95	12.6	0.61	7
KDE0v1	1.96	9.72	1.29	8
NRAPR	1.93	9.85	1.29	9
PNM L80	2.02	10.4	1.16	10
J35 L80	2.05	10.5	1.14	10

Note. The individual columns indicate the maximum mass and corresponding radius, and the central baryon number density for each EoS along with the relevant references. The asterisks mark three EoS whose maximum mass corresponds to the maximum density allowed by the available EoS table, and not to a marginally stable star.

References. (1) Rikovska Stone et al. (2003), (2) Akmal et al. (1998), (3) Wiringa et al. (1988), (4) Urbanec et al. (2010a), (5) Glendenning (1985), (6) Gandolfi et al. (2010), (7) Rikovska Stone et al. (2007), (8) Agrawal et al. (2005), (9) Steiner et al. (2005), (10) Newton et al. (2013).

assume NS spacetime approximated by the Hartle–Thorne geometry (Hartle 1967; Hartle & Thorne 1968).[8]

Based on the Hartle–Thorne approximation, the Keplerian orbital frequency can be expressed as (Abramowicz et al. 2003a)

$$\Omega_K = \frac{\mathcal{F}}{x^{3/2}}\left[1 - \frac{j}{x^{3/2}} + j^2 F_1(x) + qF_2(x)\right], \quad (3)$$

where

$$F_1(x) = [48 - 80x + 4x^2 - 18x^3 + 40x^4 + 10x^5 + 15x^6 - 15x^7](16(x-2)x^4)^{-1} + A(x),$$
$$F_2(x) = \frac{5(6 - 8x - 2x^2 - 3x^3 + 3x^4)}{16(x-2)x} - A(x),$$
$$A(x) = \frac{15(x^3-2)}{32}\ln\left(\frac{x}{x-2}\right).$$

The radial and vertical epicyclic frequencies are then described by the following terms

$$\nu_r^2 = \frac{\mathcal{F}^2(x-6)}{x^4}[1 + jH_1(x) - j^2 H_2(x) - qH_3(x)], \quad (4)$$

$$\nu_\theta^2 = \frac{\mathcal{F}^2}{x^3}[1 - jG_1(x) + j^2 G_2(x) + qG_3(x)], \quad (5)$$

where

$$H_1(x) = \frac{6(x+2)}{x^{3/2}(x-6)},$$
$$H_2(x) = [8x^4(x-2)(x-6)]^{-1}[384 - 720x - 112x^2 - 76x^3 - 138x^4 - 130x^5 + 635x^6 - 375x^7 + 60x^8] + C(x),$$
$$H_3(x) = \frac{5(48 + 30x + 26x^2 - 127x^3 + 75x^4 - 12x^5)}{8x(x-2)(x-6)} - C(x),$$
$$C(x) = \frac{15x(x-2)(2 + 13x - 4x^2)}{16(x-6)}\ln\left(\frac{x}{x-2}\right),$$
$$G_1(x) = \frac{6}{x^{3/2}},$$
$$G_2(x) = [8x^4(x-2)]^{-1}[48 - 224x + 28x^2 + 6x^3 - 170x^4 + 295x^5 - 165x^6 + 30x^7] - B(x),$$
$$G_3(x) = \frac{5(6 + 34x - 59x^2 + 33x^3 - 6x^4)}{8x(x-2)} + B(x),$$
$$B(x) = \frac{15(2x-1)(x-2)^2}{16}\ln\left(\frac{x}{x-2}\right).$$

3.1. Results for the RP Model

Assuming the above formulae, we have calculated 3D-χ^2 maps for the RP model. In the left panel of Figure 3 we show the behavior of the best χ^2 as a function of M and j for several color-coded values of $\tilde{q}$. For each value of $\tilde{q}$ there is a preferred $M - j$ relation. We find that, although such a relation has a global minimum, the gradient of χ^2 along the relation is always much lower than the gradient in the perpendicular direction. In other words, χ^2 maps for a fixed $\tilde{q}$ are of the same type as the maps calculated in the Kerr spacetime. It then follows that there is a global $M - j - \tilde{q}$ degeneracy in the sense discussed by Török et al. (2012); see their Figure 3.

As emphasized by Urbanec et al. (2010b), Török et al. (2010), Kluźniak & Rosińska (2013), Török et al. (2014), Rosińska et al. (2014), and Boshkayev et al. (2015), Newtonian effects following from the influence of the quadrupole moment act on the orbital frequencies in a way opposite to that which is related to relativistic effects following from the increase of the angular momentum. The behavior of the relations shown in the left panel of Figure 3 is determined by this interplay. Because of this, we can see that the increased NS quadrupole moment can compensate for the increase in estimated mass given by a high angular momentum.

4. CONSIDERATION OF NS MODELS GIVEN BY CONCRETE EOS

The relations for the RP model drawn in the left panel of Figure 3 result from fitting of the 4U 1636-53 data points considering the general Hartle–Thorne spacetime. The consideration does not include strong restrictions on spacetime properties following from NS modeling based on present EoS. It can be shown that a concrete NS EoS covers only a 2D

[8] The adopted approximation represents a convenient alternative to a (more precise) numerical approach (discussed in the same context by Stella et al. 1999) or other spacetime descriptions (e.g., Manko et al. 2000; Stute & Camenzind 2002; Pappas 2015), see also Bonazzola et al. (1993, 1998), Stergioulas & Friedman (1995), Nozawa et al. (1998), Ansorg et al. (2003), and Berti et al. (2005).

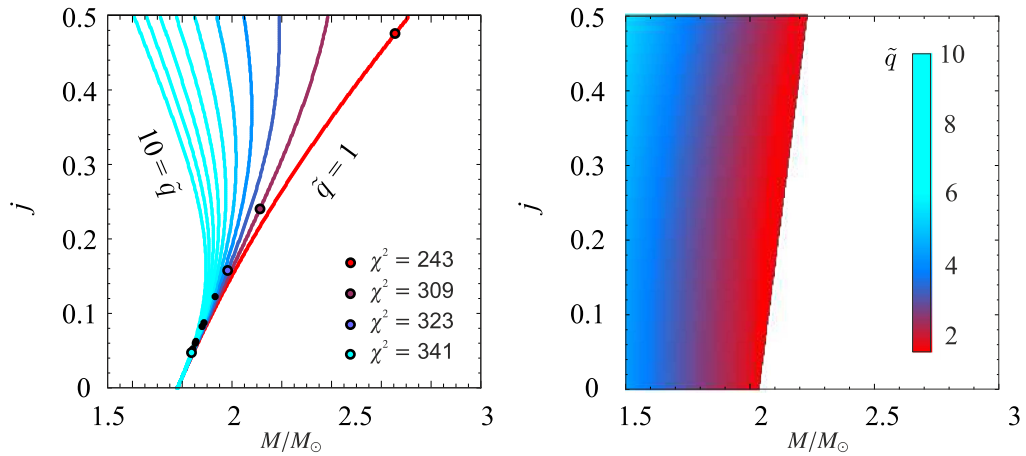

Figure 3. Left: behavior of the best χ^2 as a function of M and j for several values of $\tilde{q}$. The dots denote global minima for each value of $\tilde{q}$ (see, however, the main text, Section 3.1, for a comment on this). Right: the 2D surface in the 3D $M - j - \tilde{q}$ space given by the SLy 4 EoS.

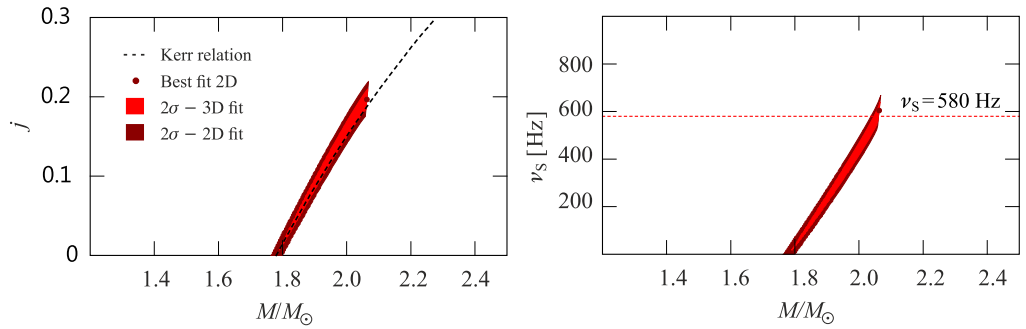

Figure 4. Left: the final $M - j$ map implied by the RP model and the Sly 4 EoS. The light color area denotes an intersection between the 2D surface given by the Sly 4 EoS and 3D volume corresponding to the 2σ confidence level given by the RP best-fit model found in the intervals of $M \in [1M_\odot, 4M_\odot]$, $j \in [0.0, 0.5]$, and $\tilde{q} \in [1, 10]$. The χ^2 minimum of 303/20d.o.f. at the 2D surface is denoted by the dark marker. The dark color area denotes the 2σ confidence level calculated when this local minimum is assumed as a global minimum, provided that the QPO frequency error bars are underestimated by a corresponding factor $\xi_{2D} = 3.9$. We can see that in this particular case, there is almost no difference between the two areas. The dashed curve indicates the $M - j$ relation obtained from the simplified consideration of Kerr spacetimes (see Section 2). Right: the same map, but drawn for the NS spin frequency ν_S. The horizontal dashed red line denotes the spin frequency measured from the X-ray bursts (i.e., $\nu_S = 580$ Hz). The minimum of χ^2 for the spin $\nu_S = 580$ Hz corresponds to $\chi^2 = 305/21$d.o.f.

surface in the 3D $M - j - \tilde{q}$ space since the quadrupole moment is determined by rotationally induced NS oblateness. Thus, when a given EoS is assumed, only the corresponding 2D surface is relevant for fitting data points by a given QPO model. Following Urbanec et al. (2013), we illustrate such a surface in the right panel of Figure 3 for the SLy 4 EoS. The color-coding of the plot is the same as the one in the left panel of the same figure.

The final $M - j$ map for the RP model and Sly 4 EoS, i.e., the values of M and j implied by the common consideration of the two panels of Figure 3, is shown in the left panel of Figure 4. The right panel of this figure then shows an equivalent map drawn for the NS mass and spin frequency ν_S.

4.1. NS Mass Inferred Assuming X-Ray Burst Measurements

The left panel of Figure 4 shows that the concrete EoS, SLy 4, considered for the RP model implies a clear $M - j$ relation. This relation exhibits only a shallow χ^2 minimum. The right panel of the same figure shows the equivalent relation between the NS mass and the spin frequency as well as its shallow minimum. Taking into account the spin frequency inferred from the X-ray bursts, 580 Hz, we can find from Figure 4 that the NS mass and angular momentum have to take values of

$$M = (2.06 \pm 0.01)M_\odot, \quad j \doteq 0.2. \tag{6}$$

These values are in a good agreement with those inferred from the simplified consideration using Kerr spacetimes (see Figure 2). Considering the shallow χ^2 minima denoted in Figure 4, it may be interesting that its frequency value almost coincides with the measured spin frequency of 580 Hz.

5. DISCUSSION AND CONCLUSIONS

In addition to the Sly 4 EoS, we have investigated a wide set of 17 other EoS that are based on different theoretical models. All these EoS are listed in Table 2, where we show the maximum NS mass allowed by each EoS as well as the corresponding NS radius and the central number density. All these EoS are compatible with the highest observed NS masses

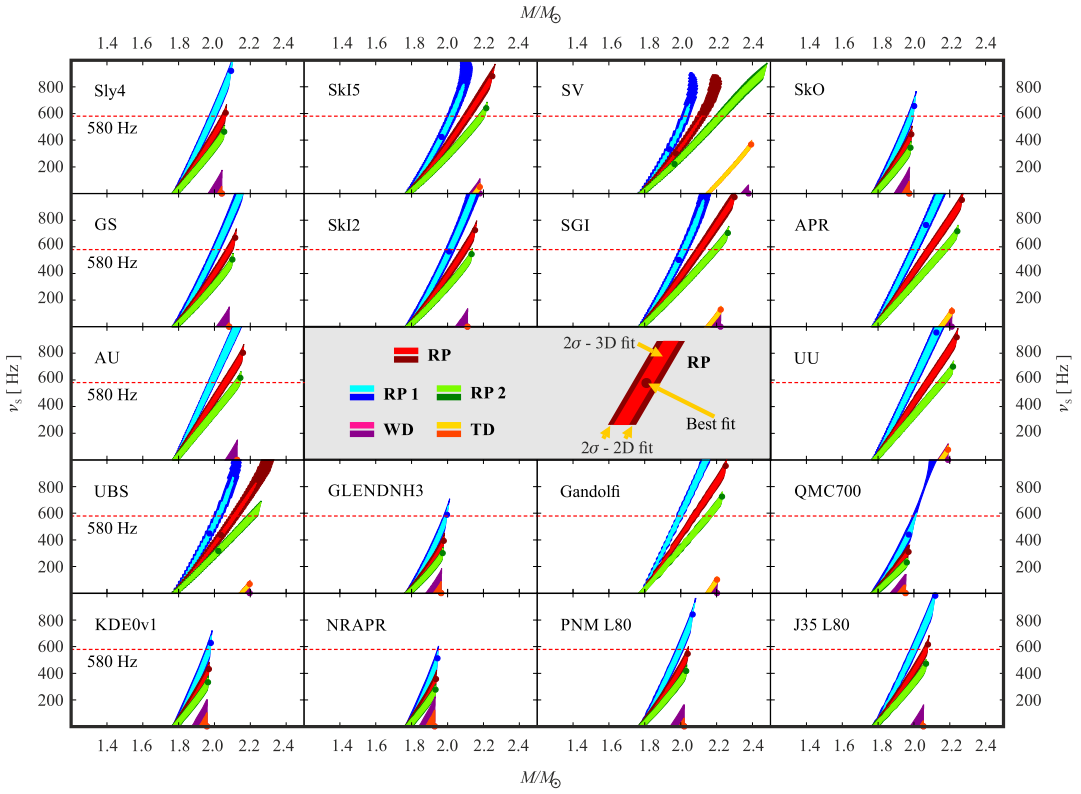

Figure 5. Mass-spin maps for the considered QPO models and 18 different EoS. The light color area denotes an intersection between the 2D surface given by the EoS and 3D volume corresponding to 2σ confidence level associated to the best fit for a given model and the intervals of $M \in [1M_\odot, 4M_\odot]$, $j \in [0.0, 0.5]$, and $\tilde{q} \in [1, 10]$. The χ^2 minimum at the 2D surface is denoted by the dark marker. The dark color area denotes the 2σ confidence level calculated when this local minimum is assumed as a global one providing that the QPO frequency error bars are underestimated by a corresponding factor ξ_{2D}. The horizontal dashed red lines denote spin frequency measured from the X-ray bursts (i.e., $\nu_S = 580$ Hz).

(see, e.g., Klähn et al. (2006), Steiner et al. (2010, 2015), Klähn et al. (2007), Dutra et al. (2012), and Dutra et al. (2014) for various tests of EoS and their applications, and Demorest et al. (2010) and Antoniadis et al. (2013) for the highest observed NS masses).

In Figure 5 we show several relations between the mass and spin frequency obtained for the RP model and our large set of EoS. These relations are similar to those implied by the Sly 4 EoS discussed above. However, we can see that in several cases, a given EoS does not provide any match for the NS spin of 580 Hz. This can rule out the combination of the considered RP model and given specific EoS. The selection effect comes from the correlation between the estimated mass and angular momentum and the limits on maximal mass allowed by the individual EoS.

5.1. Selecting Combinations of QPO Models and EoS

We also found an analogical selection effect for the other four examined QPO models. The corresponding $M - j$ maps are shown in Figure 5. The results for all considered models are summarized in Table 3. The table shows which of the models and EoS are compatible, and which of them are not. Overall, there are 39 matches from the 90 investigated cases for the NS spin frequency of 580 Hz. We can therefore conclude that for the NS spin frequency in 4U 1636-53 to be close to 580 Hz, we can exclude 51 of the 90 considered combinations of EoS and QPO models. This result follows from the requirement of the relatively high masses implied by the individual QPO models and from the increase in these masses with the NS spin.

5.2. Implications for QPO Models

When we assume that the Hartle–Thorne geometry is restricted to the range of angular momentum and scaled quadrupole moment $\{j, \tilde{q}\} \in \{[0, 0.4], [1, 10]\}$, the four investigated QPO models imply a relatively broad range of NS mass, $M \in [1.6, 3.4]\, M_\odot$ ($M \in [1.8, 2.5]\, M_\odot$ when $j = 0$). In Figure 6 we illustrate a corresponding comparison between the data and some individual fits. From inspecting Figure 6, we can see that the quality of the fits is rather poor (represented by $\chi^2/\text{d.o.f.} \sim 10$, see Table 3). The comparison between data and curves drawn for the RP model indicates the possible presence of systematic errors within the model. This also holds for the RP1, RP2, and WD model. The trend is somewhat better only in the case of the TD model. This has also been noted by Lin et al. (2011). However, when we take into account requirements given by present EoS and the NS spin of 580 Hz, the TD model is ruled out (see the green curve in the bottom right panel of Figure 6). The range of NS mass that corresponds to the considered models is then reduced to $M \in [2.0, 2.2]\, M_\odot$.

Remarkably, the consideration of Hartle–Thorne spacetime does not improve the quality of the fits. For instance, the deviation of the RP model curve from the data discussed by Lin

Table 3
Results for the Considered EoS and QPO Models

	RP Model			RP1 Model			RP2 Model		
	$\xi_{H+T} = 3.6$, $\xi_{\rm Kerr} = 3.1$			$\xi_{H+T} = 3.6$, $\xi_{\rm Kerr}$=3.3			$\xi_{H+T} = 3.9$, $\xi_{\rm Kerr} = 3.5$		
EoS	M	j	$\chi^2_{\rm min}$	M	j	$\chi^2_{\rm min}$	M	j	$\chi^2_{\rm min}$
SLy 4	2.06 ± 0.01	0.19	305	1.99 ± 0.02	0.21	302	X	X	X
SkI5	2.11 ± 0.01	0.25	323	2.02 ± 0.01	0.27	321	2.19 ± 0.02	0.23	327
SV	2.12 ± 0.01	0.28	345	2.03 ± 0.01	0.30	334	2.22 ± 0.02	0.27	355
SkO	X	X	X	1.98 ± 0.01	0.20	302	X	X	X
Gs	2.08 ± 0.01	0.22	309	2.01 ± 0.02	0.24	307	X	X	X
SkI2	2.10 ± 0.01	0.23	313	2.01 ± 0.02	0.25	311	2.14 ± 0.01	0.21	395
SGI	2.11 ± 0.01	0.25	319	2.02 ± 0.02	0.26	314	2.19 ± 0.02	0.23	328
APR	2.09 ± 0.01	0.22	309	2.00 ± 0.02	0.23	304	2.17 ± 0.02	0.21	320
AU	2.06 ± 0.01	0.20	305	1.98 ± 0.02	0.20	301	2.13 ± 0.02	0.19	315
UU	2.08 ± 0.01	0.21	306	1.99 ± 0.02	0.22	302	2.16 ± 0.02	0.20	317
UBS	2.11 ± 0.01	0.26	325	2.02 ± 0.01	0.27	317	2.21 ± 0.02	0.25	338
GLENDNH3	X	X	X	2.00 ± 0.01	0.22	303	X	X	X
Gandolfi	2.08 ± 0.01	0.21	307	1.99 ± 0.01	0.22	303	2.15 ± 0.02	0.20	318
QMC700	X	X	X	2.01 ± 0.01	0.27	332	X	X	X
KDE0v1	X	X	X	1.97 ± 0.01	0.19	301	X	X	X
NRAPR	X	X	X	$1.95 \pm 0.01^*$	0.18^*	7196	X	X	X
PNM L80	2.04 ± 0.01	0.19	340	2.00 ± 0.01	0.22	303	X	X	X
J35 L80	2.07 ± 0.01	0.21	306	2.00 ± 0.01	0.23	304	X	X	X

Note. Values of $\xi = \sqrt{\chi^2_{\rm min}/{\rm dof}}$ corresponding to global minima of $\chi^2_{\rm min}$ in Hartle–Thorne spacetime are compared to values obtained for Kerr spacetimes in Török et al. (2012). Asterisks denote that the indicated values of M and j are connected to the dark color area in Figures 4 and 5. In this case there is no intersection between the spin frequency curve in the 2D EoS plane and the 2σ level 3D volume around the global minima of the QPO model fit in the Hartle–Thorne spacetime. The local minimum, $\chi^2_{\rm 2Dmin}$, at the 2D EoS plane is then assumed as a global minimum provided that the QPO frequency error bars are underestimated by a corresponding factor, $\xi_{\rm 2D} = \sqrt{\chi^2_{\rm 2Dmin}/{\rm dof}}$. The *X*-symbol indicates that the spin frequency 580 Hz is not reached even in this case. For the TD and WD models, the spin frequency is not reached.

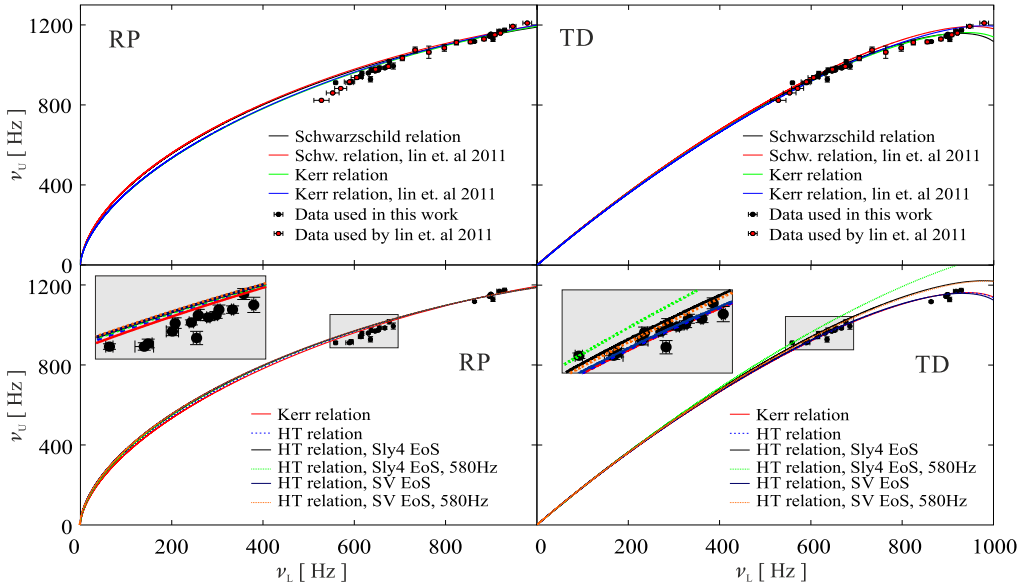

Figure 6. Twin-peak QPO data and examples of their individual fits. Top: best fits of data used in this work (black dots) vs. best fits of data (red dots) used by Lin et al. (2011). Bottom: best fits assuming Kerr spacetime denoted by red lines ($\chi^2_{\rm min,RP} = 189/20$d.o.f., $\chi^2_{\rm min,TD} = 122/20$d.o.f). Best fits in Hartle–Thorne spacetimes are denoted by blue lines ($\chi^2_{\rm min,RP} = 243/19$d.o.f, $\chi^2_{\rm min,TD} = 123/19$d.o.f.). Best fits in Hartle–Thorne spacetimes restricted to the parametric 2D surface given by SLy 4 EoS are denoted by black lines ($\chi^2_{\rm min,RP} = 303/20$d.o.f, $\chi^2_{\rm min,TD} = 2514/20$d.o.f). Best fits in Hartle–Thorne spacetimes restricted to the parametric 2D surface given by SV EoS are denoted by dark blue lines ($\chi^2_{\rm min,RP} = 327/20$d.o.f, $\chi^2_{\rm min,TD} = 129/20$d.o.f). Best fits in Hartle–Thorne spacetimes restricted by SLy 4 Eos and NS spin 580 Hz are denoted by green lines ($\chi^2_{\rm min,RP} = 305/21$d.o.f, $\chi^2_{\rm min,TD} = 15725/21$d.o.f). Best fits in Hartle–Thorne spacetimes restricted by SV EoS and NS spin 580 Hz are denoted by orange lines ($\chi^2_{\rm min,RP} = 344/21$d.o.f, $\chi^2_{\rm min,TD} = 2233/21$d.o.f).

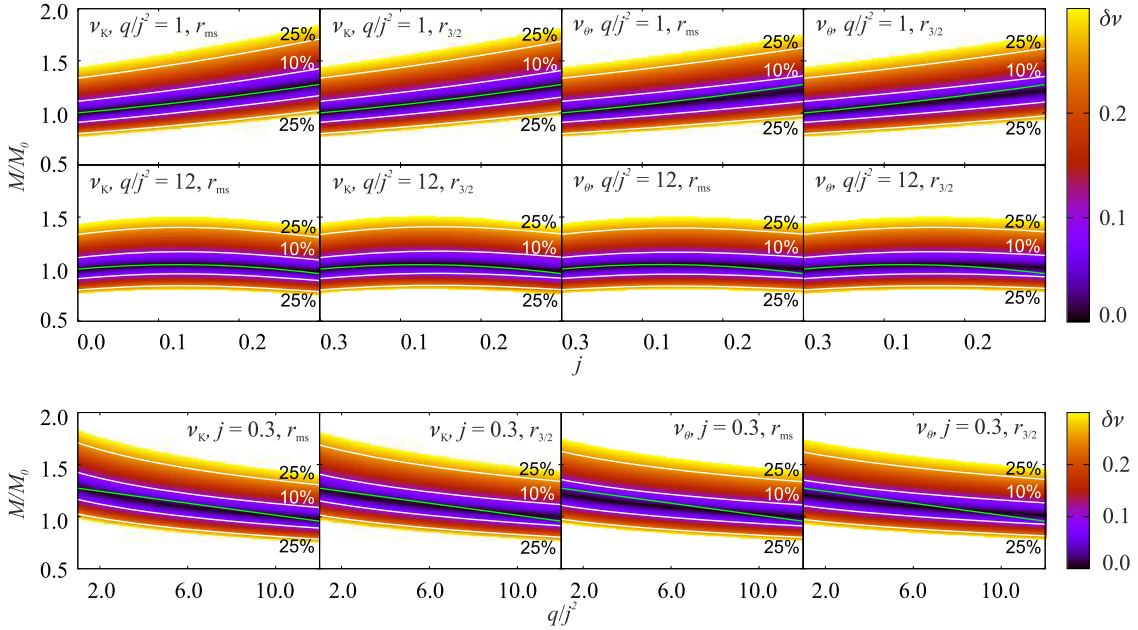

Figure 7. Color-coded maps indicating values of the dimensionless difference between the characteristic frequencies of orbital motion $\delta\nu \equiv (\nu(M_0) - \nu(M, j, q))/\nu(M_0)$ calculated assuming the Schwarzschild spacetimes ($M = M_0$) and Hartle–Thorne spacetimes. Individual panels assume the chosen fixed values of parameters j and $\tilde{q}$. Combinations of parameters indicated by green curves are given by relation (7), $M = M_0(1 + 0.7j + 1.02j^2 - 0.32q)$. Frequencies are calculated at characteristic radii $r_{3:2}$ and r_{ms}, where the Keplerian and periastron precession frequencies are in a 3:2 and 1:1 ratio.

et al. (2011) is present when we assume Hartle–Thorne as well as Kerr spacetime. There is $\Delta\chi \equiv \sum \mathrm{sign}(\chi_i)\chi_i^2 \sim -150$ for the bottom part of the curve ($i \in \{1 \dots 14\}$), while it is $\Delta\chi \sim +20$ for the top part of the curve ($i \in \{15 \dots 22\}$). The possibly required non-geodesic corrections discussed by Török et al. (2012) and Lin et al. (2011) therefore do not depend on the chosen spacetime description (see also Török et al. 2016, in this context). This conclusion is in a good agreement with the suggestion of Török et al. (2012), who implied that the parameters of RP model fits within Hartle–Thorne spacetime should exhibit a degeneracy approximated as

$$M = M_0(1 + 0.7j + 1.02j^2 - 0.32q), \qquad (7)$$

where $M_0 = 1.78M_\odot$ for 4U 1636-53. This degeneracy is illustrated in Figures 7 and 8, where we also quantify its validity for the other models discussed here.

5.3. Consideration of Low-frequency QPOs

Strong restrictions to the model and implied NS mass may be obtained when low-frequency QPOs are considered. This can be clearly illustrated for the RP model, which associates the observed low-frequency QPOs with the Lense–Thirring precession that occurs at the same radii as the periastron precession. Within the framework of the model, the Lense–Thirring frequency ν_{LT} represents a sensitive spin indicator (Stella & Vietri 1998a, 1998b; Morsink & Stella 1999; Stella et al. 1999). In our previous paper (Török et al. 2012) we carried out a simplified estimate of the underlying NS angular momentum and mass assuming Kerr spacetimes, arriving at values of $j \sim 0.25 \div 0.35$ and $M \sim (2.2 \div 2.4)M_\odot$. These values appeared too high when confronted with the

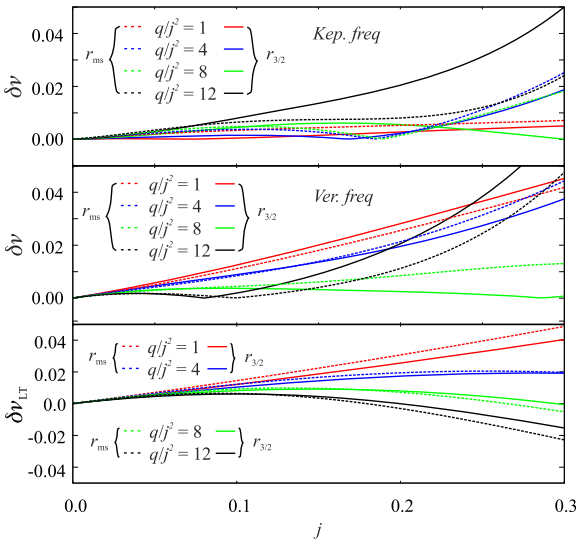

Figure 8. Dimensionless quantity $\delta\nu$ plotted for different values of q/j^2 and relation (7). We do not include panels for radial and periastron precession frequencies here because the values are the same as for the Keplerian frequency.

implications of the set of 5 EoS assumed within the paper. As discussed here in Section 2, the extended set of EoS can be more compatible with the expectations based on the consideration of Lense–Thirring precession. It is straightforward to extend our previous estimate to Hartle–Thorne spacetime and all 18 EoS. The results of such an extension are included in

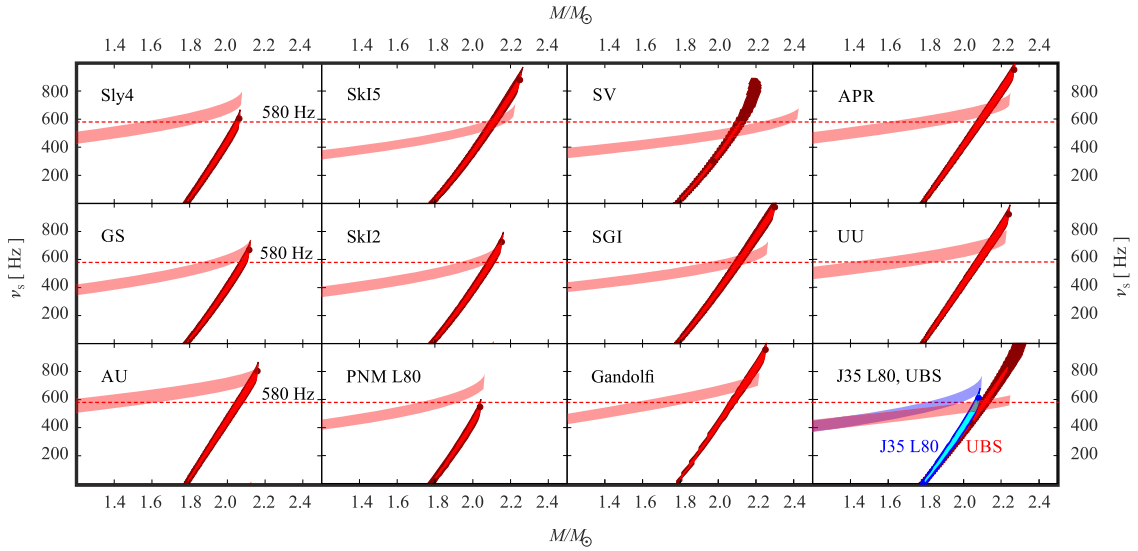

Figure 9. Consideration of RP model assuming both low- and high-frequency QPOs and 13 EoS. The RP model mass-spin maps from Figure 5 are confronted with requirements following from the identification of low-frequency QPOS with the Lense–Thirring precession frequency. The last panel includes the consideration of two different EoS.

Figure 9. We show there 13 EoS that are compatible with the observed twin-peak QPOs and RP model, and demonstrate that 8 of these EoS do not meet the requirements that are based on the consideration of Lense–Thirring precession. Only 5 EoS are therefore compatible with the model.

We would like to acknowledge the Czech grant GAČR 209/12/P740, and internal grants of the Silesian University in Opava, SGS/11,23/2013, SGS/14,15/2016 and IGS/12/2015. Z.S. acknowledges the Albert Einstein Center for Gravitation and Astrophysics supported by the Czech Science Foundation grant No. 14-37086G. We are grateful to Marek Abramowicz, Wlodek Kluzniak (CAMK), John Miller (University of Oxford), Will Newton (Texas A&M University-Commerce), Luigi Stella (INAF), and Jiřina Stone (Oak Ridge National Laboratory) for many useful discussions. We also thank to the anonymous referee for the comments and suggestions that greatly helped us to improve the paper. Furthermore, we would like to acknowledge the hospitality of the University of Oxford and the Astronomical Observatory in Rome. Last but not least, we express our sincere thanks to the concierges of the Mlýnská hotel in Uherské Hradiště for their kind help and participation in organizing frequent workshops of the Silesian university and the Astronomical institute.

REFERENCES

Abramowicz, M. A., Almergren, G. J. E., Kluźniak, W., & Thampan, A. V. 2003a, arXiv:gr-qc/0312070
Abramowicz, M. A., Bulik, T., Bursa, M., & Kluźniak, W. 2003b, A&A, 404, L21
Abramowicz, M. A., Karas, V., Kluźniak, W., Lee, W. H., & Rebusco, P. 2003c, PASJ, 55, 467
Abramowicz, M. A., & Kluźniak, W. 2001, A&A, 374, L19
Agrawal, B. K., Shlomo, S., & Au, V. K. 2005, PhRvC, 72, 014310
Akmal, A., Pandharipande, V. R., & Ravenhall, D. G. 1998, PhRvC, 58, 1804
Aliev, A. N., & Galtsov, D. V. 1981, GReGr, 13, 899
Alpar, M. A., & Shaham, J. 1985, Natur, 316, 239
Ansorg, M., Kleinwächter, A., & Meinel, R. 2003, A&A, 405, 711
Antoniadis, J., Freire, P. C. C., Wex, N., et al. 2013, Sci, 340, 448
Barret, D., & Boutelier, M. 2008, NewAR, 51, 835
Barret, D., Olive, J.-F., & Miller, M. C. 2005, MNRAS, 361, 855
Barret, D., Olive, J.-F., & Miller, M. C. 2006, MNRAS, 370, 1140
Belloni, T., Homan, J., Motta, S., Ratti, E., & Méndez, M. 2007, MNRAS, 379, 247
Belloni, T., Méndez, M., & Homan, J. 2005, A&A, 437, 209
Berti, E., White, F., Maniopoulou, A., & Bruni, M. 2005, MNRAS, 358, 923
Bonazzola, S., Gourgoulhon, E., & Marck, J.-A. 1998, PhRvD, 58, 104020
Bonazzola, S., Gourgoulhon, E., Salgado, M., & Marck, J. A. 1993, A&A, 278, 421
Boshkayev, K., Quevedo, H., Abutalip, M., Kalymova, Z., & Suleymanova, S. 2015, arXiv:1510.02016
Boutelier, M., Barret, D., Lin, Y., & Török, G. 2010, MNRAS, 401, 1290
Bursa, M. 2005, in Proc. RAGtime 6/7, Workshops on Black Holes and Neutron Stars, ed. S. Hledík & Z. Stuchlík (Opava: Silesian Univ.), 39
Čadež, A., Calvani, M., & Kostić, U. 2008, A&A, 487, 527
Chandrasekhar, S., & Miller, J. C. 1974, MNRAS, 167, 63
Demorest, P. B., Pennucci, T., Ransom, S. M., Roberts, M. S. E., & Hessels, J. W. T. 2010, Natur, 467, 1081
Dutra, M., Louren co, O., Avancini, S. S., et al. 2014, PhRvC, 90, 055203
Dutra, M., Louren co, O., Sá Martins, J. S., et al. 2012, PhRvC, 85, 035201
Galloway, D. K., Muno, M. P., Hartman, J. M., Psaltis, D., & Chakrabarty, D. 2008, ApJS, 179, 360
Gandolfi, S., Illarionov, A. Y., Fantoni, S., et al. 2010, MNRAS, 404, L35
Germanà, C., Kostić, U., Čadež, A., & Calvani, M. 2009, in AIP Conf. Ser. 1126, SIMBOL-X: Focusing on the Hard X-Ray Universe, ed. J. Rodriguez & P. Ferrando (Melville, NY: AIP), 367
Gilfanov, M., Churazov, E., & Revnivtsev, M. 2000, MNRAS, 316, 923
Glendenning, N. K. 1985, ApJ, 293, 470
Hartle, J. B. 1967, ApJ, 150, 1005
Hartle, J. B., & Thorne, K. S. 1968, ApJ, 153, 807
Horák, J., Abramowicz, M. A., Kluźniak, W., Rebusco, P., & Török, G. 2009, A&A, 499, 535
Kato, S. 2001, PASJ, 53, 1
Kato, S. 2007, PASJ, 59, 451
Kato, S. 2008, PASJ, 60, 111
Kähn, T., Blaschke, D., Sandin, F., et al. 2007, PhLB, 654, 170
Kähn, T., Blaschke, D., Typel, S., et al. 2006, PhRvC, 74, 035802
Kluźniak, W., & Abramowicz, M. A. 2001, arXiv:astro-ph/0105057
Kluźniak, W., & Abramowicz, M. A. 2002, arXiv:astro-ph/0203314
Kluźniak, W., Abramowicz, M. A., Kato, S., Lee, W. H., & Stergioulas, N. 2004, ApJL, 603, L89

Kluźniak, W., & Rosińska, D. 2013, MNRAS, 434, 2825
Kostić, U., Čadež, A., Calvani, M., & Gomboc, A. 2009, A&A, 496, 307
Lamb, F. K., Shibazaki, N., Alpar, M. A., & Shaham, J. 1985, Natur, 317, 681
Lin, Y.-F., Boutelier, M., Barret, D., & Zhang, S.-N. 2011, ApJ, 726, 74
Manko, V. S., Mielke, E. W., & Sanabria-Gómez, J. D. 2000, PhRvD, 61, 081501
Méndez, M. 2006, MNRAS, 371, 1925
Miller, J. C. 1977, MNRAS, 179, 483
Miller, M. C., Lamb, F. K., & Psaltis, D. 1998, ApJ, 508, 791
Morsink, S. M., & Stella, L. 1999, ApJ, 513, 827
Mukhopadhyay, B. 2009, ApJ, 694, 387
Newton, W. G., Gearheart, M., & Li, B.-A. 2013, ApJS, 204, 9
Nozawa, T., Stergioulas, N., Gourgoulhon, E., & Eriguchi, Y. 1998, A&AS, 132, 431
Pappas, G. 2015, MNRAS, 454, 4066
Pétri, J. 2005, A&A, 439, L27
Psaltis, D., Wijnands, R., Homan, J., et al. 1999, ApJ, 520, 763
Rezzolla, L., Yoshida, S., & Zanotti, O. 2003, MNRAS, 344, 978
Rikovska Stone, J., Guichon, P. A. M., Matevosyan, H. H., & Thomas, A. W. 2007, NuPhA, 792, 341
Rikovska Stone, J., Miller, J. C., Koncewicz, R., Stevenson, P. D., & Strayer, M. R. 2003, PhRvC, 68, 034324
Rosińska, D., Kluźniak, W., Stergioulas, N., & Wiśniewicz, M. 2014, PhRvD, 89, 104001
Steiner, A. W., Gandolfi, S., Fattoyev, F. J., & Newton, W. G. 2015, PhRvC, 91, 015804
Steiner, A. W., Lattimer, J. M., & Brown, E. F. 2010, ApJ, 722, 33
Steiner, A. W., Prakash, M., Lattimer, J. M., & Ellis, P. J. 2005, PhR, 411, 325
Stella, L., & Vietri, M. 1998a, in Abstracts of the XIX Texas Symp. on Relativistic Astrophysics and Cosmology, ed. J. Paul, T. Montmerle, & E. Aubourg (Saclay, France: CEA)
Stella, L., & Vietri, M. 1998b, ApJL, 492, L59
Stella, L., & Vietri, M. 1999, PhRvL, 82, 17
Stella, L., & Vietri, M. 2001, in ASP Conf. Ser. 2000, X-ray Astronomy, ed. R. Giacconi, S. Serio, & L. Stella (San Francisco, CA: ASP), 213
Stella, L., Vietri, M., & Morsink, S. M. 1999, ApJL, 524, L63
Stergioulas, N., & Friedman, J. L. 1995, ApJ, 444, 306
Strohmayer, T. E., & Markwardt, C. B. 2002, ApJ, 577, 337
Stuchlík, Z., Konar, S., Miller, J. C., & Hledík, S. 2008, A&A, 489, 963
Stuchlík, Z., Kotrlová, A., & Török, G. 2013, A&A, 552, A10
Stuchlík, Z., Kotrlová, A., Török, G., & Goluchová, K. 2014, AcA, 64, 45
Stuchlík, Z., Urbanec, M., Kotrlová, A., Török, G., & Goluchová, K. 2015, AcA, 65, 169
Stute, M., & Camenzind, M. 2002, MNRAS, 336, 831
Titarchuk, L., & Wood, K. 2002, ApJL, 577, L23
Török, G. 2009, A&A, 497, 661
Török, G., Abramowicz, M. A., Bakala, P., et al. 2008a, AcA, 58, 15
Török, G., Abramowicz, M. A., Bakala, P., et al. 2008b, AcA, 58, 113
Török, G., Bakala, P., Stuchlik, Z., & Čech, P. 2008c, AcA, 58, 1
Török, G., Bakala, P., Šrámková, E., et al. 2012, ApJ, 760, 138
Török, G., Bakala, P., Šrámková, E., Stuchlík, Z., & Urbanec, M. 2010, ApJ, 714, 748
Török, G., Goluchová, K., Horák, J., et al. 2016, MNRAS, 457, L19
Török, G., & Stuchlík, Z. 2005, A&A, 437, 775
Török, G., Stuchlík, Z., & Bakala, P. 2007, CEJPh, 5, 457
Török, G., Urbanec, M., Adámek, K., & Urbancová, G. 2014, A&A, 564, L5
Urbanec, M., Bělták, E., & Stuchlík, Z. 2010a, AcA, 60, 149
Urbanec, M., Miller, J. C., & Stuchlík, Z. 2013, MNRAS, 433, 1903
Urbanec, M., Török, G., Šrámková, E., et al. 2010b, A&A, 522, A72
van der Klis, M. 2005, AN, 326, 798
van der Klis, M. 2006, in Compact stellar X-ray sources, ed. W. Lewin & M. van der Klis (Cambridge: Cambridge Univ. Press), 39
Wagoner, R. V. 1999, PhR, 311, 259
Wagoner, R. V., Silbergleit, A. S., & Ortega-Rodríguez, M. 2001, ApJL, 559, L25
Wang, D. H., Chen, L., Zhang, C. M., et al. 2015, MNRAS, 454, 1231
Watts, A. L. 2012, ARA&A, 50, 609
Wiringa, R. B., Fiks, V., & Fabrocini, A. 1988, PhRvC, 38, 1010
Zhang, C.-M. 2005, ChJAS, 5, 21

Paper IV

II.4. Epicyclic Oscillations in the Hartle-Thorne External Geometry

Urbancová Gabriela, Urbanec Martin, Török Gabriel, Stuchlík Zdeněk, Blaschke Martin & Miller John C.

The Astrophysical Journal, 2019,
Volume 877, Issue 2, article id. 66, 17 pp.

The Astrophysical Journal, 877:66 (17pp), 2019 June 1 https://doi.org/10.3847/1538-4357/ab1b4c

Epicyclic Oscillations in the Hartle–Thorne External Geometry

Gabriela Urbancová[1,2], Martin Urbanec[1], Gabriel Török[1], Zdeněk Stuchlík[1], Martin Blaschke[1], and John C. Miller[3]
[1] Institute of Physics, Faculty of Philosophy and Science, Silesian University in Opava, Bezručovo nám. 13, CZ-74601 Opava, Czech Republic
gabriela.urbancova@fpf.slu.cz
[2] Astronomical Institute of the Czech Academy of Sciences, Boční II 1401, CZ-14100 Prague, Czech Republic
[3] Department of Physics (Astrophysics), University of Oxford, Keble Road, Oxford OX1 3RH, UK
Received 2017 December 19; revised 2019 April 8; accepted 2019 April 19; published 2019 May 28

Abstract

The external Hartle–Thorne geometry, which describes the spacetime outside a slowly rotating compact star, is characterized by the gravitational mass M, angular momentum J, and quadrupole moment Q of the star and gives a convenient description, which, for the rotation frequencies of more than 95% of known pulsars, is sufficiently accurate for most purposes. We focus here on the motion of particles in these spacetimes, presenting a detailed systematic analysis of the frequency properties of radial and vertical epicyclic motion and of orbital motion. Our investigation is motivated by X-ray observations of binary systems containing a rotating neutron star that is accreting matter from its binary companion. In these systems, twin high-frequency quasi-periodic oscillations (QPOs) are sometimes observed with a frequency ratio approaching 3:2 or 5:4, and these may be explained by models involving the orbital and epicyclic frequencies of quasi-circular geodesic motion. In our analysis, we use realistic equations of state for the stellar matter and proceed in a self-consistent way, following the Hartle–Thorne approach in calculating both the corresponding values of Q, M, and J for the stellar model and the properties of the surrounding spacetime. Our results are then applied to a range of geodetical models for QPOs. A key feature of our study is that it implements the recently discovered universal relations among neutron-star parameters so that the results can be directly used for models with different masses M, radii R, and rotational frequencies $f_{\rm rot}$.

Key words: stars: oscillations – stars: neutron – stars: rotation – X-rays: binaries

1. Introduction

Exterior spacetimes of rotating compact stars have been studied extensively for many years. Pioneering work was done by Hartle and Thorne who developed a slow-rotation approximation (Hartle 1967; Hartle & Thorne 1968), describing the structure of the star itself and also of the surrounding vacuum spacetime, constructed as a perturbation of a corresponding spherically symmetric non-rotating solution, with the perturbation being taken up to second order in the star's angular velocity Ω. In this approximation, the exterior spacetime is fully determined by the gravitational mass M, angular momentum J, and quadrupole moment Q of the rotating star, with the inner boundary of the exterior region being given by the stellar radius R.

Solutions for the equivalent problem without the restriction to slow rotation can be constructed using numerical-relativity codes such as RNS (Stergioulas & Friedman 1995) and LORENE/nrotstar (Bonazzola et al. 1998; Gourgoulhon et al. 2016). However, there are certain advantages to working with the Hartle–Thorne method, including that of having an analytic solution for the vacuum metric outside the star. The main topic of this paper concerns the motion of particles around rotating neutron stars, and we use the rotationally induced change in the frequency with which a test particle orbits the star at the marginally stable circular orbit as a key quantity for comparing different approaches. Comparison of the Hartle–Thorne values for this with those coming from the numerical-relativity codes shows good agreement for dimensionless spins $j = J/M^2 \simeq 0.5$,[4] suggesting applicability of other results obtained using the Hartle–Thorne approximation in most astrophysically relevant situations, although this is something that requires further checking. Comparisons between numerical-relativity and analytical spacetimes have been discussed by a number of authors (see, for example, Nozawa et al. 1998; Berti & Stergioulas 2004; Berti et al. 2005). Something not considered in the present paper is the role of the magnetic field of a neutron star for affecting the motion of particles in its vicinity. Discussion of this can be found in articles by Sanabria-Gómez et al. (2010), Bakala et al. (2012), Gutierrez-Ruiz et al. (2013), and others.

Details and overviews of rotating neutron stars and related physics can be found especially in the books by Weber (1999) and Friedman & Stergioulas (2013) and in the review article by Paschalidis & Stergioulas (2017).

Rotating neutron stars are usually observed as pulsars, either isolated or in binary systems. In binary systems, they can reach high rotation frequencies due to accretion of matter from the binary companion which increases both the star's gravitational mass and its angular momentum (and hence its rotational speed). The rotational frequencies can reach hundreds of Hz (the fastest currently known pulsar rotates with frequency 716 Hz Hessels et al. 2006). Within this work, we are interested mostly in neutron stars that are in Low-Mass X-ray Binaries (LMXBs), where the neutron star is accompanied by a low-mass ordinary star. Observations of some of these objects exhibit the phenomenon of twin high-frequency quasi-periodic oscillations (QPOs; van der Klis 2006).

These QPOs consist of two adjacent peaks in the X-ray power spectrum and have been observed in a number of sources. They often have a lower frequency of 600–800 Hz and an upper frequency of 900–1200 Hz, and there is clustering of the observed frequency ratios particularly at around 3:2 but also at around 4:3 and 5:4 (Belloni et al. 2007; Török et al. 2008a, 2008b, 2008c; Boutelier et al. 2010). Similar clustering

[4] Throughout this paper, we are using units for which $c = G = 1$.

is observed in microquasars (LMXBs containing black holes) where the frequencies are fixed at the ratio of 3:2 and can be explained as resulting from a nonlinear resonance between radial and vertical oscillation modes of an accretion disk around the black hole (Török et al. 2005). Therefore, we can anticipate that the 3:2 (4:3 and 5:4) resonance should play a role also in systems containing neutron stars instead of black holes (Török et al. 2008b). Nevertheless, it is still unclear whether or not the clustering in the distribution of frequency ratios is a real effect (Gilfanov et al. 2003; Méndez 2006; Boutelier et al. 2010; Montero & Zanotti 2012; Ribeiro et al. 2017).

There have been several attempts to explain the physical origin of QPOs using simple orbital models based on motion of matter around a central object (e.g., Stella & Vietri 1998, 1999; Wagoner 1999; Abramowicz & Kluźniak 2001; Kluzniak & Abramowicz 2001; Stella & Vietri 2001; Wagoner et al. 2001; Abramowicz et al. 2003b). A large set of references to models for neutron-star QPOs, along with a direct comparison between them, can be found in Török et al. (2010, 2012, 2016). A more elaborate model that included corrections to the orbital motion due to finite thickness of the accretion disk has been investigated by Török et al. (2016) and was particularly successful in the case of 4U1636-53 where it was shown that the observed frequency pairs could be explained by a torus with its center (maximum of density) located at positions that were variable but always at large enough radius to allow accretion onto the central object via the inner cusp. This model has been called the cusp torus model (see the papers by Rezzolla et al. 2003; Abramowicz et al. 2006; Šrámková et al. 2007; Ingram & Done 2010; Fragile et al. 2016; Török et al. 2016, 2017, 2018; de Avellar et al. 2017; Mishra et al. 2017; Parthasarathy et al. 2017 and references therein). Within this model, the highest observed frequencies correspond to the torus being located close to the marginally stable orbit and being small enough so that the correction due to the finite thickness of the disk could be neglected, enabling one to put constraints on the radius of the central object.

Motivated by the cusp torus model, we here make a detailed study of quasi-circular epicyclic motion in the external Hartle–Thorne geometry, using the formulas obtained previously by Abramowicz et al. (2003a). We begin our analysis by using the Hartle–Thorne approach to calculate neutron-star properties for a range of realistic equations of state for the neutron-star matter, and demonstrate how the influence of the different prescriptions for the equation of state can be hidden if one plots particular combinations of neutron-star properties against one another. These results are manifestations of the universal relations that have been discovered rather recently (Maselli et al. 2013; Urbanec et al. 2013; Yagi & Yunes 2013a, 2013b; Pappas 2015; Reina et al. 2017) and have been studied extensively under various circumstances (Chakrabarti et al. 2014; Doneva et al. 2014a, 2014b, 2015; Haskell et al. 2014; Pani et al. 2015; Sham et al. 2015; Silva et al. 2016; Staykov et al. 2016).

We then move on to discuss properties of particle motion around the star, showing the radial profiles for the orbital (Keplerian) frequency of circular motion and the radial and vertical frequencies of epicyclic quasi-circular motion. These profiles are relevant down to the radius of the innermost stable circular geodesic. We then study the frequency ratio of the oscillatory modes related to various geodetical models that have been proposed for explaining twin HF QPOs: the relativistic precession model and its variants (Stella & Vietri 1998, 1999), an epicyclic resonance model (Török et al. 2005), a tidal disruption model (Kostić et al. 2009), and a warped disk-oscillation model (Kato 2004).[5]

In Section 2, we give a brief introduction to the Hartle–Thorne methodology and then present results for neutron-star models constructed using our set of equations of state. In Section 3, we present general properties of the radial profiles for the orbital frequency, the epicyclic frequencies, and the precession frequencies and also describe the behavior of the maximum of the profile for the radial epicyclic frequency. In Section 4, we show radial profiles for the frequency ratios corresponding to various models for HF QPOs, and in Section 5, we compare models calculated using the Hartle–Thorne approach with fully numerical models not restricted to slow rotation. The main results presented within Sections 1–5 are parameterized in terms of the NS mass, angular momentum, and quadrupole moment. This allows their convenient application for interpreting neutron-star X-ray variability data within the context of the universal relations. We end with a short summary in Section 6.

2. The Hartle–Thorne Approach for Calculating Models of Rotating Compact Stars

The Hartle–Thorne approach (Hartle 1967; Hartle & Thorne 1968) is a convenient scheme for calculating models of compact stars in slow and rigid rotation and, since its introduction, has been used and discussed by many other authors. In this scheme, deviations away from spherical symmetry are considered as being small perturbations and treated by means of series expansions with terms up to second order in the star's angular velocity Ω being retained.

The metric line element takes the form (in standard Schwarzschild coordinates):

$$\begin{aligned} ds^2 = &-e^{2\nu}[1 + 2h_0(r) + 2h_2(r)P_2]dt^2 + e^{2\lambda} \\ &\times \left\{1 + \frac{e^{2\lambda}}{r}[2m_0(r) + 2m_2(r)P_2]\right\}dr^2 \\ &+ r^2[1 + 2k_2(r)P_2]\{d\ \theta^2 + [d\phi - \omega(r)dt]^2 \sin^2\theta\}, \end{aligned} \tag{1}$$

where ν and λ are functions of the radial coordinate r, and reduce to those of the spherically symmetric vacuum Schwarzschild solution in the exterior, $\omega(r)$ is a perturbation of order Ω, which represents the dragging of inertial frames, and the perturbation functions $h_0(r)$, $h_2(r)$, $m_0(r)$, $m_2(r)$, and $k_2(r)$ are of order Ω^2 and are functions only of the radial coordinate with the non-spherical angular dependence on the latitude θ being given by the Legendre polynomial $P_2 = P_2(\theta) = [3\cos^2(\theta) - 1]/2$.

The interior metric is found by solving the Einstein equations with the stress–energy tensor on the right-hand side being that for a perfect fluid rotating rigidly with angular velocity Ω, while the exterior solution is found by solving the vacuum Einstein equations, and constants appearing in the calculations are determined by matching these two

[5] The epicyclic frequencies in the case of fully numerical models for rapidly rotating neutron stars have been studied in (Pappas 2012) and (Gondek-Rosińska et al. 2014).

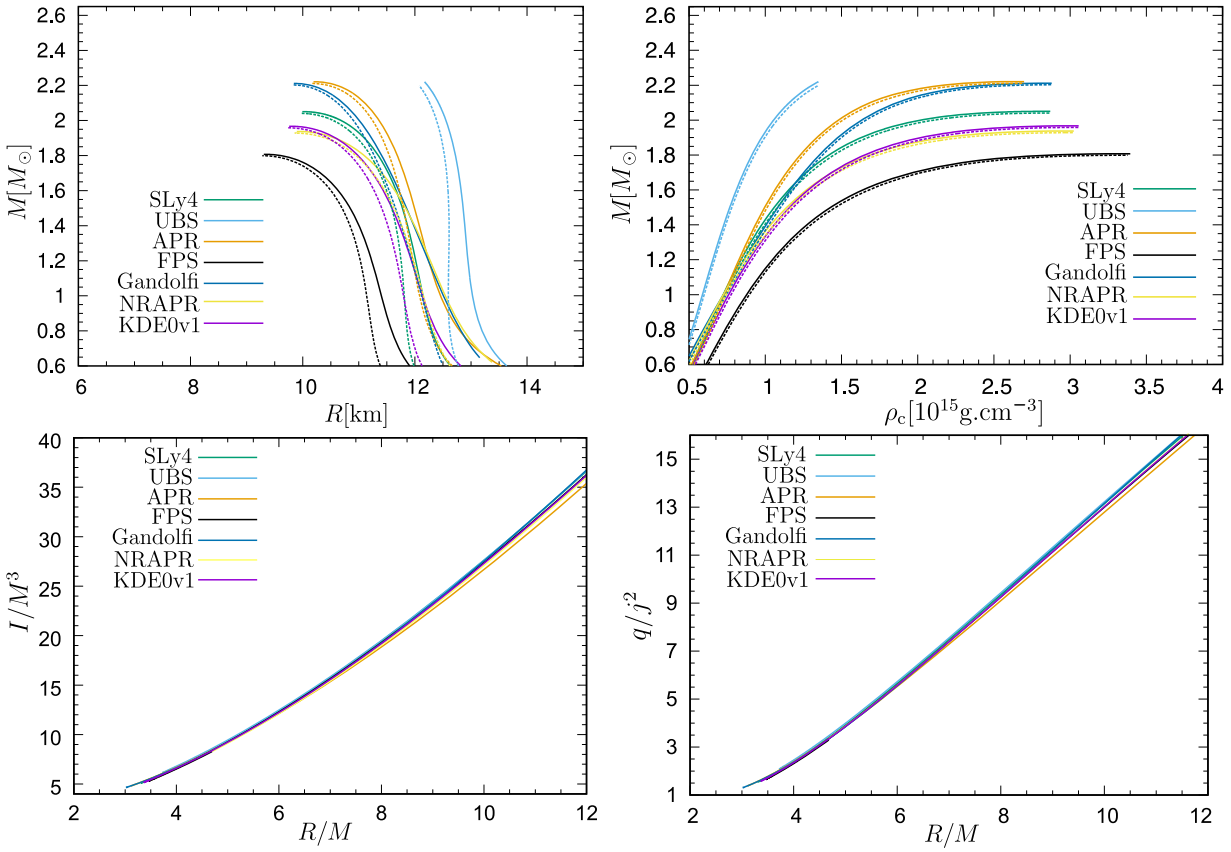

Figure 1. Top panels: mass vs. radius (left) and mass vs. central energy density (right) are plotted for a selection of equations of state, with the sequences of rotating and non-rotating stars being represented with solid and dashed lines respectively. The rotating ones all have a rotation frequency of 400 Hz and the value of R given for them is the equatorial radius ($R = R_{\rm eq}$). Bottom panels: the dimensionless quantities I/M^3 (left) and $q/j^2 = QM/J^2$ (right) are plotted against the inverse compactness R/M. All of the quantities in the bottom panels are in geometrical units, with $c = G = 1$.

solutions at the surface of the star.[6] The exterior solution can be expressed in terms of the star's gravitational mass M, angular momentum J, and quadrupole moment Q, and[7] it can be useful to rewrite the external metric in the terms of the dimensionless quantities: $j = J/M^2$, a dimensionless angular momentum, and $q = Q/M^3$, a dimensionless quadrupole moment (Abramowicz et al. 2003a). Quadrupole moments of rotating stars have been under investigation in the past and various definitions can be applied, for additional details, see, e.g., the discussions by Bonazzola & Gourgoulhon (1996) and Pappas & Apostolatos (2012b), Friedman & Stergioulas (2013).

Within our calculations, we also introduce another quadrupole parameter $\tilde{q} = q/j^2 = QM/J^2$ that is also dimensionless. Since $q \sim \Omega^2$ and $j \sim \Omega$, $\tilde{q}$ is independent of the star's rotation speed within the Hartle–Thorne approximation (a similar property has been shown to apply for rapidly rotating neutron stars as well, extending also to appropriately scaled higher-order moments; Pappas & Apostolatos 2012a, 2012b, 2014; Yagi et al. 2014.).

2.1. Models of Rotating Neutron Stars

Here we present results of calculations made using the Hartle–Thorne approach in order to determine the relations satisfied by the main neutron-star properties for a range of equations of state. For each EoS, we show a sequence of models rotating at 400 Hz (with masses up to the maximal one) and a second similar sequence with zero rotation, for comparison. Models satisfying the slow-rotation criterion will lie between the two (the motivation for focusing on 400 Hz will be explained later). The models of rotating neutron stars are constructed by solving a set of ordinary differential equations for the perturbation functions; the approach used has been extensively described in the literature and we will not repeat that here, see, e.g., Hartle & Thorne (1968), Chandrasekhar & Miller (1974), Miller (1977), Weber & Glendenning (1992), Benhar et al. (2005), Paschalidis & Stergioulas (2017).

[6] As pointed out quite recently by Reina & Vera (2015) and Reina (2016), special care is required when doing this for models having a density discontinuity at the surface in order to avoid getting wrong values for rotational corrections to the mass, but this issue does not arise for the models being discussed here.

[7] Note that throughout that we follow the convention of taking Q to be *positive for an oblate object*, as used by Hartle & Thorne.

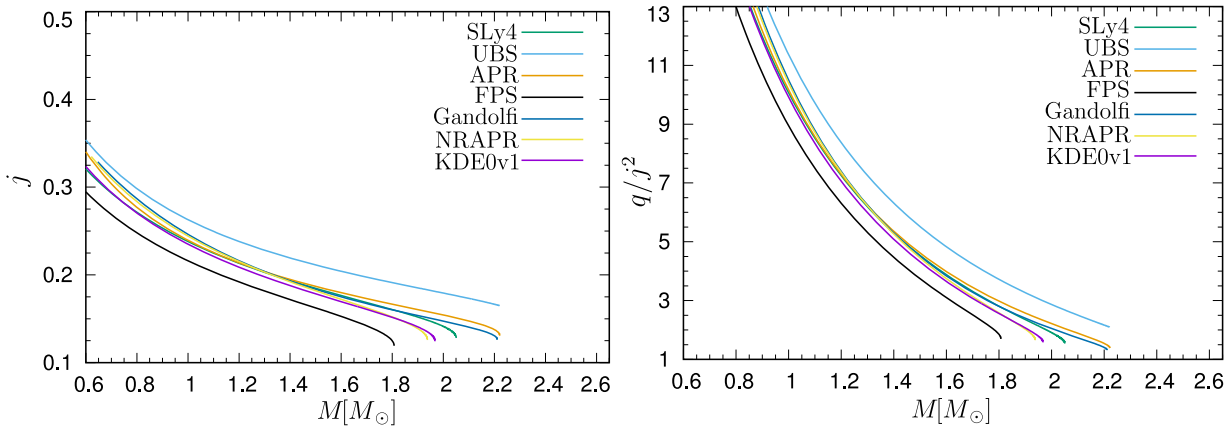

Figure 2. Values of $j = J/M^2$ (left panel) and $\tilde{q} = q/j^2 = QM/J^2$ (right panel) plotted against gravitational mass for stars rotating at 400 Hz.

For our set of equations of state describing nuclear matter, we have selected SLy4 (Stone et al. 2003), UBS (Urbanec et al. 2010), APR (Akmal et al. 1998), FPS (Lorenz et al. 1993), Gandolfi (Gandolfi et al. 2010), NRAPR (Steiner et al. 2005), and KDE0v1 (Agrawal et al. 2005). These follow various approaches to nuclear matter theory and lead to neutron-star models with different properties. Figure 1 shows mass–radius relations (top left) and mass as a function of the central energy density (top right) for both rotating models (solid lines) and non-rotating models (dashed lines). The different colors correspond to the different equations of state. For the rotating models, the equatorial radius is the quantity plotted as R. By comparing the right and left panels, one can see that the more compact stars (having smaller total radius for a given mass) are also having higher central energy densities, as would be expected. From the right panel, one can see the mass becoming less sensitive to central density as the maximum is approached. The existence of the maximum mass is important for testing equations of state using astronomical observations: quite recent observations of two solar mass neutron stars (Demorest et al. 2010; Antoniadis et al. 2013) rule out many equations of state, and from our selection of nuclear matter models, one can see that FPS is not applicable for these two objects.

The bottom panels of Figure 1 show the extent to which particular combinations of neutron-star parameters are universally related to the inverse compactness R/M (we are again using geometrical units here, so that all quantities are measured in units of length or its powers). As we will see, making use of this quasi-universal behavior can be extremely convenient for investigating orbital motion. For given R and M, one can immediately obtain the value of I/M^3 from the relation in the bottom left panel of Figure 1 and hence calculate the dimensionless angular momentum $j = J/M^2 = 2\pi f_{\rm rot} I/M^2$ for particular values of star's rotational frequency $f_{\rm rot}$. The dimensionless quadrupole moment $q = Q/M^3$ can then be obtained by using the relation in the bottom right panel together with the value of j.

This approach enables one to skip making the calculations of neutron-star models for all possible equations of state and central parameters and to use just global properties of the star (its mass and radius) for calculating all parameters of the external spacetime for the required rotational frequency.

For illustration, in Figure 2 we demonstrate results from detailed modeling: the left panel shows values of j as a function of the gravitational mass for stars rotating with $f_{\rm rot} = 400$ Hz. Within the Hartle–Thorne approximation, $j = J/M^2$ depends linearly on rotational frequency, and so one can easily find j for other values of $f_{\rm rot}$ by simple linear scaling. The maximal value of j is that for a star rotating at its mass-shedding limit and, for neutron stars, reaches values of 0.65–0.7 (Lo & Lin 2011). The right panel shows the values of $\tilde{q} = QM/J^2$ as a function of gravitational mass. It can be seen that for neutron stars with $M \geqslant 1.2\ M_\odot$, the values of $\tilde{q}$ are less than 10, and we will use this later as a maximum in our investigation of the motion of particles in the field of rotating neutron stars, to keep us within the limits of astrophysicaly interesting objects.

In this section, we have discussed the universal behavior of the parameters j and $\tilde{q}$ and how they are related to the mass, radius, and rotational frequency of neutron-star models calculated using realistic equations of state. In the following sections, we will make use of this for studying the motion of particles in the spacetime outside rotating neutron stars within the Hartle–Thorne approximation. A similar investigation, but using a different model for the spacetime around the rotating neutron stars, has been performed by Pachón et al. (2012) who presented their results in a more condensed form than being done here. Our approach is appropriate for any model of the rotating neutron stars since we plot the results in a way that is not dependent on any particular choice of equation of state.

3. The External Hartle–Thorne Geometry and the Frequencies of Epicyclic Motion

Since our main interest here is to investigate free-particle motion external to the surface of rotating neutron stars, we will next discuss this part of the spacetime (for $r > R$ to lowest order) in greater detail. We should stress that all of the discussions within this section and the next one, apply *only to the region outside the surface of the neutron star*. Any reference to free-particle motion that would seem to occur inside the neutron star needs to be disregarded.

As we have been discussing, the external Hartle–Thorne geometry can be expressed in terms of three parameters, for which we here take the gravitational mass M, the dimensionless

angular momentum j, and the dimensionless quadrupole moment q, in the form (Abramowicz et al. 2003a)[8]:

$$\begin{aligned} g_{tt} &= -(1 - 2M/r)[1 + j^2 F_1(r) + qF_2(r)], \\ g_{rr} &= (1 - 2M/r)^{-1}[1 + j^2 G_1(r) - qF_2(r)], \\ g_{\theta\theta} &= r^2[1 + j^2 H_1(r) + qH_2(r)], \\ g_{\phi\phi} &= r^2 \sin^2\theta[1 + j^2 H_1(r) + qH_2(r)], \\ g_{t\phi} &= g_{\phi t} = -2(M^2/r) j \sin^2\theta, \end{aligned} \tag{2}$$

where

$$\begin{aligned} F_1(r) &= -[8Mr^4(r - 2M)]^{-1}[u^2(48M^6 - 8M^5 r - 24M^4 r^2 \\ &\quad - 30M^3 r^3 - 60M^2 r^4 + 135Mr^5 - 45r^6) \\ &\quad + (r - M)(16M^5 + 8M^4 r - 10M^2 r^3 \\ &\quad - 30Mr^4 + 15r^5)] + A_1(r), \\ F_2(r) &= [8Mr(r - 2M)]^{-1}(5(3u^2 - 1)(r - M)(2M^2 \\ &\quad + 6Mr - 3r^2)) - A_1(r), \\ G_1(r) &= [8Mr^4(r - 2M)]^{-1}((L(r) - 72M^5 r) - 3u^2(L(r) \\ &\quad - 56M^5 r)) - A_1(r), \\ L(r) &= (80M^6 + 8M^4 r^2 + 10M^3 r^3 + 20M^2 r^4 \\ &\quad - 45Mr^5 + 15r^6), \\ A_1(r) &= \frac{15r(r - 2M)(1 - 3u^2)}{16M^2} \ln\left(\frac{r}{r - 2M}\right), \\ H_1(r) &= (8Mr^4)^{-1}(1 - 3u^2)(16M^5 + 8M^4 r - 10M^2 r^3 \\ &\quad + 15Mr^4 + 15r^5) + A_2(r), \\ H_2(r) &= (8Mr)^{-1}(5(1 - 3u^2)(2M^2 - 3Mr - 3r^2)) - A_2(r), \\ A_2(r) &= \frac{15(r^2 - 2M^2)(3u^2 - 1)}{16M^2} \ln\left(\frac{r}{r - 2M}\right), \\ u &= \cos\theta. \end{aligned}$$

$$E_1(r) = \frac{48M^7 - 80M^6 r + 4M^5 r^2 - 18M^4 r^3 + 40M^3 r^4 + 10M^2 r^5 + 15Mr^6 - 15r^7}{16M^2(r - 2M)r^4} + \frac{15(r^3 - 2M^3)}{32M^3} \ln\left(\frac{r}{r - 2M}\right),$$

$$E_2(r) = \frac{5(6M^4 - 8M^3 r - 2M^2 r^2 - 3Mr^3 + 3r^4)}{16M^2(r - 2M)r} - \frac{15(r^3 - 2M^3)}{32M^3} \ln\left(\frac{r}{r - 2M}\right).$$

For $j = 0$ and $q = 0$, the external Hartle–Thorne geometry reduces to the standard Schwarzschild one. The Kerr geometry taken up to second order in the dimensionless angular momentum $a = Mj$, and using the standard Boyer-Lindquist coordinates, can be obtained from the external Hartle–Thorne geometry by setting $q = j^2$ and making the coordinate transformations

$$r_{\rm BL} = r - \frac{a^2}{2r^3}[(r + 2M)(r - M) + \cos^2\theta(r - 2M)(r + 3M)], \tag{3}$$

$$\theta_{\rm BL} = \theta - \frac{a^2}{2r^3}(r + 2M)\cos\theta \sin\theta. \tag{4}$$

3.1. Radial Profiles of the Orbital Frequency and the Epicyclic Frequencies

Formulas for the frequencies of circular and epicyclic motion in the external Hartle–Thorne geometry have been calculated in Abramowicz et al. (2003a) and used by many authors, see, e.g., Török et al. (2008c, 2014) and Boshkayev et al. (2014, 2015). Here we give the relations for the orbital (Keplerian) frequency and the radial and vertical epicyclic frequencies, which are needed for the twin HF QPO models based on geodesic quasi-circular motion and were presented in Török et al. (2008c).

The Keplerian frequency is given by

$$\nu_K(r; M, j, q) = \frac{c^3}{2\pi GM} \frac{M^{3/2}}{r^{3/2}} \times \left[1 - j\frac{M^{3/2}}{r^{3/2}} + j^2 E_1(r) + qE_2(r)\right], \tag{5}$$

where

The radial epicyclic frequency ν_r and the vertical epicyclic frequency ν_θ are given by

$$\nu_r^2(r; M, j, q) = \left(\frac{c^3}{2\pi GM}\right)^2 \frac{M^3(r - 6M)}{r^4} \times [1 + jC_1(r) - j^2 C_2(r) - qC_3(r)], \tag{6}$$

[8] Note misprints in the original paper.

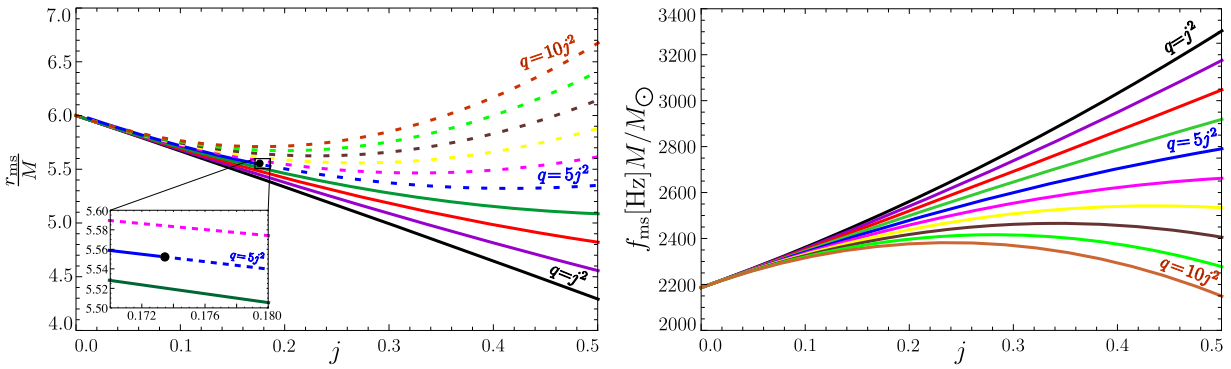

Figure 3. Left panel: the radial position of the marginally stable circular orbit $r_{\rm ms}$; dashed lines correspond to the inferred location of the marginally stable orbit being below the surface of the neutron star. Right panel: the orbital frequency $f_{\rm ms}$ at $r_{\rm ms}$.

$$\nu_\theta^2(r; M, j, q) = \left(\frac{c^3}{2\pi GM}\right)^2 \frac{M^3}{r^3} \times [1 - jD_1(r) + j^2 D_2(r) + qD_3(r)], \quad (7)$$

where

$$C_1(r) = \frac{6M^{3/2}(r+2M)}{r^{3/2}(r-6M)},$$

$$C_2(r) = \frac{384M^8 - 720M^7 r - 112M^6 r^2 - 76M^5 r^3 - 138M^4 r^4 - 130M^3 r^5 + 635M^2 r^6 - 375Mr^7 + 60r^8}{8M^2 r^4 (r-2M)(r-6M)} + B_1(r),$$

$$C_3(r) = \frac{5(48M^5 + 30M^4 r + 26M^3 r^2 - 127M^2 r^3 + 75Mr^4 - 12r^5)}{8M^2 r(r-2M)(r-6M)} - B_1(r)$$

$$B_1(r) = \frac{15r(r-2M)(2M^2 + 13Mr - 4r^2)}{16M^3(r-6M)} \ln\left(\frac{r}{r-2M}\right),$$

$$D_1(r) = \frac{6M^{3/2}}{r^{3/2}},$$

$$D_2(r) = \frac{48M^7 - 224M^6 r + 28M^5 r^2 + 6M^4 r^3 - 170M^3 r^4 + 295M^2 r^5 - 165Mr^6 + 30r^7}{8M^2 r^4 (r-2M)} - B_2(r)$$

$$D_3(r) = \frac{5(6M^4 + 34M^3 r - 59M^2 r^2 + 33Mr^3 - 6r^4)}{8M^2 r(r-2M)} + B_2(r),$$

$$B_2(r) = \frac{15(2r-M)(r-2M)^2}{16M^3} \ln\left(\frac{r}{r-2M}\right).$$

We next demonstrate the dependence of the radial profiles of the orbital and epicyclic frequencies on the parameters j and q. For each of the frequency profiles, we choose the values of the spin parameter as $j = 0.1, 0.2, 0.3, 0.5$ so as to fully cover the range that might be relevant for application to astrophysically interesting models of neutron stars or strange stars, while staying within the limit of validity of the slow-rotation approximation $(j/j_{\rm max})^2 \ll 1$. It has been shown that $j_{\rm max} \sim 0.65$–0.7 for neutron stars and that it could be larger for strange (quark) stars (Lo & Lin 2011). For objects that are less compact than these, the value of $j_{\rm max}$ could be significantly larger.

Values of the quadrupole parameter q are calculated taking $\tilde{q} = q/j^2 = 1, 2, 3, 4, 5, 10$ for each of the values of j. This selection of values for j and q covers the relevant situations and is obtained from modeling of the neutron stars as described in the previous section or, for example, in Urbanec et al. (2013).

In general relativity, stable circular orbital motion is restricted to radii larger than that of the marginally stable orbit which, in the external Hartle–Thorne geometry, is given by

$$r_{\rm ms} = 6M\left[1 \mp j\frac{2}{3}\sqrt{\frac{2}{3}} + j^2\left(\frac{251647}{2592} - 240\ln\frac{3}{2}\right) + q\left(-\frac{9325}{96} + 240\ln\frac{3}{2}\right)\right], \quad (8)$$

with the $-$ and $+$ referring to co-rotating and counter-rotating motion, respectively. Only outside this orbit can quasi-circular geodesic motion be stable, giving rise to possibly observable quasi-periodic oscillatory effects. Properties of the marginally stable orbit have been discussed in detail in, for example, Török et al. (2014), Cipolletta et al. (2017) and are shown here

The Astrophysical Journal, 877:66 (17pp), 2019 June 1

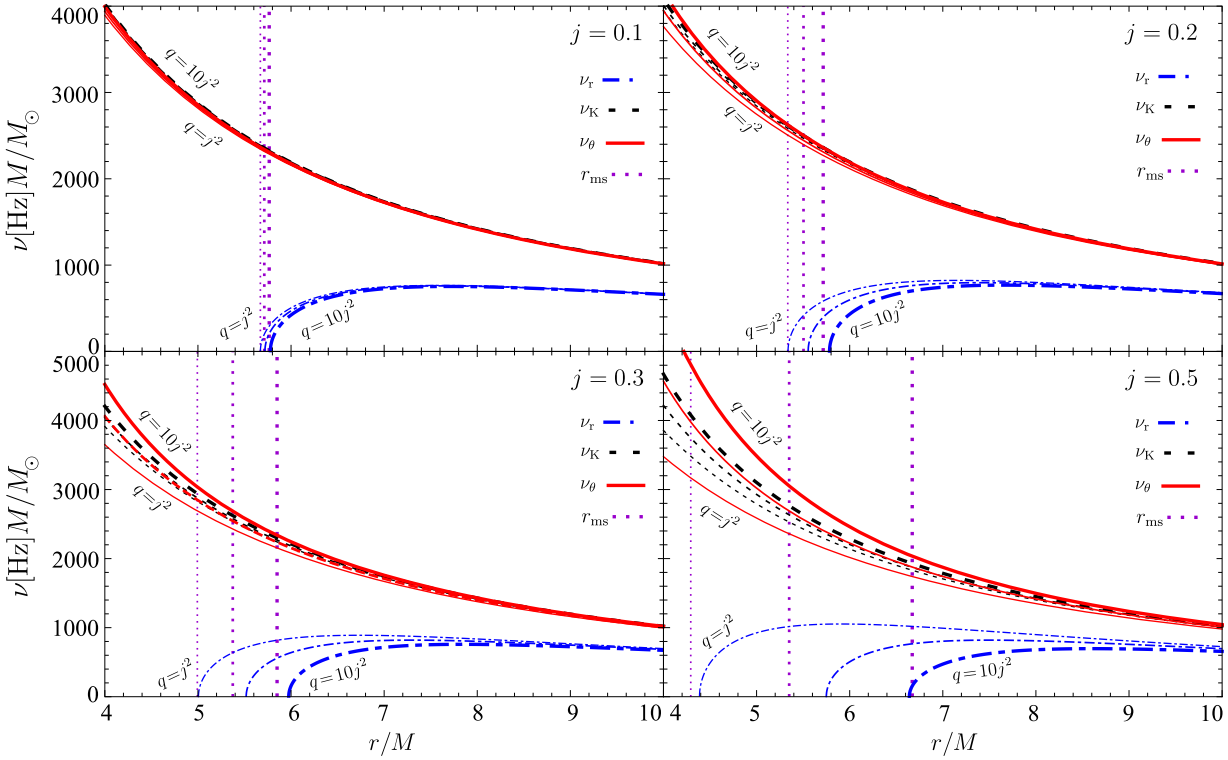

Figure 4. The radial profile of the orbital frequency ν_K and the epicyclic frequencies ν_r, ν_θ for $j = 0.1$, 0.2, 0.3, 0.5. The increasing thickness of the lines represents increasing values of $q/j^2 = 1$, 5, 10. The vertical dotted lines are calculated values of r_{ms} for each q/j^2, as given by Equation (8). Note that stable circular orbits are possible only for $r > r_{ms}$.

in Figure 3. In the left frame, one can see that the radius of the marginally stable orbit r_{ms} always decreases with increasing j near to $j = 0$, but can reach a minimum and then become increasing for higher values of j if q/j^2 is large enough. This sort of behavior can have a relevant impact on the observed distribution of rotational frequencies of QPO sources (Török et al. 2014). The position of the surface of the neutron star can be calculated from the universal relations (Yagi & Yunes 2006), given that q/j^2 is directly related to the inverse compactness of the star R/M. Results can be seen on the left side of Figure 3. In the zoomed area, note the curve for $q/j^2 = 5$ where a dot indicates the position of the surface. For the rest of the specified values of q/j^2, r_{ms} is situated above the surface for $q/j^2 < 5$ and below the surface for $q/j^2 > 5$, within the range of j shown.

The formula for the orbital frequency at r_{ms} can be calculated up to second order in the star's angular velocity as

$$f_{ms} = \frac{c^3}{2\pi GM 6\sqrt{6}}\left[1 + \frac{11j}{6\sqrt{6}} + \frac{1}{864}j^2\left(-160583 + 397710\ln\frac{3}{2}\right) + \frac{5}{32}q\left(1193 - 2946\ln\frac{3}{2}\right)\right]. \quad (9)$$

The right panel of Figure 3 shows f_{ms} plotted against j as calculated from this.

In the discussion above, we have used the term "marginally stable orbit" thinking only of the external vacuum region but, in reality, for a given model of the neutron star, this location may not exist in the external region: the equatorial radius of the star R_{eq} with given parameters M, j, and q can be *larger* than the r_{ms} as calculated in a vacuum exterior spacetime with the same parameters. In the remainder of this paper, we will be using the term "innermost stable circular orbit" (ISCO) in a non-standard way, to refer either to the orbit at r_{ms}, if it exists outside the star, or otherwise to a surface-skimming orbit at R_{eq}. One should bear in mind that, in practice, a particle on a surface-skimming orbit would be subject to various physical effects, which we are not including here.

In order to obtain a complementary point of view, in Figure 4 we show the radial profiles of the orbital and epicyclic frequencies for specified values of j, together with the profiles for the local value of the Keplerian frequency ν_K. One can see that the influence of the parameters j and q/j^2 increases with decreasing radius, and is relatively small at radii $r \sim 10M$ for all of the three frequency profiles; in all three cases, the influence of q/j^2 increases with increasing j. For the orbital frequency, the role of the parameters j and q is the smallest, and it is significantly stronger for the profile of the vertical epicyclic frequency which has a similar behavior to that of the orbital frequency. The most important influence is in the case of the radial epicyclic frequency —the shift of the marginally stable circular orbit, corresponding to the radius where the radial epicyclic frequency vanishes, is significantly shifted even for spin $j = 0.1$. For $j = 0.3$, it is shifted from $r_{ms} \sim 5M$ for $q/j^2 = 1$ to $r_{ms} \sim 5.8M$ for $q/j^2 = 10$, and in the extreme case of $j = 0.5$, the shift is from $r_{ms} \sim 4.4M$ for $q/j^2 = 1$ to $r_{ms} \sim 6.6M$ for $q/j^2 = 10$. Clearly,

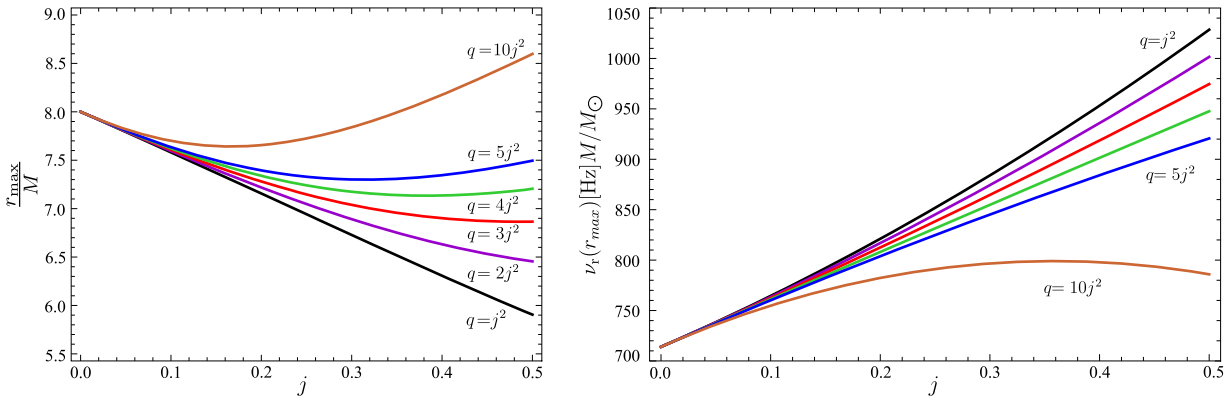

Figure 5. Left panel: the radius at which the profile of the radial epicyclic frequency $\nu_{\rm r}$ has its maximum. Right panel: the value of $\nu_{\rm r}$ at $r_{\max}$.

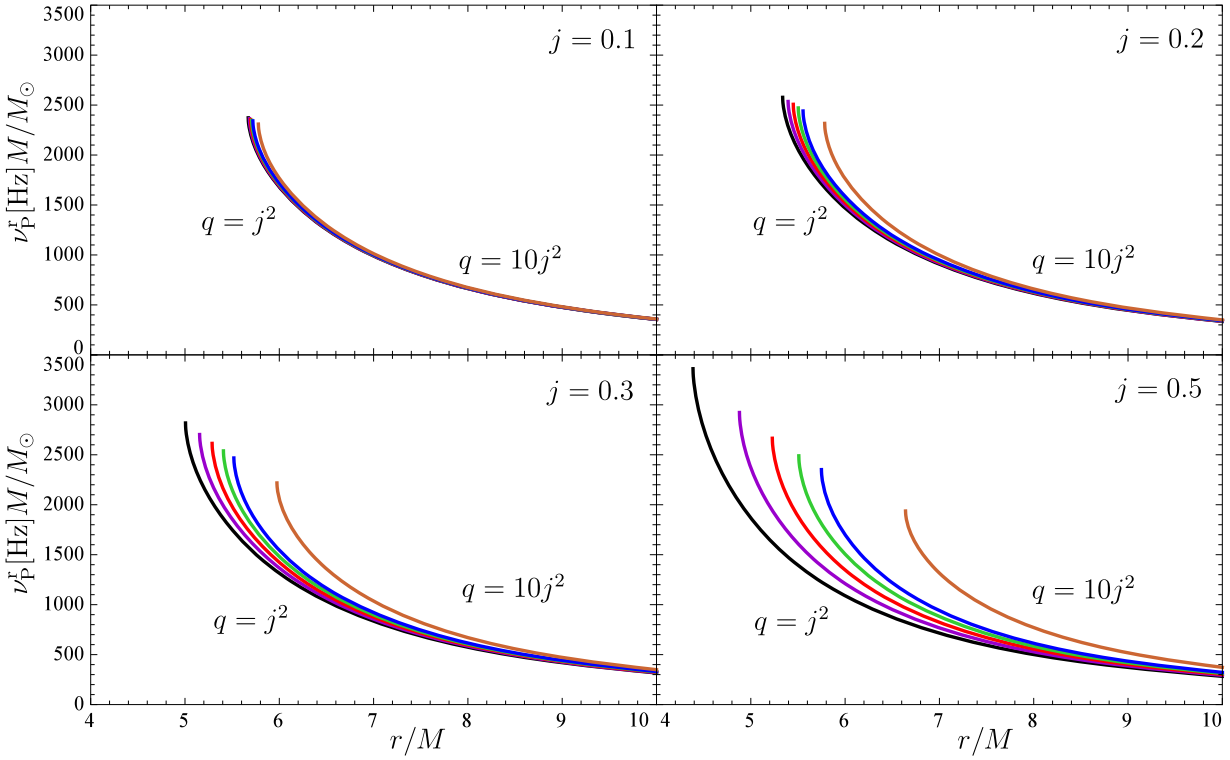

Figure 6. The radial profile of the periastron precession frequency $\nu^{\rm r}_{\rm P}$.

the role of the quadrupole moment is most significant for the radial epicyclic motion where it affects also the values at the maxima of radial epicyclic frequency.

One can see that, contrary to the case of the Kerr black hole spacetime, the vertical epicyclic frequency can be larger than the orbital frequency. This phenomenon has been observed also for Newtonian quadrupole gravitational fields (Gondek-Rosińska et al. 2014) and general relativistic solutions with multipole structure of the Manko type (Pappas 2012). A similar crossing of the radial profiles of the radial and vertical oscillations has been found also for axisymmetric string loops in the Kerr black hole spacetime (Stuchlík & Kološ 2014, 2015). This type of behavior was discovered by Morsink & Stella (1999) around rapidly rotating neutron stars with a very stiff equation of state and was also found for analytical approximations to these spacetimes (Pappas 2012; Pappas & Apostolatos 2013). Recently it has been discussed by Kluźniak & Rosińska (2013) in the context of Newtonian gravity and then further considered by Gondek-Rosińska et al. (2014) for rapidly rotating relativistic strange stars. Its relation to the higher-order multipole moments of spacetimes around compact objects can be found in Pappas 2017).

Clearly, the quadrupole parameter q/j^2 is playing an important role and this needs to be investigated further. In

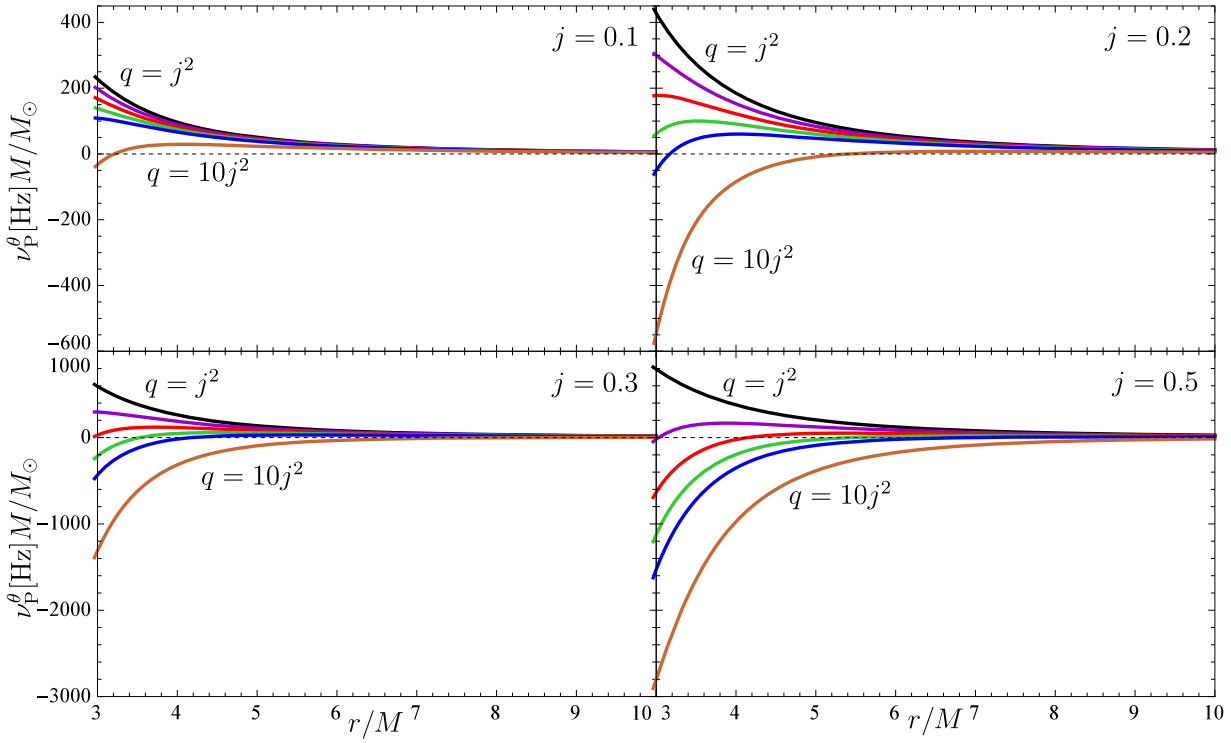

Figure 7. The radial profile of the nodal precession frequency $\nu_{\rm P}^{\theta}$.

the next subsections, we will look in greater detail at the value of the radial epicyclic frequency at its maximum.

3.2. Local Extrema of the Radial Epicyclic Frequency

Of the three frequencies describing orbital motion investigated above, the radial epicyclic frequency is the only one that is non-monotonic in r/M for small j. We will now investigate further the radius at which $\nu_{\rm r}$ has its maximum and the values which it takes there. The location of the maximum can be found by solving the equation

$$\frac{d\nu_r}{dr} = 0. \tag{10}$$

The solution can be found analytically, and is

$$r_{\rm max} = 8M\left[1 - \frac{47}{64\sqrt{2}}j + \frac{-12596207 + 43683840\ln\frac{4}{3}}{147456}j^2 - \frac{5}{576}\left(-9835 + 34128\ln\frac{4}{3}\right)q\right]. \tag{11}$$

The radial epicyclic frequency at $r_{\rm max}$ is then given by

$$\nu_{\rm r}(r_{\rm max}) = \sqrt{\frac{c^3}{64\sqrt{2}\pi GM}\left[1 + \frac{15}{16\sqrt{2}}j + \frac{-3972109 + 13824000\ln\frac{4}{3}}{8192}j^2 + \frac{5}{16}q\left(1553 - 5400\ln\frac{4}{3}\right)\right]}, \tag{12}$$

or, in a simplified form

$$\nu_{\rm r}(r_{\rm max}) = \sqrt{\frac{714.011}{M}(1 + 0.663j + 0.587j^2 - 0.15q)}. \tag{13}$$

The left panel of Figure 5 shows the locations of the maximum $r_{\rm max}$ plotted as a function of j, and the right panel shows the values of $\nu_{\rm r}$ at $r_{\rm max}$. One can see that q/j^2 is having an impact rather similar to that in the case of the marginally stable circular orbit, with a minimum appearing in the curves for larger values of q/j^2 and moving to smaller values of j as q/j^2 is increased. From the right panel, one sees that the largest values of q/j^2 may even cause $\nu_{\rm r}(r_{\rm max})$ to become a decreasing function of j at high enough rotation speeds.

3.3. Precession Frequencies

For matter orbiting around neutron stars, the quantities that may be directly observable could be related to combinations of the epicyclic frequencies, rather than to the frequencies themselves. In particular, the precession frequencies (periastron or nodal) may play an important role.

The periastron precession frequency is given by

$$\nu_{\rm P}^{\rm r} = \nu_K - \nu_r, \tag{14}$$

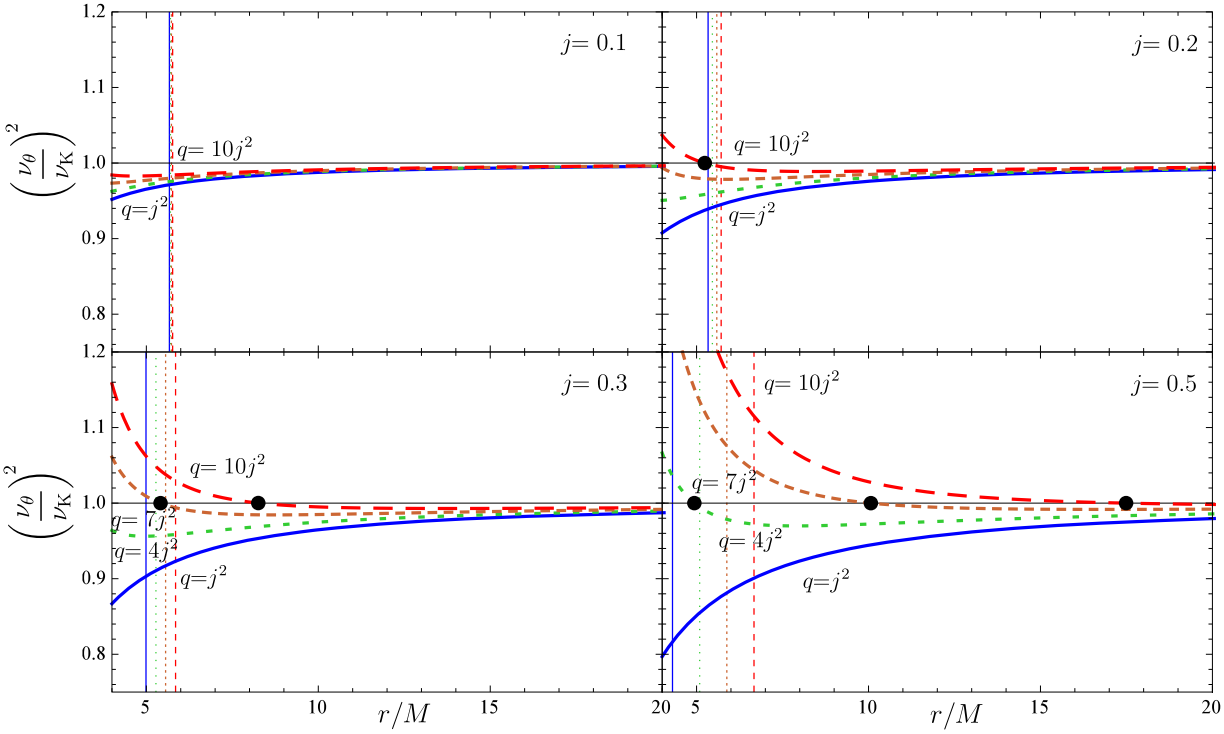

Figure 8. Points where the Keplerian and vertical epicyclic frequencies are equal.

while the nodal precession frequency is given by

$$\nu_{\rm P}^{\theta} = \nu_K - \nu_\theta, \tag{15}$$

with ν_K, ν_r, and ν_θ being given by Equations (5)–(7).

For calculation of precession frequencies, we again chose $j = 0.1, 0.2, 0.3, 0.5$, and we varied the quadrupole parameter q in the range $q/j^2 = 1, 2, 3, 4, 5, 10$ for each value of j. Results are plotted in Figures 6 and 7. In both cases, the impact of q/j^2 becomes progressively more significant as j increases. Note that the nodal precession frequency can become negative, since the radial epicyclic frequency can be higher than the orbital frequency. For low values of j, this happens only if q/j^2 is large and then only very near to $r = 3M$, while for larger values of j it happens also for smaller q/j^2.

3.4. Comparison of the Keplerian Frequency and the Vertical Epicyclic Frequency

As mentioned previously, within Newtonian theory it has been found by Gondek-Rosińska et al. (2014) that the vertical epicyclic frequency can be larger than the frequency of orbital motion if the central object is sufficiently oblate and we have seen that this can happen also for neutron stars (in general relativity) even if they are *not* very non-spherical. Here, we calculate the ratio of vertical epicyclic frequency to Keplerian frequency of orbital motion, and investigate when it is larger than one. The square of the ratio of these two frequencies can be written as

$$\left[\frac{\nu_\theta(r; M, j, q)}{\nu_K(r; M, j, q)}\right]^2 = 1 - jK(r) + j^2 L(r) - qM(r), \tag{16}$$

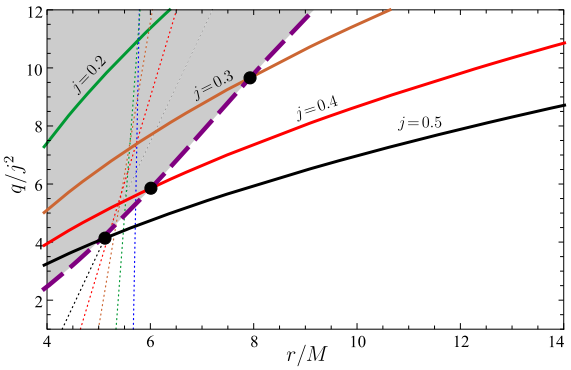

Figure 9. The value of q/j^2 giving $\nu_\theta = \nu_{\rm K}$ is plotted as a function of r/M for various values of j. The dotted lines show the value of $r_{\rm ms}$ for each j and the purple dashed line marks the stellar surface.

where

$$K(r) = 4M^{3/2}r^{-3/2},$$

$$L(r) = \frac{3}{8}M^{-2}r^{-2}(8M^4 + 35M^2r^2 - 30Mr^3 + 15r^4) + N(r),$$

$$M(r) = \frac{15}{8}M^{-2}(7M^2 - 6Mr + 3r^3) + N(r),$$

$$N(r) = \frac{45}{16}M^{-3}(M - r)(2M^2 - 2Mr + r^2)\ln\left(\frac{r}{r - 2M}\right).$$

We plot the results in Figure 8, marking the cases where the Keplerian frequency is equal to the vertical epicyclic

The Astrophysical Journal, 877:66 (17pp), 2019 June 1 Urbancová et al.

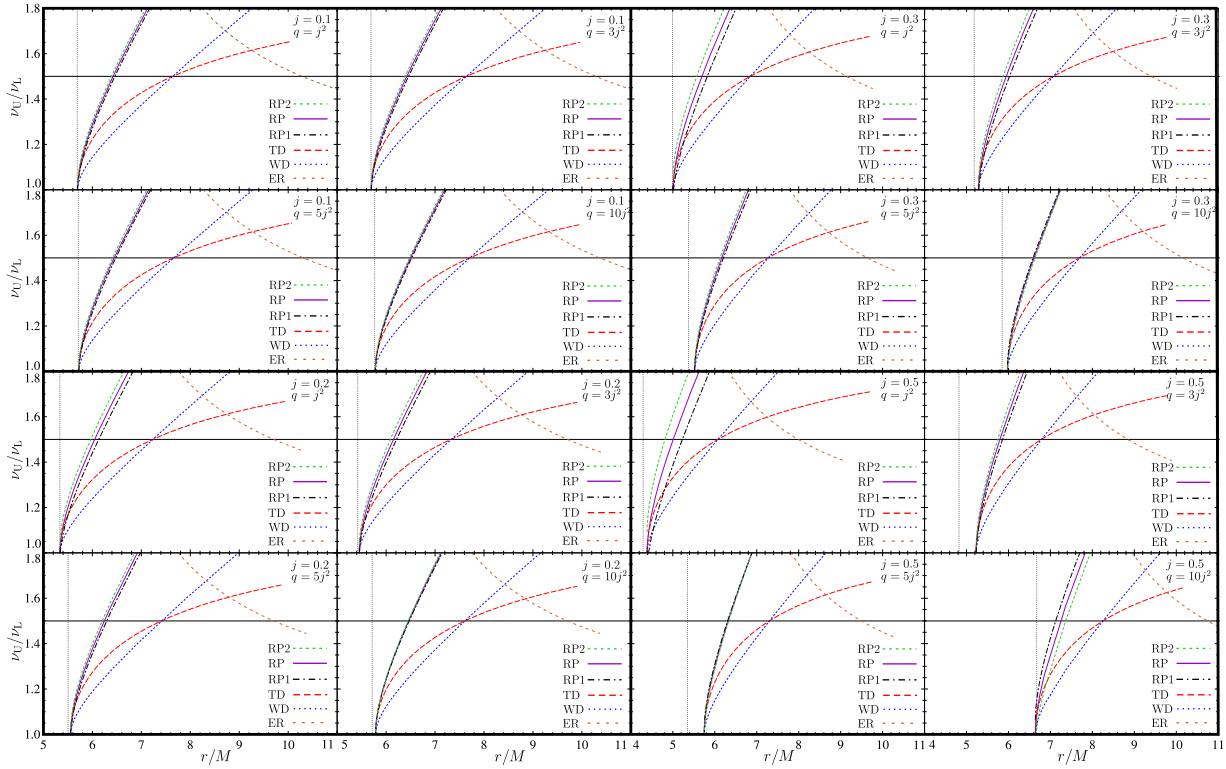

Figure 10. The orbital models of QPOs (with $j = 0.1, 0.2, 0,3, 0.5$). The dependence of ν_U/ν_L on r/M is shown. The vertical dotted line indicates the location of the marginally stable orbit r_{ms}, as given by Equation (8), and the horizontal line indicates the ratio $\nu_U : \nu_L = 3 : 2$.

Table 1
An Overview of the Orbital Models of QPOs, with Specification of the Upper ν_U and Lower ν_L Frequencies

Frequency	RP	TD	WD	RP1	RP2	ER
ν_U	ν_K	$\nu_K + \nu_{rad}$	$2\nu_K - \nu_{rad}$	ν_θ	$2\nu_K - \nu_\theta$	ν_θ
ν_L	$\nu_K - \nu_{rad}$	ν_K	$2(\nu_K - \nu_{rad})$	$\nu_K - \nu_{rad}$	$\nu_K - \nu_{rad}$	ν_{rad}

frequency. These points correspond to situations where the relativistic nodal frequency vanishes and changes sign.

The position where the nodal frequency vanishes needs to be compared with that of the marginally stable circular geodesic for the values of j and q/j^2 being used, because the effect of nodal frequency switching is relevant only in the regions where the circular geodesic motion is stable against perturbations, i.e., outward of the marginally stable circular orbit at r_{ms}. We have calculated the locations of r_{ms} using the relation (8), and these are shown as vertical lines in Figure 8 with the line-style corresponding to that for the ν_θ/ν_K profile with same value of q/j^2. We can see some cases (especially for low values of j) where $\nu_\theta/\nu_K = 1$ occurs at a radius below r_{ms}. On the other hand, for higher values of j and q/j^2, $\nu_\theta > \nu_K$ can occur also for orbits that are stable with respect to radial perturbations.

We now investigate the locations where

$$\left[\frac{\nu_\theta(r; M, j, q)}{\nu_K(r; M, j, q)}\right]^2 = 1. \tag{17}$$

Since ν_θ is always equal to ν_K in the non-rotating Schwarzschild case, one cannot find the location for the nodal switching point as an expansion around the Schwarzschild value. The values of q/j^2 satisfying (17) are given by

$$\frac{q}{j^2} = 1 + \frac{64M^{9/2}\sqrt{r} - 48jM^5}{15jr^2\left[-2M(7M^2 - 6Mr + 3r^2) - 3(M - r)(2M^2 - 2Mr + r^2)\ln\left(\frac{r}{r-2M}\right)\right]}, \tag{18}$$

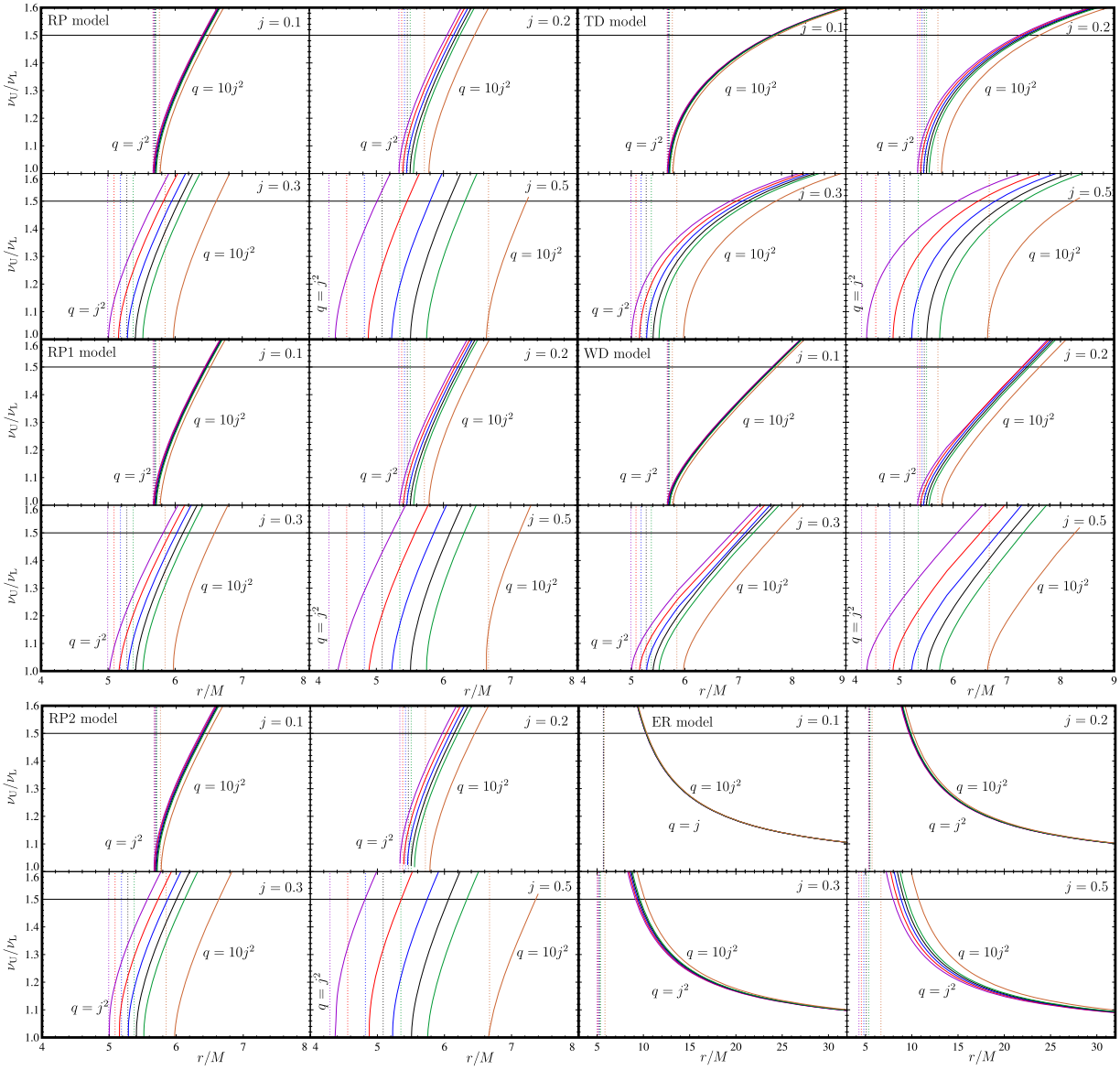

Figure 11. Individual results for each of the orbital QPO models: RP, RP1, RP2, TD, WD, ER (top left to bottom right panels). The ratio ν_U/ν_L is plotted against r/M for each model. The vertical dotted lines indicate the location of the marginally stable orbit r_{ms} for each value of q.

and in Figure 9, we plot these against r/M for $j = 0.2, 0.3, 0.4, 0.5$. The dotted lines show the value of r_{ms} for each j and the purple dashed line indicates the stellar surface; we have marked the point on each of the j curves beyond which r is greater than both of those limits.

4. Models of Twin HF QPOs and the Frequency Ratios in the Hartle–Thorne Geometry

In the previous section, we investigated the behavior of the orbital, epicyclic, and precession frequencies. We have seen that as j increases, the role of the quadrupole term becomes increasingly important. In this section, we focus on particular combinations of frequencies that play key roles for models of QPOs—the twin peaks observed in power spectra of LMXBs. The origin of these peaks is still under investigation, but several candidate models are using frequencies associated with orbital motion around the central objects.

4.1. Frequency Ratios of Oscillatory Modes for the Twin HF QPO Models

In this section, we study the behavior of the frequencies of oscillatory modes given by some current models for the twin HF QPOs observed in atoll and Z-sources, where a neutron star is accreting matter from a low-mass companion (for the differences between atoll and Z-sources see Hasinger & van der Klis 1989). We consider the specific models presented in

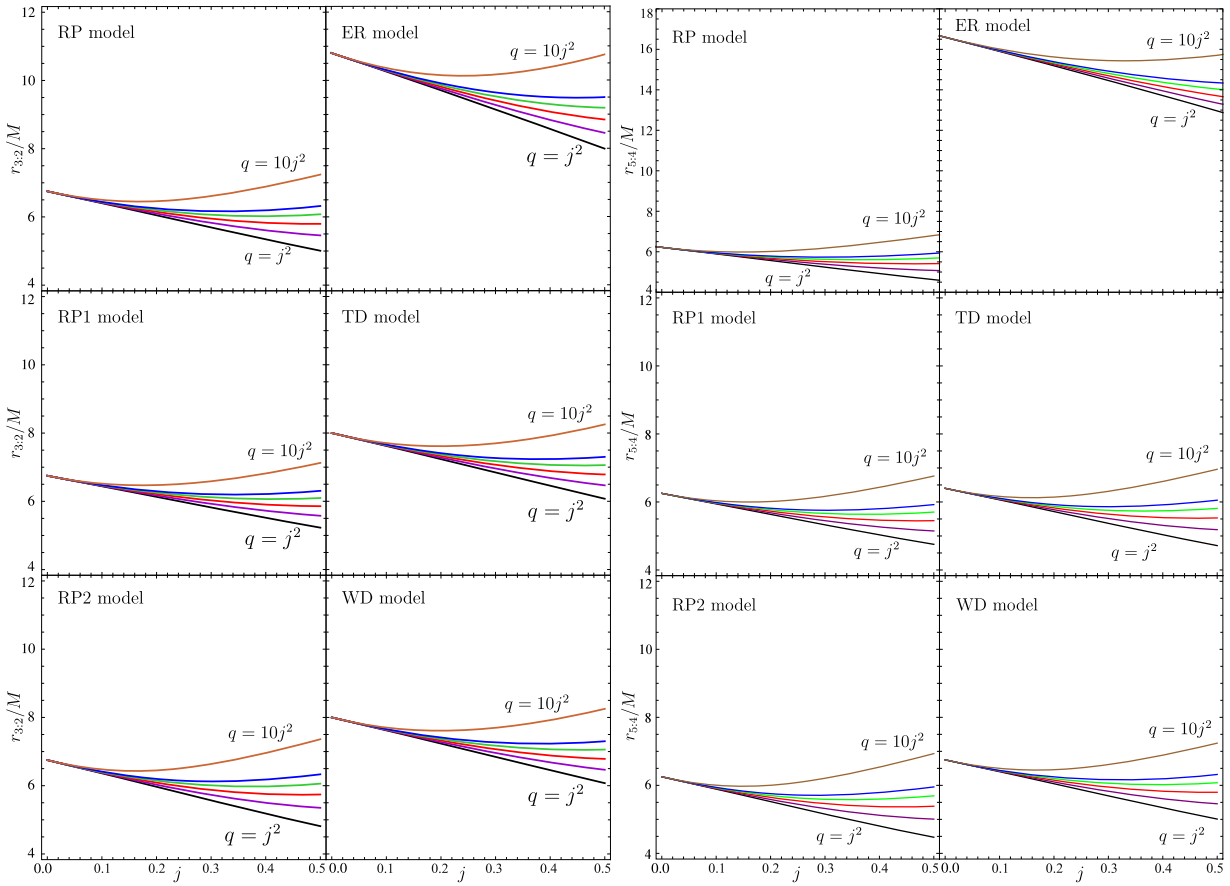

Figure 12. The locations where the resonant QPO ratios 3:2 and 5:4 are generated. For each of the models, $r_{3:2}/M$ (left panels) and $r_{5:4}/M$ (right panels) are plotted against j for $q/j^2 = 1, 2, 3, 4, 5, 10$.

Table 1, where we also give the combinations of frequencies that are attributed to the upper and lower observed peaks in each case. Our selection of models is based on Török et al. (2011). None of the models is currently uniquely preferred, because each of them has (different) theoretical problems. The RP (Relativistic Precession) model (Stella & Vietri 1999) considers relativistic epicyclic motion of blobs at various radii in the inner parts of the accretion disk; The TD (Tidal Disruption) model (Čadež et al. 2008) proposes that the QPOs are generated by a tidal disruption of large accreting inhomogeneities; The WD (Warped Disk) model (Kato 2001) considers a somewhat exotic disk geometry that causes a doubling of the observed lower QPO frequency; The ER (Epicyclic Resonance) model (Abramowicz & Kluźniak 2001) involves different combinations of axisymmetric disk-oscillation modes; RP1 (Bursa et al. 2005) and RP2 (Török et al. 2007) use different combinations of non-axisymmetric disk-oscillation modes. We are considering here only geodesic oscillation models where the oscillatory modes are combinations of the orbital and epicyclic frequencies of near-circular geodesic motion in the equatorial plane.

In Figure 10, we show the radial profiles of the frequency ratio ν_U/ν_L for all of the six QPO models being considered here.

As in the previous section, we use the values $j = 0.1$, 0.2, 0.3, 0.5, which includes the maximal range of the spin parameter j for the Hartle–Thorne approximation (Urbanec et al. 2013), and for the quadrupole parameter q we use values obtained from taking $q/j^2 = 1$, 3, 5, 10, covering the most astrophysically relevant models for rotating neutron stars. It can be seen that for the RP models, the ratio $\nu_U/\nu_L = 3/2$ occurs just slightly outside the location of the marginally stable orbit, meaning that the QPOs will generally be related to the region very close to the inner edge of the accretion disk, but for the TD and WD models the radius is larger and it is even more so for the ER model. However, all of the considered models are giving the radius where $\nu_U/\nu_L = 3/2$ as being between r_{ms} and $r = 11M$.

We also note that the RP, RP1, and RP2 models give extremely similar profiles, with only very minor differences. The profiles of the WD and TD models are different, but they always cross each other at the frequency ratio 3:2. For the ER model, the ratio diverges at the marginally stable orbit, since the radial epicyclic frequency has to vanish there, and this is the only case where the ratio decreases with increasing radius. In all of the models, the radial profiles depend only slightly on the quadrupole parameter for small values of $j < 0.2$, but the dependence increases with increasing j, and for $0.3 < j < 0.5$

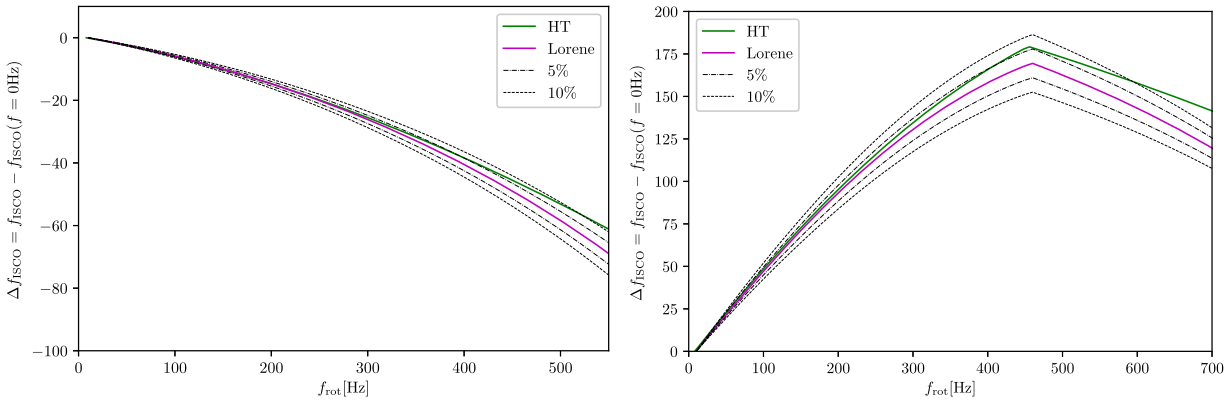

Figure 13. $\Delta f_{\rm ISCO}$ is plotted as a function of $f_{\rm rot}$ as calculated using the Hartle–Thorne and Lorene approaches. The gravitational mass of the non-rotating star is $M = 1.2M_{\odot}$ (left panel) and $M = 1.4M_{\odot}$ (right panel). See the text for details.

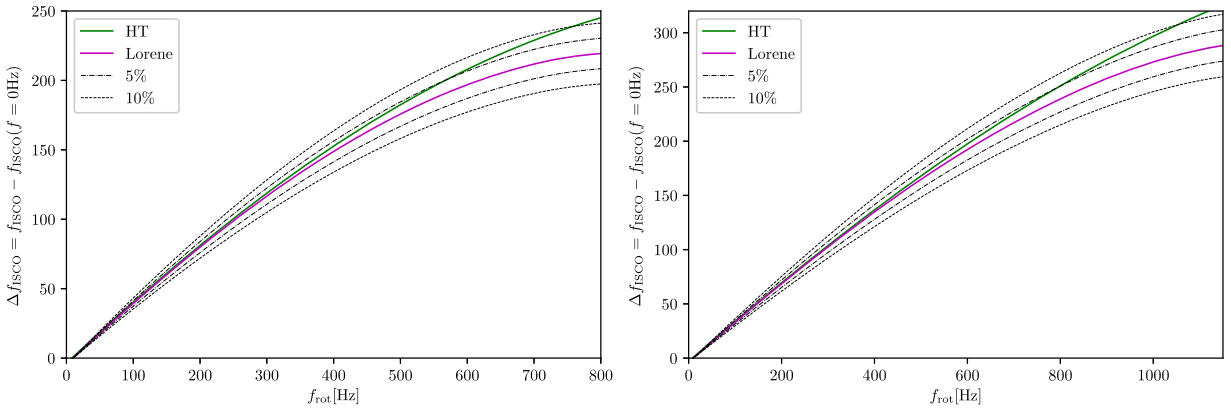

Figure 14. $\Delta f_{\rm ISCO}$ is plotted as a function of $f_{\rm rot}$ as calculated using the Hartle–Thorne and Lorene approaches. The gravitational mass of the non-rotating star is $M = 1.6M_{\odot}$ (left panel) and $M = 1.8M_{\odot}$ (right panel). See the text for details.

it can be very strong, especially close to the marginally stable orbit.

In Figure 11, we show these results plotted for each of the QPO models separately, using $j = 0.1, 0.2, 0.3, 0.5$, as before, and $q/j^2 = 1, 2, 3, 4, 5, 10$. Here one can appreciate better the role of j and q/j^2 for varying the position of marginally stable orbit. Note the qualitative difference between the results for the ER model and the others.

4.2. The Frequency Ratio 3:2 in the Twin HF QPO Models

Observational data for QPOs demonstrates the importance of the frequency ratio 3:2 (Boutelier et al. 2010) and so we have calculated how the location where this ratio is generated varies as a function of j. The left panels of Figure 12 show this for each of our QPO models for $q/j^2 = 1, 2, 3, 4, 5, 10$. Note that the behavior of $r_{3:2}/M$ demonstrates a qualitatively similar behavior to that for the location of the marginally stable orbit: for small values of q/j^2, the resonance radius decreases with increasing spin, as for Kerr black holes, but for large enough q/j^2 it reaches a minimum and then increases again.

The right panels of Figure 12 show equivalent results for the ratio 5:4, which are quite similar.

5. Comparison of Results from the Hartle–Thorne Approach and the Lorene/Nrotstar Numerical Code

In this section, we test the range of validity of the Hartle–Thorne approach by comparing results obtained with it against ones given by the publicly available Lorene/nrotstar code (Gourgoulhon et al. 2016). We compare models having the same gravitational mass for a static non-rotating star M_0 and then keep constant the value of the central pressure (and the energy or enthalpy density) when we move to rotating models. We use the APR equation of state (Akmal et al. 1998) for making the comparison.

We focus on the quantity $\Delta f_{\rm ISCO} = f_{\rm ISCO} - f_{\rm ISCO}(f = 0\ {\rm Hz})$, where $f_{\rm ISCO}$ is here the frequency at the innermost stable orbit (either the marginally stable circular orbit at $r = r_{\rm ms}$ or the equatorial surface-skimming orbit at $r = R_{\rm eq}$ when $R_{\rm eq} > r_{\rm ms}$, as discussed previously (see also Pappas 2015 for discussion of when the surface of the neutron star lies above/below $r_{\rm ms}$).

This quantity is zero in the non-rotating case and its leading order in the slow-rotation expansion goes as $f_{\rm rot}$ while the order of its first neglected term goes as $\mathcal{O}(f_{\rm rot}^3)$, i.e., the relative error is of order $\mathcal{O}(f_{\rm rot}^2)$. This is also the case for $\nu_{\rm P}^{\theta}$, but the quantities $f_{\rm ISCO}$ and ν_P^r have non-zero values for the non-rotating case, i.e., the leading term is of $\mathcal{O}(f_{\rm rot}^0)$, and since the

The Astrophysical Journal, 877:66 (17pp), 2019 June 1

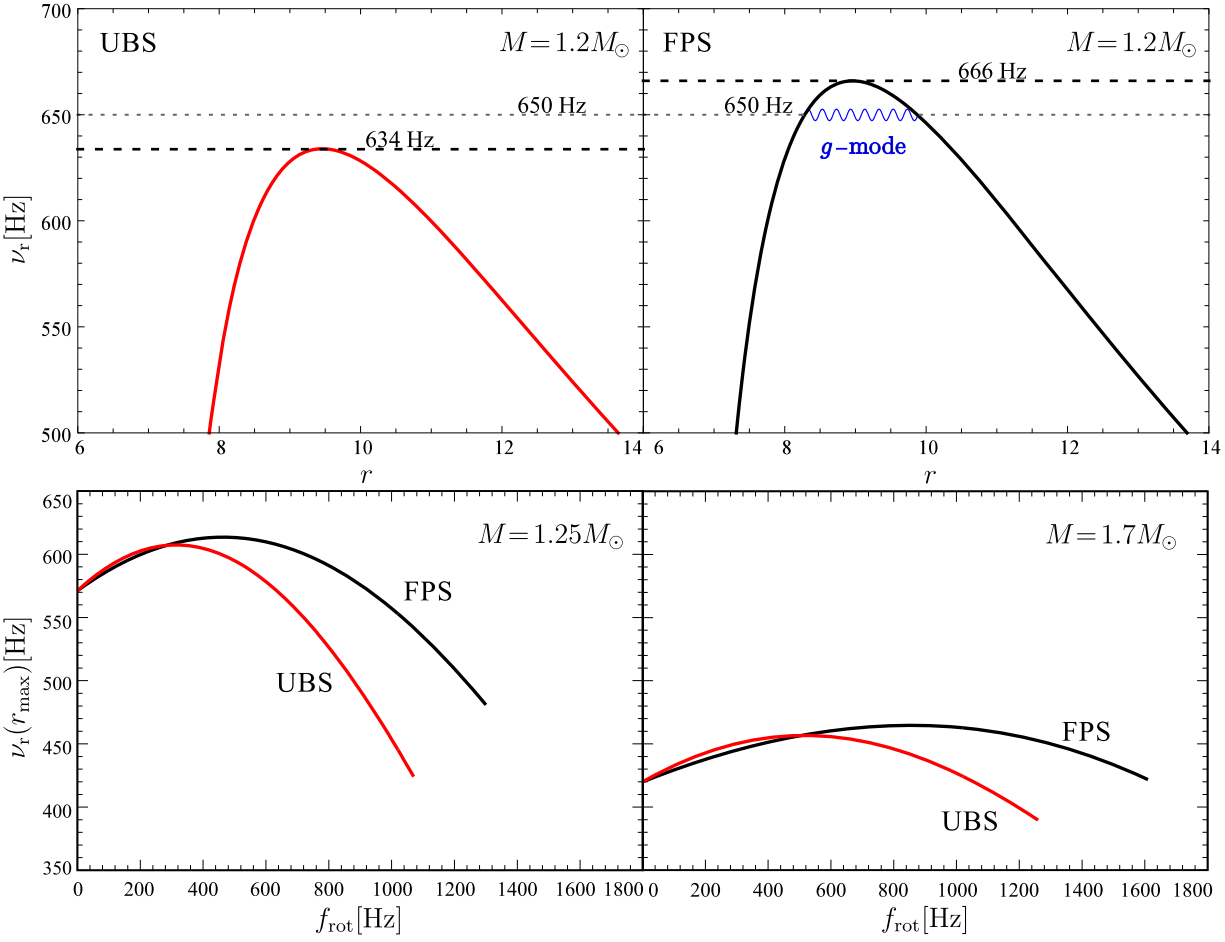

Figure 15. Upper panels: the radial profile of the radial epicyclic frequency ν_r for stars with gravitational mass 1.2 $M_\odot$ rotating with frequency of 580 Hz for two selected equations of state. The dashed horizontal lines indicate the values of $\nu_r(r_{max})$ determining the trapping of discoseismic g-modes. The dotted horizontal line indicates a particular value of the trapped g-mode frequency at 650 Hz, which is allowed for the FPS EoS but not for UBS. Lower panels: the maximum radial epicyclic frequency, calculated using Equation (12), plotted as a function of the stellar rotational frequency for stars with gravitational mass 1.25 $M_\odot$ (left panel) and 1.7 $M_\odot$ (right panel).

first neglected term is again $\mathcal{O}(f_{rot}^3)$, this means that the relative error is of order $\mathcal{O}(f_{rot}^3)$, one order higher than that for ν_P^θ. Because of this ν_P^θ is likely to be the quantity most liable to error and so it is sensible to use as our key test quantity $\Delta f_{ISCO} = f_{ISCO} - f_{ISCO}(f = 0\,\mathrm{Hz})$, which has an error of the same order as the most sensitive quantity of interest. This is not a foolproof argument because of different coefficients in the expansions of the quantities concerned, but it should be a reasonable guide.

For the ISCO frequency in the Hartle–Thorne approach, we calculate a gravitational mass M for the rotating star, a dimensionless angular momentum J/M_0^2 and a dimensionless quadrupole moment Q/M_0^3, use these to calculate the radius r_{ms} from Equation (8) and then find the Keplerian frequency at this radius using Equation (5). If r_{ms} is less than R_{eq}, then the latter is used instead in Equation (5). For the gravitational mass of the non-rotating star we take $M_0 = 1.2, 1.4, 1.6, 1.8M_\odot$. The rotational frequencies are taken up to the frequency where the difference between the Hartle–Thorne and Lorene values for Δf_{ISCO} reaches ∼10%. The results of the comparison are shown in Figures 13 and 14, where we show also the 5% and 10% intervals around the Lorene values. The positive gradients correspond to r_{ms} being used, and the negative gradients to R_{eq}. Since we are dealing with specific models here, the location of the stellar surface is directly known.

The two approaches are in excellent agreement for the lower rotation frequencies, as expected; when differences begin to emerge, Hartle–Thorne is giving higher values for Δf_{ISCO} in all cases. We see that for lower masses, the difference between the Lorene and Hartle–Thorne values of Δf_{ISCO} are smaller than 10% up to frequencies of about 500 Hz, while for higher masses, the rotational frequencies can go up to 700 Hz (for $M = 1.6M_\odot$) or 1000 Hz (for $M = 1.8M_\odot$). Since it is generally believed that neutron stars in QPO sources have accreted matter from the companion star, they should have rather high masses.

6. Summary

We have examined the behavior of the orbital frequency, the radial epicyclic frequency, and the vertical epicyclic frequency in the external Hartle–Thorne geometry for rotating compact stars. The primary parameters of the geometry are the gravitational mass M, the angular momentum J, and the quadrupole moment Q, and we have calculated the corresponding values for these from models of neutron stars constructed using realistic equations of state for nuclear matter. Our approach can be applied for any future equation of state if the universal relations are used as described in Section 2.[9] Apart from the individual frequencies, we have also investigated the behavior of combinations of them which are involved in some models for QPOs observed in X-rays from LMXBs.

We have seen that the dimensionless angular momentum j and dimensionless quadrupole moment q play an important role for the behavior of the orbital and epicyclic frequencies, especially for the ratio between the vertical epicyclic frequency and the Keplerian frequency, becoming particularly important for stars rotating with the higher angular velocities. Our investigation was motivated by the observations of QPOs in the X-ray spectra of LMXBs, and we have investigated the behavior of the frequencies relevant for several of the models proposed for explaining these.

It may seem redundant to spend time with additional models, but at present we do not know which model may be relevant for the sources of QPOs and are not even sure whether only one model will be applicable for all of them. If the radiation does come from the accretion disk and is modulated by its oscillations, different oscillation modes may well be involved for different sources, depending on the geometry of the binary system. For example, if the equatorial plane of the compact object is the same as the orbital plane of the binary system, one may expect radial perturbations of the disk caused by matter falling in from the donor star. On the other hand, if the equatorial plane of the compact star is almost perpendicular to the orbital plane of the binary, one may expect vertical perturbations of the disk instead. This is something that may well be clarified in the near future.

Finally, we note that the results presented here can be relevant not only for the particular models mentioned in Section 4 but also for a wider class of orbital models. For instance, the maximum of the radial epicyclic frequency determines propagation of some discoseismic modes (Kato et al. 1998; Wagoner et al. 2001) and so there would be an application for making estimates of stellar spin rates based on association of QPOs with oscillations trapped near to the inner edge of thin accretion disks (Kato 1989, 2001). This is illustrated in Figure 15 where we show the dependence of the maximum value of the radial epicyclic frequency $\nu_r(r_{max})$ for compact and highly oblate stars. Similar examples can be found for the vertical epicyclic frequency and models dealing with the Lense–Thirring precession effect (Ingram et al. 2009, 2015; Rosińska et al. 2014; Wiśniewicz et al. 2015; Tsang & Pappas 2016). The formulas given in Section 3 for determining the epicyclic frequencies (and the ratio between the vertical epicyclic frequency and the Keplerian frequency) can therefore be used in various applications, especially within the context of the universal relations.

[9] During the refereeing process and preparation of the revised version of this manuscript, a paper by Luk & Lin (2018) has been published where it is demonstrated that the frequency at the marginally stable orbit around rotating neutron stars is also a universal function of the neutron-star properties.

G.U. and Z.S. acknowledge the Albert Einstein Center for Gravitation and Astrophysics supported by the Czech Science Foundation grant No. 14-37086G. M.U. and G.T. were supported by Czech Science Foundation grant No.17-16287S. G.U., M.U., and Z.S. are grateful for very kind hospitality from the University of Oxford and for fruitful discussions there; the stay in Oxford was partly supported by grant LTC18058. They acknowledge the internal grants of the Silesian University Opava FPF SGS/14,15/2016 and SGS/12,13/2019. Some of the equations of state used in this work were kindly provided to the authors by J. R. Stone. The authors also acknowledge fruitful discussions with Marek A. Abramowicz concerning particular aspects of models of rotating stars and properties of their spacetimes. We would like to thank the referee for very helpful comments and suggestions and for pointing out several references that we missed in the previous version of our manuscript.

Software: Mathematica (version 11.3, Wolfram Research 2018) and LORENE/nrotstar (Bonazzola et al. 1998; Gourgoulhon et al. 2016).

References

Abramowicz, M. A., Almergren, G. J. E., Kluzniak, W., & Thampan, A. V. 2003a, arXiv:gr-qc/0312070
Abramowicz, M. A., Blaes, O. M., Horák, J., Kluźniak, W., & Rebusco, P. 2006, CQGra, 23, 1689
Abramowicz, M. A., Bulik, T., Bursa, M., & Kluźniak, W. 2003b, A&A, 404, L21
Abramowicz, M. A., & Kluźniak, W. 2001, A&A, 374, L19
Agrawal, B. K., Shlomo, S., & Au, V. K. 2005, PhRvC, 72, 014310
Akmal, A., Pandharipande, V. R., & Ravenhall, D. G. 1998, PhRvC, 58, 1804
Antoniadis, J., Freire, P. C. C., Wex, N., et al. 2013, Sci, 340, 448
Bakala, P., Urbanec, M., Šrámková, E., Stuchlík, Z., & Török, G. 2012, CQGra, 29, 065012
Belloni, T., Homan, J., Motta, S., Ratti, E., & Mendez, M. 2007, MNRAS, 379, 247
Benhar, O., Ferrari, V., Gualtieri, L., & Marassi, S. 2005, PhRvD, 72, 044028
Berti, E., & Stergioulas, N. 2004, MNRAS, 350, 1416
Berti, E., White, F., Maniopoulou, A., & Bruni, M. 2005, MNRAS, 358, 923
Bonazzola, S., & Gourgoulhon, E. 1996, A&A, 312, 675
Bonazzola, S., Gourgoulhon, E., & Marck, J.-A. 1998, PhRvD, 58, 104020
Boshkayev, K., Bini, D., Rueda, J., et al. 2014, GrCo, 20, 233
Boshkayev, K., Rueda, J., & Muccino, M. 2015, ARep, 59, 441
Boutelier, M., Barret, D., Lin, Y., & Török, G. 2010, MNRAS, 401, 1290
Bursa, M. 2005, in RAGtime 6/7: Workshops on Black Holes and Neutron Stars, ed. S. Hledík & Z. Stuchlík, 39
Čadež, A., Calvani, M., & Kostić, U. 2008, A&A, 487, 527
Chakrabarti, S., Delsate, T., Gürlebeck, N., & Steinhoff, J. 2014, PhRvL, 112, 201102
Chandrasekhar, S., & Miller, J. C. 1974, MNRAS, 167, 63
Cipolletta, F., Cherubini, C., Filippi, S., Rueda, J. A., & Ruffini, R. 2017, PhRvD, 96, 024046
de Avellar, M. G., Porth, O., Younsi, Z., & Rezzolla, L. 2017, arXiv:1709.07706
Demorest, P. B., Pennucci, T., Ransom, S. M., Roberts, M. S. E., & Hessels, J. W. T. 2010, Natur, 467, 1081
Doneva, D. D., Yazadjiev, S. S., & Kokkotas, K. D. 2015, PhRvD, 92, 064015
Doneva, D. D., Yazadjiev, S. S., Staykov, K. V., & Kokkotas, K. D. 2014a, PhRvD, 90, 104021
Doneva, D. D., Yazadjiev, S. S., Stergioulas, N., & Kokkotas, K. D. 2014b, ApJL, 781, L6
Fragile, P. C., Straub, O., & Blaes, O. 2016, MNRAS, 461, 1356
Friedman, J. L., & Stergioulas, N. 2013, Rotating Relativistic Stars (Cambridge: Cambridge Univ. Press)
Gandolfi, S., Illarionov, A. Y., Fantoni, S., et al. 2010, MNRAS, 404, L35
Gilfanov, M., Revnivtsev, M., & Molkov, S. 2003, A&A, 410, 217

Gondek-Rosińska, D., Kluźniak, W., Stergioulas, N., & Wiśniewicz, M. 2014, PhRvD, 89, 104001
Gourgoulhon, E., Grandclément, P., Marck, J.-A., Novak, J., & Taniguchi, K. 2016, LORENE: Spectral methods differential equations solver, Astrophysics Source Code Library, ascl:1608.018
Gutierrez-Ruiz, A. F., Valenzuela-Toledo, C. A., & Pachon, L. A. 2013, 19 arXiv:1309.6396
Hartle, J. B. 1967, ApJ, 150, 1005
Hartle, J. B., & Thorne, K. S. 1968, ApJ, 153, 807
Hasinger, G., & van der Klis, M. 1989, A&A, 225, 79
Haskell, B., Ciolfi, R., Pannarale, F., & Rezzolla, L. 2014, MNRAS, 438, L71
Hessels, J. W. T., Ransom, S. M., Stairs, I. H., et al. 2006, Sci, 311, 1901
Ingram, A., & Done, C. 2010, MNRAS, 405, 2447
Ingram, A., Done, C., & Fragile, P. C. 2009, MNRAS, 397, L101
Ingram, A., Maccarone, T. J., Poutanen, J., & Krawczynski, H. 2015, ApJ, 807, 53
Kato, S., Fukue, J., & Mineshige, S. 1998, Black hole Accretion Disks (Kyoto: Kyoto Univ. Press)
Kato, S. 1989, PASJ, 41, 745
Kato, S. 2001, PASJ, 53, 1
Kato, S. 2004, PASJ, 56, 905
Kluzniak, W., & Abramowicz, M. A. 2001, AcPPB, 32, 3605
Kluźniak, W., & Rosińska, D. 2013, MNRAS, 434, 2825
Kostić, U., Čadež, A., Calvani, M., & Gomboc, A. 2009, A&A, 496, 307
Lo, K.-W., & Lin, L.-M. 2011, ApJ, 728, 12
Lorenz, C. P., Ravenhall, D. G., & Pethick, C. J. 1993, PhRvL, 70, 379
Luk, S.-S., & Lin, L.-M. 2018, ApJ, 861, 141
Maselli, A., Cardoso, V., Ferrari, V., Gualtieri, L., & Pani, P. 2013, PhRvD, 88, 023007
Méndez, M. 2006, MNRAS, 371, 1925
Miller, J. C. 1977, MNRAS, 179, 483
Mishra, B., Vincent, F. H., Manousakis, A., et al. 2017, MNRAS, 467, 4036
Montero, P. J., & Zanotti, O. 2012, MNRAS, 419, 1507
Morsink, S. M., & Stella, L. 1999, ApJ, 513, 827
Nozawa, T., Stergioulas, N., Gourgoulhon, E., & Eriguchi, Y. 1998, A&AS, 132, 431
Pachón, L. A., Rueda, J. A., & Valenzuela-Toledo, C. A. 2012, ApJ, 756, 82
Pani, P., Gualtieri, L., & Ferrari, V. 2015, PhRvD, 92, 124003
Pappas, G. 2012, MNRAS, 422, 2581
Pappas, G. 2015, MNRAS, 454, 4066
Pappas, G. 2017, MNRAS, 466, 4381
Pappas, G., & Apostolatos, T. A. 2012a, arXiv:1211.6299
Pappas, G., & Apostolatos, T. A. 2012b, PhRvL, 108, 231104
Pappas, G., & Apostolatos, T. A. 2013, MNRAS, 429, 3007
Pappas, G., & Apostolatos, T. A. 2014, PhRvL, 112, 121101
Parthasarathy, V., Kluzniak, W., & Cemeljic, M. 2017, MNRAS Letters, 470, L34
Paschalidis, V., & Stergioulas, N. 2017, LRR, 20, 7
Reina, B. 2016, MNRAS, 455, 4512
Reina, B., Sanchis-Gual, N., Vera, R., & Font, J. A. 2017, MNRAS, 470, L54
Reina, B., & Vera, R. 2015, CQGra, 32, 155008
Rezzolla, L., Yoshida, S., & Zanotti, O. 2003, MNRAS, 344, 978
Ribeiro, E. M., Méndez, M., Zhang, G., & Sanna, A. 2017, MNRAS, 471, 1208
Rosińska, D., Kluźniak, W., Stergioulas, N., & Wiśniewicz, M. 2014, PhRvD, 89, 104001
Sanabria-Gómez, J. D., Hernández-Pastora, J. L., & Dubeibe, F. L. 2010, PhRvD, 82, 124014
Sham, Y.-H., Chan, T. K., Lin, L.-M., & Leung, P. T. 2015, ApJ, 798, 121
Silva, H. O., Sotani, H., & Berti, E. 2016, MNRAS, 459, 4378
Šrámková, E., Torkelsson, U., & Abramowicz, M. A. 2007, A&A, 467, 641
Staykov, K. V., Doneva, D. D., & Yazadjiev, S. S. 2016, PhRvD, 93, 084010
Steiner, A. W., Prakash, M., Lattimer, J. M., & Ellis, P. J. 2005, PhR, 411, 325
Stella, L., & Vietri, M. 1998, ApJ, 492, L59
Stella, L., & Vietri, M. 1999, PhRvL, 82, 17
Stella, L., & Vietri, M. 2001, in ASP Conf. Ser. 234, X-ray Astronomy 2000, ed. R. Giacconi, S. Serio, & L. Stella (San Francisco, CA: ASP), 213
Stergioulas, N., & Friedman, J. L. 1995, ApJ, 444, 306
Stone, J. R., Miller, J. C., Koncewicz, R., Stevenson, P. D., & Strayer, M. R. 2003, PhRvC, 68, 034324
Stuchlík, Z., & Kološ, M. 2014, PhRvD, 89, 065007
Stuchlík, Z., & Kološ, M. 2015, GReGr, 47, 27
Török, G., Abramowicz, M. A., Bakala, P., et al. 2008a, AcA, 58, 15
Török, G., Abramowicz, M. A., Bakala, P., et al. 2008b, AcA, 58, 113
Török, G., Abramowicz, M. A., Kluźniak, W., & Stuchlík, Z. 2005, A&A, 436, 1
Török, G., Bakala, P., Stuchlík, Z., & Cech, P. 2008c, AcA, 58, 1
Török, G., Bakala, P., Šrámková, E., et al. 2012, ApJ, 760, 138
Török, G., Bakala, P., Šrámková, E., Stuchlík, Z., & Urbanec, M. 2010, ApJ, 714, 748
Török, G., Goluchová, K., Horák, J., et al. 2016, MNRAS, 457, L19
Török, G., Goluchová, K., Šrámková, E., et al. 2017, in Proc. RAGtime: Workshops on Black Holes and Neutron Stars, ed. S. Hledík & Z. Stuchlík (Opava: Silesian Univ.), 523
Török, G., Goluchová, K., Šrámková, E., et al. 2018, MNRAS Letters, 473, L136
Török, G., Kotrlová, A., Šrámková, E., & Stuchlík, Z. 2011, A&A, 531, A59+
Török, G., Stuchlík, Z., & Bakala, P. 2007, CEJPh, 5, 457
Török, G., Urbanec, M., Adámek, K., & Urbancová, G. 2014, A&A, 564, L5
Tsang, D., & Pappas, G. 2016, ApJL, 818, L11
Urbanec, M., Beták, E., & Stuchlík, Z. 2010, AcA, 60, 149
Urbanec, M., Miller, J. C., & Stuchlík, Z. 2013, MNRAS, 433, 1903
van der Klis, M. 2006, in Stellar X-Ray Sources, ed. W. H. G. Lewin (Cambridge: Cambridge Univ. Press), 39
Wagoner, R. V. 1999, PhR, 311, 259
Wagoner, R. V., Silbergleit, A. S., & Ortega-Rodríguez, M. 2001, ApJ, 559, L25
Weber, F., & Glendenning, N. K. 1992, ApJ, 390, 541
Weber, F. 1999, Pulsars as Astrophysical Laboratories for Nuclear and Particle Physics (New York: Taylor & Francis Group)
Wiśniewicz, M., Gondek-Rosińska, D., Kluźniak, W., & Stergioulas, N. 2015, arXiv:1503.06636
Wolfram Research, I 2018, Mathematica, Version 11.3 (Champaign, IL)
Yagi, K., Kyutoku, K., Pappas, G., Yunes, N., & Apostolatos, T. A. 2014, PhRvD, 89, 124013
Yagi, K., & Yunes, N. 2006, arXiv:gr-qc/1608.02582v1
Yagi, K., & Yunes, N. 2013a, Sci, 341, 365
Yagi, K., & Yunes, N. 2013b, PhRvD, 88, 023009